306319320R

Interaction of Proteins with Oligo(ethylene glycol) Self-Assembled Monolayers

A thesis submitted in partial fulfilment of the requirements to proceed to the degree of

Doctor of Philosophy

at the University of Oxford



by

Maximilian W. A. Skoda

Wadham College and Physical Chemistry



Physical and Theoretical Chemistry Laboratory

South Parks Road

Oxford OX1 3QZ

Wadham College

Parks Road

Oxford OX1 3PN

Interaction of Proteins with Oligo(ethylene glycol) Self-Assembled Monolayers

Maximilian W. A. Skoda
Wadham College

Doctor of Philosophy
Trinity Term 2007

The aim of this thesis is the study of protein resistant oligo(ethylene glycol) (OEG) self-assembled monolayers (SAMs) using in situ techniques, such as neutron reflectivity (NR), polarisation modulation infrared spectroscopy (PMIR) and small-angle x-ray scattering (SAXS). In order to elucidate the mechanisms that lead to the non-fouling properties of these SAMs, the SAM-water, protein-protein and protein-SAM interactions have been studied separately.

NR measurements, focused on the solid-liquid interface between OEG SAMs and water, show clear evidence of an extended layer with reduced density water. The reduction in density is up to 10% compared to the bulk value, and extends up to 5 nm into the bulk. The effective area (density reduction×length) of this reduced density water layer did not significantly change when the temperature was reduced to 5 °C. In a complementary study, the interaction of water with protein-resistant $HS(CH_2)_{11}(OCH_2CH_2)_3OMe$ monolayers was examined using in and ex situ PMIR. In particular, shifts in the position of the characteristic C-O-C stretching vibration were observed after the monolayers had been exposed to water. The shift in frequency increased when the SAM was observed in direct contact with a thin layer of water. It was found that the magnitude of the shift also depended on the surface coverage of the SAM. These results suggest a rather strong interaction of oligo(ethylene glycol) SAMs with water and indicate the penetration of water into the upper region of the monolayer. These findings indicate the presence of a tightly bound water layer at the SAM-water interface.

Further NR studies of the interface between OEG SAMs and a highly concentrated protein solution revealed an oscillating protein density profile. A protein depleted region of about 4-5 nm close to the SAM was followed by a more densely populated region of 5-6 nm. These oscillations were then rapidly damped out until the bulk value was reached. The influence of temperature and salt concentration on the protein density profile was small, indicating a rather minor contribution of electrostatic interactions to the protein repulsive force. SAXS measurements of OEG coated gold colloids mixed with proteins in solution did also not show any pronounced salt concentration dependence of the colloid-protein interaction.

The strong association of water with the SAM and the layer of tightly bound water, together with the lack of electrostatic repulsion, suggest that the adsorption of proteins is energetically hindered by the presence of a strongly bound hydration layer.

Acknowledgements

It is customary to thank all those who have helped me with the completion of this thesis, whether more directly in scientific matters, or in other ways by providing me with education, money, genes or friendship.

Indubitably, I have to thank Prof. F. Schreiber for offering me the interesting topic, his ceaseless advice and the opportunity to work in changing environments at various universities across Europe.

I would also like to thank the following people:

Prof. M. Grunze for his support during my time in Heidelberg, and in particular Dr. R. Dahint for his support, help with beamtimes and for many fruitful discussions.

Dr. R. K. Thomas for his advice both in scientific and in organaisatorial matters.

Dr. R. M. J. Jacobs for his support in the Surface Analysis Facility, for his help on numerous beamtimes, for discussions and for the careful proof-reading of my thesis.

Dr. F. Zhang for the work and help with the SAXS experiments.

Dr. R. Martin and S. Zorn for very enjoyable beamtimes (and games of pool).

Of course, the neutron and x-ray work would not have been possible without the support of M. Wolff, J. Webster, S. Holt and C. Martin.

For technical support I would like to acknowedge the excellent work of the mechanical workshops of the PTCL in Oxford and that of the Angewandte Physik in Tübingen. Also, here thank you very much to K. Hagdorn.

Thanks to Alex, Alex, Mirco, Petra and Ute for their help and the very pleasant atmosphere within the group. Special thanks to Stefan and Alex, who have gone through thick and thin from the very beginning. In particular, Stefan, thank you for so many chats, scientific and other. And thank you Alex, for your help, particularly in computer matters, for the squash games and the coffee breaks.

For the workless part of life I would like to thank Alana, Bindi, Christian, Christof, Dennis, Julia, Julia, Jutta, Katrina, Markus, Tina, Wolfgang, and of course there are too many others, friends, near and far, old and new, who cannot be all mentioned.

Most importantly, I would like to thank my wonderful wife Hannah for her patience and understanding. Finally, I would like to express my deepest gratitude to my parents, for their trust in me and all their sacrifices.

Contents

I. Introduction and theoretical background **13**

1. Introduction **15**
1.1. Motivation 15
1.2. Research objectives 16
1.3. Scope of this thesis 16

2. Literature review **19**
2.1. Protein resistant self-assembled monolayers 19
2.2. Monolayer protected clusters 21
2.3. Protein-protein and protein-surface interactions 21
2.3.1. Protein-protein interactions 21
2.3.2. Theory of protein adsorption 23

3. Experimental theory **27**
3.1. Infrared Spectroscopy 27
3.1.1. Theoretical background 27
3.1.2. The infrared spectrometer 29
3.1.3. Fourier Transform Infrared Spectroscopy (FTIR) 31
3.1.3.1. Calculation of the interferogram 32
3.1.3.2. Wave optics 34
3.1.3.3. Reflection absorption infrared spectroscopy (RAIRS) 35
3.1.4. Polarisation modulation (PMIRRAS) 37
3.2. Neutron Reflectivity (NR) 40
3.2.1. Roughness 45
3.2.2. Off-specular reflectivity 45
3.3. Small-angle x-ray scattering 46
3.3.1. Scattering from proteins in solution 51
3.3.2. Scattering from colloidal particles 54
3.4. Ellipsometry 55
3.5. UV-vis spectroscopy 56

References **58**

II. Results and discussion **63**

4. Experimental practical **65**
4.1. Sample preparation 65
4.1.1. SAMs on flat substrates 65
4.1.2. Preparation of surface modified gold colloids 67

4.2. Neutron reflectometers 68
4.2.1. ADAM at ILL 68
4.2.2. SURF at ISIS 69
4.3. Liquid cell for neutron reflectivity 69
4.4. Data treatment for neutron reflectivity 71
4.5. Index matching for neutron reflectivity 73
4.6. The infrared spectrometers 75
4.7. The liquid cell for PMIRRAS 75
4.8. Small-angle x-ray scattering 78
4.9. X-ray reflectivity 79

5. Behaviour of Water at the SAM/water interface **81**
5.1. Introduction 81
5.2. Water density at the interface: OEG SAMs 82
5.2.1. Data fitting and interpretation 82
5.2.2. Neutron reflectivity at room temperature 85
5.2.3. Temperature dependence 89
5.3. Water density at the interface: Alkanethiol SAMs 92
5.4. Solvation of an OEG SAM (PM-IRRAS) 94
5.4.1. Band assignments 95
5.4.2. Experimental details 96
5.4.3. Oligo(ethylene glycol) C-O-C Region (ex situ) 98
5.4.4. Oligo(ethylene glycol) C-O-C Region (in situ) 100
5.4.5. Coverage Dependence 105
5.4.6. Conclusions 108
5.5. Simulation and optimisation of the PMIRRAS signal 108
5.5.1. Mathematical framework and implementation 108
5.5.2. Comparison of calculations and experiments 114
5.6. OEG SAMs in contact with non-polar solvents 119

6. Protein-protein interactions in solution **123**
6.1. Introduction 123
6.2. Experimental details 124
6.3. Low Ionic Strength, I<0.3 M, E+SC Model Fit 125
6.4. Moderate Ionic Strength, I = 0.3 and 0.5 M 132
6.5. High Ionic Strength, I > 0.5 M, E+SW Model Fit 133
6.6. Interaction Phase Diagram 138
6.7. Conclusions 139

7. Proteins at the SAM/water interface **141**
7.1. SAMs on flat interfaces 141
7.1.1. Introduction 141
7.1.2. Results from neutron reflectivity: sensitivity 144
7.1.3. Results from neutron reflectivity: density profiles 146
7.1.4. Sensitivity of models 152
7.1.5. Salt effects 154
7.1.6. Effect of Temperature 159
7.1.7. Conclusions 163
7.2. SAMs on curved interfaces 165

7.2.1. Characterisation of OEG decorated gold colloids 165
7.2.2. Effect of ionic strength (NaCl) on functionalised gold colloidal and protein solutions 168
7.2.3. Interaction of proteins with OEG functionalised gold colloids in mixed solutions 170
7.2.4. Discussion of the interactions in mixed solutions 176
7.2.5. Conclusions 179

References **180**

8. Summary and conclusion **187**
8.1. Summary and perspectives 187
8.2. Methodical achievements 189

A. Implementation of Abeles' matrix formalism **191**
A.1. Hansen's notation implemented in IgorPro 191
A.2. Calculation of the mean square electric field at the metal surface . . 194

B. Measured water layer thicknesses for in situ PMIRRAS **197**

C. Fitting software **199**

D. List of acronyms and symbols **201**

E. Photographs of experimental setup **203**

Part I.

Introduction and theoretical background

1. Introduction

1.1. Motivation

Oligo (OEG) and Poly (Ethylene Glycol) (PEG) are materials of tremendous importance for bio-technological applications, such as bio-sensing [1,2] or model membranes [3,4]. In particular, it has been found that OEG (and PEG) coated surfaces are resistant to protein adsorption [5], although the underlying mechanisms of this resistance have yet to be fully established. Several mechanisms have been discussed, and the subject is still in the focus of research and a matter of debate. While the mechanisms leading to a repulsion of proteins in the vicinity of the PEG SAM can be theoretically explained by the resistance to dehydration and steric confinement of the swollen polymer [6,7], the same arguments are not valid for the densely packed and conformationally restricted OEG SAMs. For the efficient development of custom designed protein resistant coatings a thorough understanding of the underlying mechanisms leading to the repulsion of proteins for OEG SAMs is necessary. Recently, long-range repulsive forces have been observed between protein coated AFM tips and protein resistant SAMs of EG3-OMe (Au/S-$(CH_2)_{11}(OCH_2CH_2)_3$-OCH_3) [8]. The measured repulsive potential scaled with the Debye length of the solution which suggests a negative surface charge within the EG3-OMe layer. Based on these results, an electrostatic origin of the repulsive forces between proteins and EG3-OMe was proposed. It has been suggested that this repulsive potential arises from a tightly bound layer of hydroxide ions which preferentially penetrate into the Self-Assembled Monolayers (SAM) and create a net negative electrostatic potential [9], which then acts against the also negatively charged protein molecules. The repulsive forces observed in AFM measurements are consistent with the protein resistant character of the SAMs, but the principal drawback of this experimental approach is that it cannot study the protein moving freely in solution, and the per-

turbation of constraining the protein to the AFM tip may be severe. Due to the subtlety of the competing mechanisms and the numerous factors that have an impact on the protein resistance, the issue of the provenience of protein resistance in OEG SAMs remains a subject of controversy [?, 10]. It is clear however, that the understanding of the water-OEG interaction is a vital step required to elucidate the mechanism of protein resistance. Recent findings [11, 12] suggest that a variation of the surface density impacts on the protein resistance. Theoretical work by Wang et al [13] implies that OEG conformers which have gauche rotations of opposite directions around neighbouring ethylene glycol (EG) units are penetrated by water, because in these structures water can form double and triple hydrogen bonds with up to three oxygen atoms along the (EG) molecule [14].

1.2. Research objectives

The major research objective pursued by this project was the in-depth understanding of the interaction of proteins with functionalised surfaces. Non-fouling, self-assembled monolayer protected surfaces were of particular interest, due to their importance for a variety of applications, and because the mechanisms on a molecular level leading to protein resistance were still not fully understood. The focus of the research was on the investigation of the relevant protein-monolayer systems *in situ*. For this purpose appropriate methods such as neutron reflectivity and polarisation modulation infrared spectroscopy have been employed and the experimental conditions have been precisely adjusted in order to achieve the necessary sensitivity for quantitative studies.

1.3. Scope of this thesis

The contents of this thesis is divided into six chapters. The first chapter gives a short motivation for the present work and contains a brief statement on the research objectives. A review of literature relevant for the research and the results described in this thesis is given in Chapter 2. The theoretical background for the techniques employed is presented in Chapter 3, with an emphasis on neutron reflectivity, polarisation modulation infrared spectroscopy and x-ray small-angle scattering. Chapter

4 gives a description of the experimental details, the materials used and of the experimental setups. The central part is found in Chapters 5 to 7, where all findings and experimental results are presented and discussed. In Chapter 5 the interaction of water with self-assembled monolayers is addressed, while Chapter 6 is concerned with the interaction of proteins with each other in solution. With these prerequisites, the structure of the solid-liquid interface and the resulting interactions of proteins with oligo (ethylene glycol) terminated monolayers are illuminated. Finally, the most important achievements of this project are summarised in Chapter 8.

2. Literature review

2.1. Protein resistant self-assembled monolayers

Self-assembled monolayers (SAMs) are a relatively new, but rapidly growing field of research. From their discovery through the pioneering work of Nuzzo and Allara in 1983 [15], SAMs on gold based on a variety of molecular building blocks have been studied, and have also been employed for numerous applications, such as protective coatings, wetting control, friction and lubrication control, as model systems for surface chemistry and bio-related applications [16, 17], to name a few.

Oligo(ethylene glycol) (OEG) and poly(ethylene glycol) (PEG) are materials of tremendous importance to biotechnological applications, such as biosensing [1,2] and model membranes [3, 4]. In particular, Prime and Whitesides [5] found that OEG-coated (and PEG-coated) surfaces are resistant to protein adsorption, although the underlying mechanisms of this resistance have yet to be fully established.

For PEG based SAMs Jeon et al. [6] have proposed a repulsion mechanism that originates from changes in the interaction free energy caused by the compression of the polymer chains upon the approach of the protein. They calculated the steric repulsion free energy considering the osmotic and elastic effects of chain compression and compared this with the van der Waals and hydrophobic interaction free energies. They found that for sufficiently long chains and surface density of the PEG monolayer, the steric repulsion overcomes the other two attractive contributions.

Jeon et al. used the following expressions for the three contributions:

STERIC INTERACTION

$$\frac{\Delta F_s}{kT} = \frac{k_1}{a^2}\left(\frac{7}{5}\frac{k_2}{k_1}\right)^{5/12} N\sigma^{11/6}\left\{\left[\left(\frac{L_0}{L}\right)^{5/4} - 1\right] + \frac{5}{7}\left[\left(\frac{L_0}{L}\right)^{7/4} - 1\right]\right\}. \qquad (2.1)$$

Here, N is the number of oligomer units of the PEG molecule, D is the average distance between two terminally attached PEG chains, a is the first dimension of the crystallographic unit cell, and $\sigma = a^2/D^2$ is the surface density. k_1 and k_2 are experimentally determined constants involving osmotic and elastic contributions, respectively. Attractive van der Waals contributions, which become important only for short chain lengths, are described using the non-retarded HAMAKER constants $A(i)$ for the interactions between the various media in the system (water, protein, water in PEG, PEG, substrate):

VAN DER WAALS INTERACTION

$$\frac{\Delta F_a}{kT} = -\frac{1}{12\pi kT}\left[\frac{A(1)}{d^2} + \frac{A(2)}{(d+t)^2} + \frac{A(3)}{(d+t')^2} + \frac{A(4)}{(d+t+t')^2}\right]. \qquad (2.2)$$

The hydrophobic interaction between the hydrophobic substrate and an assumed hydrophobic surface on the protein was approximated from experiments to be:

HYDROPHOBIC INTERACTION

$$\frac{\Delta F_h}{kT} = -0.1359e^{-s/14}(\text{Å}^{-2}), \qquad (2.3)$$

where s is the distance in Å between the hydrophobic surfaces.

Jeon et al. came to the conclusion that the protein resistance of PEG SAMs is a steric effect of the surface attached polymer chains, and that a high surface density and long chain length of the PEG are desirable for protein resistance.

A comprehensive study on OEG SAMs and factors that determine their protein resistance was given by Herrwerth et al. [9]. It was suggested that internal and terminal hydrophilicity plays a major role, as well as the lateral packing density. Other studies by Vanderah et al. [11] revealed that protein adsorption is minimised at a lateral packing density of 60-80%, while the amount of adsorbed protein increases for lower surface coverage, and also for very high surface coverage (>80%). The adsorption at high SAM coverage is attributed to a change in the molecular conformation from helical to all-trans [9].

2.2. Monolayer protected clusters

Self-assembled monolayers can not only be used for the coating of flat surfaces, rather monolayer protected clusters (MPCs) that employ functional organic groups on the nanoparticle surface for the selective binding of proteins have come into the focus of intensive research. This method offers the possibility to influence cellular processes such as protein-protein interactions or enzyme activity. This represents a rather new and exciting field of research, which offers plentiful possibilities. For instance, recently Rotello et al. could achieve surface recognition and activity inhibition of α-chymotrypsin by developing mixed monolayer protected nanoparticles with anionic functional groups [18]. Other novel kinds of mixed monolayer protected nanoparticles can be used for specific interactions which target biological molecules. Such a mixed monolayer is composed of a protective component and a binding component. Ethylene glycol oligomers can be employed as the protective component, while the binding component is chosen to interact specifically with the protein or biomolecule of interest [19].

2.3. Protein-protein and protein-surface interactions

2.3.1. Protein-protein interactions

Interactions between protein macromolecules in solution are a key factor in determining the phase behaviour of biological systems. Also, the phase behaviour determines whether one can get good quality protein crystals for x-ray diffraction, which is critical in obtaining the protein's three-dimensional structure and in elucidating its biochemical role [20–22]. George and Wilson [23] proposed a relation between protein crystallisation behaviour and the osmotic second virial coefficient, A_2, which represents the interaction potential between a pair of macromolecules in solution. A positive value of A_2 implies a repulsive interaction, and a negative value indicates an attractive interaction. On the basis of measurements of a variety of proteins, they found that protein crystallisation occurs only when A_2 lies within a narrow window. These studies provide a way to understand the mechanism of protein crystallisation and a guide for optimisation of conditions for protein crystallisation [24–29]. On the other hand, the protein interaction and aggregation processes are also very im-

portant in understanding many physiological problems, for example, diseases such as Alzheimer's or Kreutzfeld-Jacob and Parkinson's, which are caused by protein or peptide association phenomena, and the short-range order of crystallin proteins accounts for the eye lens transparency [22, 30]. In vivo, the biochemical function of proteins requires the cooperation of the ions around them. Therefore, studies on the effect of ionic strength and the nature of ions on protein interaction have attracted much attention in biophysics [24, 25, 31–34]. Studies show that the interaction strongly depends on the nature of the salt used at a fixed ionic strength, which is known as the Hofmeister effect [24, 25, 32].

Protein solutions can be modelled as a charged, colloidal system, and their phase behaviour under low ionic strength can be described by the Derjaguin-Landau-Verwey-Overbeek (DLVO) theory [35]. The DLVO theory describes the interaction between charged colloids as a combined hard-sphere interaction, electrostatic repulsive interaction, and a van der Waals attractive interaction. Under low ionic strength, the DLVO theory describes the phase behaviour of a protein solution satisfactorily [24, 25, 36]. However, many studies indicate that the DLVO theory cannot fully explain the rich phase behaviour of protein solutions [22, 24, 37–40]. In some cases, a temperature-induced liquid-liquid phase separation has been observed in protein solutions [41, 42]. Theoretical and experimental studies indicate that a short-range attractive interaction is present and dominates the liquid-liquid phase separation and equilibrium cluster formation [24, 25, 31, 32, 43–47]. Although the van der Waals attractive potential is able to account for the liquid-liquid phase separation of a protein solution without adding salt, other nonspecific interactions, such as hydration forces or hydrophobic interactions, may also be involved [24, 25, 46]. For example, Petsev and Vekilov studied interactions of the protein apoferritin in aqueous solutions, and they found that the second osmotic virial coefficient exhibits a minimum when plotted as a function of salt concentration. They argue that the repulsive interaction at high salt concentration comes from a hydration effect [48]. In another example, Chen and co-workers [31, 32, 49] studied lysozyme and cytochrome c under high salt concentration, and they found an increase of $I(0)$ and even a new peak at very low momentum transfer in small-angle neutron scattering (SANS). These results were also attributed to a short-range attractive interaction. Whether the increase of the forward intensity is induced by a weak, long-range attraction is

still a matter of debate [49,50], and the nature of the attractive interaction potential rising from these studies is still not fully understood.

2.3.2. Theory of protein adsorption

The adsorption of proteins plays an important role in biological processes. At the cellular level proteins adsorbed to the cell membrane can act as ion channels, catalysts or transport enzymes. In general, protein adsorption is accompanied by changes in the secondary and tertiary structure. However, the structure of proteins is highly complex and the various hydrophilic, hydrophobic, charged and neutral amino acid residues render the protein amphiphilic, and are partly responsible for the high surface reactivity of proteins. This is the reason why proteins are found to adsorb on a multitude of surfaces, such as organic materials, metals, glass an so on. Due to the far reaching implications in biology, medicine and bio-technology, it is crucial to understand the driving forces for protein adsorption on a molecular level.

More recently, coatings have been developed which are able to prevent and control the non-specific adsorption of proteins. A subgroup, namely oligo (ethylene glycol) terminated thiol based surface coatings are in the focus of this thesis. However, an understanding of the protein *resistant* properties of coatings inevitably require the knowledge of the mechanisms which lead to *adsorption*. The following section will give a brief overview over forces and interactions that are involved in the process of protein adsorption to surfaces. Beyond the three more dominant interactions (van der Waals, electrostatic and hydrophobic interactions) introduced in this section, there are also other effects to be considered, such as the change in conformational entropy of a protein upon adsorption or the phenomenon of counter-ion evaporation, which can become important under certain conditions. However, these very specific effects are beyond the scope of this work and are only mentioned for the sake of completeness.

Van der Waals interactions The interaction between (neutral) atoms can be described using van der Waals (dispersion) interactions. These dispersion interactions are of short range (compared to for example electrostatic interactions) for molecules and consist of a sum of Keesom, Debye, and London contributions. Because the total van der Waals interaction between two macroscopic bodies is simply the sum

of van der Waals contributions between individual atoms, this concept can be applied to macromolecules, such as polymers and proteins, and to colloidal systems. In the approach used by HAMAKER (1937) the dispersion energy contributions from individual atom-atom interactions is approximated by a pairwise summation. Under consideration of the geometry the van der Waals interaction energy between a sphere and wall, and between two spheres, in a solvent, can be written as [51]

SPHERE-PLANE

$$\frac{\Delta F}{kT} = -\frac{A_{213}}{6kT}\left(\frac{R}{d} + \frac{R}{d+2R} + \ln\frac{d}{d+2R}\right) \tag{2.4}$$

and

SPHERE-SPHERE

$$\frac{\Delta F}{kT} = -\frac{A_{213}}{6kT}\left(\frac{2R_1R_2}{r^2-(R_1+R_2)^2} + \frac{2R_1R_2}{r^2-(R_1-R_2)^2} + \ln\frac{r^2-(R_1+R_2)^2}{r^2-(R_1-R_2)^2}\right) \tag{2.5}$$

respectively, where R is the radius of the sphere and d is the nearest distance between sphere and plane, and R_1, and R_2 are the radii of the spheres, r is the centre-to-centre distance between the spheres, k is the BOLTZMANN constant and T is the absolute temperature. A_{213} are the HAMAKER constants, dependent only on the polarisabilities of spheres, wall and solvent. The total HAMAKER constant is composed of HAMAKER constants of the individual objects (A_{ii}) as

$$A_{213} \simeq \left(\sqrt{A_{22}} - \sqrt{A_{11}}\right)\left(\sqrt{A_{33}} - \sqrt{A_{22}}\right). \tag{2.6}$$

Thus, the interaction of two identical bodies across a third medium is always attractive. Furthermore, because HAMAKER constants are usually of the order of kT, van der Waals interactions only become significant at very small separation distances.

Electrostatic interactions A discussion of the electrostatic interactions between a charged protein and a planar surface with homogeneous and constant surface charge σ density mediated by an electrolyte solution is given by [52]. The internal electro-

static potential of the protein, which is treated as a continuum colloidal particle, is written as

$$\nabla^2 \Phi^i = -\frac{\rho^i}{\epsilon^i}, \tag{2.7}$$

where ρ^i represents the charge distribution and ϵ^i the dielectric permittivity of the protein interior. The internal charge distribution consists of the charged amino acid sites,

$$\rho^i = \sum_k q_k \delta\left(\mathbf{x} - \mathbf{x}_k\right) \tag{2.8}$$

in which the locations of the charges are $\mathbf{x}_k$, $\delta(x)$ represents the Dirac delta function, and q_k gives the magnitude of charge k. For a z:z electrolyte, the exterior electrostatic potential Φ^e is described by the linearised POISSON-BOLTZMANN equation

$$\nabla^2 \Phi^e = \kappa^2 \Phi^e, \tag{2.9}$$

where $\kappa = (2e^2 z^2 \rho^\infty)/\epsilon^e kT$, e is the electronic charge, z the ion valency, k the Boltzmann constant, T the temperature, and ρ^∞ the bulk concentration of electrolyte before dissociation. The potentials can only be calculated numerically in the case of a protein, due to its complex geometry. With these prerequisites the total free energy of the system can be computed:

$$F = \frac{1}{2} \int_{\partial P} \sigma \Phi^e dA + \frac{1}{2} \sum_{k=1}^{n} q_k \Phi^i(x_k) \tag{2.10}$$

where ∂P represents the planar, charged surface. With this expression, the free energy change in bringing a protein molecule from free solution to a given position and orientation in the vicinity of a surface can be computed.

Hydrophobic interactions The antipathy between non-polar molecules and polar solvents, such as water, in mostly due to the strong interaction of the solvent molecules with each other, for instance via hydrogen bonding. This can lead to an effective attraction between the hydrophobic species in an aqueous medium. Moreover, there is a length scale dependence of the solvation free energy [53]: if one considers hydrophobic spheres with diameters much smaller than 1 nm, then the solvation free energy scales with the *volume* excluded by the solute (sphere). For spheres with diameters larger than 1 nm, the solvation free energy scales with the

surface of the excluded volume. This is due to the fact that the formation of a hydrogen bond network in the vicinity of a large hydrophobic object is geometrically impossible [54].

The resulting effect can induce drying. This drying can lead to a strong attraction between large hydrophobic objects, such as a protein and a hydrophobic surface. This "hydrophobic effect" can lead to changes of the net free energy much larger than kT [54]. The hydrophobic effect therefore represents the major driving force for protein adsorption.

3. Experimental theory

3.1. Infrared Spectroscopy

3.1.1. Theoretical background

Infrared spectroscopy is a resonant technique, which can be used to excite vibrational states within molecules in the range of about 10 to 13000 cm^{-1}. Usually this spectral range is roughly divided into three regions by convention:

region	wavelength range [μm]	wavenumber range [cm^{-1}]
near infrared (NIR)	0.77-2.5	13000-4000
mid infrared (MIR)	2.5-50	4000-200
far infrared (FIR)	50-1000	200-10

Vibrations observed in the NIR region are mainly overtones, the MIR contains the fundamental vibrations, and in the FIR only backbone vibrations can be observed.

Only the vibrations of molecules in which the dipole moment changes during the vibration ($\partial \boldsymbol{\mu}_{el}/\partial r \neq 0$) are infrared active. Thus the excitation of the vibrational states has to be connected with a change in the dipole moment of the molecule in order to be detected as an absorption line in the spectrum:

$$\Delta I \approx \text{probability of absorption} \sim \left[\boldsymbol{E} \cdot \frac{\partial \boldsymbol{\mu}_{el}}{\partial r}\right]^2 \tag{3.1}$$

Many functional groups have absorption frequencies which are largely independent of molecular environment. These characteristic absorption bands serve as a 'finger-print' for the identification of the functional group. For the simple case of diatomic molecules, the absorption frequency can be approximated by a *harmonic oscilla-*

tor model. The quantum mechanical treatment of the harmonic oscillator leads to discrete values for the oscillator energy [55]:

$$E_n = h\nu_0 \left(n + \frac{1}{2} \right), \tag{3.2}$$

where $n = 0, 1, 2, 3, ...$ are the allowed quantum numbers for the vibrational states and ν_0 is the eigenfrequency of the oscillator:

$$\nu_0 = \frac{1}{2\pi} \sqrt{\frac{k}{\mu}};\ \mu = \frac{m_1 \cdot m_2}{m_1 + m_2}, \tag{3.3}$$

where μ is the reduced mass of the two atoms and k is the 'spring' constant, dependent upon the bond strength. From this model it follows that the vibrational states are equidistant and that a molecule can change its energy level ($\Delta\nu = \pm 1$) by absorbing or emitting a photon of energy $h\nu_0$. The harmonic oscillator model however, cannot account for a series of phenomena observed in real molecules. For instance, a molecule will dissociate when the amplitude of the vibration is too large. Equally, the repulsive potential rises more quickly when the vibrating atoms approach each other, a consequence of the PAULI principle. Therefore, the more realistic model of the *an-harmonic oscillator* (e.g. the MORSE potential) can be employed. In this model, the energy levels are no longer equidistant, rather they converge into a continuum at the dissociation energy. Within this model, considering the quantum mechanical selection rules, not only transitions to the neighbouring energy level are possible (fundamental vibrations), but also excitations to higher levels are allowed ($\Delta\nu = \pm 2, \pm 3, ...$). These vibrations are called overtones and their intensities (probabilities of absorption or emission) decay rapidly with Δv. At room temperature, almost all excitations originate from the ground state ($E_0 = h\nu/2$), since only this is generally occupied [55].

In general, transitions in rotational and translational states are also induced alongside with the vibronic excitations. However, the rotational fine structure is only visible for molecules in the gas phase. Since most studies in this thesis are concerned with soft condensed matter, these excitations are only of minor interest.

The vibrational state of an oscillating molecule in which the frequency of vibration is the same in all directions, is called the normal mode. If only those normal modes

which do not involve translations of rotations of the molecule are considered, the resulting vibrations can be divided into two categories:

- **Valence or stretching vibrations (ν)** The vibration amplitude is collinear to the bond axis and the bond *length* varies periodically. In the case of symmetrically equivalent atomic groups, the group vibration can be either symmetric (ν_s) or a(nti)-symmetric (ν_{as}), depending on whether the symmetry of the molecule is preserved.

- **Deformation vibrations (δ)** If the bond *angle* changes during the vibration, while the bond length remains almost constant, this is called a deformation (or bending) vibration. Here too, depending on the preservation of molecular symmetry, symmetric (δ_s) and asymmetric (δ_{as}) vibrations can occur. Depending on the direction of the deformation with respect to the bond axis, special sub-types of deformation vibrations can be defined: *rocking* (r), *twisting* (τ) and *wagging* (w) vibrations. In a planar molecule these vibrations can be either in- or out-of-plane.

The number of possible vibrations in a molecule consisting of n atoms can be determined by symmetry considerations. Such a molecule possesses $3n$ degrees of freedom. However, three of these are degrees of freedom for translation and another two, or three, in the case of non-linear molecules, are associated with rotational motion. The total number of possible vibrational modes is thus $3n - 5$ for a linear molecule and $3n - 6$ for a non-linear one.

3.1.2. The infrared spectrometer

A modern Fourier transform infrared spectrometer usually consists of the following main components (**Figure 3.1**): light source, reference laser, MICHELSON interferometer, beam optics, sample compartment and detector. This section will describe the basic working principles of a generic spectrometer; details about the experimental setup used in this thesis can be found in the following chapter.

Radiation sources The most common and widely used light source is the so-called *Globar*. It is suitable for use in the mid-IR region, its spectrum reaching down to approximately 100 cm^{-1}. It is a silicon carbide rod of 5 to 10 mm width and 20 to

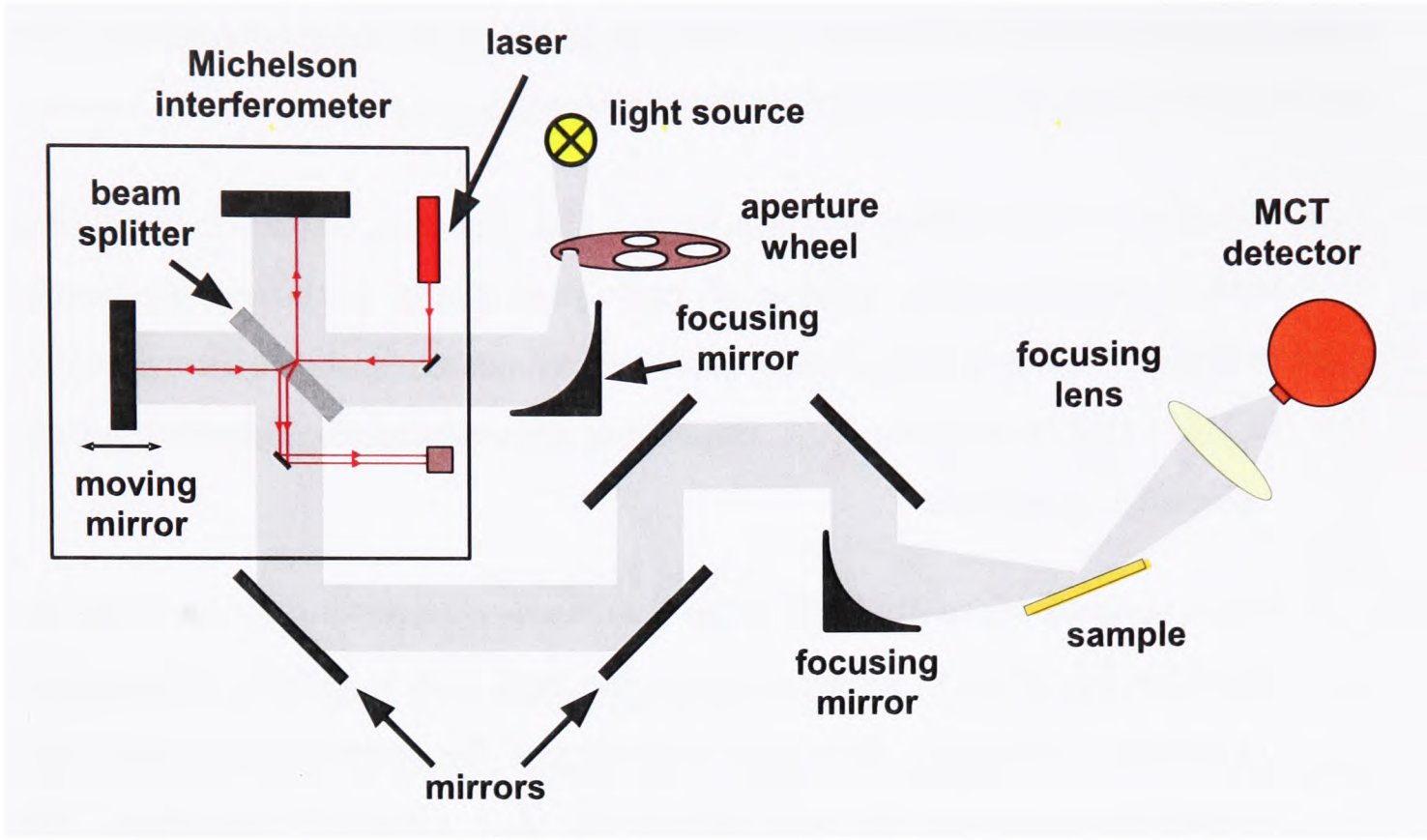


Figure 3.1.: Sketch (top view) of an infrared spectrometer.

50 mm length which is electrically heated up to 1500 K. Due to its high power intake, it requires water cooling during operation. Another source for the mid-IR region is the NERNST rod. This light source consists of several ceramic rods, a few centimetres long and few millimetres thick, composed of a mixture of certain (rare earth) oxides (e.g., zirconium oxide ZrO2, yttrium oxide Y_2O_3 and erbium oxide Er_2O_3 at a ratio of 90:7:3 by weight). It operates at a higher temperature than the Globar, of about 1900 K, with an intensity maximum at ~1-2 μm. Unlike the Globar, the NERNST rod has the disadvantage that it requires auxiliary heating, since it is not conductive at room temperature. It is also rather sensitive to mechanical stress. For the far infrared region, high pressure mercury vapour lamps can be used.

Michelson interferometer An ellipsoidal mirror creates a parallel beam of light from the light source. This parallel beam is divided into two (ideally of equal intensity) beams by a *beam splitter*[1] One beam is reflected onto a fixed mirror, the other transmitted to a *moving mirror*. Both beams are reflected back to the beam splitter, where they reunite with an optical path difference x giving rise to an interference signal.

[1]The beam splitter usually consists of a thin layer of a high refractive index material (e.g. germanium $n = 4$ or silicon $n = 3.6$) sandwiched between two plates of an IR transparent crystal (typically an alkaline halogenide). The reflectivity of the thin layer is adjusted appropriately according to the Fresnel formulae (**Equations 3.13- 3.15**)

Reference laser The zero crossings of helium/neon (HeNe) laser (632.8 nm or 15800 cm^{-1}) signal are used for the precise determination of the optical path difference in the MICHELSON interferometer. The laser beam is coupled into the interferometer and the moving mirror gives rise to a monochromatic interference of the laser light, together with the infrared light.

Detectors Thermo-elements and photo diodes can be employed for the detection of infrared light. However, due to their superior sensitivity, two detector types are mainly used, the liquid nitrogen cooled $Hg_{1-x}Cd_xTe$ (MCT) and the DTGS (deuterated triglycine sulfate) detector, the latter operating at room temperature by means of the temperature dependent change in polarisation of a ferroelectric substance.

Scan modes Two different spectrometers have been used for the present thesis (**Chapter 4.6**). The operation of the moving mirror was thus different: the Digilab FTS 6000 spectrometer operated in *step-scan* and the Bruker VERTEX70 in *rapid-scan* mode. In rapid scan mode, the mirror is moved with constant velocity, which introduces a modulation of frequency

$$f_{\tilde{\nu}} = 2v_m\tilde{\nu} \tag{3.4}$$

into the interferogram intensity signal. Here v_m denotes the velocity of the moving mirror. Typical velocities are around 0.5 cm/s, corresponding to modulation frequencies of 1-5 kHz. The signal in this frequency range is then electronically filtered using a bandpass filter prior to the detector.

3.1.3. Fourier Transform Infrared Spectroscopy (FTIR)

The MICHELSON interferometer causes an interference of the outgoing light waves. In the simple case of monochromatic light of wavelength λ, the intensity of the outgoing signal oscillates like a cosine as a function of the retardation x of the moving mirror: if the optical path between beam splitter and both fixed and moving mirror are equal, the interference will be constructive. If the total optical path difference is $x = \lambda/2$, the outgoing waves will have a phase difference of $\lambda/2$ and the total amplitude will

vanish. In more general terms, this relationship can be described by the following equation:

$$I(x) = 2I_0RT(1 + \cos(2\pi\tilde{\nu}x)), \tag{3.5}$$

where I_0 is the intensity of the incoming light, R and T are the reflection and transmission of the beam splitter respectively ($R + T = 1$) and $\tilde{\nu}$ is the wavenumber of the IR beam. In the case of polychromatic light, I_0, R and T are functions of the wavelength and the observed intensity becomes

$$I(x) = 2\int_0^\infty I_0(\tilde{\nu})\,R(\tilde{\nu})\,T(\tilde{\nu})\,(1 + \cos(2\pi\tilde{\nu}x))\,d\tilde{\nu} \tag{3.6}$$

If $I(\infty)$ is defined as the intensity at very large optical path lengths, i.e. retardations much larger than the wavelength, then the $\cos(2\pi\tilde{\nu}x)$ terms average out to zero. The resulting *interferogram function* $F(x)$ then reads

$$F(x) = I(x) - I(\infty) = \int_0^\infty A(\tilde{\nu})\cos(2\pi\tilde{\nu}x)\,d\tilde{\nu}, \tag{3.7}$$

where $A(\tilde{\nu}) = 2I_0(\tilde{\nu})\,R(\tilde{\nu})\,T(\tilde{\nu})$ is the intensity of the source as a function of the wavenumber, including corrections for the transmission of the beam splitter.

The spectral intensity is then obtained by a FOURIER transform of the interferogram function:

$$A(\tilde{\nu}) = 2\int_{-\infty}^\infty F(x)\cos(2\pi\tilde{\nu}x)\,dx. \tag{3.8}$$

The optical retardation x is accurately determined from the zero crossings of the interference fringes of the reference laser mentioned in the previous section. Since in practice the interferogram function is sampled in discrete steps and the optical retardation is finite, i.e. the limits of the integral **Equation 3.8** are finite, the spectral resolution $\Delta\tilde{\nu}$ depends on the maximum retardation, in practice of the order of a few centimetres.

3.1.3.1. Calculation of the interferogram

The computation of the final spectrum, as described above, involves a FOURIER transformation. However, some further considerations are necessitated by the fact that experimentally recorded interferograms are digitised, finite and not symmetric

to the origin ($x = 0$). The computation of the spectrum comprises the following steps:

Apodisation The recorded interferogram is finite and drops to zero abruptly at both ends, which causes disruptions in the line shape of the calculated spectrum. The apodisation creates a smooth transition to zero at both end of the interferogram by multiplying it with an apodisation function, i.e. a suitable function, e.g. a trapezoid or triangle. It is thereby possible to suppress distortions in the line shape. [56]

Zerofilling The interferogram is extended by the addition of zero-values, which leads to an increase in the number of points in the spectrum. The resulting interpolation leads to a smoothing of the calculated curve. Since the additional zeroes do not contain any spectral information, the spectral resolution is not increased.

Fourier transformation The measured intensity-retardation spectrum has to be converted into an intensity-wavenumber spectrum via a FOURIER transformation. A fast numerical algorithm uses the fact that the interferogram is digital, i.e. discrete.

Phase correction In most cases only a one-sided interferogram is recorded (retardations for $x > 0$). The result of the FOURIER transform is therefore complex:

$$A(\tilde{\nu}) = 2 \int_0^\infty F(x) \exp(2\pi i \tilde{\nu} x)\, dx. \tag{3.9}$$

The process of calculating the relevant real spectrum from the complex one is called phase correction.

Reference spectrum For an IR spectrometer, the incident intensity from the light source varies strongly with wavelength (similar to black body spectrum) and the relative change in intensity is small $\left(\Delta I/I \approx 10^{-4} - 10^{-5}\right)$. Therefore the last step is the normalisation of the spectrum by a reference spectrum. This can be achieved either by using the spectrum of the bare substrate or by using the s and p polarised spectra respectively.

In practice, the ordinate of a spectrum is usually given in *absorbance* units

$$A = \varepsilon bc = -\log_{10} \frac{I}{I_0} = -\log_{10} \frac{I_0 - \Delta I}{I_0} = -\log_{10} \left(1 - \frac{\Delta I}{I_0}\right), \tag{3.10}$$

which is essentially equivalent to the fractional change in intensity as long as it is small (if x is small, then $\log(1-x) \sim x$) and

$$A = \varepsilon bc = \frac{\Delta I}{I_0}. \tag{3.11}$$

3.1.3.2. Wave optics

The reflection and refraction of waves at an interface between two media with different properties are well known phenomena and can be applied (with corresponding modifications) not only for the propagation of light, for instance in the infrared region, but also for neutron and x-ray scattering. In this section some generic formulae will be presented which will then be adapted to the particular application in the following sections. The various aspects of the phenomena can be divided into two classes [57]:

1. Kinematic properties
   a) Angle of reflection equals angle of refraction
   b) SNELL's law: $n_1 sin(\theta_1) = n_2 sin(\theta_2)$, where θ_1 and θ_2 are the angles of the incidence and the refraction and n_1, n_2 are refractive indices in the two media.
2. Dynamic properties
   a) Intensities of reflected and refracted radiation.
   b) Phase changes and polarisation

For plane waves $\psi(x,t) = \psi_0 e^{i\mathbf{k}\cdot\mathbf{x}-i\omega t}$, the wave equation can be written in the form of the HELMHOLTZ equation

$$(\nabla^2 + n^2 k^2)\psi = 0, \tag{3.12}$$

where n is the refractive index and k is the wavenumber. In the case of neutrons, the refractive index is related to the scattering length of a nucleus (**Section 3.2**) and ψ denotes the neutron wave-function, in the case of light ψ represents the electric field vector and n is related to the permittivity ϵ and the magnetic permeability μ (**Section 3.1.3.3**) and for x-rays the refractive index is a function of the electron

density of the material. For the description of the behaviour of waves at an interface it is useful to recall the FRESNEL equations described in the following section, which relate incoming, outgoing and transmitted waves. The symbols and coordinate system are shown in **Figure 3.2**.

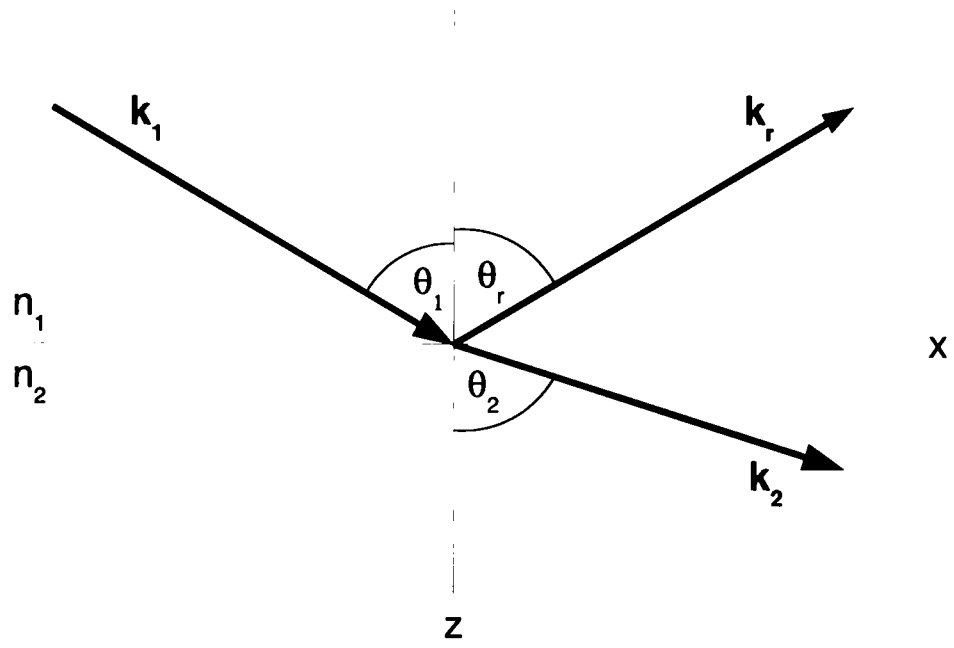


Figure 3.2.: Schematic of incoming wave with wave vector $\mathbf{k}_1$ at angle θ_1, creating a reflected wave $\mathbf{k}_r$ and a refracted wave $\mathbf{k}_2$.

3.1.3.3. Reflection absorption infrared spectroscopy (RAIRS)

For the study of thin films on surfaces, FTIR represents another state-of-the art technique. It is particularly useful for the investigation of monolayers on a reflective metallic substrate, since the spectral information is very sensitive to the vibrational modes of the adsorbed molecules. This use of FTIR is often referred to as infrared reflection absorption spectroscopy (IRRAS). The generic optical configuration for FT-IRRAS experiments is shown in **Figure 3.3**. The relations between the amplitudes of incident, reflected and refracted waves, can be described using the FRESNEL equations. These can be derived for electromagnetic waves using the MAXWELL equations and applying the appropriate boundary conditions at the interface between materials with different refractive index: the normal components of $\mathbf{D}$ and $\mathbf{B}$ are continuous and the tangential components of $\mathbf{E}$ and $\mathbf{H}$ are continuous.

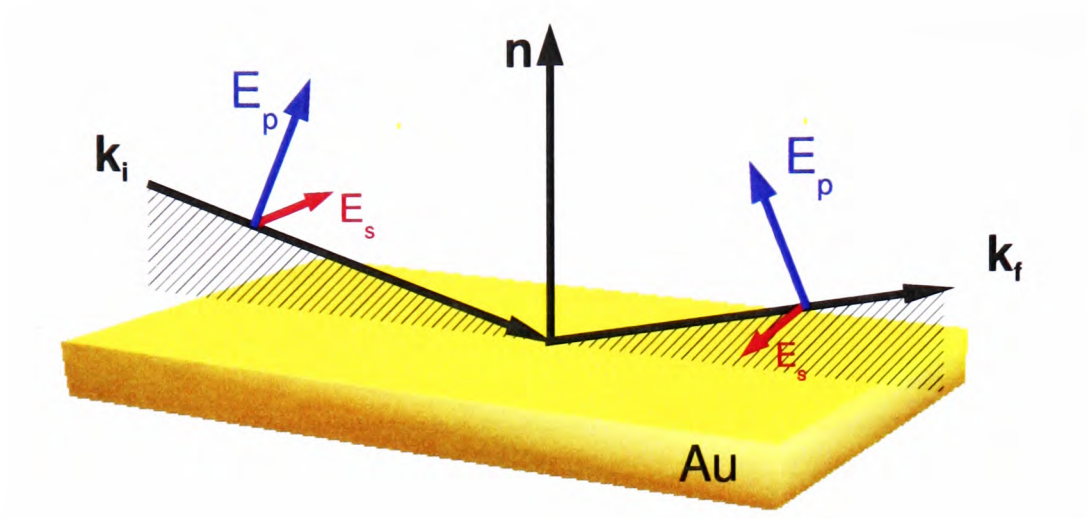


Figure 3.3.: Reflection of linearly polarised light at a metal surface showing the s- and p-polarised components.

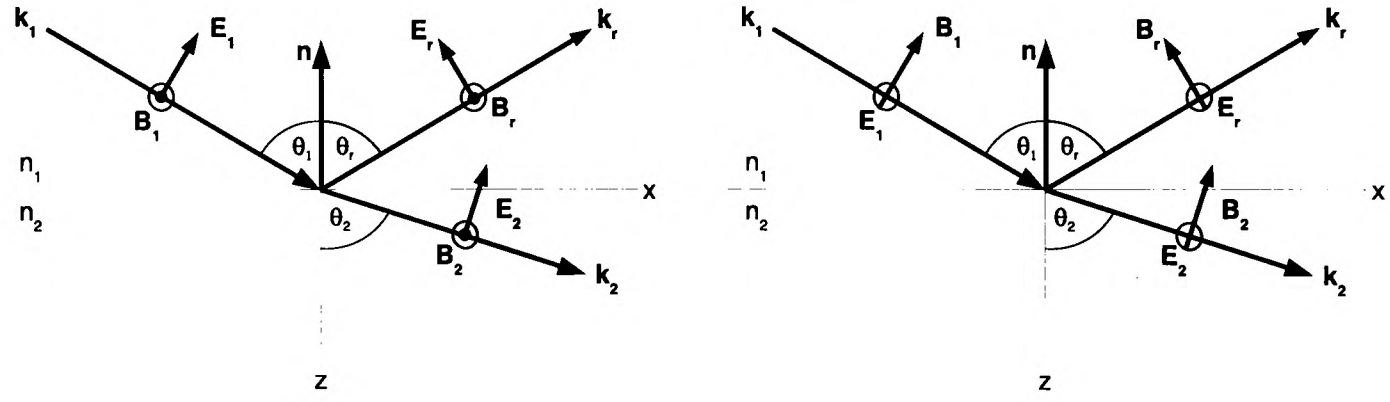


Figure 3.4.: Reflection and refraction at an interface with polarisation (a) parallel and (b) perpendicular to the plane of incidence.

It is convenient to consider two separate cases, one in which the incident plane wave is linearly polarised with its polarisation vector perpendicular to the plane of incidence (the plane defined by **k** and **n**), and the other in which the polarisation vector is parallel to the plane of incidence (**Figure 3.3**). The FRESNEL reflection and transmission coefficients $r_{p,s}$ and $t_{p,s}$ can be expressed as follows by using the refractive index n, the angle of incidence θ_1 and the refractive angle θ_2, according to SNELL's law (see **Section 3.1.3.2**).

PARALLEL (P) POLARISATION

$$r_p = \frac{E_r}{E_1} = \frac{\hat{n}_1 \cos\theta_2 - \hat{n}_2 \cos\theta_1}{\hat{n}_1 \cos\theta_2 + \hat{n}_2 \cos\theta_1} \tag{3.13}$$

$$t_p = \frac{E_2}{E_1} = \frac{2\hat{n}_1 \cos\theta_1}{\hat{n}_1 \cos\theta_2 + \hat{n}_2 \cos\theta_1} \tag{3.14}$$

PERPENDICULAR (S) POLARISATION

$$r_s = \frac{E_r}{E_1} = \frac{\hat{n}_1 \cos\theta_1 - \hat{n}_2 \cos\theta_2}{\hat{n}_1 \cos\theta_1 + \hat{n}_2 \cos\theta_2} \tag{3.15}$$

$$t_p = \frac{E_2}{E_1} = \frac{2\hat{n}_1 \cos\theta_1}{\hat{n}_1 \cos\theta_1 + \hat{n}_2 \cos\theta_2} \tag{3.16}$$

In these equations only non-magnetic materials were assumed, and therefore $\mu = 1$. For absorbing materials the refractive indices $\hat{n}_j$ and the angles θ_j become complex and have an imaginary part:

$$\hat{n} = n + ik \tag{3.17}$$

3.1.4. Polarisation modulation (PMIRRAS)

Only vibrational modes that have a transition dipole (or a component of the transition dipole) perpendicular to the surface can be observed in infrared spectroscopy on metal surfaces.[2] The polarisation modulation technique has the following advantages for the study thin layers: no reference sample is needed, the background subtraction is performed implicitly using the different behaviour of s- and p-polarised light at conducting surfaces and the dynamic range of the AD-converter can be improved.

The photo-elastic modulator (PEM) is the core piece of the PMIRRAS setup. It modulates the polarisation of the incoming infrared light at high frequencies, typically 74 kHz. The intensity modulation frequency of the spectrometer is less than 5 kHz, therefore the detector signal can be demodulated using a band pass filter. In addition, the high PEM frequency has the advantage that s- and p-polarised light

[2] Note that this rule only applies to very good conductors – it does not apply to molecules adsorbed on semiconductors or insulators. Also, it only applies to molecules bonded right at the interface molecules located some distance away from the interface will still have some net electric field parallel to the surface.

are both measured within a short time interval, thereby minimising the influence of instrumental drifts.

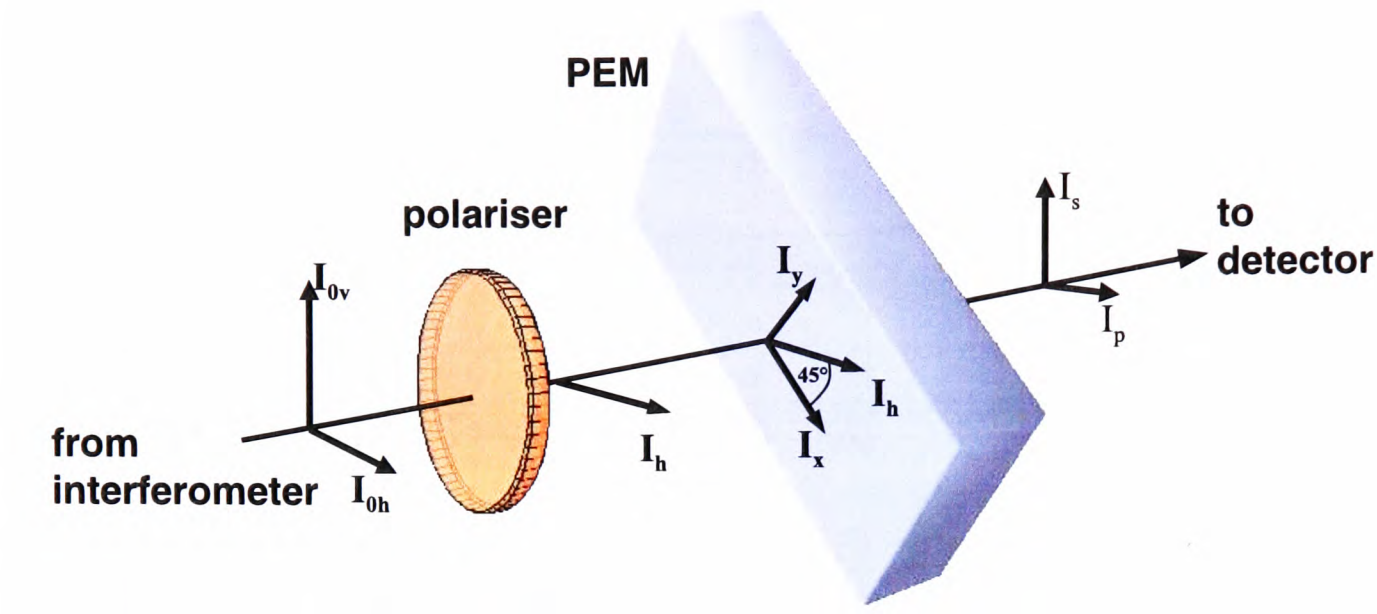


Figure 3.5.: Simplified optical setup with photo-elastic modulator.

The optical setup for polarisation modulation is shown in **Figure 3.5**. The incident light is p-polarised with respect to the sample and has a 45° angle with respect to the PEM. The PEM rotates the polarisation vector continuously between s- and p-polarisation, by a change in the refractive index in the x-direction. According to Hipps and Crosby [58] the time dependent amplitudes of the s- and p-polarised components measured by the detector can be written as

$$I_p^{det}(\widetilde{\nu},t) = \frac{1}{2}\left(1+\cos[\phi_0\cos(\omega_{PEM}t+\Phi_{PEM})]\right) I_h(\widetilde{\nu},t) \tag{3.18}$$

$$I_s^{det}(\widetilde{\nu},t) = \frac{1}{2}\left(1-\cos[\phi_0\cos(\omega_{PEM}t+\Phi_{PEM})]\right) I_h(\widetilde{\nu},t) \tag{3.19}$$

with ω_{PEM} and Φ_{PEM} being the modulation frequency and arbitrary phase introduced by the PEM, and

$$\phi_0 = \frac{GV_{PEM}}{\lambda} \tag{3.20}$$

depends linearly on the voltage of the applied modulation and is inversely related to the wavelength of the light. The full expression can be written using the identity 9.1.44 from [59]

$$\cos(\omega_{PEM}t)) = J_0(\phi_0) + 2\sum_{k=1}^{\infty}(-1)^k J_{2k}(\phi_0)\cos(2k\omega_{PEM}t+\Phi_{PEM}) \tag{3.21}$$

where $J_i(A)$ are BESSEL functions of integer order. In principle, this complex signal requires a detector with infinite bandwidth. However, the absolute values of the amplitudes of the BESSEL functions decrease rapidly with increasing order, so that in practice only the zeroth and second order ($k = 1$) BESSEL functions are sufficient to demodulate the signal.

The detector measures the sum of the modulated s- and p-components, which can be described using Equations 3.4, 3.5 for $I_h(\tilde{\nu}, t)$ and 3.19

$$I_{total}^{det} = \Big\{ I_p^{det} + I_s^{det} + (I_p^{det} - I_s^{det}) J_0(\phi_0) + (I_p^{det} - I_s^{det}) \times J_2(\phi_0) \cos(2\omega_{PEM} t + \Phi_{PEM}) \Big\} I_0 RT[1 + \cos(\pi f_{\tilde{\nu}} t)] \tag{3.22}$$

This detector signal contains a high frequency component due to the PEM modulation (terms containing $\cos(2k\omega_{PEM}t)$) and the low frequency component from the interferometer (terms containing $\cos(\pi\tilde{\nu}t)$). The two components are separated electronically using band filters and a lock-in amplifier (LIA). The high frequency signal is demodulated by multiplication with $U = U_0 \cos(2\omega_{LIA}t + \Phi_{LIA})$. $\omega_{LIA} = 2\omega_{PEM}$ and $\Phi_{LIA} = \Phi_{PEM}$ are adjusted automatically by the lock-in amplifier. Thus two signals are obtained: one reference signal containing the averaged I_p^{det} and I_s^{det} components and the difference signal containing just information from the sample surface:

$$\langle I \rangle_{ref} = \Big\{ I_p^{det} + I_s^{det} + (I_p^{det} - I_s^{det}) J_0(\phi_0) \Big\} \cos(\pi f_{\tilde{\nu}} t) \tag{3.23}$$

and

$$\Delta I_{sample} = (I_p^{det} - I_s^{det}) J_2(\phi_0) \cos(\pi f_{\tilde{\nu}} t) \tag{3.24}$$

For a metallic substrate the term $(I_p^{det} - I_s^{det})$ will be much smaller than $(I_p^{det} + I_s^{det})$, since reflectivities for both polarisations are similar in magnitude[3]. Thus, the experimentally relevant signal is

$$\frac{\Delta R}{R} = \frac{\Delta I_{sample}}{\langle I \rangle_{ref}} \approx \frac{I_p^{det} - I_s^{det}}{I_p^{det} + I_s^{det}} J_2(\phi_0) \tag{3.25}$$

It has to be pointed out that this treatment is strictly valid only for one wavelength of incident light λ for which the PEM amplitude V_{PEM} has been optimised

[3]This is not applicable to dielectric substrates, where I_p and I_s can be very different.

(**Equation 3.20**). The second order BESSEL function can be regarded as a wavelength dependent efficiency function of the polarisation modulation process. In practice, the PEM is manually adjusted such that the BESSEL function has a maximum in the wavelength region of interest. For the studies of organic monolayers in this thesis the PEM was set to 1500 cm^{-1} for the fingerprint region of the OEG monolayers and the proteins and to 2900 cm^{-1} to study the CH stretching region. Due to its periodic nature, the BESSEL function exhibits a second, smaller maximum at twice the wavenumber of the first maximum; therefore, a PEM setting of approximately 1500 cm^{-1} allows the simultaneous study of fingerprint and CH stretching region. In particular cases other settings have been also used in order to maximise the signal.

Note that simulation results obtained in this thesis of the signal and its dependence on experimental parameters, such as angle of incidence, thickness and refractive indices of the stratified medium will be presented in **Section 5.5**.

3.2. Neutron Reflectivity (NR)

By measuring the reflected intensity over the incoming intensity of a well collimated beam striking at an interface, as a function of the incident angle and wavelength, the concentration profile giving rise to a reflectivity curve is determined. The wavelengths of the neutrons used for reflectivity are of the order of a few Ångstroms and a resolution of a fraction of a nanometre can be achieved, so that information is gained at the molecular level. Unlike x-rays it is not destructive and can be used at buried interfaces, which are not easily accessible to other techniques, such as liquid/liquid or solid/liquid, as well as at solid/air and liquid/air interfaces. It is particularly useful for soft-matter studies since neutrons are strongly scattered by light atoms like H, C, O and N which are contained by most organic and biological materials. The scattering amplitudes vary for different nuclei, creating a contrast between different materials. The fact, that the sign of the phase change differs among isotopes, the most prominent example being the hydrogen isotopes H and D, makes it possible to vary the contrast of molecules by targeted H/D substitution without changing the chemical structure. This particular technique of contrast matching, or adjust-

ment is of particular interest and was used for the enhancement of the sensitivity of measurements for the present work.

Refractive index and Fresnel equations At this point it is necessary to define a few concepts. An interface is defined as the position between media of two different refractive indices. The neutron refractive index of medium j is given as:

$$n_j = 1 - \delta + i\beta, \tag{3.26}$$

The quantities δ and β are linked to the coherent scattering length and the incoherent absorption cross-sections of the material [60]:

$$\delta = \frac{\lambda^2 N b}{2\pi} = \frac{\lambda^2}{2\pi} N_A \sum_i \frac{\rho_i}{A_i}(b_{0,i} + b_i') \tag{3.27}$$

$$\beta = \frac{\lambda N \mu_N}{4\pi} = \frac{\lambda^2}{2\pi} N_A \sum_i \frac{\rho_i}{A_i}|b_i''| \tag{3.28}$$

where N is the atomic number density, b is the coherent scattering length, the product $Nb = \rho_z$ is the scattering length density, μ_N is the attenuation coefficient and λ is the neutron wavelength. b_0 represents the bound coherent scattering length and b', b'' are the real and imaginary dispersion terms. For the general case of a compound material, ρ_i is the physical density and A_i denotes the atomic weight of the isotope i. Strictly, then the refractive index is a complex number. For most materials, however, with the exception of those containing the elements, Li, B, Cd, Sm, or Gd, the adsorption cross-section is effectively zero, i.e. $\sigma_a \gg 0$, and therefore equation 3.26 reduces to:

$$n = 1 - \frac{\lambda^2 N b}{2\pi} = 1 - \frac{\lambda^2 \rho_z}{2\pi} \tag{3.29}$$

Neutrons can be treated in close analogy to the framework for electromagnetic waves, as described in Sections 3.1.3.2 and 3.1.3.3. The neutrons of mass m_n, energy E in a potential V assume a wavelike behaviour that obeys the SCHRÖDINGER equation for the neutron wave function ψ

$$\left[-\frac{\hbar^2}{2m_n}\nabla^2 + V\right]\psi = E\psi, \tag{3.30}$$

which is the quantum mechanical equivalent of the HELMHOLTZ equation (**Eq. 3.12**). If the neutrons are regarded as plane waves with amplitude a_i propagating in the x-z plane (see **Figure 3.6**), then their wave function can be written as:

$$\psi_{1,2,r}(\mathbf{r}) = a_{1,2,r} \exp(i\mathbf{k}_{1,2,r} \cdot \mathbf{r}) \tag{3.31}$$

where the indices $1, 2$ and r denote the incident, transmitted and reflected wave respectively.

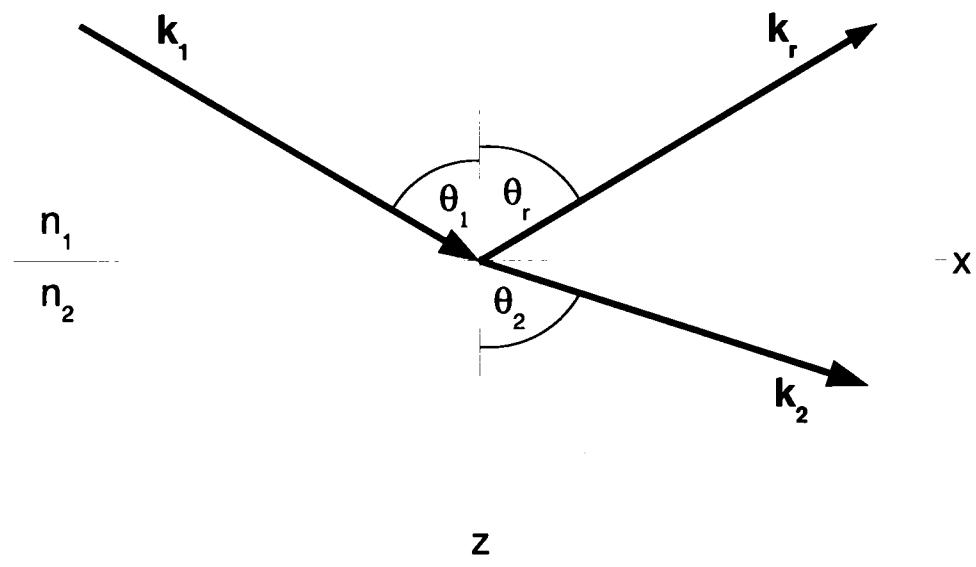


Figure 3.6.: Schematic of incoming wave with wave vector $\mathbf{k}_1$ at angle θ_1, creating a reflected wave $\mathbf{k}_r$ and a refracted wave $\mathbf{k}_2$.

Instead of the required continuity of the electric and magnetic fields at an interface, the boundary conditions for the neutron wavefunction demand that the wave and its derivative must be continuous at the interface. Because the x component of the wave function is conserved across the interface, the wave function for the z component can be written separately as

$$\psi = \begin{cases} \exp(ik_1^z z) + r\exp(-ik_1^z z) & \text{for } z < 0 \\ t\exp(ik_2^z z) & \text{for } z \geq 0 \end{cases} \tag{3.32}$$

where r and t are the reflection and transmission coefficients in the FRESNEL sense. The continuity of the x component at the interface of media with refractive indices n_1 and n_2 yields SNELL's law

$$\cos\theta_1 = \frac{n_1}{n_2} \cdot \cos\theta_2, \tag{3.33}$$

where θ_1 is the the angle of incidence of the neutron wave with wave vector $\mathbf{k_1}$ with respect to to the interface, θ_2 is the angle of the transmitted wave with wave vector $\mathbf{k_2}$. The outgoing wave $\mathbf{k_r}$ is reflected at angle θ_r. The FRESNEL equations can be derived from the continuity of ψ and $d\psi/dz$ at $z = 0$:

$$r \equiv \frac{\psi_r}{\psi_1} = \frac{k_1^z - k_2^z}{k_1^z + k_2^z}, \quad \text{and} \quad t \equiv \frac{\psi_2}{\psi_1} = \frac{2k_1^z}{k_1^z + k_2^z}. \tag{3.34}$$

Under the assumption of small incident angles ($\theta_i \ll 1$), the condition for total reflection $\cos\theta_f = 1$ yields

$$\frac{n_1}{n_2} = \cos\theta_i \tag{3.35}$$

$$\frac{n_1}{n_2} \approx 1 - \frac{\theta_i^2}{2} \tag{3.36}$$

and hence for the critical angle θ_c of total reflection

$$\theta_c = \sqrt{\frac{\rho_2 - \rho_1}{\frac{\pi}{\lambda^2} - \frac{\rho_1}{2}}}. \tag{3.37}$$

This simplifies to

$$\theta_c = \sqrt{\frac{\lambda^2 \rho_2}{\pi}}, \tag{3.38}$$

if the first medium is air or vacuum, i.e. $\rho_1 = 0$.

The momentum transfer Q_z perpendicular to the interface is given by

$$Q_z = \frac{4\pi}{\lambda} \sin\theta$$

Multiple scattering and Parratt's exact method The FRESNEL equations derived above are only valid for a system with one interface, where both media are assumed to be semi-infinite, such that no reflection from the lower end of the second medium can occur. When additional layers are added, multiple reflections will occur within each finite layer and the reflectivity of each interface comprises a sum over all possible reflections from subsequent layers (geometric series). In this sum the individual contributions have to be added including the phase difference $\exp(iQ_j d_j)$ introduced by the jth layer. The total reflectivity of a slab (medium 1) sandwiched between two semi-infinite media (media 0 and 2) can the be expressed using the limit of the geometric series:

$$r_{slab} = \frac{r_{01} + r_{12}\exp(iQ_1 d)}{1 + r_{01} r_{12}\exp(iQ_1 d)}, \tag{3.40}$$

where $r_{i,j}$ are the FRESNEL reflectivities between media i and j, d is the thickness of the slab and $Q_1 = 2k_1 \sin\theta_1$. The reflectivity of a stack of N layers can be calculated recursively using the formula [61]:

$$r\prime_{j-1,j} = \frac{r_{j-1,j} + r_{j,j+1}\exp(iQ_j d)}{1 + r_{j-1,j} r_{j,j+1}\exp(iQ_j d)}. \tag{3.41}$$

Here, the wave-vector transfer $Q_j = 2k_j \sin\theta_j$ in the jth layer is related to the scattering vector in vacuum Q:

$$Q_j = \sqrt{Q - 16\pi(Nb)_j}. \tag{3.42}$$

The beginning of the recursion is given by the assumption that the semi-infinite substrate does not give rise to multiple reflections.

Kinematical approximation Whenever PARRATT's recursive algorithm is too time consuming or the system cannot be described by a series of homogeneous layers, a *kinematical approximation* can be employed, which can be expressed as a FOURIER transform of the scattering length density profile $\rho(z)$, which can be an analytical function:

$$R(Q) = R_F(Q)\left|\frac{1}{\rho_0}\int_0^\infty \frac{d\rho(z)}{dz} e^{iQz} dz\right|, \tag{3.43}$$

where ρ_0 is the scattering length density of the topmost phase and R_F is the FRESNEL reflectivity of a sharp planar interface. However, the *master formula* (**3.43**) does

not include multiple scattering and is therefore only valid for Q-values much larger than Q_c, the critical value below which total reflection occurs. In the case of a graded interface, that is if the transition between individual layers is assumed to be an error function $\rho(z) = erf\left(z/\sqrt{2}\sigma\right)$, where σ is a measure of the width of the graded region, then **Equation 3.43** can be evaluated explicitly, yielding [62]:

$$R(Q) = R_F(Q)e^{-Q^2\sigma^2}. \tag{3.44}$$

3.2.1. Roughness

In the description of the reflectivity in the previous section it was assumed that each interface between layers of different scattering length density are either ideally flat or there is a graded transition, and all neutrons are scattered specularly, that is the momentum transfer is perpendicular to the interface. Real interfaces however, are not perfectly flat or uniformly graded. Rather, a real surface has some degree of roughness, which means that the height of the interface varies randomly over a finite area. Following the discussion in the book by Als-Nielsen and McMorrow [62], the effect of uncorrelated interfacial roughness leads to same factor $\exp(-Q_z^2\sigma^2)$ as for the uniformly graded interface, that diminishes the FRESNEL reflectivity similar to the DEBYE-WALLER factor. Here $\sigma = \sqrt{\langle h^2 \rangle}$ denotes the root-mean-square roughness. This means that reflectivity experiments cannot distinguish between these two types of roughness. A further important consequence is the fact that for uncorrelated roughness the scattering is still confined to the specular direction.

3.2.2. Off-specular reflectivity

In the previous section it was shown that uncorrelated roughness adds a scattering contribution to the specular signal. If the heights of the interface (surface) at different points are correlated in some way, this correlated roughness gives rise to scattering, which is not entirely specular any more, and the momentum transfer **Q** has an additional x component (see **Figure 3.7**). This phenomenon is referred to as *diffuse* or *off-specular* reflectivity and gives rise to a broader peak on which the specular peak is superimposed. The lateral correlation distance ξ (coherence length) is then related to the inverse of the width of the off-specular peak. For the systems studied in this work the contributions to off-specular scattering are usually small,

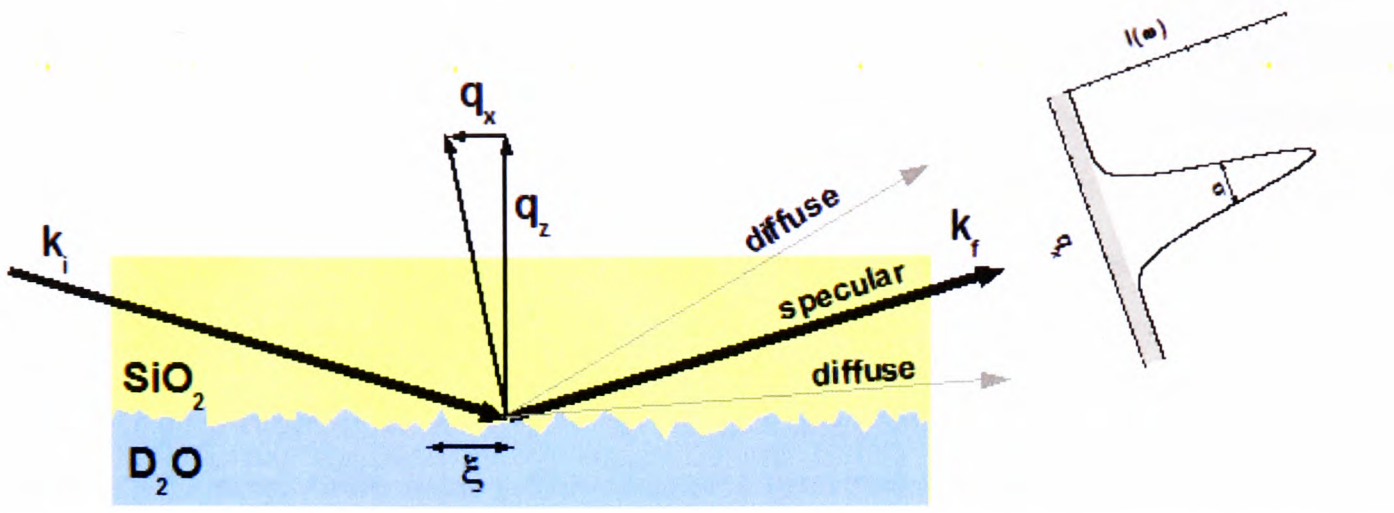


Figure 3.7.: Measurement of the off-specular reflectivity provides information about the length scale of in-plane structural correlations. For transverse-Q_x scans (i.e., rocking curves), the scattering angle 2θ is held constant while θ_i and θ_f are varied equally in opposite directions ($\theta_i + \theta_f = const.$). The width of the diffuse peak is indirectly related to the inverse of the coherence length ξ of the in-plane roughness.

except for samples with a very high protein concentration or contrast matched solutions with high content of hydrogen nuclei. In those cases the major part of the diffuse scattering is caused by small-angle scattering from the proteins in solution and by the incoherent scattering form hydrogen nuclei contained in the protein and the solution. Then, the diffuse component has to be subtracted from the measured signal as described in **Section 4.4**, in order to obtain the true specular reflectivity.

3.3. Small-angle x-ray scattering

SAXS (small-angle X-ray scattering) is a small-angle scattering (SAS) technique where the elastic scattering of X-rays (wavelength 0.1-0.2 nm) by a sample which has inhomogeneities in the nm-range, is recorded at very low angles (typically 0.1 10°). In this angular range, information about the shape and size of macromolecules or colloids and characteristic distances of partially ordered materials is contained. SAXS is capable of delivering structural information of objects between 5 and 25 nm, of repeat distances in partially ordered systems of up to 150 nm. USAXS (ultra-small angle X-ray scattering) can resolve even larger dimensions.

In the present work SAXS was used to study the interactions of proteins and monolayer protected nanoparticles individually and with each other, in aqueous solutions.

The advantage over crystallography is that the samples need not be crystalline and the measurement is non-destructive; NMR methods encounter problems with macromolecules of higher molecular mass (>30000-40000). However, owing to the random orientation of dissolved or partially ordered molecules, spatial averaging occurs which leads to a loss of information.

The principle of small-angle scattering can be explained using classical electrodynamics. The electric field of the incoming wave induces dipole oscillations in the atoms. The accelerated charges generate secondary waves that add at large distances (far field approach) to the overall scattering amplitude. All secondary waves have the same frequency but may have different phases caused by different path lengths. The generic experimental setup is comprised of a source of collimated radiation, the

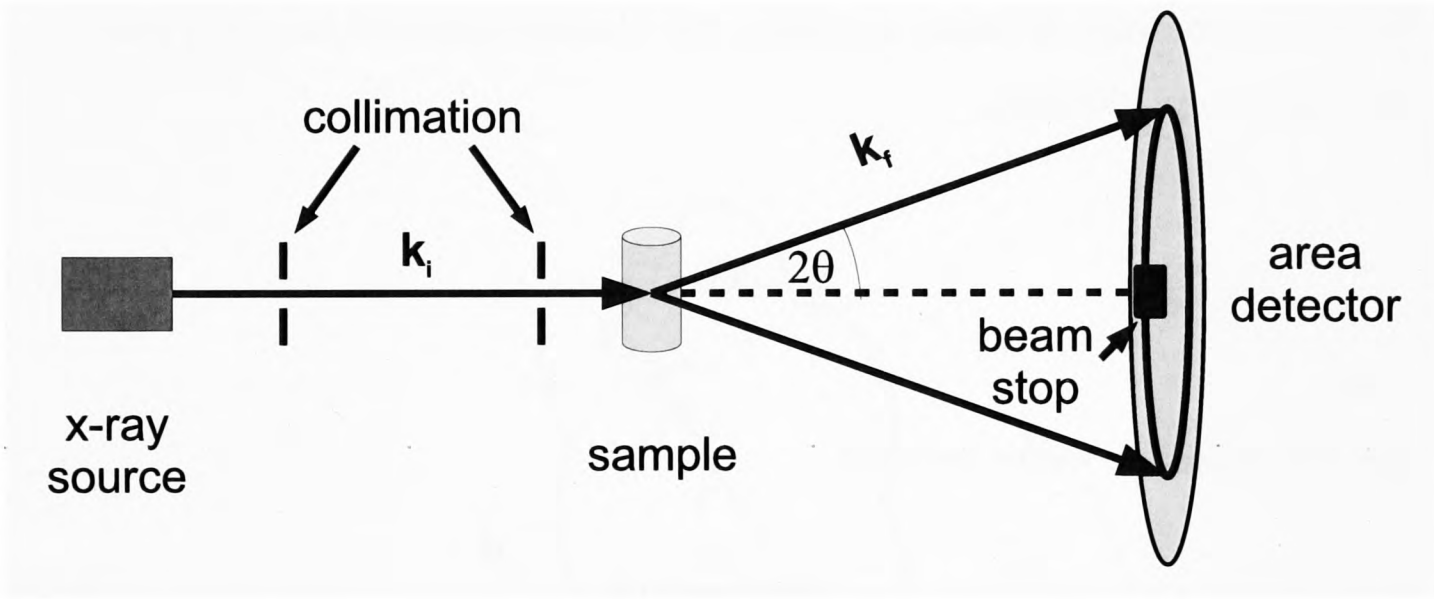


Figure 3.8.: Generic sketch of the scattering geometry in a small-angle scattering experiment.

sample and the detector (**Figure 3.8**). The radiation is directed to a small volume V, typically a few mm^3, of the sample of interest, and the scattered intensity is measured with the detector. The directly transmitted radiation is usually blocked by a 'beam stop' before it reaches the detector. The detector records the flux of radiation scattered into a solid angle $d\Omega$. This flux I(λ,Q), can be described in general terms as

$$I(\lambda, \boldsymbol{Q}) = I_0(\lambda) \cdot d\Omega \cdot \eta(\lambda) \cdot T \cdot V \cdot \frac{\partial \sigma}{\partial \Omega}(\boldsymbol{Q}), \tag{3.45}$$

where $I_0(\lambda)$ is the incident flux, $\eta(\lambda)$ is the detector efficiency, T the sample transmission and $\frac{\partial \sigma}{\partial \Omega}(\boldsymbol{Q})$ the differential cross-section. The scattering vector or momentum

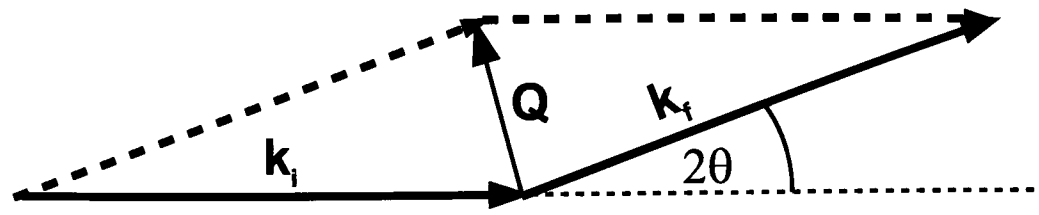


Figure 3.9.: Momentum transfer in small-angle scattering.

transfer $\boldsymbol{Q}$ is defined as (**Figure 3.9**)

$$\boldsymbol{Q} = \boldsymbol{k}_f - \boldsymbol{k}_i. \tag{3.46}$$

For the special case of elastic scattering, the absolute values of incoming and scattered waves are identical,

$$k_f = k_i = \frac{2\pi}{\lambda}, \tag{3.47}$$

and the scattering vector becomes

$$Q = \frac{4\pi}{\lambda} \sin\theta. \tag{3.48}$$

Together with Bragg's law $n\lambda = 2d\sin\theta$, this relation determines the experimentally observable length scale d according to

$$Q = \frac{2\pi}{d}. \tag{3.49}$$

While I_0, $d\Omega$ and $\eta(\lambda)$ are quantities which depend on the source and the detector, transmission, sample volume and differential cross-section are determined by the sample. Information about the sample, such as size, shape, and structure can be extracted from the differential cross-section. The generic description of the differential cross-section is

$$\frac{\partial\sigma}{\partial\Omega}(\boldsymbol{Q}) = N_p \cdot V_p^2 \cdot (\Delta\rho)^2 \cdot P(\boldsymbol{Q}) \cdot S(\boldsymbol{Q}) + B_{inc}, \tag{3.50}$$

where N_p is the number of scatterers (e.g. protein molecules or colloidal particles) per unit volume in the solution, V_p is the volume of a single scatterer and $\Delta\rho = (\rho_p - \rho_s)$, is the difference between the electron density of the scatterers and that of the solvent, and is usually called the scattering contrast. $P(\boldsymbol{Q})$ is the *form factor* of an individual scatterer, i.e. the scattering from a single particle after orientational averaging. $S(\boldsymbol{Q})$ is the *structure factor*, which contains information on the inter-particle interactions. B_{inc} is the isotropic, or incoherent scattering background from the sample and the environment.

The meaning of form and structure factor will be discussed in the following, because they are the quantities which contain information about the scatterers and their interactions with each other.

FORM FACTOR

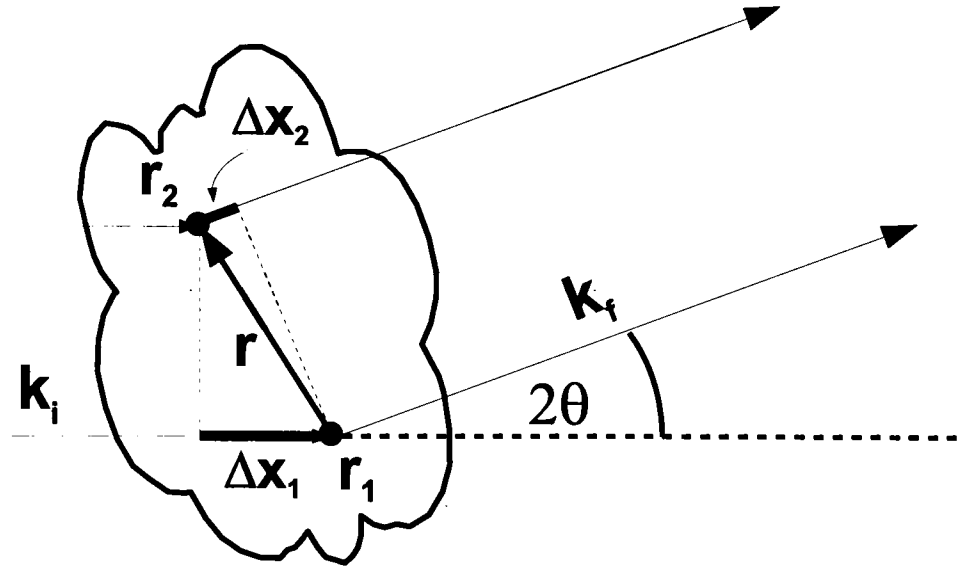


Figure 3.10.: Scattering by different parts of the same scattering centre. The phase difference of the outgoing waves $\boldsymbol{k}_1$ and $\boldsymbol{k}_2$ is $\Delta\phi = (\Delta x_2 - \Delta x_1)k$, where $\Delta x_{1,2} = \boldsymbol{r} \cdot |\boldsymbol{k}_{1,2}|$. Therefore $\Delta\phi = (-\boldsymbol{r} \cdot \frac{1}{k}\boldsymbol{Q})k = -\boldsymbol{r} \cdot \boldsymbol{Q}$

When the incoming radiation is scattered by different volume elements of the same object (protein or colloidal particle), the outgoing waves have a phase difference $\boldsymbol{Q} \cdot \boldsymbol{r}$ and interfere with each other (**Figure 3.10**), thereby modulating the differential cross-section $\frac{\partial\sigma}{\partial\Omega}(\boldsymbol{Q})$. This interference depends upon the shape, size and composition of the scattering particle. The form factor can be then written as

$$P(\boldsymbol{Q}) = \left| \int_V \Delta\rho(\boldsymbol{r}) \exp(-i\boldsymbol{Q} \cdot \boldsymbol{r}) d\boldsymbol{r} \right|^2 . \tag{3.51}$$

Analytical expressions can be found for the most common shapes [63]:

Sphere of radius R_p	$P(\boldsymbol{Q}) = \left[\frac{3(\sin(QR_p)-QR_p\cos(QR_p))}{(QR_p)^3}\right]^2$
Disc of negligible thickness and radius R_p (J_1 is a first-order Bessel function)	$P(\boldsymbol{Q}) = \frac{2}{(QR_p)^2}\left[1-\frac{J_1(2QR_p)}{QR_p}\right]$
Gaussian random coil with z-average radius of gyration Rg, polydispersity (Y+1) and $u = \frac{(QR_g)^2}{(1+2Y)}$	$P(\boldsymbol{Q}) = \frac{2\left[(1+uY)^{\frac{-1}{Y}}+u-1\right]}{(1+Y)u^2}$
Oblate ellipsoidal form factor (averaged) with radii a×b×b $u = Qb\left[(a/b)^2x^2+(1-x)^2\right]^{1/2}$	$P(\boldsymbol{Q}) = \left\langle\lvert F(Q)\rvert^2\right\rangle = \int_0^1 dx \left\lvert\frac{3(\sin u - u\cos u)}{u^3}\right\rvert^2$

STRUCTURE FACTOR

In an idealised solution, where the scatterers (e.g. protein molecules) are well-separated from each other, i.e. there is no position or orientation correlation between them, the *structure factor* $S(\boldsymbol{Q}) = 1$, and the total scattering only has contributions from the form factor $P(\boldsymbol{Q})$. With increasing protein concentration, interference effects between proteins cannot be neglected, and the structure factor becomes important in the total scattering intensity. The structure factor takes the form

$$S(\mathbf{Q}) = 1 + \frac{4\pi N_p}{QV}\int_0^\infty [g(r)-1]\, r\sin(\mathbf{Qr})dr, \tag{3.52}$$

and describes the effect of inter-particle interference on the differential cross-section. It therefore depends on the degree of local ordering in the sample, which may be caused by interactions between the scatterers. This local ordering within the sample can be described by the *radial distribution function*

$$G(r) = \frac{4\pi N_p r^2}{V} g(r),$$

which is related to the function $g(r)$, with r being the radial distance from any scattering centre in the sample. $G(r)$ usually shows a damped oscillatory behaviour, with the maxima corresponding to the distance of each nearest-neighbour coordination shell.

3.3.1. Scattering from proteins in solution

For a polydisperse or non-spherical system, in an average structure factor approximation, equation (3.50) becomes

$$\frac{\partial\sigma}{\partial\Omega}(\boldsymbol{Q}) = N_p \cdot V_p^2 \cdot (\Delta\rho)^2 \cdot P(\boldsymbol{Q}) \cdot \overline{S}(\boldsymbol{Q}) + B_{inc}, \tag{3.53}$$

$\overline{S}(\boldsymbol{Q})$ is the effective structure factor, and is calculated using a monodisperse structure factor at an effective sphere diameter. In the case of a protein solution, the system is monodisperse but non-spherical (ellipsoidal). The effective sphere diameter is then calculated by equating the second virial coefficient, A_2, of the ellipsoid to a sphere having the same A_2 [64]. This effective sphere diameter is then used to calculate the effective structure factor $S(\boldsymbol{Q})$ [64, 65].

$\overline{S}(\boldsymbol{Q})$ in the low $\boldsymbol{Q}$ range strongly depends on the interaction potential between protein molecules. The structure factor at the origin $\overline{S}(\boldsymbol{Q}=0)$ is equal to the normalised osmotic compressibility. With repulsive interactions, the protein molecules are uniformly distributed and $S(0)$ is lower than unity, while with attractive interactions, fluctuations dominate the particle distribution and $\overline{S}(0)$ is larger than unity [24, 25, 46]. Therefore, a detailed analysis of the structure factor can provide information on the nature of interaction potentials.

According to Curtis, [33] the interaction potential $U(r)$ for a pair of protein molecules in a salt solution with a centre-to-centre distance, r, can be expressed by the sum of the following spherically symmetric potentials:

$$U(r) = U_{HS}(r) + U_{SC}(r) + U_V(r) + U_{OS}(r) + U_A(r). \tag{3.54}$$

Here, $U_{HS}(r)$ is the hard-sphere potential related to the excluded-volume effect, $U_{SC}(r)$ is the screened Coulomb potential, $U_V(r)$ is the van-der-Waals attractive potential, $U_{OS}(r)$ is the depletion potential caused by the excluded-volume effect

of the salt ions, and $U_A(r)$ is a potential employed to account for self-association of proteins. A general structure factor should consider all the potentials described above. However, studies on the total interaction potential of proteins in salt solution indicate that depending on the salt concentration, the interaction is dominated by only one or two of these potentials at any particular salt concentration. Therefore, the total potential can be simplified.

Screened Coulomb structure factor, $S_{SC}(Q)$: At lower ionic strength, I<0.3M, a structural model developed by Hayter and Penfold [66], [67] based on an interaction potential between charged colloidal particles consisting of a hard sphere plus a screened Coulomb potential was used:

$$U_{SC}(r) = \begin{cases} \frac{z^2 e^2}{\varepsilon(1+\kappa_D R)^2} \frac{\exp[-\kappa_D(r-2R)]}{r} & \text{for } r > 2R \\ \infty & \text{for } r \leq 2R \end{cases} \tag{3.55}$$

The charge of the protein, z, is assumed to be uniformly distributed on the surface, e is the electronic charge and ϵ is the dielectric constant of the solvent. R is the effective sphere radius of an oblate ellipsoid with axes a×b×c. κ_D is the inverse of the Debye screening length and is determined by the ionic strength, I, of the solution.

$$\kappa_D^{-1} = \left(\frac{10^3 \varepsilon k_B T}{8\pi e^2 I N_A} \right)^{1/2} \tag{3.56}$$

The structure factor $S(Q)$ is the Fourier transformation of the spherically averaged pair correlation function $g(r)$:

$$S(Q) = 1 + N_p \int 4\pi r^2 [g(r) - 1] \frac{\sin(Qr)}{Qr} dr, \tag{3.57}$$

where N_p is the number density of particles. The correlation function $g(r)$ was obtained by solving the Ornstein-Zernike (OZ) equation (eq. 3.58) by using the mean-spherical approximation (MSA) closure relation (eq. 3.59).

$$h(r_{12}) = c(r_{12}) + \rho \int dr_3 c(r_{13}) h(r_{23}) \tag{3.58a}$$

$$h(r) = g(r) - 1, \tag{3.58b}$$

where $r = r_{ij}$ the distance between a pair of particles, $h(r)$ is total correlation function and $c(r)$ the direct correlation function. If $c(r)$ can be expressed by the interaction potential $U(r)$, the Ornstein-Zernike equation becomes a closed integral equation for $h(r)$.
In the MSA,

$$c(r) = \frac{-U(r)}{k_B T} \text{ for } r > 2R \tag{3.59a}$$

$$h(r) = -1 \text{ for } r < 2R \tag{3.59b}$$

The closed analytic form of the direct correlation function $c(r)$ and the structure factor $S(q)$ was obtained by Hayter and Penfold [66].

Square well structure factor, $S_{SW}(Q)$: At high salt concentration, the surface charges are highly screened and a net attractive potential was found for many protein systems [24,25,31,32,49]. This net attractive potential may originate from van-der-Waals interactions, the depletion force caused by excluding the volume of ions or other interactions such as hydration forces or a hydrophobic force. For the following data analysis a square-well potential will be used to describe the net attractive interaction at high ionic strength, which is characterised by a hard-core repulsion for small interparticle distances, and by a constant attraction potential within a narrow shell (**Equation 3.60**) [68]

$$U_{SW}(r) = \begin{cases} \infty & \text{for } r < 2R \\ -\Delta & \text{for } 2\text{R} \leq r \leq 2R\delta \\ 0 & \text{for } r > 2R \end{cases}, \tag{3.60}$$

where Δ is the well depth. Positive well depths correspond to an attractive potential and negative well depths correspond to a potential "shoulder". δ is the well width defined as multiples of the particle diameter ($2R$). Thus, the interaction separation between a pair of particles is 2R(δ-1). An analytical form of the structure factor was obtained by Sharma et al. by solving the Ornstein-Zernike equation in the mean spherical approximation [68]. This solution has been compared to Monte Carlo simulations for a square well fluid, showing the limitation of the application to a well depth $\Delta < 1.5\ k_B T$ and a volume fraction $\phi < 0.08$ [65].

Hard Sphere structure factor, $S_{HS}(Q)$: At moderate ionic strength, the surface charge is sufficiently screened. The overall interparticle interaction is rather weak, and the protein molecules interact with each other mainly through hard sphere (excluded volume effect) interactions [69].

$$U_{HS}(r) = \begin{cases} 0 & \text{for } r > 2R\delta \\ \infty & \text{for } r \leq 2R \end{cases} \tag{3.61}$$

In this case, the Ornstein-Zernike equation is solved using the Percus-Yevick (PY) closure [65, 69].

$$c(r) = g(r)\left[1 - \exp\left(\frac{U_{HS}(r)}{k_B T}\right)\right], \tag{3.62}$$

where $g(r)$ is the pair correlation function. Within the Percus-Yevick closure, the Ornstein-Zernike equation can be solved numerically. The structure factor $S_{HS}(Q)$ was then obtained by **Equation 3.57**.

3.3.2. Scattering from colloidal particles

The number densities of the colloidal solutions used in this thesis, namely gold and silver nanoparticles, are at the order of 10^{12} particles per millilitre, which corresponds to a volume fraction less than 0.003%. Therefore the solution can be regarded as dilute solution of non-interacting particles. The gold and silver nanoparticles, whether commercial or self-made, are spherical and have a polydispersity of size at the order of 10-20% of the particle diameter. The total scattering intensity in such a polydispersed and dilute colloidal solution with homogeneous electron density is given by [70, 71]:

$$I(Q) = N_0 \Delta\rho \int_0^\infty f(r) r^6 P^2(Qr)\, dr, \tag{3.63}$$

where N_0 is the number of the colloidal particles per unit volume and $\Delta\rho$ is the difference in scattering length densities between colloid and solvent (water), and $f(r)$ is the normalised Gaussian distribution function: where r is the average radius as determined in the data fitting procedure and σ is the standard deviation that

corresponds to the width of the size distribution. $P(Qr)$ is the form factor of a spherical colloid:

$$P\left(Qr\right) = \frac{3\left(\sin\left(Qr\right) - Qr\cos\left(Qr\right)\right)}{\left(Qr\right)^3}. \tag{3.64}$$

Since the colloidal particles can be regarded as non-interacting, a structure factor can be taken to be unity.

3.4. Ellipsometry

Another technique used for the characterisation of (organic) thin films is ellipsometry. This technique determines the change in the polarisation state of light reflected from a sample. The notation in this section referring to polarisation states (s and p) and plane of incidence will be the same as in **Section 3.1.3.3**. The polarisation change can be described in terms of the two paramters Δ and Ψ. These values are related to the ratio of the Fresnel reflection coefficients for p- and s-polarised light:

$$\rho \equiv \frac{r_p}{r_s} = \tan\Psi \cdot e^{i\Delta} = f(n_i, k_i, d_i, ...). \tag{3.65}$$

This is a complex ratio, where $\tan\Psi$ measures the ratio of the modulus of the amplitude reflection ratio and the phase difference between p- and s-polarised reflected light is given by Δ. The previously defined Fresnel coefficients (**Equation 3.13, 3.15**) give the complex amplitude of the reflected light.

Ellipsometry is very sensitive and reproducible, because the measured value is a ratio of two physical quantities. The measurement of the phase difference Δ allows a high sensitivity for very thin films. It is a non-destructive, non-contact and absolute technique, which does not require any reference measurements. Ellipsometry has the advantage of measuring both phase and amplitude ratio and in addition, given its sensitivity to the change in polarisation, it is less sensitive to light intensity fluctuations.

Not being a 'one-to-one' method[4] , the evaluation of an ellipsometric measurement requires the construction of a model and the knowledge of as many sample parameters as possible. In other words, **Equation 3.65** represents a set of linear equations with two known parameters (Δ and Ψ). Without the additional knowledge of some

[4]The same resulting phase difference and amplitude reflection ratio can be achieved by two or more different sets of optical constants.

of the optical constants (n_i, k_i), the thickness, or repeated measurements at different angles, the system remains under-determined.

In this thesis, ellipsometry has been used as a laboratory based method, complementary to the scattering methods used to characertise the samples. In particular, the thickness of SAMs and adsorbates has been determined and the thickness of the water layer between SAM and barium fluoride prism in the PMIRRAS experiments has been monitored. In all cases a model including the known optical constants of substrate, SAM or water, and ambient medium has been employed and the thickness information was obtained by least-square fitting.

Variable-angle ellipsometry measurements of the thickness of the water layer in the cell as described in **Section 5.4.2** were performed on a Picometer ellipsometer (Beaglehole Instruments, Wellington, New Zealand), equipped with a HeNe laser at 632.8 nm. This phase-modulated instrument measures x and y, which are related to the real (Re) and imaginary (Im) parts of the reflectivity by

$$x = \frac{2Re(r)}{1 + Re(r)^2 + Im(r)^2} \tag{3.66a}$$

and

$$y = \frac{2Im(r)}{1 + Re(r)^2 + Im(r)^2} \tag{3.66b}$$

3.5. UV-vis spectroscopy

Ultraviolet-visible (UV-vis) spectroscopy is used to excite electronic transitions in molecules in the visible and adjacent ultraviolet spectral region (190-1100 nm). The basic setup of a UV-vis spectrometer consists of a light source, for instance a xenon light bulb, a monochromator (usually a CZERNY-TURNER monochromator) which generates individual wavelengths from the full spectrum of the light source and a detector (usually a photomultiplier tube). The sample is placed between monochromator and detector, and the transmitted intensity is recorded for each wavelength.

UV-vis spectroscopy can be used for the determination of the concentration of solutions, by measuring the intensity of the transmitted light I_{trans} and employing the BEER-LAMBERT law:

$$A = \alpha l c, \tag{3.67}$$

which relates the absorbance $A = \log(I_0/I_{trans})$ of a sample to its thickness l, its concentration c and the molar absorptivity α of the sample.

In the present work UV-vis spectroscopy was used for two purposes:

(i) for the exact calibration of the concentration of protein solutions (**Section 6**),

(ii) for the observation of colloidal gold solutions and binary mixtures of monolayer protected gold clusters and proteins (**Section 7.2**).

The description of the scattering and absorption cross sections for colloidal solutions, especially for metallic particles is given by the MIE theory. A more recent approach by Haiss et al. [72] even presents formulae for the determination of size and concentration from UV-vis spectra. In their approach the extinction cross section σ_{ext} of a spherical particle with radius R embedded in a medium with dielectric function ϵ_m at a wavelength λ can be represented by

$$\sigma_{ext} = \frac{2\pi}{|k|^2} \sum (2L+1) Re(a_L + b_L), \tag{3.68}$$

where $k = 2\pi\sqrt{\epsilon_m}/\lambda$ is the wave vector, $a_L(R,\lambda)$ and $b_L(R,\lambda)$ are the scattering coefficients in terms of Ricatti-Bessel functions $\eta_L(x)$ and $\psi_L(x)$, which are defined by

$$a_L = \frac{m\psi_L(mx)\psi'_L(x) - \psi'_L(mx)\psi_L(x)}{m\psi_L(mx)\eta'_L(x) - \psi'_L(mx)\eta_L(x)} \tag{3.69}$$

$$b_L = \frac{\psi_L(mx)\psi'_L(x) - m\psi'_L(mx)\psi_L(x)}{\psi_L(mx)\eta'_L(x) - m\psi'_L(mx)\eta_L(x)} \tag{3.70}$$

$x = kR$ is the size parameter and $m = n/n_m$, where n is the complex refractive index of the particle and n_m is the real refractive index of the surrounding medium.

With the aid of these expressions it is possible to determine the size of colloidal gold particles in solution by measuring the UV-vis absorption spectrum. UV-vis spectra were also used to observe the transfer reaction of thiol molecules onto gold nanoparticles, which caused a peak shift in the absorption spectrum.

Bibliography

[1] M. Riepl, K. Enander, B. Liedberg, M. Schaferling, M. Kruschina, and F. Ortigao. Functionalized surfaces of mixed alkanethiols on gold as a platform for oligonucleotide microarrays. *Langmuir*, 18:7016–7023, 2002.

[2] S. Svedhem, L. Ohberg, S. Borrelli, R. Valiokas, M. Andersson, S. Oscarson, S. C. T. Svensson, B. Liedberg, and P. Konradsson. Synthesis and self-assembly of globotriose derivatives: A model system for studies of carbohydrate-protein interactions. *Langmuir*, 18:2848–2858, 2002.

[3] J. Lahiri, P. Kalal, A. G. Frutos, S. J. Jonas, and R. Schaeffler. Method for fabricating supported bilayer lipid membranes on gold. *Langmuir*, 16:7805–7810, 2000.

[4] A.T.A. Jenkins, R.J. Bushby, S.D. Evans, W. Knoll, A. Offenhausser, and S.D. Ogier. Lipid vesicle fusion on μcp patterned self-assembled monolayers: Effect of pattern geometry on bilayer formation. *Langmuir*, 18(8):3176–3180, 2002.

[5] K. L. Prime and G. M. Whitesides. Adsorption of proteins onto surfaces containing end-attached oligo(ethylene oxide): A model system using self-assembled monolayers. *J. Am. Chem. Soc.*, 115(23):10714–10721, July 1993.

[6] S. I. Jeon, J. H. Lee, J. D. Andrade, and P. G. de Gennes. Protei-surface interactions in the presence of polyethylene oxide. *J. Coll. Int. Sci.*, 142(1):149–157, August 1990.

[7] P.G. de Gennes. Polymer solutions near an interface. 1. adsorption and depletion layers. *Macromlecules*, 14:1637–1644, March 1981.

[8] K. Feldman, G. Hähner, N. D. Spencer, P. Harder, and M. Grunze. Probing resistance to protein adsorption of oligo(ethylene glycol)-terminated self-assembled monolayers by scanning force microscopy. *J. Am. Chem. Soc.*, 121(43):10134 –10141, October 1999.

[9] S. Herrwerth, W. Eck, S. Reinhardt, and M. Grunze. Factors that determine the protein resistance of oligoether self-assembled monolayers - internal hydrophilicity, terminal hydrophilicity, and lateral packing density. *J. Am. Chem. Soc.*, (125):9359–9366, July 2003.

[10] R.S. Kane, P. Deschatelets, and G.M. Whitesides. Kosmotropes form the basis of protein-resistant surfaces. *Langmuir*, 19(6):2388–2391, 2003.

[11] D. J. Vanderah, H. La, J. Naff, V. Silin, and K. A. Rubinson. Control of protein adsorption: Molecular level structural and spatial variables. *J. Am. Chem. Soc.*, 126(42):13639 –13641, October 2004.

[12] J. Zheng, L. Li, S. Chen, and S. Jiang. Molecular simulation study of water interactions with oligo (ethylene glycol)-terminated alkanethiol self-assembled monolayers. *Langmuir*, 20(20):8931 –8938, Spetember 2004.

[13] R. L. C. Wang, H. J. Kreuzer, and M. Grunze. The interaction of oligo(ethylene oxide) with water: a quantum mechanical study. *PCCP*, 2:3613–3622, 2000.

[14] M. Zolk, F. Eisert, J. Pipper, S. Herrwerth, W. Eck, M. Buck, and M. Grunze. Solvation of oligo(ethylene glycol)-terminated self-assembled monolayers studied by vibrational sum frequency spectroscopy. *Langmuir*, 16(14):5849–5852, 2000.

[15] R. G. Nuzzo and D. L. Allara. Adsorption of bifunctional organic disulfides on gold surfaces. *J. Am. Chem. Soc.*, 105(13):4481–4483, 1983.

[16] F. Schreiber. Structure and growth of self-assembling monolayers. *Prog. Surf. Sci.*, 65:151–257, 2000.

[17] F. Schreiber. Self-assembled monolayers: from 'simple' model systems to biofunctionalized interfaces. *J. Phys.: Condens. Matter*, 16:R881–R900, July 2004.

[18] N. O. Fischer, C. M. McIntosh, J. M. Simard, and V. M. Rotello. Inhibition of chymotrypsin through surface binding using nanoparticle-based receptors. *Proc. Natl. Acad. Sci. U. S. A.*, 99:5018, 2002.

[19] M. Zheng and X. Huang. Nanoparticles comprising a mixed monolayer for specific bindings with biomolecules. *J. Am. Chem. Soc.*, 126:12047, 2004.

[20] S. D. Durbin and G. Feher. Protein crytallization. *Annu. Rev. Phys. Chem.*, 47:171–204, 1996.

[21] V. J. Anderson and H. N. W. Lekkerkerker. Insights into phase transition kinetics from colloid science. *Nature*, 416:811–815, 2002.

[22] R. Piazza. Protein interactions and association: an open challenge for colloid science. *Curr. Opin. Colloid Interface Sci.*, 8:515–522, 2004.

[23] A. George and W. W. Wilson. Predicting protein crystallization from a dilute solution property. *Acta Crystallogr. Sect. D*, 50(4):361–365, Jul 1994.

[24] A. Tardieu, A. Le Verge, M. Malfois, F. Bonneté, S. Finet, M. Riès-Kautt, and L. Belloni. Proteins in solution: from x-ray scattering intensities to interaction potentials. *J. Cryst. Growth*, 196:193–203, 1999.

[25] F. Bonneté, S. Finet, and A. Tardieu. Second virial coefficient: variations with lysozyme crystallization conditions. *J. Cryst. Growth*, 196:403–414, 1999.

[26] F. Bonneté and D. Vivarès. Interest of the normalized second virial coefficient and interaction potentials for crystallizing large macromolecules. *Acta Crystallogr. Sect. D*, 58(10 Part 1):1571–1575, Oct 2002.

[27] M. Muschol and F. Rosenberger. Interactions in undersaturated and supersaturated lysozyme solutions: static and dynamic light scattering results. *J. Chem. Phys.*, 103:10424–10432, 1995.

[28] M. Muschol and F. Rosenberger. Liquid-liquid phase separation in supersaturated lysozyme solutions and associated precipitate formation. *J. Chem. Phys.*, 107:1953–1962, 1997.

[29] A. M. Kulkarni, N. M. Dixit, and C. F. Zukoski. Ergodic and non-ergodic phase transitions in globular protein suspensions. *Faraday Discuss.*, 123:37–50, 2003.

[30] M. Delaye and A. Tardieu. Short-range order of crystallin proteins accounts for eye lens transparency. *Nature*, 302:415–417, 1983.

[31] B. Lonetti, E. Fratini, S.H. Chen, and P. Baglioni. Viscoelastic and small-angle neutron scattering studies of concentrated protein solutions. *Phys. Chem. Chem. Phys.*, 6:1388–1395, 2004.

[32] P. Baglioni, E. Fratini, B. Lonetti, and S.-H. Chen. Structural arrest in concentrated cytochrome c solutions: the effect of ph and salts. *J. Phys.: Condens. Matter*, 16:S5003–S5022, 2004.

[33] R. A. Curtis, J. M. Prausnitz, and H. W. Blanch. Protein-protein and protein-salt interactions in aqueous protein solutions containing concentrated electrolytes. *Biotechnol. Bioeng*, 57:11–21, 1998.

[34] D. E. Kuehner, H. W. Blanch, and J. M. Prausnitz. Salt-induced protein precipitation: Phase equilibria from an equation of state. *Fluid Phase Equilib.*, 116:140–147, 1996.

[35] J. Israelachvili. *Intermolecular and surface forces.* Academic Press: New York, 1992.

[36] G. Pellicane, D. Costa, and C. Caccamo. Theory and simulation of short-range models of globular protein solutions. *J. Phys.: Condens. Matter*, 16(42):S4923–S4936, 2004.

[37] M. L. Broide, T. M. Tominc, and M. D. Saxowsky. Using phase transitions to investigate the effect of salts on protein interactions. *Phys. Rev. E*, 53(6):6325–6335, Jun 1996.

[38] J. Narayanan and X. Y. Liu. Protein interactions in undersaturated and supersaturated solutions: A study using light and x-ray scattering. *Biophys. J.*, 84(1):523–532, 2003.

[39] O. D. Velev, E. W. Kaler, and A. M. Lenhoff. Protein interactions in solution characterized by light and neutron scattering: Comparison of lysozyme and chymotrypsinogen. *Biophys. J.*, 75(6):2682–2697, 1998.

[40] A. Striolo, D.B. Bratko, J-Z. Wu, N. Elvassore, H.W. Blanch, and J.M. Prausnitz. Forces between non-uniformly charged colloids from molecular simulation. *J. Chem. Phys.*, 116(17):7733–7743, 2002.

[41] V. G. Taratuta, A. Holschbach, G. M. Thurston, D. Blankschtein, and G. B. Benedek. Liquid-liquid phase separation of aqueous lysozyme solutions: effects of ph and salt identity. *J. Phys. Chem.*, 94:2140–2144, 1990.

[42] John A. Thomson, Peter Schurtenberger, George M. Thurston, and George B. Benedek. Binary liquid phase separation and critical phenomena in a protein/water solution. *Proc. Natl. Acad. Sci. USA*, 84(20):7079–7083, 1987.

[43] Gi. Foffi, G. D. McCullagh, A. Lawlor, E. Zaccarelli, K. A. Dawson, F. Sciortino, P. Tartaglia, D. Pini, and G. Stell. Phase equilibria and glass transition in colloidal systems with short-ranged attractive interactions: Application to protein crystallization. *Phys. Rev. E*, 65(3):031407, Mar 2002.

[44] A. Stradner, H. Sedgwick, F. Cardinaux, W. C. K. Poon, S. U. Egelhaaf, and P. Schurtenberger. Equilibrium cluster formation in concentrated protein solutions and colloids. *Nature*, 432:492–496, 2004.

[45] A. Stradner, G. Thurston, and P. Schurtenberger. Tuning short-range attractions in protein solutions: From attractive glasses to equilibrium clusters. *J. Phys.: Condens. Matter*, 17:S2805–S2816, 2005.

[46] M. Malfois, F. Bonneté, L. Belloni, and A. Tardieu. A model of attractive interactions to account for fluid-fluid phase separation of protein solutions. *J. Chem. Phys.*, 105:3290–3300, 1996.

[47] F. Sciortino, S. Mossa, E. Zaccarelli, and P. Tartaglia. Equilibrium cluster phases and low-density arrested disordered states: The role of short-range attraction and long-range repulsion. *Phys. Rev. Lett.*, 93(5):055701, 2004.

[48] D. N. Petsev and P. G. Vekilov. Evidence for non-dlvo hydration interactions in solutions of the protein apoferritin. *Phys. Rev. Lett.*, 84:1339–1342, 2000.

[49] Y. Liu, E. Fratini, P. Baglioni, W. R. Chen, and S. H. Chen. Effective long-range attraction between protein molecules in solutions studied by small angle neutron scattering. *Phys. Rev. Lett.*, 95:118102, 2005.

[50] A. Stradner, F. Cardinaux, and P. Schurtenberger. Effective long-range attraction between protein molecules in solution studied by small angle neutron scattering'. *Phys. Rev. Lett.*, 96(21):219801, 2006.

[51] C. M. Roth, B. L. Neal, and A. M. Lenhoff. Van der waals interactions involving proteins. *Biophys J.*, 70(2):977–987, 1996.

[52] C. M. Roth and A. M. Lenhoff. Electrostatic and van der waals contributions to protein adsorption: computation of equilibrium constants. *Langmuir*, 9(4):962–972, 1993.

[53] D. M. Huang, P. L. Geissler, and D. Chandler. Scaling of hydrophobic solvation free energies. *J. Phys. Chem. B*, 105(28):6704–6709, 2001.

[54] K. Lum, D. Chandler, and J. D. Weeks. Hydrophobicity at small and large length scales. *J. Phys. Chem. B*, 103(22):4570–4577, 1999.

[55] R. Winter and F. Noll. *Methoden der Biophysikalischen Chemie.* B.G. Teubner Stuttgart, 1998.

[56] T. Butz. *Fouriertransformation für Fußgänger.* B. G. Teubner Leipzig, 1998.

[57] J. D. Jackson. *Classical Electrodynamics.* John Wiley, N.Y., third edition edition, 1999.

[58] K. W. Hipps and G. A. Crosby. Applications of the photoelastic modulator to polarization spectroscopy. *J. Phys. Chem*, 83:555, 1979.

[59] M. Abramowitz and I. A. Stegun, editors. *Handbook of Mathematical Functions.* National Bureau of Standards, 1964.

[60] A. S. Brown, S. A. Holt, P. M. Saville, and J. W. White. Neutron and x-ray reflectometry: Solid multilayers and crumpling films. *Aust. J. Phys.*, 50:391–405, 1997.

[61] L. G. Parratt. Surface studies of solids by total reflection of x-rays. *Phys. Rev.*, 95(2):359–369, Jul 1954.

[62] J. Als-Nielsen and D. McMorrow. *Elements of Modern X-Ray Physics.* John Wiley & Sons Ltd, 2001.

[63] S. M. King. Small angle neutron scattering. *http://www.isis.rl.ac.uk/largescale/loq/documents/sans.htm*, 1995.

[64] A. Isihara. Determination of molecular shape by osmotic measurement. *J. Chem. Phys.*, 18:1446–1449, 1950.

[65] http://www.ncnr.nist.gov/programs/sans/data/index.html. Technical report, NIST.

[66] J. B. Hayter and J. Penfold. An analytic structure factor for macroion solutions. *Mol. Phys.*, 42:109–118, 1981.

[67] J. P. Hansen and J. B. Hayter. Interaction of proteins in solution from small-angle scattering: A perturbative approach. *Mol. Phys.*, 46:651–656, 1982.

[68] R. V. Sharma and K. C. Sharma. The structure factor and the transport properties of dense fluids having molecules with square well potential, a possible generalization. *Physica*, 89A:213–218, 1977.

[69] N. W. Ashcroft and J. Lekner. Structure and resistivity of liquid metals. *J. Phys. Rev.*, 145:83–90, 1966.

[70] J. Ilavsky. Irena 2 package of sas data evaluation and modeling macros for igor pro. *http://www.uni.aps.anl.gov/ ilavsky/irena.html*, 2006.

[71] S. R. Kline. Reduction and analysis of sans and usans data using igor pro. *J Appl. Cryst.*, 39(6):895, 2006.

[72] W. Haiss, N.T.K. Thanh, J. Aveyard, and D.G. Fernig. Determination of size and concentration of gold nanoparticles from uv-vis spectra. *Anal.Chem.*, 2007.

Part II.

Results and discussion

64

4. Experimental practical

4.1. Sample preparation

4.1.1. SAMs on flat substrates

The self-assembling monolayers used in this thesis were grown using the well-known 'thiols-on-gold route'. This is a comparatively simple preparation method that yields reproducible, high-quality monolayers if certain cleaning procedures and preparation protocols are followed strictly.

Glassware All glassware was meticulously cleaned according to the following protocol. First, the containers were thoroughly rinsed with ultra-pure water (18.2 MΩ·cm) from a commercial Millipore Milli-Q© Gradient water purification system. The glassware was then immersed in a bath of Decon_90 overnight, then thoroughly rinsed again, filled with 30 % hydrogen peroxide solution, and either left overnight, or heated to about 60°C for four hours. Finally, the containers were rinsed again with ultrapure water, and blown dry with nitrogen, or placed in a hot cupboard at 120 °C until dry.

Substrates The preparation of an homogeneous, flat and smooth surface is one of the key factors for obtaining good monolayers. In particular a low surface roughness is crucial, not only for the formation of the monolayer, but also for the quality of subsequent measurements, such as neutron reflectivity. Two kinds of substrates were used for the neutron reflectivity and in-house experiments respectively.

Large area (100×80 mm^2) SiO_2 (quartz) blocks were used for the former technique due to the comparatively low flux of neutrons. The quartz blocks with a thickness of 12.7 mm were purchased from CrysTec, Berlin, Germany. The root mean square (RMS) roughness was about 1-2 Å (sometimes less) as determined by AFM over an area of 1 μm^2.

For laboratory based techniques, such as infrared spectroscopy (RAIRS), ellipsometry and x-ray reflectivity, prime-grade silicon ⟨100⟩ wafers were used, with a thickness of 585 μm and a diameter of 100 mm. Wafers were purchased from Compart Technology Ltd., UK and Si-Mat Silicon Materials, Germany. These standard wafers had a native oxide layer of about 1-2 nm. The root mean square roughness was about 1-2 Å. Both substrates were used as received.

The procedure for the metal coatings was identical for both types of substrates. First a layer of either 1-2 nm of titanium or 5-10 nm of chromium was applied by thermal evaporation. Prior to the evaporation, the wafers were oxygen plasma-cleaned in order to remove any organic impurities from the surface. Then, a gold layer with a thickness ranging from 35 to 70 nm for the quartz samples and 100 nm for the silicon wafers was added. The gold-coated samples were stored under argon until needed. The gold-coated silicon wafers were split into suitable pieces, usually with an area of 1×2 cm^2. Larger and smaller sized wafer pieces were also tested, in order to exclude any effects of the sample size on the SAM formation and the measurement process, especially when studied at grazing angles of incidence. Great care was taken to avoid scratching of the gold surface. Potential dust was removed by gently blowing a nitrogen stream on the surface.

Thiols The following thiols have been obtained from the sources given and were used as received:

Molecule	Source
HS-$(CH_2)_n$-CH_3 ($n = 14, 16, 18$)	PCI Heidelberg, Sigma-Aldrich, ProChimia
HS-$(CD_2)_{18}$-CD_3	ProChimia
HS-$(CH_2)_{11}$-$(O\text{-}CH_2\text{-}CH_2)_3$-$OCH_3$ (EG3OMe)	PCI Heidelberg, ProChimia
HS-$(CD_2)_{16}$-$(O\text{-}CH_2\text{-}CH_2)_3$-$OCH_3$	ProChimia
HS-$(CD_2)_{12}$-$(O\text{-}CD_2\text{-}CD_2)_3$-$OCD_3$	ProChimia
HS-$(CH_2)_{11}$-$(O\text{-}CH_2\text{-}CH_2)_6$-$OCH_3$ (EG6OMe)	ProChimia

SAM formation Self-assembled monolayers were grown from 500 μmol solutions of the particular thiol in ethanol, unless otherwise stated. Absolute ethanol purissimum pro analysi was purchased from Riedel-de Haën and used as received. The pre-cut, gold-coated wafer pieces were cleaned in an ozone producing reactor for one

hour. After the samples had cooled down, they were thoroughly rinsed with ethanol and immediately submerged in the thiol solution. The solution containing the sample was stored at room temperature and the typical time for SAM formation was 20 hours, except for the coverage dependence studies, where the SAM formation was interrupted after given periods of time, thereby resulting in monolayers with partial coverage. After the monolayer was complete, the sample was carefully removed from the thiol solution and immediately copiously rinsed with absolute ethanol in order to remove physisorbed molecules. The sample was then blow-dried in a gentle argon stream and the sample stored under argon until used.

4.1.2. Preparation of surface modified gold colloids

Citrate-stabilised gold colloids with various diameters were purchased from British BioCell International (BBI) and Sigma-Aldrich and were used as received. The mono-dispersed gold colloids with various diameters were modified by directly adding 0.1 mg/mL EG6OMe to the colloid solution. This corresponds to an excess of EG6OMe by a factor of between 10^2 and 10^3, based on a simple calculation considering the total surface area of gold colloids and the cross-section of the thiol molecule. Weisbecker et al. [1] reported detailed studies on the stability of various aliphatic thiols on gold colloids. They found that although alkanethiols with $HS(CH_2)_nR$, R=CH3, or OH, lead to fast flocculation, oligo(ethylene glycol) thiols with $HS(CH_2)_{11}(OCH_2CH_2)_yOH$, y>3, stabilise the gold colloids. After incubation at room temperature for more than 4 hours, the stability of modified colloids was examined. The modified gold colloids are stable in the experimental conditions to temperature (5-70 °C), NaCl concentration (0-1.0 M), and pH (1.3-12.4). A second transfer reaction following the procedure of Aslan and Pérez-Luna [2] involving the nonionic surfactant polyoxyethylene (20) sorbitan monolaurate (Tween 20) was also tried and compared to the direct transfer. No differences in the colloidal stability were observed and therefore the direct method was used. The direct transfer of thiols onto citrate-stabilised gold colloids is simpler and has the further advantage that no excess Tween20 remains in the system.

4.2. Neutron reflectometers

Neutron reflectivity data presented in this thesis was taken at the research facilities at ISIS, Rutherford-Appleton Laboratory, UK, using the SURF reflectometer and at the Institut Laue-Langevin (ILL) in France, using the ADAM reflectometer. ISIS is a pulsed neutron spallation source and the ILL a neutron reactor. The sample geometry at the two instruments (SURF and ADAM) is different and the basic features will be described below.

4.2.1. ADAM at ILL

The ADAM reflectometer [3] is an angle dispersive fixed wavelength instrument, operating at a wavelength of 4.41 Å, which combines high flux due to a focusing monochromator with a high Q resolution. The sample is mounted vertically on a Huber goniometer, which is advantageous when measuring with liquid samples, because potential air bubbles will rise to the upper end of the sample and can be excluded from the illuminated area. The most important instrument characteristics are listed in **Table 4.1**. The lowest accessible angle outside the direct beam

Monochromator		
type	wavelength	resolution
PG (002), vertically focusing	4.4Å 2.2Å ($\lambda/2$)	$\Delta\lambda$ / λ = 0.006
Collimation		
horizontal: pair of slits ($\sim$ 2 m apart), 0.1 - 10 mrad		
monochromator-to-sample-distance 3250 mm		
Sample		
flux (with open slits)		orientation
$\sim 2 \cdot 10^6$ n cm^{-2} s^{-1}		vertical
^{3}He Detector		
distance to sample		background (beam closed)
1660 mm		$\sim$ 2 counts/minute

Table 4.1.: Overview over the ADAM instrument characteristics.

corresponds to $Q_{min} \approx 0.003$ Å^{-1}, which is of particular importance when index matched samples are measured (see also **Section 4.5**): A low Q_{min} allows the accurate measurement of the critical edge, that appears at very low Q-values, which

in turn facilitates the normalisation procedure. Neutrons are counted using a 1-dimensional ^{3}He pencil detector. The counting time at each angle was adjusted to yield sufficiently small error bars over the whole Q-range.

4.2.2. SURF at ISIS

Data acquisition of the SURF instrument [4] differs from that of the ADAM instrument, the former being a Time-Of-Flight instrument. This implies that for a given incident angle of the neutron beam, the reflected intensity is recorded simultaneously over a range of neutron energies, respectively Q_z values. To extend the q_z range

angle	Q-range [Å^{-1}]	ΔQ/Q
0.07	0.002-0.028	0.05
0.25	0.008-0.10	0.05
0.8	0.027-0.32	0.05

Table 4.2.: Overview over the SURF instrument settings.

to the desired range (0.003 to 0.3 Å^{-1}) three incident angles 0.07, 0.25 and 0.8 degrees have been used. The corresponding Q-ranges and the experimental resolution are listed in **Table 4.2**. The measured Q_z ranges for the three angle settings were chosen to overlap such that data points from neighbouring angular regions could be merged. The sample slits were set differently for each of the three incident angles in order to illuminate the same surface area. An illumination correction as described in **Section 4.4** was therefore not necessary. Data from the three angle settings were merged by averaging in the overlap region using a macro from the software package OpenGenie [5], thereby also improving the statistics in that range.

4.3. Liquid cell for neutron reflectivity

In situ neutron reflectivity experiments were performed on the gold-coated quartz blocks described in **Section 4.1.1**, which were attached with a seal to a cavity containing the aqueous solution used for the measurement. The quartz blocks were attached using two metal slabs along the long side ensuring a good seal. Three different liquid containers were used, depending on the experimental requirements. In most cases containers made of MACOR, a machinable glass ceramics containing

~7% boron with a depth of 1 mm were used. The advantage of MACOR is the high absorption for neutrons which helped to minimise the incoherent background from the bulk solution, especially for solutions containing hydrogen, such as protein and contrast adjusted solutions with H_2O content. The thickness of 1 mm was found to be sufficiently thin to reduce background scattering and thick enough for use with highly concentrated, viscous protein solutions. For temperature dependent measurements, containers made of aluminum were employed in order to optimise thermal contact with the cooling/heating unit and achieve reasonably fast and stable temperature settings. In particular cases, PTFE made sample containers were also used. **Figure 4.1** shows a schematic of the sample cell assembly. For temperatures

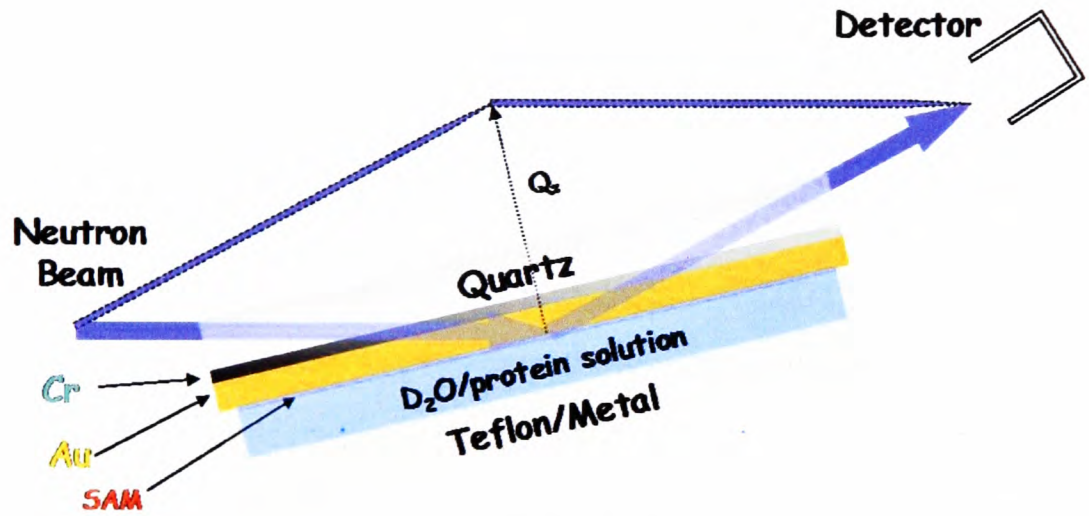


Figure 4.1.: Cell assembly for in situ neutron reflectivity measurements of monolayers in contact with aqueous solutions. The material for the liquid container was either PTFE, aluminium or MACOR (a machinable glass ceramic containing boron).

other than room temperature, the aluminium-made liquid cell was mounted on a copper block through which cooling liquid was pumped, which had been adjusted to the desired temperature in an external temperature controlled water bath. The whole liquid cell and copper block were contained inside a nitrogen flushed external double-walled container in order to reduce heat transfer and avoid condensation on the sample cell at low temperatures. The insulating space between the outer double walls was evacuated using a roughing pump. The outer container was fitted with two 1 mm thick windows made of an aluminium-magnesium (AlMg3) alloy, which has a very low absorption cross section for thermal neutrons.

4.4. Data treatment for neutron reflectivity

The raw data obtained from a neutron detector had to be corrected for sample geometry and off-specular scattering before it could be analysed with the fitting software. The data correction procedure described in this section was applied to all data sets acquired for the present work.

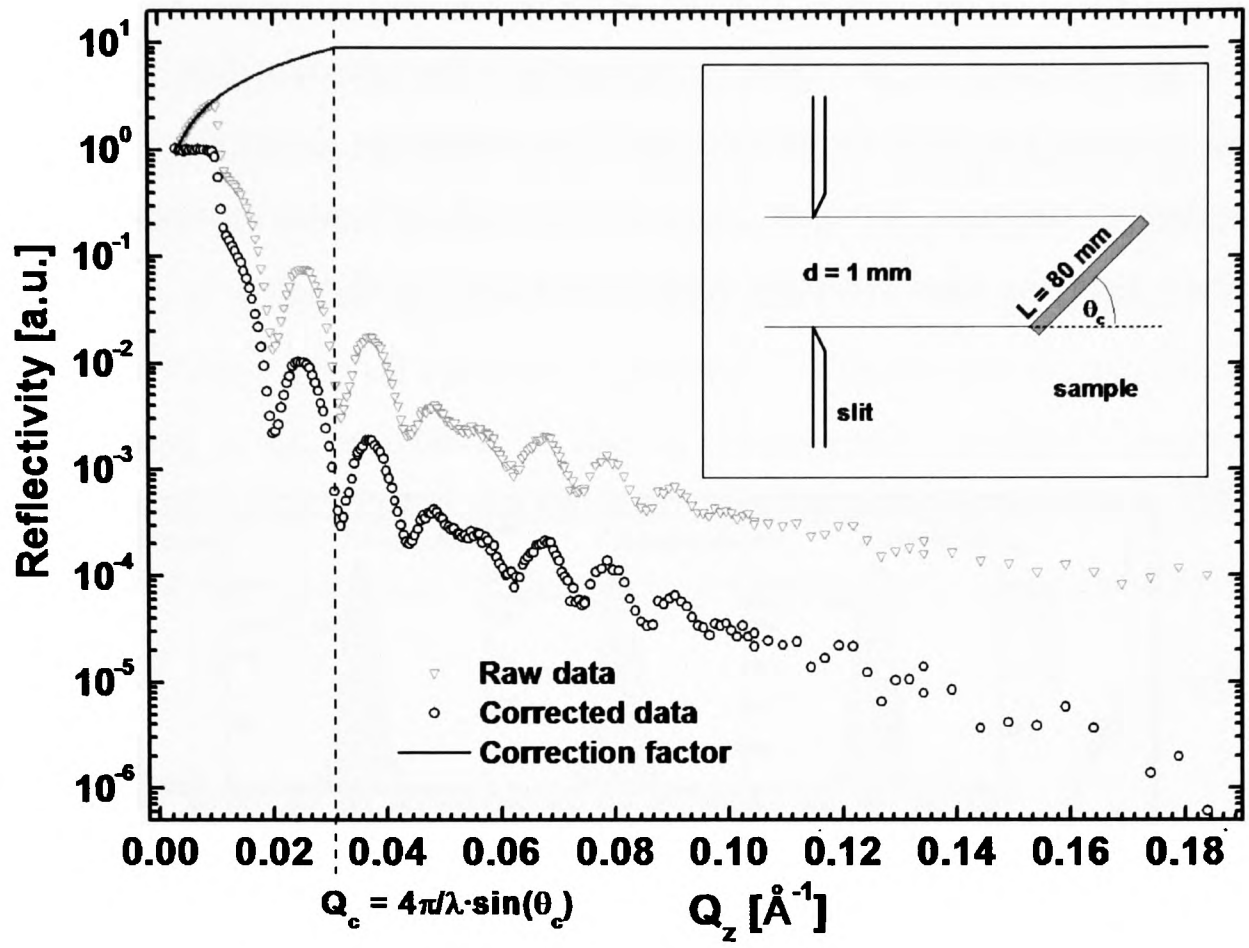


Figure 4.2.: Illumination correction. The measured reflectivity has to be corrected for angles $\theta < \theta_c$ by a factor $\frac{d}{l} \sin\theta$ determined by the beam width d and the sample length L.

Illumination correction When data is taken at an angle dispersive instrument, such as ADAM at the Institut Laue-Langevin (see **Section 4.2**), the collimated beam of finite width will over-illuminate the sample at low angles. Therefore, the measured intensity for a sample of finite width is proportionally lower than that at higher angles, where the whole beam is reflected by the sample. When the incident angle is increased, the footprint of the beam on the sample becomes smaller until all incoming neutrons hit the sample. This is a purely geometric effect and can be corrected easily. To achieve this, two methods were applied:

(i) A geometric correction factor was computed based on the size of the sample and on the beam width determined by the slits before the sample: at the critical angle θ_c

the sample of length L is fully illuminated by a neutron beam of width d. For angles $\theta < \theta_c$ the sample is over-illuminated ($d > L \sin\theta$) and the measured reflectivity has to be corrected by division by a factor $\frac{d}{l} \sin\theta$. Beyond θ_c the reflectivity is corrected by the constant factor $\frac{d}{l}$. This procedure is illustrated in **Figure 4.2**.

(ii) The correction factor was determined experimentally by fitting the measured reflectivity data in the region of total reflection. The obtained factor was then applied as described in (i). The experimental determination has the advantage that it accounts for small errors introduced by variations in the slit width and the actual illuminated area. However, this method is not applicable for contrast matched samples, where the total reflection edge is very close to $Q = 0$.

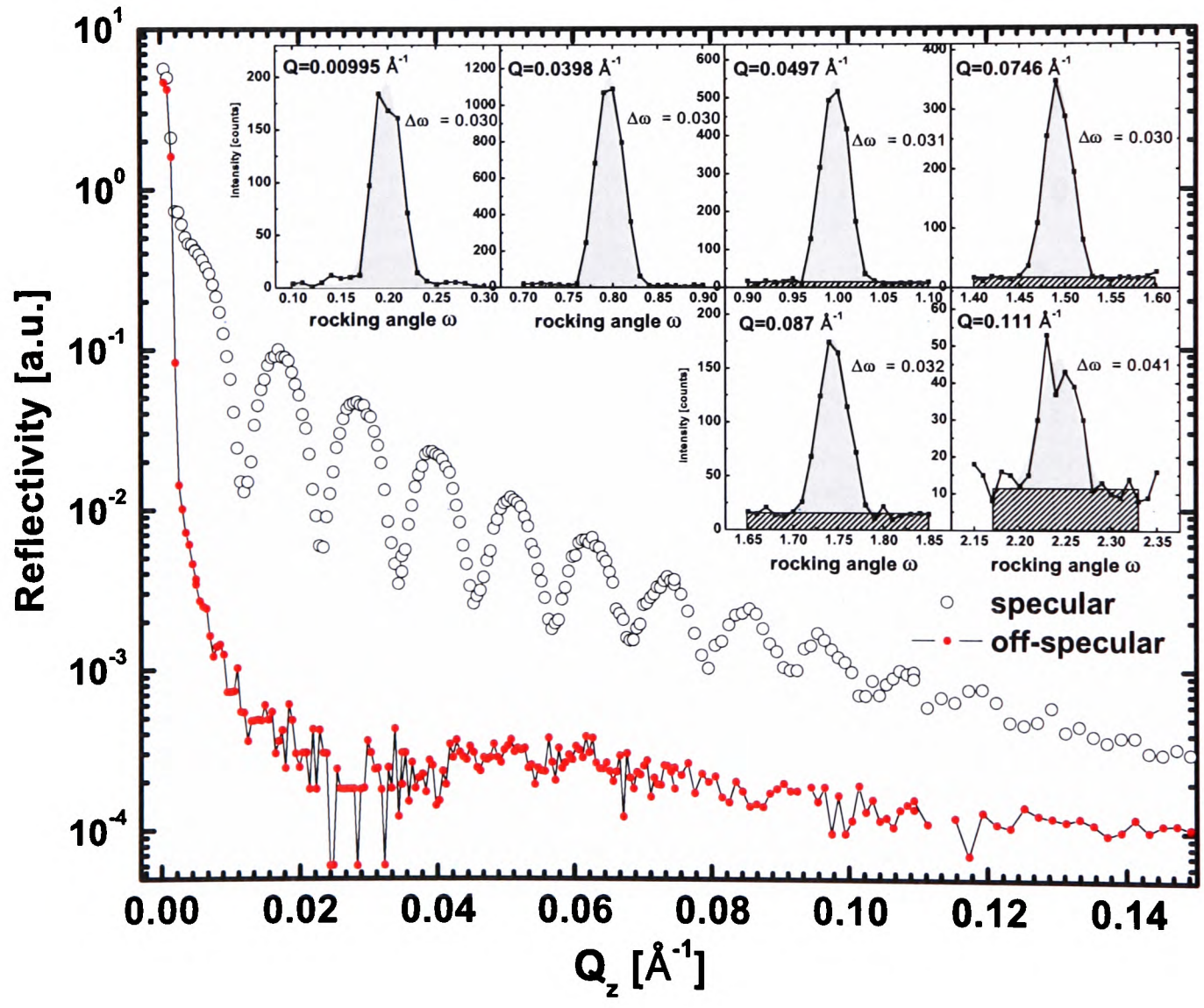


Figure 4.3.: Raw data from a reflectivity scan of a fully deutrated EG3OMe SAM with a 15 wt % $BSA/D_2O/H_2O$ contrast matched solution. The red dots show the off-specular reflectivity measured at $\theta + 2\Delta w$. Δw was taken to be the width of the largest rocking curve at $Q = 0.111$ Å^{-1}. The hatched areas under the rocking curves at different Q shows the background that was subtracted from the specular reflectivity.

Background subtraction As described in **Section 3.2.2** the specular reflectivity is superimposed on scattering background arising from surface roughness, incoherent scattering from the solution and small-angle scattering from the dissolved proteins. The true specular information was obtained by measuring the reflectivity on the specular path and then subtracting the off-specular reflectivity measured with sample angle offset by $\Delta\theta$ from the specular condition. $\Delta\theta$ for each sample was determined by rocking (Q_x) scans at several different Q_z values. The width Δw of the rocking (specular) peak was determined and the offset was set to $\Delta\theta = 2\Delta w$. Typical rocking curves for an EG3OMe sample in contact with a highly concentrated protein solution are shown in the inset of **Figure 4.3**. The hatched area under the rocking curves at different Q_z shows the background that was subtracted from the specular reflectivity. The off-specular reflectivity in **Figure 4.3** shows a broad but distinctive peak at $Q_z \approx 0.06$ Å^{-1}, that is characteristic of highly concentrated protein solutions. This peak originates from small-angle scattering in the bulk and is indicative of the interaction of the charged proteins with each other (structure factor).

4.5. Index matching for neutron reflectivity

The partially fully deuterated compounds for SAM formation listed in **Section 4.1.1** have been developed and employed in order to enhance the visibility of structural changes at the solid-liquid interface. For the rather complex system studied for this work, the chromium and gold layers gave rise to pronounced thickness oscillations in the reflectivity profile, thereby making it more difficult to identify oscillations originating from changes at the interface between SAM and aqueous phase. Here, the well known technique of index matching was employed in order to improve the situation.

The basic idea behind index matching in a layered system is to reduce contrast between layers that are not in the focus of the study, while at the same time increasing the contrast of the important layers. The strategy used for the present work is twofold:

- In the general case, the scattering length densities of SAM and liquid phase were adjusted to that of gold[1], such that in the case of a smooth transition from SAM to liquid there would be no change in the scattering length density. The only visible osclillation in the reflectivity profile would then stem from the chromium layer. Any changes in density at the solid-liquid interface would result in additional oscillations in the reflectivity curve. This theoretical situation is illustrated in **Figure 4.4**.

- Whenever a particular change in density, for instance due to a depletion layer, was suspected, it was attempted to maximise the contrast by using for instance a fully deuterated SAM and a pure D_2O liquid phase, when a reduced water density was expected at the interface.

The application of these considerations is demonstrated in **Chapters 5** and **7**.

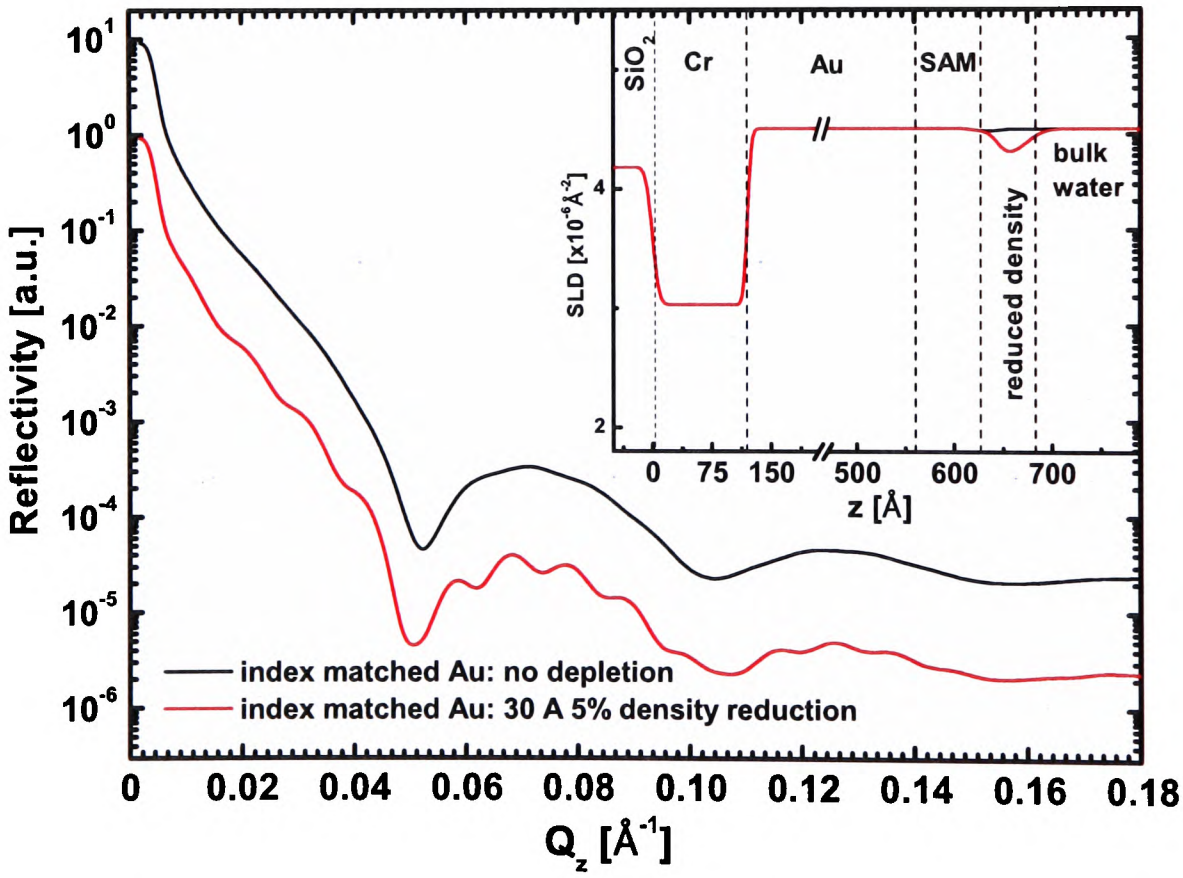


Figure 4.4.: Calculated reflectivity and corresponding real space profiles for an index (Au)-matched system. The black curve represents a perfectly matched SAM and liquid phase: only the chromium thickness oscillations are visible. The red curve shows the effect of an additional 30 Å wide layer with a water density reduced by 5% compared to the bulk: additional oscillations apear in the reflectivity curve.

[1]The scattering length density of the SAM was set to that of gold by mixing fully protonated and fully deuterated SAM molecules with the appropriate ratio during the SAM formation.

4.6. The infrared spectrometers

Two PMIR systems were employed for the experiments presented in this thesis.

a. Bruker Vertex 70. Unless otherwise stated, all spectra were recorded using a dry-air-purged Bruker Vertex 70 spectrometer with a PEM 50 polarisation modulation unit. The mirror speed was set to 10 kHz and the aperture in front of the light source was 4 mm. A KBr beam splitter was used in the MICHELSON interferometer. The resolution was 4 cm^{-1}, and the measuring time was approximately 4 min, corresponding to 256 co-added scans. The incident angle was adjusted as described in **Section 5.5**.

b. Bio-Rad FTS-6000. Part of the spectra was taken using a dry-air-purged Bio-Rad FTS-6000 FOURIER transform IR spectrometer with polarisation modulation unit. Data were collected at 20 Hz at a resolution of 8 cm^{-1}, and an undersampling ratio (UDR) of 4 was used to improve the speed of data acquisition. To avoid aliasing, we placed a UDR filter into the optical path of the IR beam, which prevents radiation at higher wavenumbers from reaching the detector.

In both spectrometers a polarisation modulator (PM) was employed, which was controlled by a Hinds Instruments PEM-90 photoelastic modulator control unit. The half-wave retardation was set at 37 kHz. The geometry was similar for both spectrometers. The sample was placed vertically between a focusing mirror and a ZnSe lens in front of the detector. A schematic view is shown in **Figure 3.1**. Some photographs are shown in the appendix (**E**).

4.7. The liquid cell for PMIRRAS

Infrared spectroscopy through a layer of liquid water or through other liquids is accompanied by a series of difficulties, such as reflection losses, absorption of the liquid etc., so that the design of the experimental setup and the choice of materials have to be tailored to the specific conditions. For the PMIRRAS experiments presented in this thesis, the goal was to observe the characteristic absorption band of an OEG or alkanethiol SAM through a thin layer of water (H_2O or D_2O) or a non-polar solvent such as trichloromethane. A similar PMIRRAS set-up for in situ electrochemical studies has been described by V. Zamlynny [6]. There, an equilateral prism

is used to couple the light into the system with minimal losses. In the present work a half-cylinder was employed to allow normal incidence with respect to the surface normal of the half-cylinder at any incident angle (**Figure 4.5**). The requirements

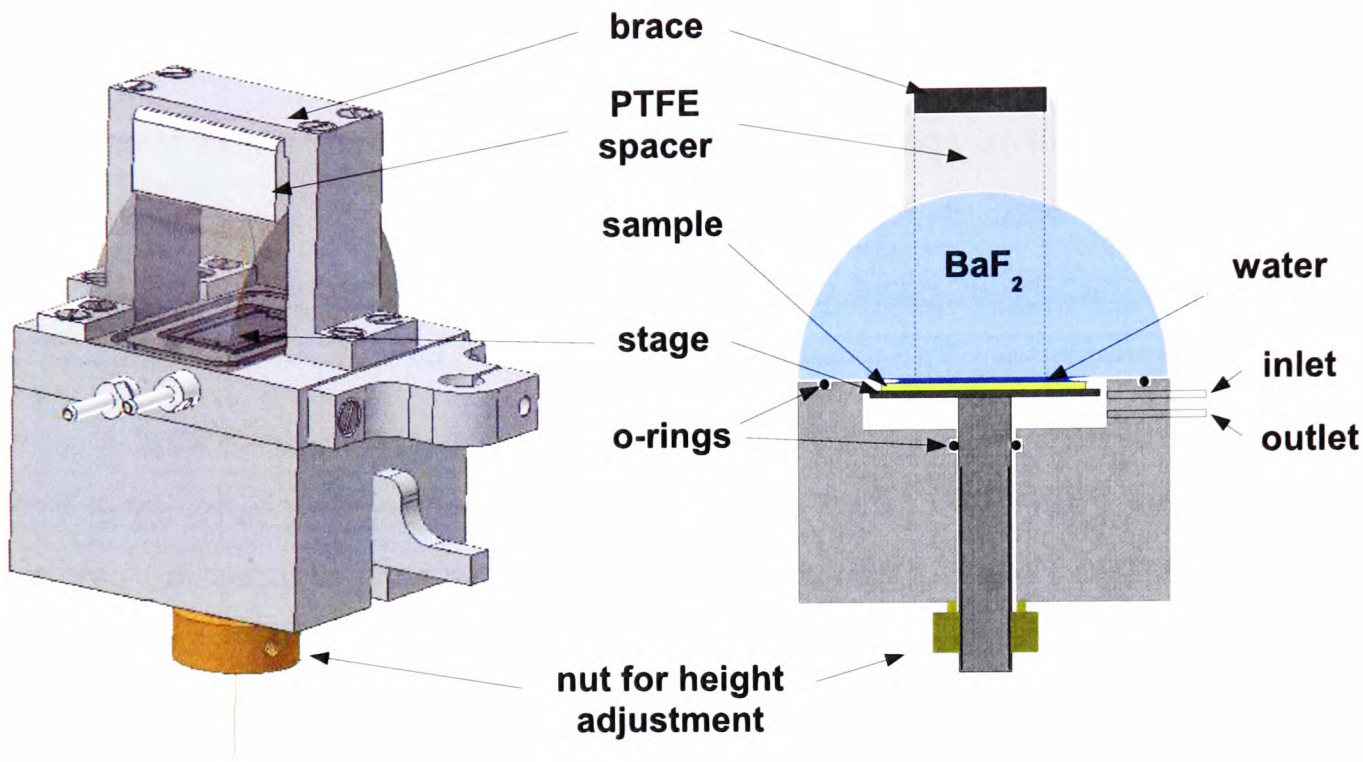


Figure 4.5.: Sketch of the cell used for in situ PMIRRAS measurements. (a) Drawing including BaF_2 equilateral prism (courtesy of A. Treftz). (b) Side view.

for the material of the half-cylinder are a high transmission in the spectral region of interest (i.e. between about 1000 and 3000 cm^{-1}) and a refractive index close to that of water in the same spectral region. Index matching of half-cylinder and liquid reduces refractive losses at the solid-liquid interface. Since most optical materials have a refractive index higher than that of water, total reflection may occur above a critical angle. These issues will be discussed in more detail in **Section 5.5**. Based on these considerations barium fluoride was chosen as the optimum material for the half-cylinder. Barium fluoride has a very low refractive index and a high transmission down to about 800 cm^{-1} (**Figure 4.6**). Calcium fluoride was also used as a second choice. However, even though the refractive index of calcium fluoride is closer to that of water (**Figure 4.7**), its transmission in the region around 1100 cm^{-1} is about 50% that of barium fluoride (**Figure 4.6**). For experiments in the CH-stretching region around 2900 cm^{-1} calcium fluoride or barium fluoride

can be used, because the transmission and refractive index are very similar for both materials.

The BaF_2 half-cylinder had a radius of 2.5 cm and a thickness of 3 cm, resulting in a flat rectangular area of 3×5 cm^2 which was facing the sample. The half-cylinder was designed to rest on a Viton seal along the outer edges of the rectangular surface, allowing the trough underneath it to be filled with the desired liquid using the in- and outlet nozzles. However, in the case of aqueous solutions it was sufficient to

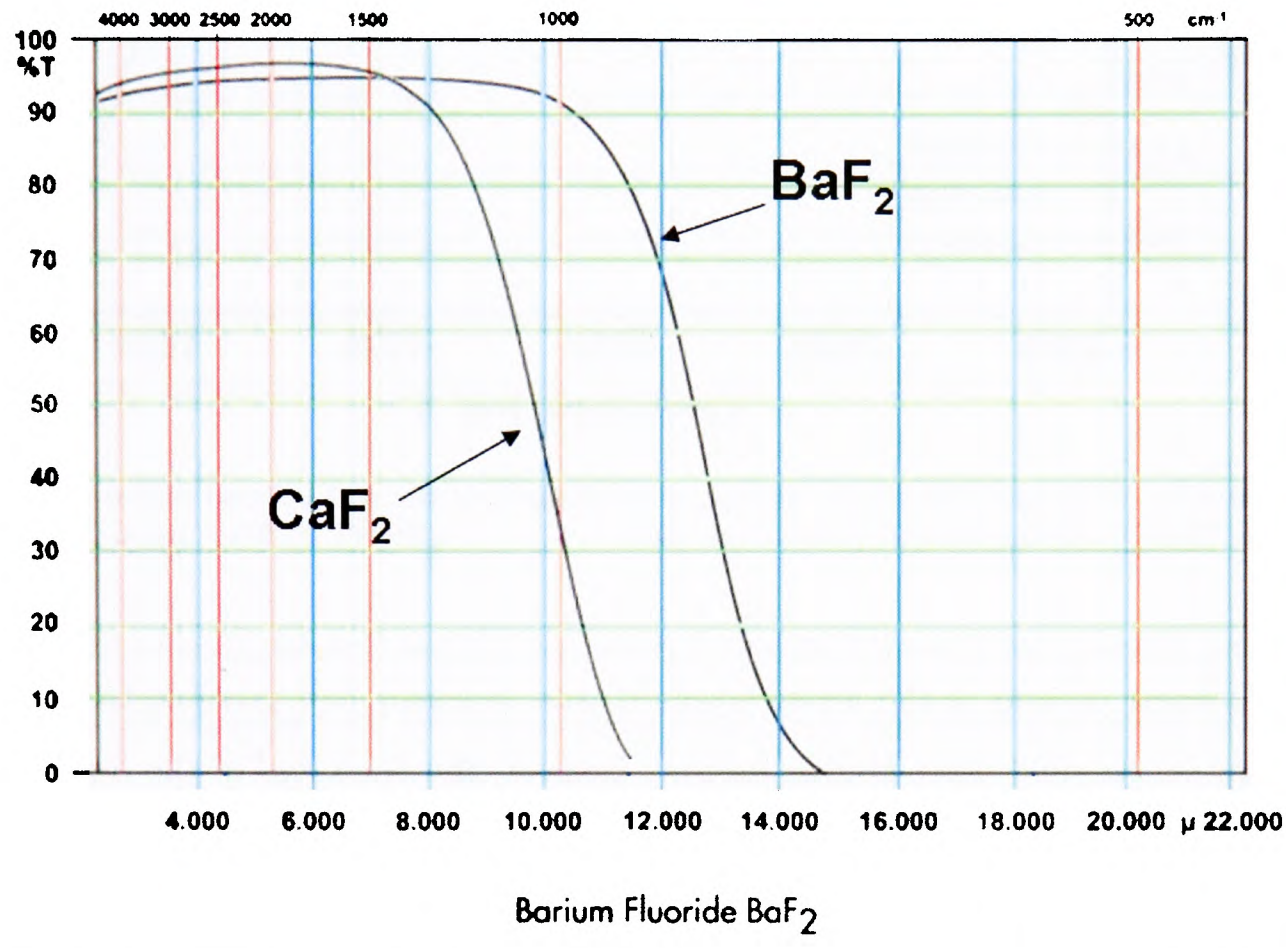


Figure 4.6.: Transmission of barium fluoride (BaF_2) and calcium fluoride (CaF_2) in the mid-infrared wavelength region. (from *www.internationalcrystal.net/optics*$_0$*2.htm*)

place a drop of the solution on the sample and press the sample gently against the half-cylinder. The surface tension was enough to keep the sample attached and prevent fast evaporation. For the use with more volatile liquids, such as $CHCl_3$, it was necessary to fill the trough. The half-cylinder was fastened with a metal clamp from the top of the round surface, which rested on a curved PTFE block, thereby distributing the pressure evenly onto the half-cylinder. The sample rested on a sample stage of 2.5×3 cm^2 which could be moved vertically by hand, using a fine thread. The appropriate thickness of a few micrometres of the liquid layer was achieved by adjusting the pressure of the sample stage against the half-cylinder. The sample cell was initially designed to accommodate an electronic micrometer gauge

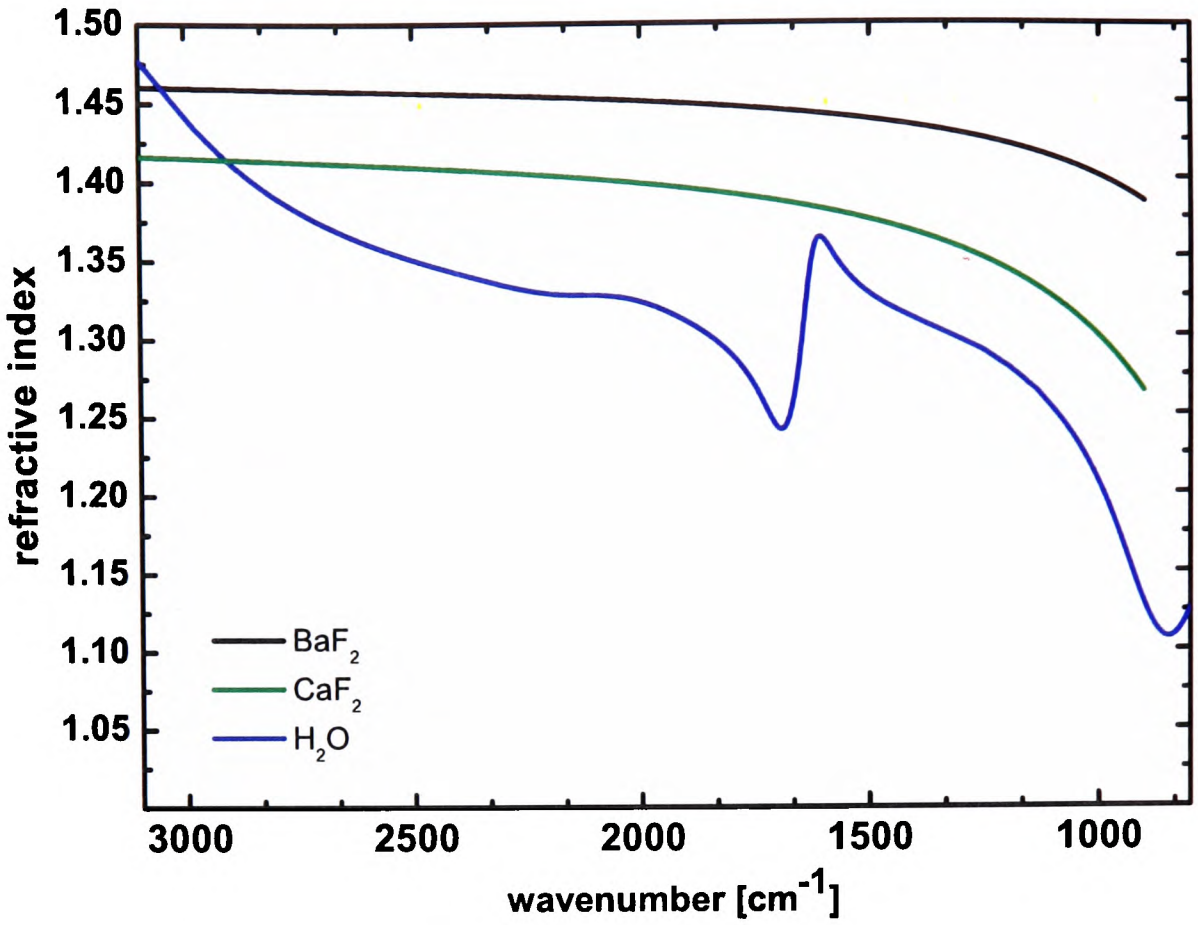


Figure 4.7.: Refractive index as a function of wavelength in the mid-infrared region for barium fluoride (BaF_2), calcium fluoride (CaF_2) and water.

for thickness control of the water layer. It was, however, not possible to calibrate the system to yield reproducible results. Instead, the thickness of the liquid layer was measured with an ellipsometer.

4.8. Small-angle x-ray scattering

Small-angle x-ray scattering measurements were carried out at station 6.2 of the Synchrotron Radiation Source (SRS) at the Daresbury Laboratory, Warrington UK [7]. The beam energy was 15.0 keV corresponding to a wavelength of 0.827 Å. The scattered intensity was registered with a 200 mm-radius quadrant detector located 3.3 m from the sample. The accessible q-range was thus from 0.013 to 0.45 $Å^{-1}$.

Protein solutions were filled into a sample cell with two mica windows (25 μm thick) separated by a 1.0 mm Teflon spacer. In order to calculate the absolute intensity. the empty cell and salt solutions were also measured. All measurements were carried out at room temperature. The resulting data were (electronically) converted to a 1D profile by integrating around an arc. The raw data were corrected for transmission. fluctuation of primary beam intensity, exposure time, and the

geometry of the detector. The detailed data correction and calibration is described in **Chapter 6**.

Additional SAXS measurements (**Figure 7.18** and **7.21b**) were performed at the JUSIFA beamline at HASYLAB/DESY, Hamburg [8] in the energy range of 11.7 - 17.5 keV. A q range from about 0.0075 to 0.28 $Å^{-1}$ was covered. The samples as well as the salt solution were filled into capillaries from Hilgenberg GmbH, Malsfeld, Germany. The capillaries are made of borosilicate glass with an inner diameter of 4.0 mm and a wall thickness of 50 μm. The capillaries were embedded into custom made aluminium holders and these holders were sealed at both ends by rubber O-rings and an M6 screw. The scattering of water or salt solution as background was measured at the same condition as used for the protein/colloidal solutions and was subtracted from the sample scattering. All scattering curves have been calibrated to absolute intensity in units of cross-section per unit volume (cm^{-1}).

4.9. X-ray reflectivity

Reflectivity measurements with x-rays for the determination of the metal layer thicknesses of the samples used for the neutron reflectivity and infrared spectroscopy experiments were performed with the BRUKER D8 ADVANCE diffractometer of the Surface Analysis Facility (SAF) at the Chemistry Research Laboratory in Oxford, UK [9]. The X-ray Source is a 2.2 kW Cu anode long fine focus ceramic x-ray tube. The running conditions for the x-Ray tube are 40 kV and 40 mA. The beam is collimated, compressed and frequency-filtered by a Göbel mirror and V-Groove to produce a collimated beam with dimensions of about 0.3 by 11 mm. The detector is a NaI dynamic scintillation detector with a maximum count rate of 2×10^6 s^{-1}. The sample is placed on stage in a high precision microprocessor-controlled, two circle goniometer with independent stepper motors and optical encoders for the θ and 2θ circles.

5. Behaviour of Water at the SAM/water interface

The experimental results described in the following sections present an investigation of the density structure at the interface. They provide information about the water, the monolayer and their interactions, by studying the unperturbed system in situ, with no additional perturbations, such as that of an AFM tip. Our neutron reflectivity measurements at room temperature reveal a region of ~5-6 nm of water adjacent to the OEG SAM, which has a density about 10% lower than the bulk phase, which can be attributed to the formation of tightly bound water layer. At 5 °C, both the extent and the density of this layer are slightly reduced, but still persist, and the integrated depletion area (depletion width × density reduction) remains comparable to that at room temperature. Further investigations by in situ PMIRRAS reveal significant peak shifts of the characteristic C-O-C mode of the OEG moieties, indicating a rather strong interaction of water with the SAM and potential water penetration into the monolayer.

5.1. Introduction

The structure and interaction of water in contact with organic matter is of great importance for the understanding of a broad range of fundamental phenomena: for example, the folding and unfolding of proteins and polymers, the interactions of colloids, and the tribological properties of functionalised surfaces in contact with aqueous solutions. The hydrophobic interaction as the driving force for certain self-assembly processes in solutions is also a matter of ongoing research. All these topics have received significant attention in recent years [10–14] and have been illuminated by our experiments.

Hence, structural deviations from the bulk properties of the water layer adjacent to an OEG functionalised interface are of significant general interest. There are indications based on scattering experiments that the water phase close to the OEG

SAM can exhibit a change in density [14]. Kim et al. [15] report an interfacial layer of water with a viscosity of up to six times that of bulk water, which extends up to 5 nm from an OEG coated surface; they discuss the implications of such a layer of "interphase" water for the protein resistance of the monolayer. In addition, theoretical studies suggest a rather strong interaction of water with oligo (ethylene glycol) terminated monolayers. Theoretical work by Wang et al. [16] suggests that OEG conformers which have gauche rotations in opposite directions around neighbouring ethylene glycol (EG) units are penetrated by water because on these structures water can form double and triple hydrogen bonds with up to three oxygen atoms along the OEG terminated molecule. These observations are also supported by the sum-frequency generation (SFG) studies of Zolk et al. [17]. According to simulations by Zheng et al. [18] the energetically most favourable conformation is adopted when there are on average three to four molecules of water associated with each OEG moiety.

In spite of the various calculations and the experiments performed on OEG SAMs in contact with aqueous solutions, the structure of the water at the solid-liquid interface and the interactions of the water molecules with the SAM are still a matter of debate. The experimental results described in the following sections present an investigation of the density structure at the interface and provide information about the water, the monolayer and their interactions.

5.2. Water density at the interface: OEG SAMs

5.2.1. Data fitting and interpretation

Neutron reflectivity was employed in order to map the density profile of the solid-liquid interface between an OEG SAM and water. The resulting curves were fitted using the Parratt32 software [19], which calculates the reflectivity profile using Parratt's recursive method based on a box model; the box model includes the three parameters thickness, scattering length density and roughness for each layer. The starting values for the metal layers in the model were taken from the quartz crystal micro-balance readings during the evaporation process and were confirmed by measuring the x-ray reflectivity in a Bruker diffractometer (see **Section 4.9**). The base model consisted of the following layers (**Figure 5.1**): a quartz substrate, an

adhesion promoter (either chromium or titanium), gold, SAM and the bulk solution (a mixture of H_2O and D_2O). An additional layer was introduced between SAM and bulk to account for the reduced density water layer. During the fitting procedure,

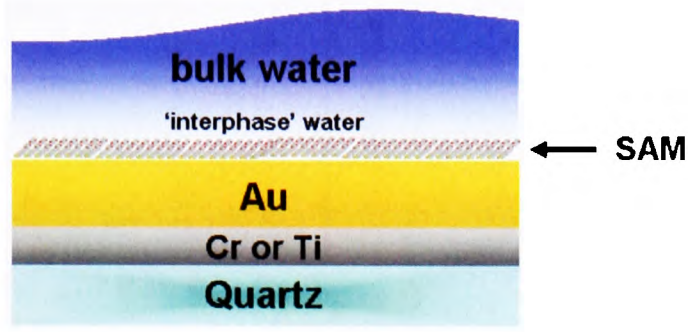


Figure 5.1.: Generic arrangement of layers on which the the fitting model was based (not to scale).

the parameters scattering length density, thickness and roughness of each individual layer were allowed to vary. After the fit had converged, the χ^2 value

$$\chi^2 = \sum_i \frac{(R_{exp}(Q_i) - R_{calc}(Q_i))^2}{\delta^2_{exp}(Q_i)} \tag{5.1}$$

was noted and used to find the best model as described in the following. In **Equation 5.1** $R_{exp}(Q_i)$ is the reflectivity value measured at Q_i, $R_{calc}(Q_i)$ is the calculated value and $\delta^2_{exp}(Q_i)$ represents the statistical error, taken to be $\sqrt{\text{count rate}}$. In order to determine the quality of the model with the additional layer, the fits with and without this layer were carefully analysed using the 'N_σ qualifier' [20]

$$N_\sigma = \frac{\chi^2 - \nu}{\sqrt{2\nu}} \tag{5.2}$$

where χ^2 is the error weighted least-squares sum, $\nu = n - p$ is the effective number of degrees of freedom, with n being the number of data points used for the fit and p the number of fitting parameters (this situation is illustrated in **Figure 5.2**). Small values $0 < |N_\sigma| < 4$ indicate a high probability for the assumed model. This quantity is derived from the properties of the χ^2 distribution and can be calculated easily. Comparison of $|N_\sigma|$ for two models with different number of parameters is comparable with the so-called HAMILTON test [21], in which the ratio

$$\mathcal{R} = \sqrt{\frac{\chi^2_0}{\chi^2_1}} \tag{5.3}$$

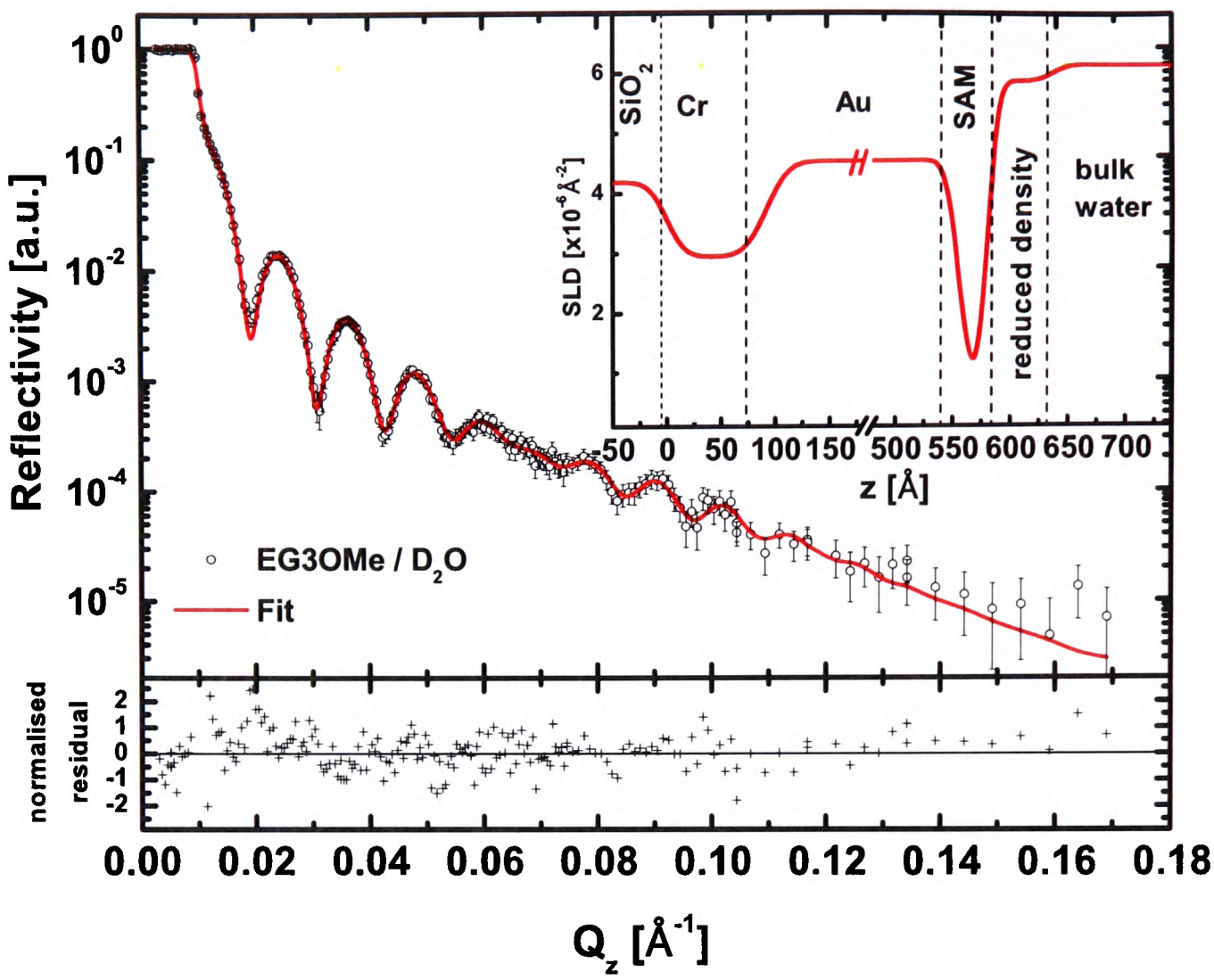


Figure 5.2.: Typical neutron reflectivity measurement. An EG3OMe terminated monolayer is measured in contact with D_2O. Fit (red solid line), real space profile (inset) and normalised residual ($[R_{exp}(Q_i) - R_{calc}(Q_i)]/\delta_{exp}(Q_i)$) are also shown.

is computed and the result compared with tabulated values of confidence intervals. Here, χ_0^2 and χ_1^2 are the least-squares sums for the models without and with one additional layer respectively. The tabulated $\mathcal{R}$ values were interpolated for the appropriate degrees of freedom of each individual fit using the interpolation formula (Ib) from ref [21]

$$\mathcal{R}_{b,\nu,\alpha} \simeq 1 + \frac{120}{\nu}\left(\mathcal{R}_{b,120,\alpha} - 1\right) \tag{5.4}$$

where ν is the actual effective number of degrees of freedom, b is the difference in number of parameters between the two compared models and α is the confidence band, which was in all cases $\alpha = 0.005$, meaning that the model without the additional layer could be rejected with a probability of 99.5%, if $\mathcal{R} > \mathcal{R}_{b,\nu,\alpha}$. Both N_σ and the HAMILTON test were used to compare models with differing numbers of parameters and to reject the more improbable model with high confidence.

5.2.2. Neutron reflectivity at room temperature

Tri(ethylene glycol) (EG3OMe) self-assembled monolayers (both deuterated and non-deuterated) were prepared using the procedure described in **Section 4.1.1**. The first neutron reflectivity measurement on each sample was performed with pure D_2O or a mixture of D_2O and H_2O, which was matched to the scattering length density of gold, for the purpose of enhanced visibility of a potential interfacial layer. This measurement was later analysed for the presence of a reduced density water layer, and it was also used as a reference for subsequent measurements with protein solutions.

At this point the literature values and the calculated values of the scattering length densities for the materials used for this work will be introduced. The following list will serve as a reference also for later sections concerned with neutron scattering.

material	SLD [$\times 10^{-6}$ Å^{-2}]
H_2O	-0.56
D_2O	6.35
Au	4.5
Cr	3.03
Ti	1.95
quartz	4.18

Table 5.1.: Literature values of neutron scattering length densities of the substrate materials used in this work.

The values listed in **Table 5.1** are literature values for the substrate, metals and solvents used in the presented experiments. The values for the monolayers and the proteins are more difficult to determine due to uncertainties in the packing density, solvent penetration and H-D exchange in the case of proteins.

For the oligo (ethylene glycol) terminated self-assembled monolayers a packing density of 0.8, i.e. 80% surface coverage was assumed as a reference value. The scattering length density (SLD) was the calculated using the formula

$$SLD = \frac{\sum_{i=1}^{N} b_{c,i}}{v_m}, \tag{5.5}$$

where $b_{c,i}$ is the bound coherent scattering length of the constituent atoms and v_m is the volume of the molecule. The volume of the molecule was calculated assuming

SAM molecule/subunit	SLD [$\times 10^{-6}$ Å^{-2}]
-CH_2-	-0.34[1]
-CD_2-	8.4[1]
-(O-CH_2-CH_2)-	0.64[1]
-(O-CD_2-CD_2)-	6.5[1]
S-$(CH_2)_{11}$-$(OCH_2CH_2)_3$-OCH_3	0.1-0.4
S-$(CD_2)_{12}$-$(OCD_2CD_2)_3$-OCD_3	6.2-6.4
S-$(CH_2)_{17}$-CH_3	-0.4 to -0.3
S-$(CD_2)_{17}$-CD_3	8.2-8.6

Table 5.2.: Literature values of neutron scattering length densities of the substrate materials used in this work. [1]Values taken from *http://www.ncnr.nist.gov/resources/sldcalc.html.*

a projected area per molecule of 21.6 Å [22] and a molecular length of 22-24 Å for a helical S-$(CH_2)_1$1-$(OCH_2CH_2)_3$-OCH_3 molecule [23]. These values were also compared with the numbers obtained by the simple addition of the scattering length densities of -CH_2-, -CD_2-, -(O-CH_2-CH_2)- and -(O-CD_2-CD_2)- molecular subunits. The approximate values listed in **Table 5.2** served as starting parameters for the fitting process.

Figure 5.3 shows a characteristic reflectivity measurement of a fully deuterated EG3OMe SAM in contact with a contrast adjusted (to the scattering length density of gold) water mixture. The scattering length densities of substrate and individual metal layers can be seen in the fitted real space profile and are in good agreement with the theoretical values.

The monolayer has a high scattering length density due to its deuteration. The fitted thickness of the SAM is 28.5 Å (**Table 5.3**), which indicates considerable swelling, due to water penetration (the thickness of a dry EG3OMe SAM is about 21-22 Å). This observation is in good agreement with our PMIRRAS measurements (see **Section 5.4**).

Two models were used to fit the experimental data: the simplest possible model consisting of substrate, the metal layers, the SAM and the bulk water, and an additional model, identical to the first except for an additional layer between SAM and bulk. The result of the significance analysis for the fits with these two models, under consideration of the additional parameters introduced by the extra layer, was

a very strong rejection of the simpler model at a 99.5 % level ($\alpha = 0.005$). The fitted values for the interfacial layer are listed in **Table 5.3**.

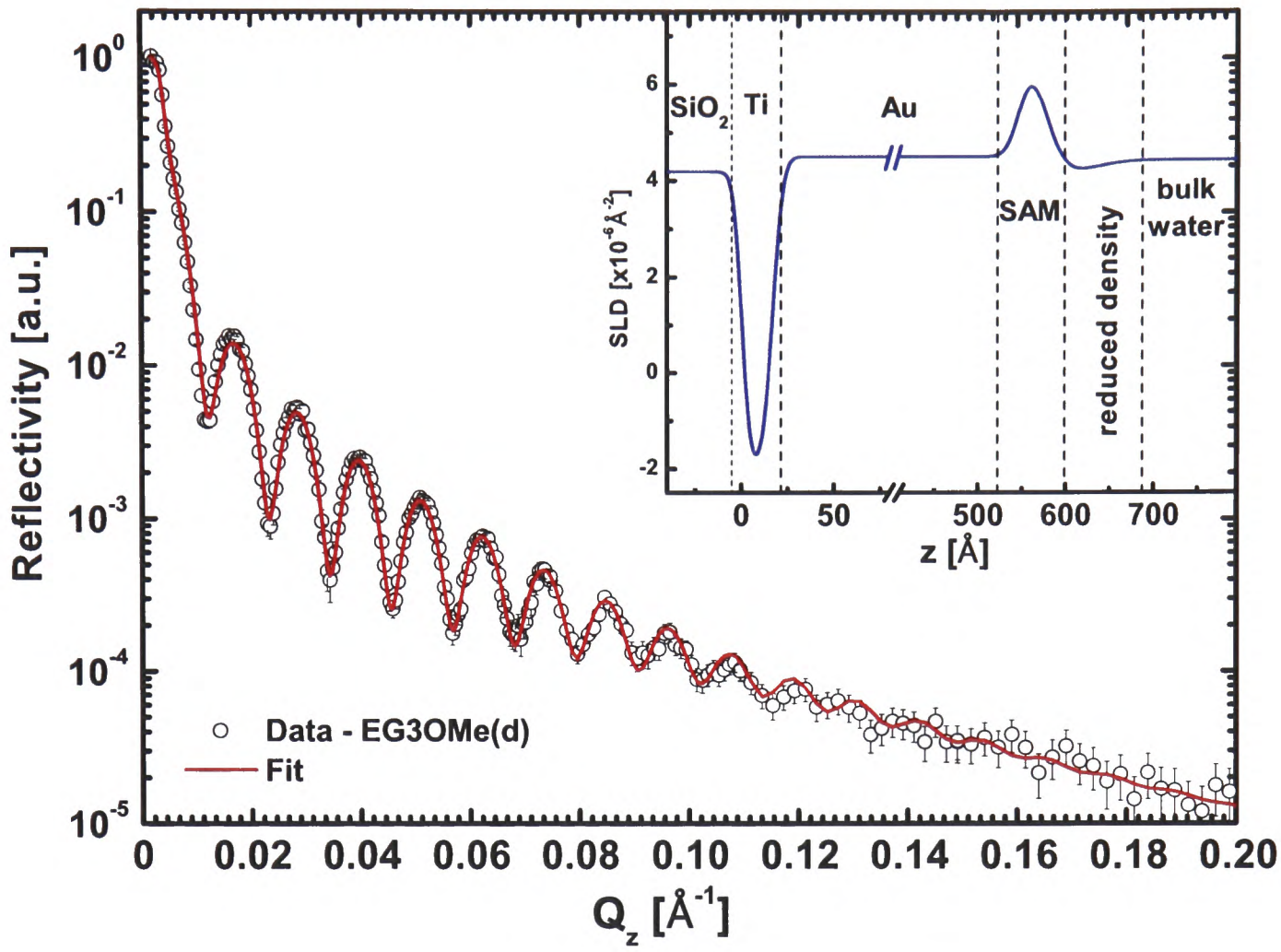


Figure 5.3.: Reflectivity data with best fit and corresponding scattering length density profile of a fully deuterated EG3OMe SAM in contact with a mixture of H_2O and D_2O. The real space profile shows a region of reduced water density close to the SAM (d≈55 Å, σ ≈23 Å, ~90% of bulk density). The fitting values are listed in **Table 5.3**.

layer	**d [Å]**	**SLD [$\times 10^{-6}$ Å^{-2}]**	σ **[Å]**
quartz	n/a	4.18	n/a
Ti	17.2	-1.95	6.6
Au	525.8	4.35	1.5
SAM	28.5	7.21	13.5
reduced density layer	54.7	4.01	24.9
bulk	n/a	4.43	23.2
Hamilton: $b = 3$, $\nu = 213$; $\mathcal{R}_{3,213,0.005} = 1.031$, $\mathcal{R} = \sqrt{\chi_0^2/\chi_1^2} = 1.186$			
N$_\sigma$ test: N_σ^1=1.058, N_σ^0=5.514			

Table 5.3.: Fit parameters for the fit in **Figure 5.3** with 228 data points, including a reduced density water layer. Confidence tests favour the model with an additional layer with a probability >99.5%.

Another example with a non-deuterated EG3OMe monolayer is shown in **Figure 5.4.** Here, the reduced density water layer is slightly wider, but the relative density reduction compared to the bulk is less pronounced (Table 5.4). The fully deuterated SAM enhances the contrast, and an interfacial layer with a density about 9.7 % lower than the bulk water density becomes visible, extending about 55 Å away from the SAM. The roughness of this layer is relatively large (~23 Å), indicating that the density is lowest close to the SAM and increases monotonically until it reaches bulk density.

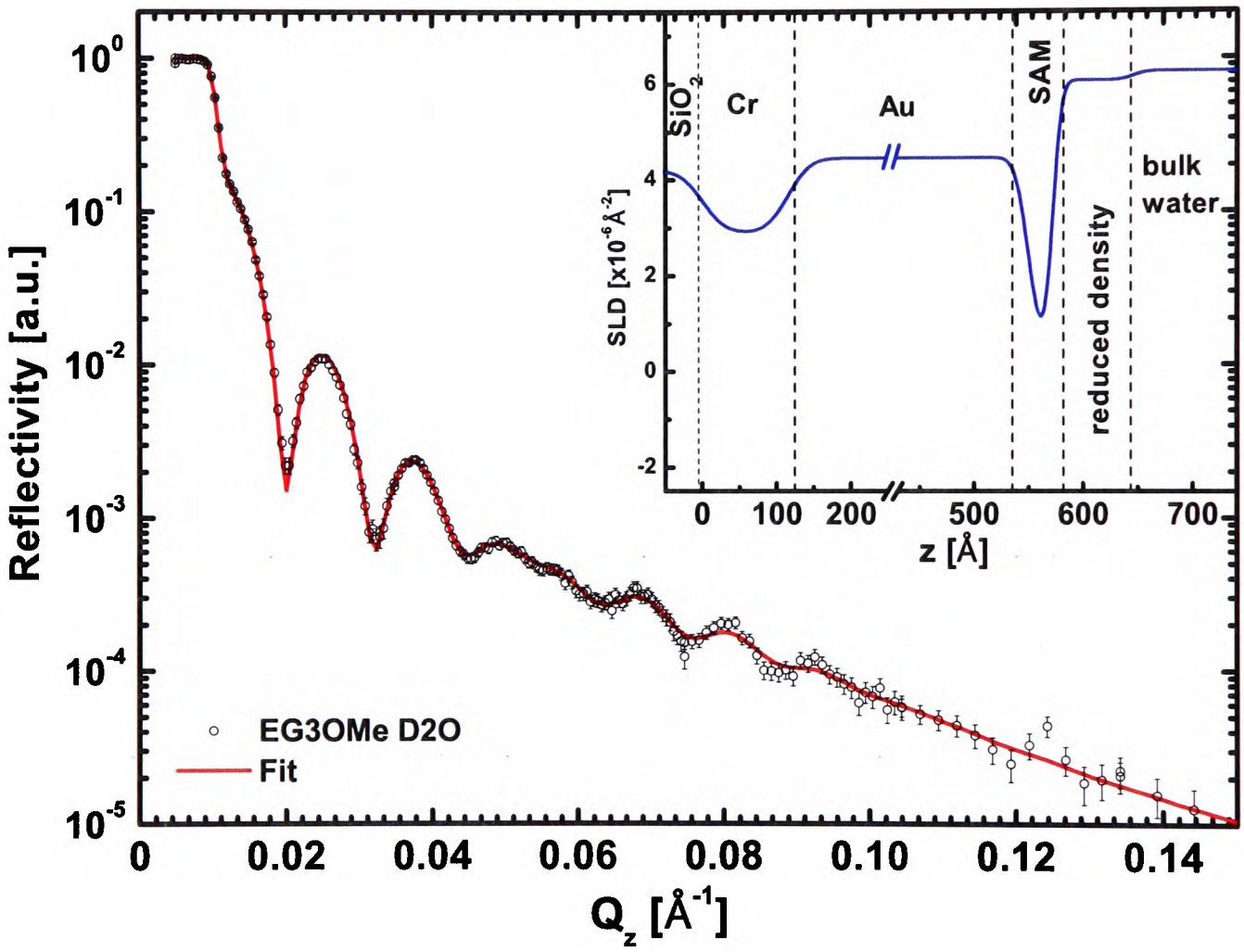


Figure 5.4.: Reflectivity data with best fit and corresponding scattering length density profile of an EG3OMe SAM in contact with pure D_2O at 25 °C. The real space profile shows a region (74 Å) of reduced water density (90% of bulk water) close to the SAM.

All measurements of EG3OMe SAMs in contact with water (D_2O/H_2O mixtures) exhibit a layer of reduced density water adjacent to the SAM. Fits for different samples have small variations in width and density of the reduced density water layer. Since the fitting of a rather narrow layer with small contrast is more sensitive to the integral of the layer than to its width and density individually, the areas of

layer	d [Å]	SLD [$\times 10^{-6}$Å^{-2}]	σ [Å]
quartz	n/a	4.18	n/a
Cr	116.1	2.99	22.9
Au	433.8	4.35	21.7
SAM	22.48	0.45	9.2
reduced density layer	73.67	6.08	6.5
bulk	n/a	6.24	6.8
Hamilton: $b = 3$, $\nu = 182$; $\mathcal{R}_{3,182,0.005} = 1.036$, $\mathcal{R} = \sqrt{\chi_0^2/\chi_1^2} = 1.081$			
N$_\sigma$ test: N$_\sigma^1$=4.596, N$_\sigma^0$=6.769			

Table 5.4.: Fit parameters for the fit in **Figure 5.4** with 197 data points, including a reduced density water layer. Confidence tests favour the model with an additional layer.

reduced density layers were compared for different samples. The average integrated depletion area was (9.48±2.72)$\times 10^{-6}$ Å^{-1} for five different measured samples.

5.2.3. Temperature dependence

In the literature there is evidence for the partial breakdown of the protein resistant properties of EG3OMe monolayers, when the temperature is lower than about 11° C [24]. These ex situ FTIR experiments revealed that SAMs of tri(ethylene glycol) terminated thiols, which were resistant to protein adsorption at room temperature, adsorbed a small amount of fibrinogen, when the solution temperature was reduced to 5° C. The amount of adsorbed protein normalised to a non-resistant reference surface of alkanethiol SAMs was found to be about 20% of that on the non-resistant surface. This value can be related to other studies of protein adsorption on hydrophilic and hydrophobic surfaces in order to establish an absolute scale for the adsorbed amount. For instance, Efimova [25] determined the volume fraction of BSA adsorbed on a TiO_2 surface to be between 0.2 and 0.4 depending on pH, and for fibrinogen double layers with volume fractions in the range of 0.1 to 0.48 were observed. Similarly Silin et al. [26] find a surface excess of $\Gamma = 80$ ng/cm^2 for BSA adsorbed on a methyl terminated alkanethiol functionalised surface. Assuming the shape of BSA to be that of a prismatic shell with dimensions 84×84×84×31.5 Å

as proposed by Ferrer et al. [27], and assuming that the preferred orientation upon adsorption is lying down, then the volume fraction can be calculated from

$$\phi = \frac{\Gamma N_A A_{BSA}}{M_w} \tag{5.6}$$

where Γ is the surface excess, A_{BSA} is the surface area required by a lying down BSA molecule, N_A is Avogadro's constant and $M_w \approx 66$ kDa is the molecular weight of BSA. Therefore a surface excess of $\Gamma = 80$ ng/cm^2 corresponds to a volume fraction of about $\phi = 0.23$ on the surface of a hydrophobic alkanethiol protected surface. All these findings indicate that the adsorbed amount of proteins on a non-resistant surface (e.g. an alkanethiol monolayer on gold) is below 50% of a monolayer. Therefore, the amount of fibrinogen adsorbed at low temperature on an EG3OMe SAM is of the order of 8% of a monolayer. For BSA, the value is expected to be even lower. Such small amounts of adsorbed protein are at the resolution limit of neutron reflectivity experiments and recent findings will be presented in **Section 7**.

However, it was suggested that the breakdown of protein resistance at low temperatures is connected to changes of the reduced density water layer. This hypothesis was verified by neutron reflectivity measurements of EG3OMe SAMs in contact with water. Reflectivity curves were measured first at room temperature using the temperature controlled sample cell (see **Section 4.3**). Then the water temperature was lowered to 5° C without any other changes to the sample, and the sample was measured again. Prior to the low temperature measurement the sample was realigned to the beam in order to account for small changes due to thermal contraction of the sample cell. There were no changes visible within the error bars between the two temperatures, as can be seen in **Figure 5.5**. The data could be fitted satisfactorily at both 25 and 5 °C using the same model and including the region with the reduced density water adjacent to the SAM. However, the best fit for the 5 °C data converged to slightly different values for the reduced density layer. The values are listed in **Table 5.5**.

According to the best fit, the reduced density water layer at 5 °C appears to be less wide (58 compared to 74 Å), but more pronounced ($[\mathrm{SLD}_{bulk} - \mathrm{SLD}_{layer}]_{5°\mathrm{C}} = 0.31$ Å^{-2} compared to $[\mathrm{SLD}_{bulk}\ \ \mathrm{SLD}_{layer}]_{25°\mathrm{C}} = 0.16$ Å^{-2}) than at room temperature. On the other hand, the integrated effective area is smaller, i.e. 13.2×10^{-6} Å^{-1}

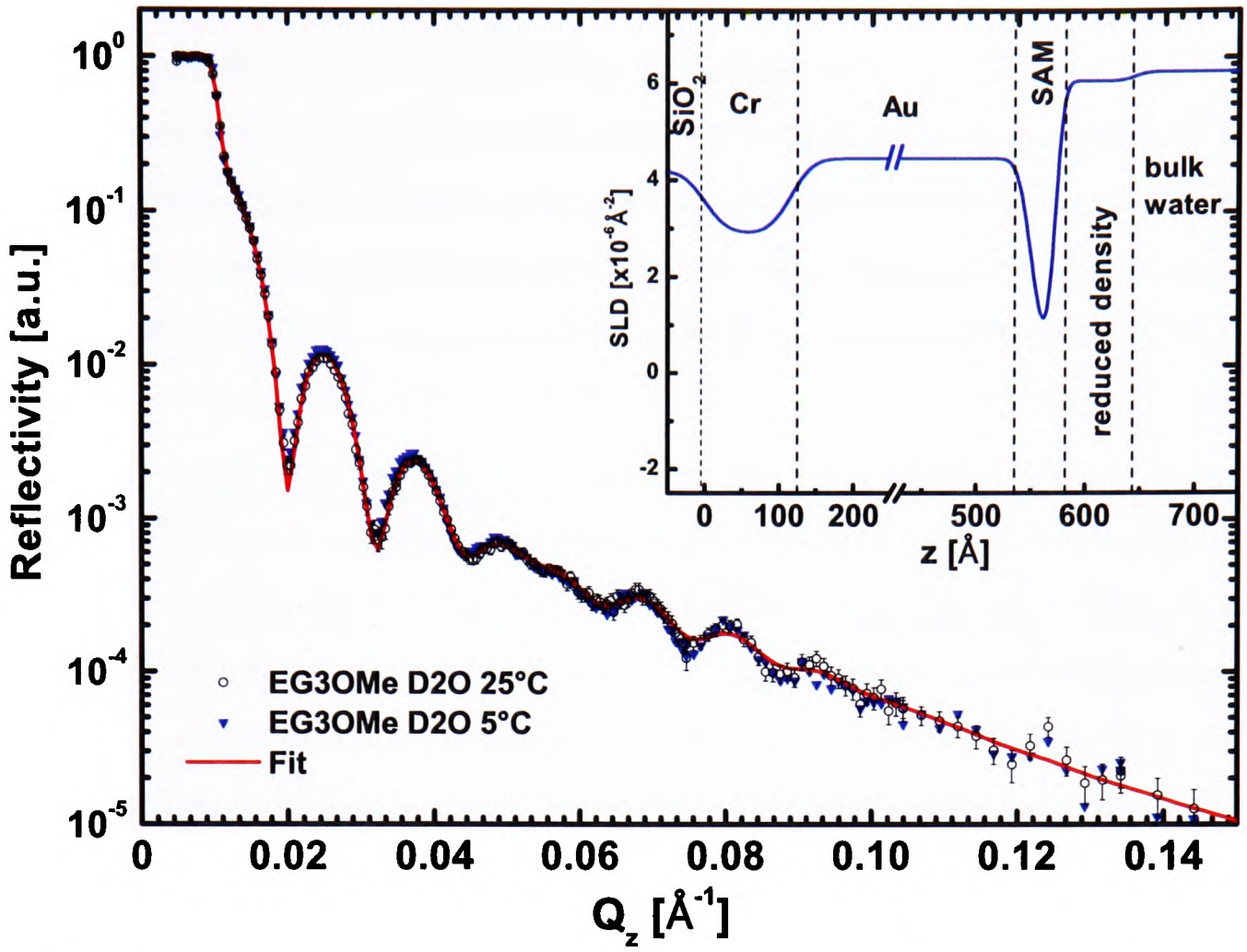


Figure 5.5.: Reflectivity data with best fit and corresponding scattering length density profile of an EG3OMe SAM in contact with pure D_2O at 25 °C (black circles, fit parameters in **Table 5.4**) and at 5 °C (blue triangles). The real space profile shows a region of reduced water density close to the SAM at both temperatures.

layer	d [Å]	SLD [$\times 10^{-6}$Å^{-2}]	σ [Å]
quartz	n/a	4.18	n/a
Cr	116.1	2.99	22.9
Au	433.8	4.35	21.7
SAM	23.6	0.333	13.4
reduced density layer	59.1	5.9	4.8
bulk	n/a	6.21	0.5
Hamilton: $b = 3$, $\nu = 182$; $\mathcal{R}_{3,182,0.005} = 1.036$, $\mathcal{R} = \sqrt{\chi_0^2/\chi_1^2} = 1.119$			
N_σ test: N_σ^1=15.55, N_σ^0=21.55			

Table 5.5.: Fit parameters for the fit of the low temperature (5 °C) data in **Figure 5.5** with 182 data points, including a reduced density water layer. Confidence tests favour the model with an additional layer.

at 5 °C in comparison with 10.6×10^{-6} Å^{-1} at 25 °C. Also, it has to be pointed out that the roughness of the reduced density water layer is 6.8 Å at room temperature and almost zero at 5 °C. This means that while the extent of the reduced density layer decreases by about 15 to 20%, the integrated area increases by about the same proportion. In the light of these results, it is clear that the breakdown of protein resistance at low temperatures for EG3OMe terminated monolayers is not or not solely connected with changes in the reduced density water layer, which is found to persist down to 5 °C.

It may be speculated that the observation of a water layer with reduced (scattering length) density is due to more ordered, tightly bound water molecules associated with the SAM. The observed thickness of this "interphase" layer of 5 to 7 nm is in agreement with observations by Kim et al. [15], who suggested that OEG functionalised surfaces could serve as a template for nucleating nano-crystalline ice, which would lead to a water layer with increased viscosity. Such a hydration layer would explain the reduced density observed in the present neutron reflectivity measurements. The degree of ordering of this "interphase" water may be higher and therefore its density lower at low temperatures, which would explain the experimental findings. However, the observed reduction of the width of the interfacial layer is below 15 Å, which is below the nominal resolution limit of $2\pi/Q_{max} \approx 30$ Å. Therefore the values obtained from the best fits have to be considered with care. It can be safely stated that the upper limit for the reduction of the "interphase" water at low temperatures is well below 20%, which still leaves a considerable depletion layer of about 50-60 Å; at the same time one must bear in mind that this reduction in width is accompanied by an increase in the density difference between bulk and "interphase".

5.3. Water density at the interface: Alkanethiol SAMs

The question of the behaviour of water at hydrophilic interfaces (in this case OEG terminated ones) has been addressed in the previous section. A related issue, which is currently the focus of research, is the behaviour of water at a hydrophobic surface. The behaviour of water with hydrophobic surfaces is thought to be one of the major driving forces for self-assembly in biological systems and protein folding. It is therefore crucial to understand the structure of water at such interfaces on a molecular

level. The most recent findings have been summarised in an article by P. Ball [28]. Experimental results are still somewhat controversial, although most studies reveal a reduced density of interfacial water over a region of 2-5 nm [12, 14].

A system comprised of alkanethiols self-assembled on gold in contact with water has been studied for this work partly because of its general interest, but principally because it served as a reference system for the OEG related measurements. In this section it is shown that our measurements confirm the existence of a water depletion region in the proximity of the alkanethiol SAM.

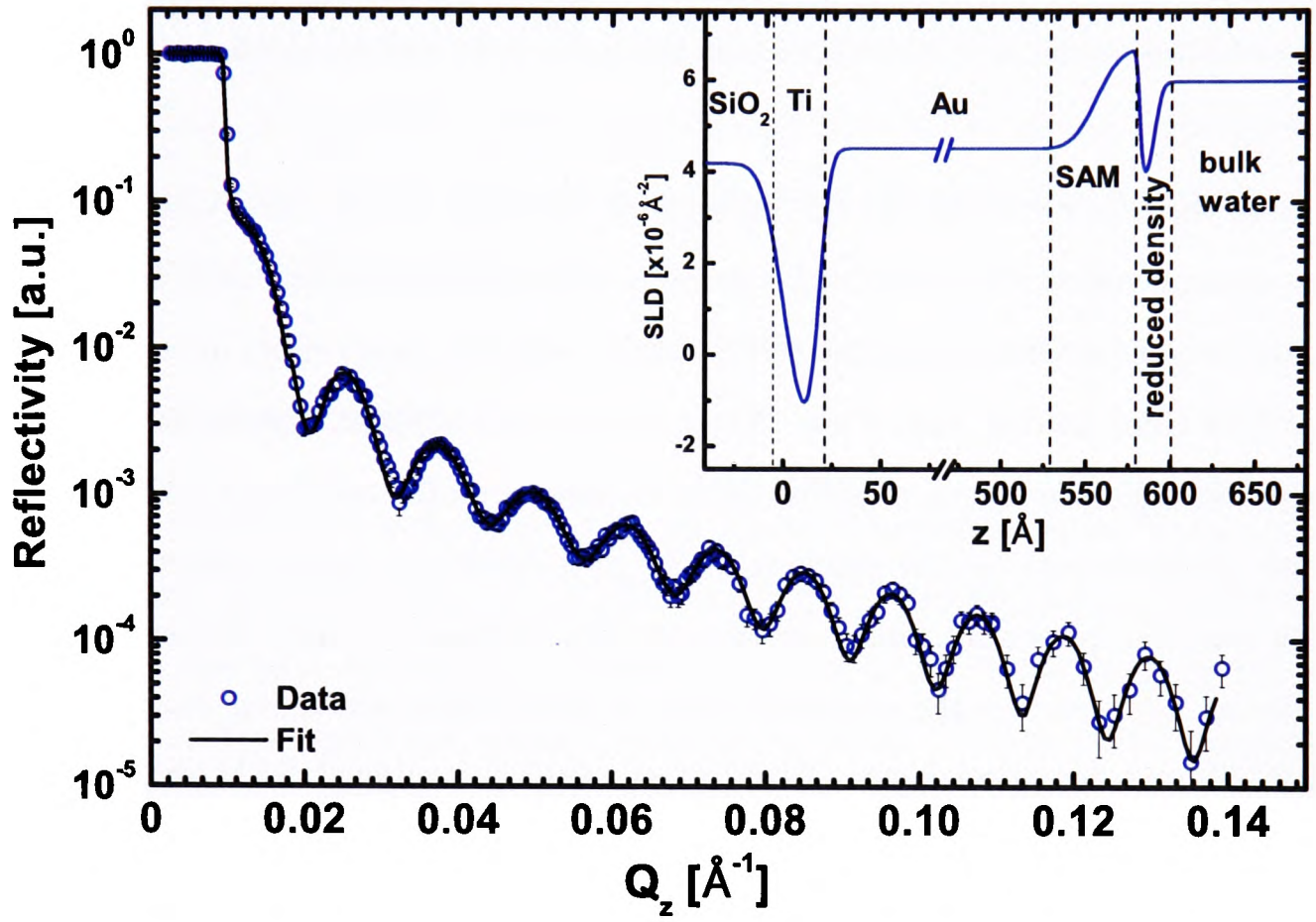


Figure 5.6.: Reflectivity data with best fit and corresponding scattering length density profile of an S-$(CD_2)_{17}$-CD_3 SAM in contact with an H_2O/D_2O at 25 °C.

Figure 5.6 shows a representative measurement of a S-$(CD_2)_{17}$-CD_3 SAM in contact with water (a D_2O/H_2O mixture with a scattering length density of 5.95×10^{-6} Å^{-2})[1]. The use of a fully deuterated SAM in this case achieves the maximum contrast between monolayer, depletion zone and liquid bulk phase. The real space profile resulting from the fit shown, reveals a region of reduced scattering length density close to SAM. The fit parameters are given in **Table 5.6**. Our measurements

[1] A D_2O/H_2O mixture with slightly reduced scattering length density (as compared to pure D_2O) was used, such that this sample could be compared to subsequent measurements with dilute protein solutions of the same scattering length density

layer	d [Å]	SLD [$\times 10^{-6}$Å^{-2}]	σ [Å]
quartz	n/a	4.18	n/a
Ti	18.5	-1.93	5.3
Au	537.5	4.502	5.6
SAM	28.1	6.8	21.3
reduced density layer	7.26	4.0	1.1
bulk	n/a	5.95	1.0
Hamilton: $b = 3$, $\nu = 183$; $\mathcal{R}_{3,183,0.005} = 1.036$, $\mathcal{R} = \sqrt{\chi_0^2/\chi_1^2} = 1.329$			
N$_\sigma$ test: N$_\sigma^1$=19.1, N$_\sigma^0$=36.23			

Table 5.6.: Fit parameters for the fit of the data in **Figure 5.6** with 183 data points, including a reduced density water layer. Confidence tests favour the model with an additional layer.

can be directly compared to the findings of Doshi et al. [29], who conducted similar neutron reflectivity measurements on a silicon/silane system with an 18-carbon chain octadecyl-tricholorosilane (OTS) SAM, which is comparable in thickness with the C18 thiol used in this work. Their system was simpler, due to the absence of gold and titanium layers, enabling them to determine the combined SAM/depletion zone thickness just by the position of the first minimum in the reflectivity profile. However, the presented results show only measurements on non-deuterated SAMs, a factor that reduces the sensitivity due to the similar scattering length densities of SAM and depletion layer. Doshi et al. find a combined SAM/depletion zone thickness in the range of 31.0 to 34.8 Å, with corresponding depletion zone thicknesses from 7.6 to 11.3 Å for a naturally aerated, i.e. not degassed system. Our results for the thiol based system with SAM thickness of about 28 Å and a depletion layer thickness of 7-8 Å are excellent agreement with the values of Doshi et al. and demonstrate the high sensitivity of our system, and in particular the benefit of contrast enhancement by deuteration.

5.4. Solvation of an OEG SAM (PM-IRRAS)[2]

In this section, a polarisation modulation infrared reflection absorption spectroscopy (PM-IRRAS) study of the influence of exposure to water of tri(ethylene glycol) (EG3)- terminated alkanethiol self-assembled monolayers was performed to com-

[2]This section is based on Skoda et al., *Langmuir*, 23, **2007**, 970.

plement the neutron reflectivity measurements of the reduced density water layer discussed in the previous section. By means of PM-IRRAS, it was possible to observe in situ (i.e., in the presence of a water layer) subtle changes in the characteristic ether vibrations originating from the region of the SAM that is in direct contact with the solvent. Unlike scattering that measures average bulk behaviour, this study offers insight into local interactions between the water and the OEG molecules.

In particular, shifts in the position of the characteristic C-O-C stretching vibration were observed after the monolayers had been exposed to water. The shift in frequency increased when the SAM was observed in direct contact with a thin layer of water. It was found that the magnitude of the shift also depended on the surface coverage of the SAM. These findings suggest a rather strong interaction of oligo(ethylene glycol) SAMs with water and indicate the penetration of water into the upper region of the monolayer.

5.4.1. Band assignments

The results presented in this section rely on precise knowledge of the characteristic band positions and their origin for an OEG monolayer. For this purpose and for sake of clarity in the later discussion, a short description of the band assignments will now be given. The fingerprint region ($\sim$1000 to 1500 cm^{-1}) of an OEG alkanethiol SAM shows a variety of absorption lines, the positions of which depend to a greater or lesser extent on the molecular conformation and the state of disorder of the SAM (liquid or solid-like). These absorption lines originate partly from vibrational excitations in the alkyl backbone or the ethylene glycol section of the SAM. The positions of these modes have been ascertained in numerous measurements performed for the present work. The most relevant modes, their assignments and a comparison with literature values are listed in **Table 5.7**.

The most prominent modes that can also be observed with high accuracy in situ, through a thin layer of liquid are:

(i) the C-O/C-C stretching band that consists of three overlapping sub-bands, which cannot be resolved (1115, 1134 and 1148 cm^{-1})

(ii) the bands in the CH stretching region between 2800 and 3000 cm^{-1}

Table 5.7.: Spectral mode assignments for EG6OMe and EG3OMe as observed in our own measurements and comparison to literature values. The ranges given for the measurements presented in this work refer to variations due to interactions with solvents.

mode assignment[a]	EG3OMe (Harder)[b]	EG6OMe (Fick)[c]	EG2 (Valiokas)[d]	EG3OMe (this work)
CH_3 asym stretch	2982 s			2983 s
CH_2 asym stretch, alkyl	2919-2925 s	2918	2918	2918-2924
CH_2 sym stretch, alkyl	2853 sh - 2855 s	2859 sh	2850	2850-2856
CH_2 sym stretch (EG)	2870 b - 2894 s	2893	~2870	~2895
CH_3 sym stretch	2819 s s			2820-2821
CH_2 scissor, alkyl	1467 sh			1460-1463
CH_2 wag (gauche) (EG)	1351	1347		1351-1352
CH_2 wag (trans) (EG)	1325 w			1326
OCH_3 rocking (EG)	1204			1202
C-O, C-C stretch	1145 sh	~1146	1143	1145-1149 sh
	1136 s			1133-1135 s
		1117 vs		1111-1116 vs
CH_2 rocking (EG)	964 m/s			961-964 m

[a] asym asymmetric, sym symmetric, wag wagging, s strong, m medium, w weak, sh shoulder. [b]Harder et al. [23], [c]Fick, J. [30], [d]Valiokas et al. [31]

Most other absorption bands are easily observable ex situ, on the dry SAM, but are usually too weak to be detected in situ due to the reduced signal-to-noise ratio.

Shifts in the band positions of these characteristic peaks induced by the interaction water and other solvents with the monolayer will be discussed in detail in the following sections.

5.4.2. Experimental details

The obvious and principal problem for the application of IR spectroscopy to the study of solid-liquid interfaces is the absorption of infrared radiation by the liquid, particularly water. To maximise the signal-to-noise ratio of the spectra, the liquid layer has to be as thin as possible. However, maybe in contrast to some electrochemical "atomic-scale" studies of ions near the interface, the liquid layer has to have a certain minimum thickness in order to mimic bulk solution or semi-infinite solution

behaviour, in particular for aqueous solutions of biological macromolecules. The optimisation and control of the liquid layer thickness is therefore crucial. Variable-angle ellipsometry measurements of the thickness of the water layer in the cell were performed on a Picometer ellipsometer (Beaglehole Instruments, Wellington, New Zealand) (see **Section 3.4**). The in situ PMIRRAS measurements described in this section have been performed using the liquid cell described in **Section 4.7**. The thickness of the water layer could be roughly adjusted by the compression of the water trapped between sample and barium fluoride half cylinder. The appropriate thickness was obtained by adjusting the thickness while observing the formation of NEWTON rings with a certain spacing. The exact thickness of the water layer was determined for representative samples by fitting a simple three-layer model (BaF2, H2O, Au) to the measured ellipsometric parameters[3] as shown in **Figure 5.7**. There is a slight deviation between simulated and experimental data which can be attributed to the non-commensurate long-range roughness of the substrate and prism. It was possible to reproducibly assemble the liquid cell to achieve measured thicknesses between 1 and 3 μm. In addition to the precise adjustment of the water

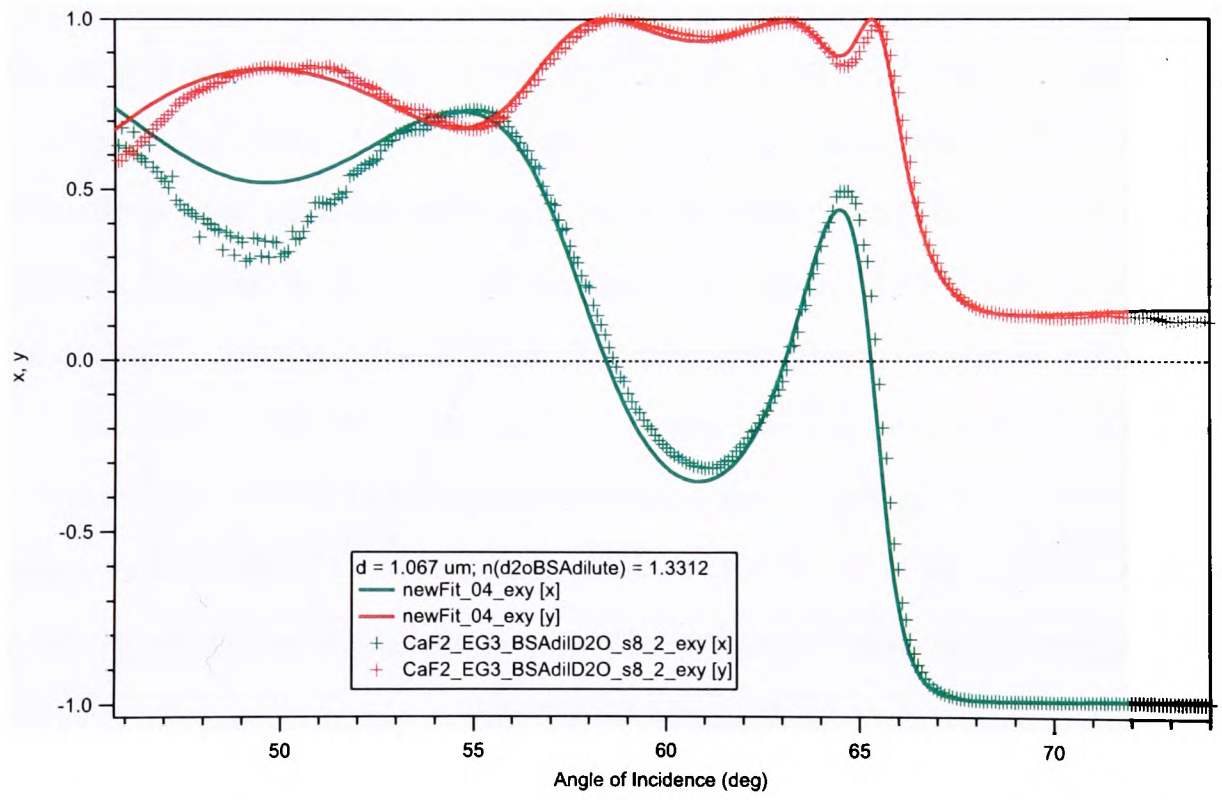


Figure 5.7.: Ellipsometric functions x (solid green) and y (solid red) simulated (dots) using a model consisting of the window material BaF2, water, and gold in order to determine the thickness of the water layer. This example shows a sample with a thickness of 1.06 μm.

[3] x and y are related to the real (Re) and imaginary (Im) parts of the reflectivity by $x = \frac{2Re(r)}{1+Re(r)^2+Im(r)^2}$ and $y = \frac{2Im(r)}{1+Re(r)^2+Im(r)^2}$ (cf. **Section 3.4**)

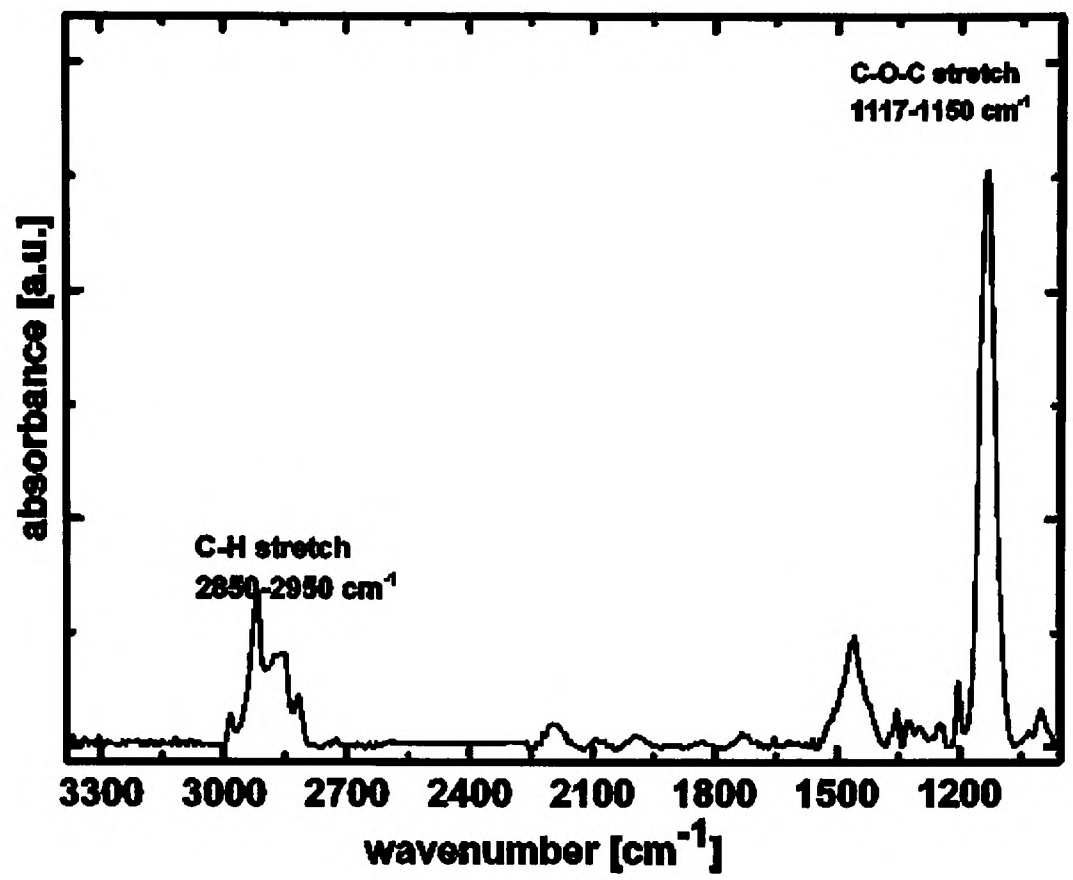
layer thickness, the angle of incidence of the incoming infrared light is crucial for obtaining a good signal-to-noise ratio. The optimum angle of incidence for each particular sample was chosen based on an optical matrix calculation which is described in detail in **Section 5.5**.

5.4.3. Oligo(ethylene glycol) C-O-C Region (Peak Shifts Ex Situ)

The first evidence for peak shifts in the C-O-C stretching band comes from ex situ measurements after the SAM has been exposed to water. **Figure 5.8a** shows a typical spectrum of an EG3-OMe SAM on gold in the mid-infrared spectral region. Characteristic C-H vibrations are visible in the range around 2900 cm^{-1}. The main feature is the sharp band at $\sim$1132 cm^{-1} arising from asymmetric C-O-C stretching vibrations, consistent with earlier work [23]. **Figure 5.8b** is an enlargement of the C-O-C region with a comparison of spectra taken before (red dots) and after (blue triangles) immersion in water.

The difference between these signals was investigated for many samples and was found to be significant and reproducible. Whereas the absolute position of the C-O-C vibration varied by 1 or 2 cm^{-1} from sample to sample, for a given sample a consistent shift in the peak position by up to 7 cm^{-1} could be observed upon exposure to water. The peak positions from the collected data were determined by a Lorentz fit to the C-O-C peak. An analysis of a set of 32 samples, which were prepared under identical conditions, showed the following results. The mean peak position of the freshly prepared samples was found at (1131.99 ± 1.34) cm^{-1}. After immersion in H_2O, the average peak position shifted to (1126.56 ± 2.00) cm^{-1}. This results in an average red shift of (5.43 ± 2.40) cm^{-1}, where the given error represents the standard deviation calculated from the peak positions and shifts of the set of samples.

The result of a red shift was consistently obtained for all samples studied, even though the magnitude varied in the given range. One of the sources of experimental uncertainty may be due to a certain variation of the SAM from sample to sample, as also observed in similar studies. [17] We also note that there was a consistent broadening (width w of the Lorentz peak) of the C-O-C peaks upon exposure to water by up to 34 cm^{-1} (the average broadening was $\langle w_{before} - w_{after} \rangle = 13.3$ cm^{-1}).



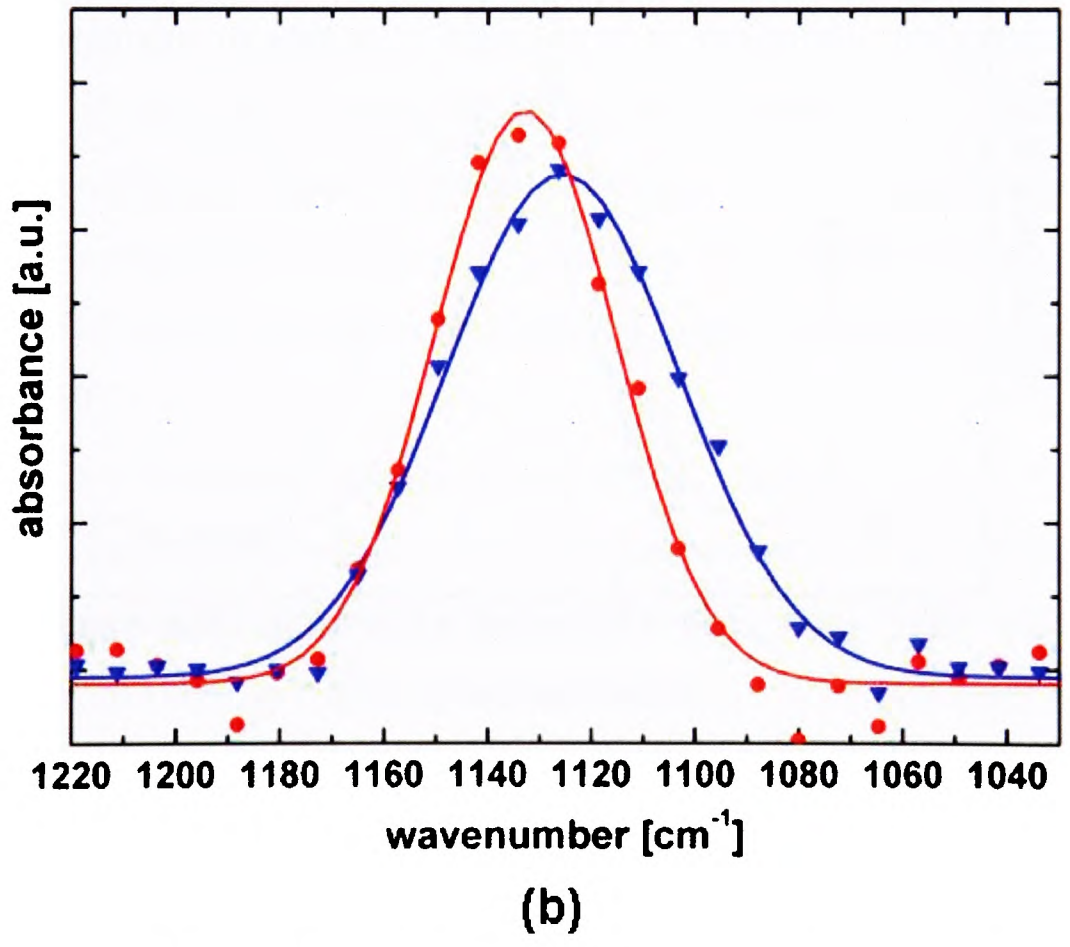


Figure 5.8.: (a) Typical ex situ spectrum (resolution 8 cm^{-1}) obtained from an EG3-OMe SAM. The characteristic features are found in the CH stretching region (2800-3000 cm^{-1}) and in the C-O-C stretching region around 1130 cm^{-1}. (b) Typical shift of the position of the C-O-C stretching vibration to lower wavenumbers. The peak of the freshly prepared EG3-OMe SAM was at 1132.8 cm^{-1} (red dots) and shifted to 1125.7 cm^{-1} after 24 h of immersion in H_2O (blue triangles).

One reason may be a certain increased level of disorder and that only a certain fraction of the EG units is associated with water.

5.4.4. Oligo(ethylene glycol) C-O-C Region (Peak Shifts In Situ)

Further and more direct evidence for water penetration into the EG section of the SAM and the subsequent disordering is provided by in situ PM-IRRAS studies of the CH and C-O-C regions. The observed alkyl CH_2 asymmetric stretch is at 2924 cm^{-1}. Values above 2918 cm^{-1} indicate an increase in the gauche-rich disordered state. [32] EG3-OMe already exhibits significant gauche defects ex situ, and a less significant change in the CH_2 peak position was observed in situ by comparison to the C-O-C antisymmetric stretching vibration.

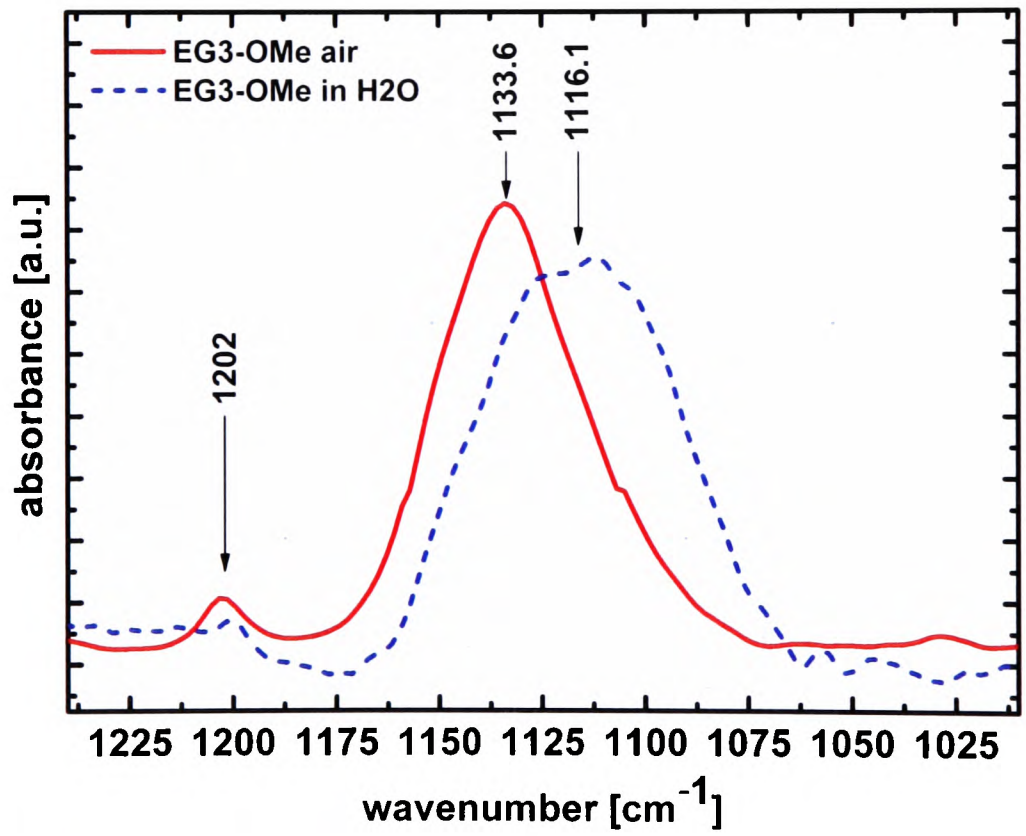


Figure 5.9.: C-O-C stretching region of an EG3-OMe SAM observed by PM-IRRAS modulated at 1500 cm^{-1} (resolution 4 cm^{-1}). The band position measured in situ is shifted to lower wavenumbers by 17.5 cm^{-1}, and the in-situ peak is broadened by 28.4 cm^{-1} (from 47.2 to 75.6 cm^{-1}).

The red shift of the C-O-C antisymmetric stretching vibration from the ethylene glycol units at the surface of the SAM observed upon immersion in water was considerably increased when observed in situ (i.e., in contact with water, see **Figure 5.9**). The peak is red shifted by 17.5 cm^{-1} and is significantly broadened from

w_{before} = 47.2 to w_{after} = 75.6 cm^{-1}. Note that the broadening is significantly larger than the line shift, suggesting that it is not simply an effect of the inhomogeneity of the system (i.e., some OEG units are associated with water but others are not, which would cause line broadening of the order of the peak shift) but a "new" or additional relaxation channel of the C-O-C modes when the atoms are associated with water. However, this interpretation would assume that only a single absorption line is observed. Although the data do not resolve any substructure, we note that in the literature [33, 34] and our own experiments the C-O-C band was shown to consist of at least three lines. Thus, the line broadening may also be due to differential line shifts.

A C-O-C peak at 1116 cm^{-1} (together with a peak at 1348 cm^{-1}) has been attributed to a more helical conformation of the ethylene glycol moieties, whereas peaks around 1140 cm^{-1} indicate an all-trans conformation [23, 34]. The red shift of the main C-O-C peak, as observed in water, can be seen as an indication of an intensity enhancement of the helical peaks when in contact with water. This is in agreement with the calculation of Wang et al. [16] that the adsorption of water on isolated $(EG)_3$ molecules is energetically most favourable on the conformers that have gauche rotations. However, solvation of the SAM also leads to amorphisation of the OEG moieties, as described by Zolk et al [17]. A subsequent measurement in air after the in-situ measurement shows, as before, a red shift of about 5 cm^{-1} (**Figure 5.10**).

Figure 5.11 illustrates the care that must be taken to make the correct band assignments. Recent articles [30,34] attribute peak frequencies to at least two factors: the molecular conformation and the degree of ordering in the SAM. More specifically, frequencies might shift if, in the case of OEG SAMs, the conformation changes from all-trans to helical or if the SAM contains more or less defects. The issue becomes even more complex because all-trans and helical phases seem to coexist in any given OEG SAM and the exact determination of the surface coverage is very difficult.

It has to be pointed out that the observation of changes in the O-H stretching and H-O-H bending modes of hydration water inside the SAM was not possible. In situ spectra show the bending mode at $\sim$1620 cm^{-1}; however, this band originates most likely from bulk-like water in the vicinity of the SAM. However, no water bands were observed in ex situ spectra. This may be due to the fact that ex situ there is a

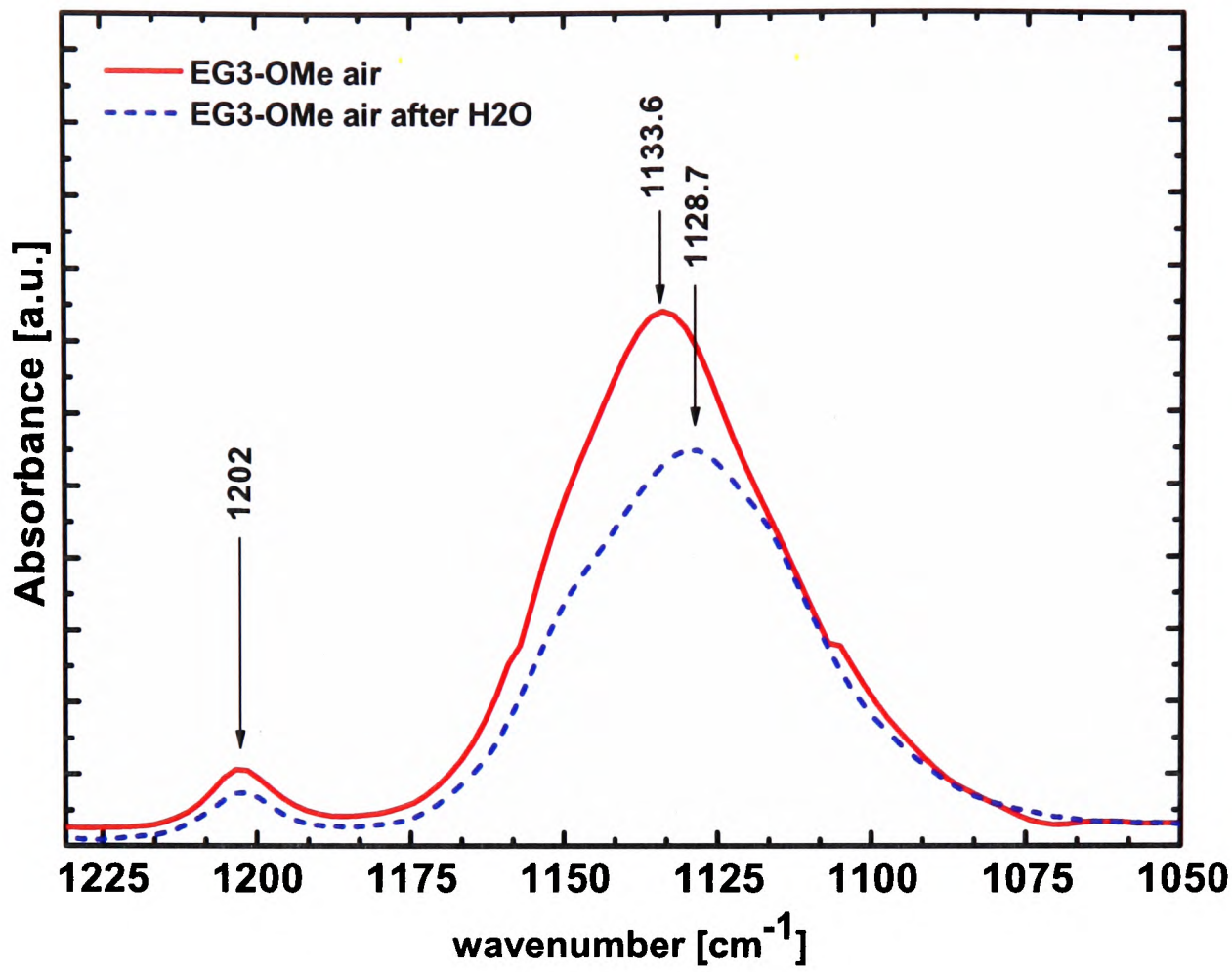


Figure 5.10.: C-O-C stretching region of an EG3-OMe SAM observed by PM-IRRAS modulated at 1500 cm^{-1} (resolution 4 cm^{-1}) and measured in air (ex situ) before (fresh wafer from thiol solution) and after exposure to water. The band position is shifted to lower wavenumbers by 4.9 cm^{-1}.

smaller number of water molecules associated with each OEG moiety (smaller than the estimated three to four in ref [18]), which is in agreement with the smaller red shift of ex situ measurements.

Although the focus of the study was on the very short chained EG3 oligomers, the slightly longer EG6OMe SAMs have also been studied. The characteristic peak positions for EG6 SAMs are very similar to those from EG3 SAMs. However, due to the tendency of EG6 monolayers preferentially to adopt a helical conformation, the main C-O-C peak has a significantly different shape compared to EG3 monolayers. The mode at 1115 cm^{-1} is much more pronounced and so is the peak at 1347 cm^{-1}. The shoulder at about 1145 cm^{-1} originating from a C-O-C mode perpendicular to the helix axis is less pronounced in situ, indicating a higher level of order. As a result of the higher crystallinity in EG6 SAMs compared to the more amorphous EG3 monolayers, and owing to the experimentally achieved excellent signal-to-noise ratio, more vibrational modes are visible in the in situ measurements and can be

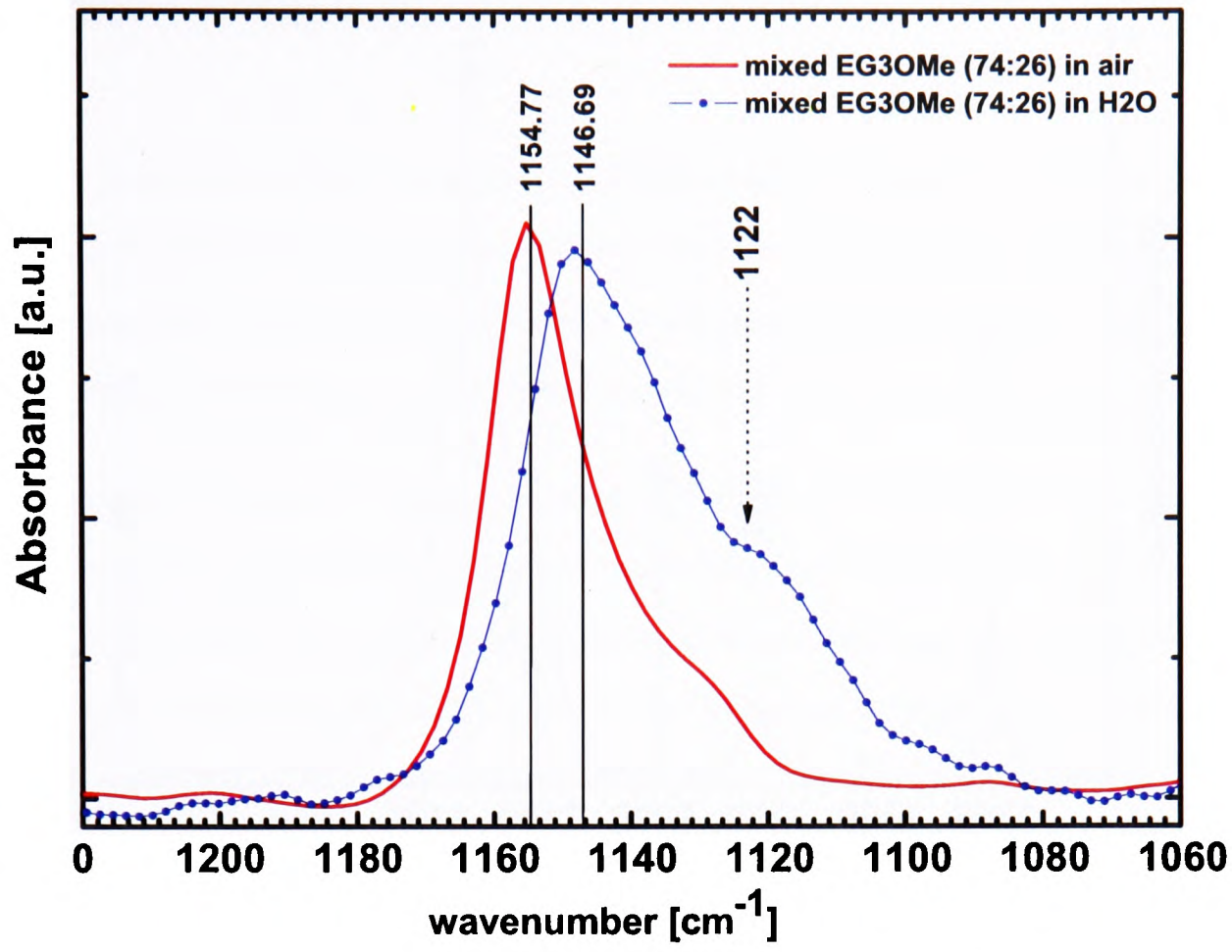


Figure 5.11.: C-O-C stretching region of a mixed (74% deuterated/ 26% protonated) EG3-OMe SAM observed by PM-IRRAS modulated at 1500 cm^{-1} (resolution 4 cm^{-1}). In air (ex situ, solid line), the peak position is at 1155 cm^{-1}, and in H2O (in situ, dashed line), it is at 1147 cm^{-1}. The band position observed in H2O is shifted to lower wavenumbers by 8.1 cm^{-1}. A more pronounced shoulder appears at about 1122 cm^{-1}.

compared to the situation in a dry SAM. As depicted in **Figure 5.12** the bands at 1347 cm^{-1}, 1243 cm^{-1} and 964 cm^{-1} are also slightly red-shifted by 1 to 2 wavenumbers. In comparison to the EG3 SAMs however, all red-shifts are smaller, which suggests that EG6 SAMs have a predominantly helical conformation and high crystallinity already ex situ and the changes induced by the exposure to water have a smaller impact. This may also explain why EG6 SAMs are in general more inert and maintain their non-fouling properties even under conditions where EG3 monolayers exhibit a partial breakdown of their protein resistance, for instance a low temperatures (see **Section 7.1.6**).

Environmental effects on vibrational spectra have also been observed for other systems [35, 36]. They represent an important piece of evidence for the interaction of molecules in SAMs with solvent molecules. For instance, Ong and co-workers, [37] using sum-frequency spectroscopy, have shown that H-bonding to C_{16} monolayers terminated with MeO, EtO, PrO, and BuO resulted in in situ blue shifts in the CH

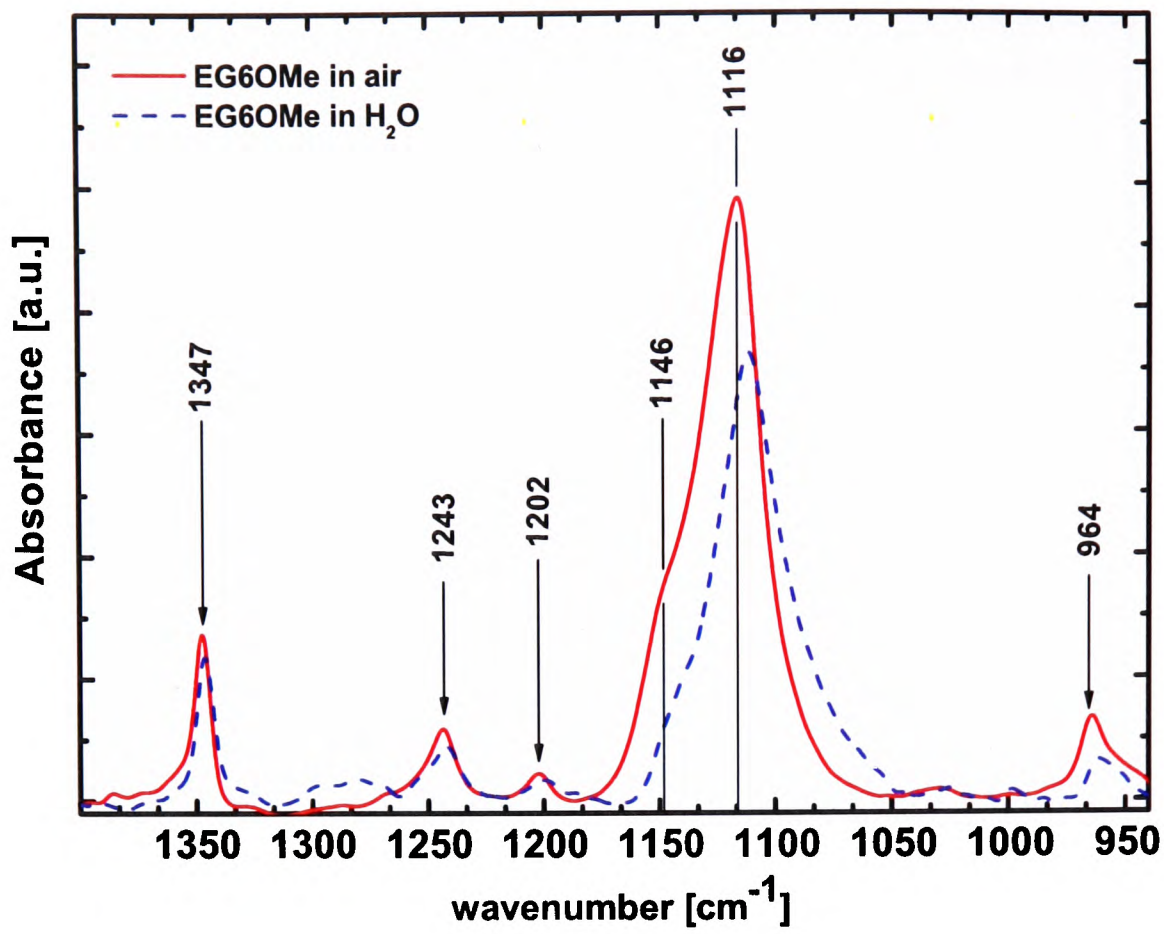


Figure 5.12.: C-O-C stretching region of an EG6-OMe SAM observed by PM-IRRAS modulated at 1050 cm^{-1} (resolution 4 cm^{-1}). In air (ex situ, red solid line), the peak position of the C-O-C mode parallel to the helix is at 1116 cm^{-1}, and in H2O (in situ, blue dashed line), it is at 1111 cm^{-1}. The band position observed in H2O is shifted to lower wavenumbers by $\sim$5 cm^{-1}. The shoulder at about 1145 cm^{-1} originating from a C-O-C mode perpendicular to the helix axis is less pronounced in situ, indicating a higher level of order.

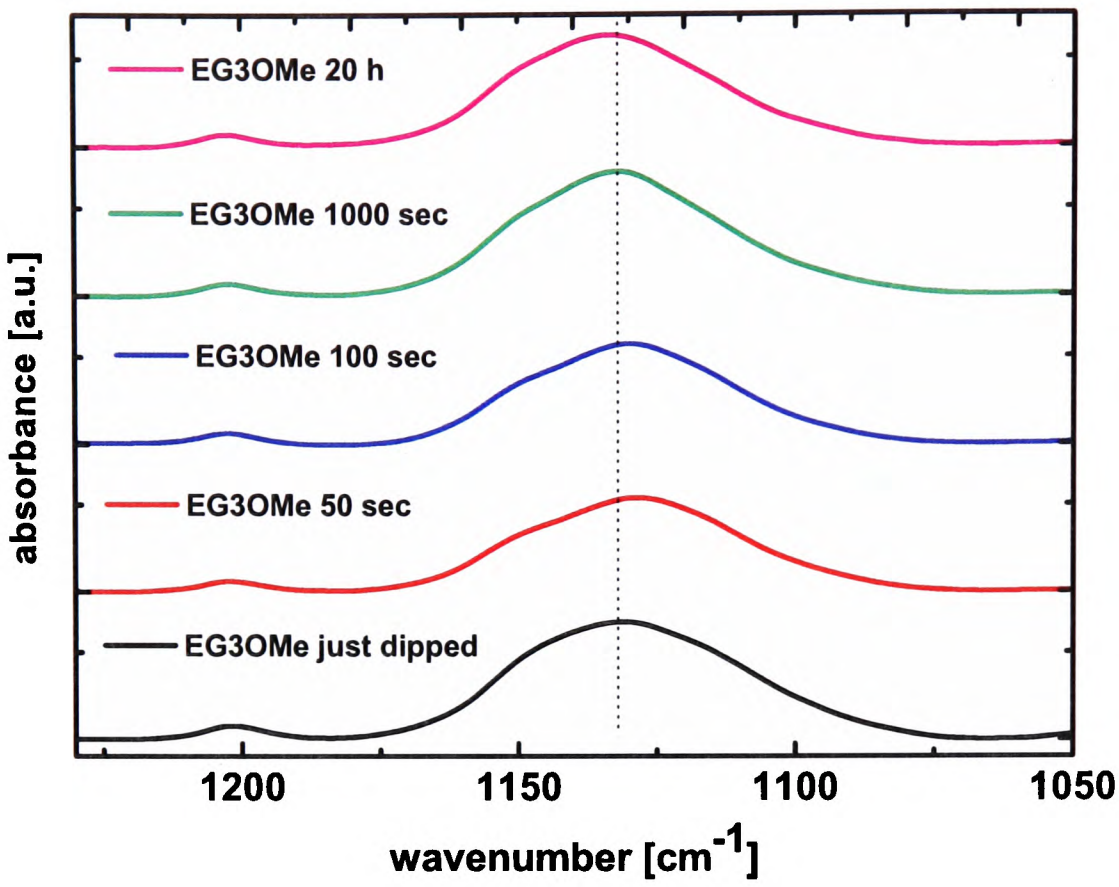
stretching bands. This blue shift is thought to arise from hydrogen bonding between water molecules and the oxygen of the ether. This observation and the argument applied to the C-O stretching mode, results in a red shift of this mode because the formation of the hydrogen bond to the oxygen lone pair would reduce the extent of electron donation to the C-H anti-bonding orbitals. This would consequently lead to a strengthening of the C-H bonds and therefore a weakening of the C-O bond, which would explain the observed red shift. Generally, Ong et al. conclude that the hydrogen bonding between the oxygen atoms and water may induce increased disorder near the surface of the monolayer. One may speculate that this association causes either a weakening in the C-O bond or an increase in the effective mass of the vibrating entity attributed to C-O-C. Both of these would lead to a decrease in frequency.

5.4.5. Coverage Dependence

There are indications that the ability of OEG-coated surfaces to withstand protein adsorption is related to the surface coverage of the oligomer molecules [18,38]. The C-O-C peak shift was therefore studied for different SAM coverages. The coverage was controlled by interrupting the SAM formation after a given period of time.

On the basis of growth kinetics studies calibrated by PMIRRAS as presented in this thesis and in agreement with previous studies on SAM growth [22,38–40], we estimate that under the present experimental conditions (room temperature, 500 μM ethanolic thiol solution) after $\sim$8 min the surface coverage amounted to $\sim$50% and after 1000 min a coverage 90% was achieved. Within this range of coverage, no significant changes in the average red shift could be observed in the ex situ measurements (**Figure 5.13a**), although the intermediate coverage regime is usually associated with a higher level of disorder [38]. In situ measurements, however, show a pronounced dependence of the peak shift as a function of immersion time (surface coverage). The peak shifts in contact with water are altogether larger than those measured ex situ, and the magnitude of the shift decreases with increasing immersion time (surface coverage) (**Figure 5.13b**).

Following the water measurements, the protein resistance of the same samples was tested by exposing the samples to a 15 wt % BSA/H_2O solution for 20 hours. After this incubation time the samples were removed from the solution by first dilution the BSA solution with copious amounts of ultrapure water in order to avoid accidental Langmuir-Blodgett like transfer of proteins onto the surface. The samples were the rinsed with ultrapure water and blow dried in a soft nitrogen stream. **Figure 5.14** illustrates that the sample with the lowest coverage (shortest thiol immersion time) shows the highest protein adsorption, and the adsorbed amount decreases with increasing OEG surface coverage. The sample with 20 h SAM formation time, where it can be expected that surface coverage and packing are highest, shows a slight indication of an amide I band at approximately 1660 cm^{-1}. This is in agreement with other studies [30,38], which have demonstrated that EG3 SAMs with very high lateral packing density partially lose their ability to withstand protein adsorption. However, in the experiments conducted for this thesis, as shown in **Figure 5.14**,



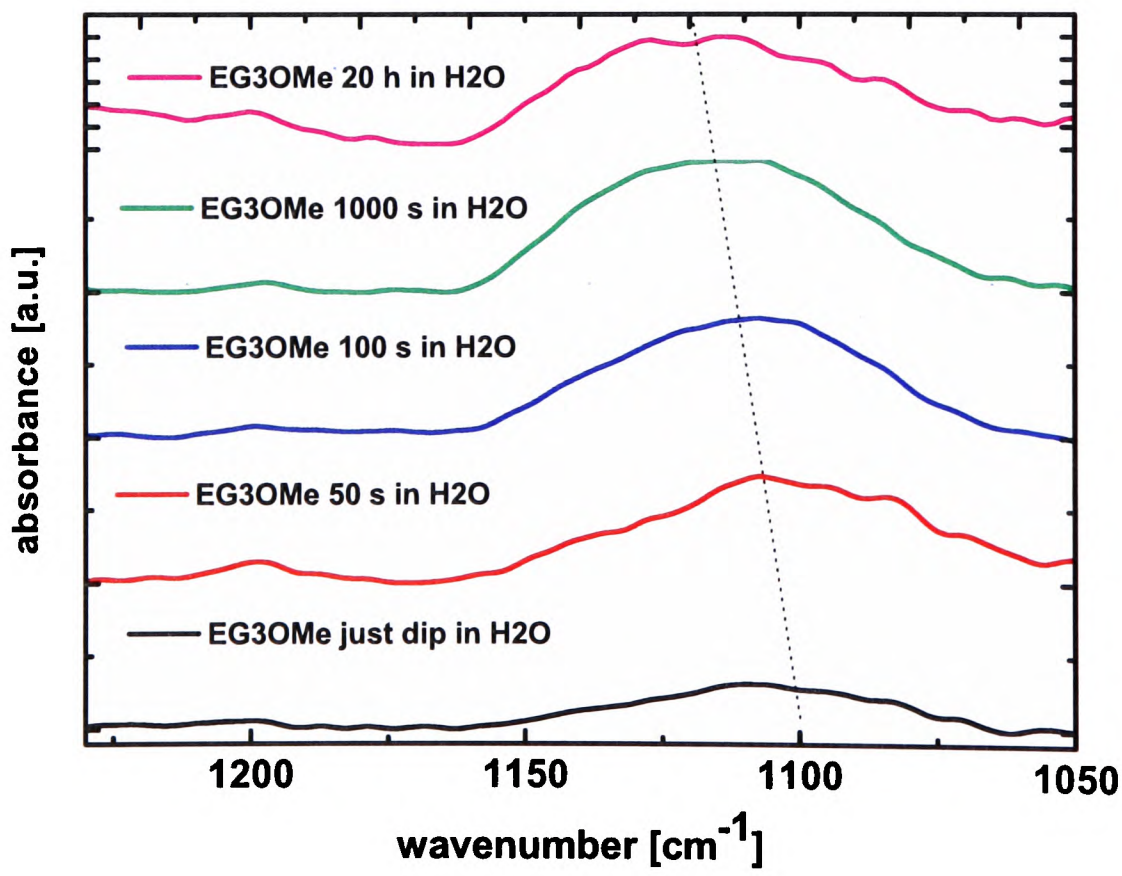


Figure 5.13.: C-O-C peaks (resolution 4 cm^{-1}) for different surface coverages (immersion times) in (a) air and (b) H_2O. SAM formation was interrupted after 1, 50, 100, and 1000 s and 20 h (from bottom to top, respectively). For short immersion times (i.e., low surface coverage), the peak shift is larger.

the observed amide peak at high surface coverage was only slightly above the noise level, such that no definitive conclusion can be drawn from these data.

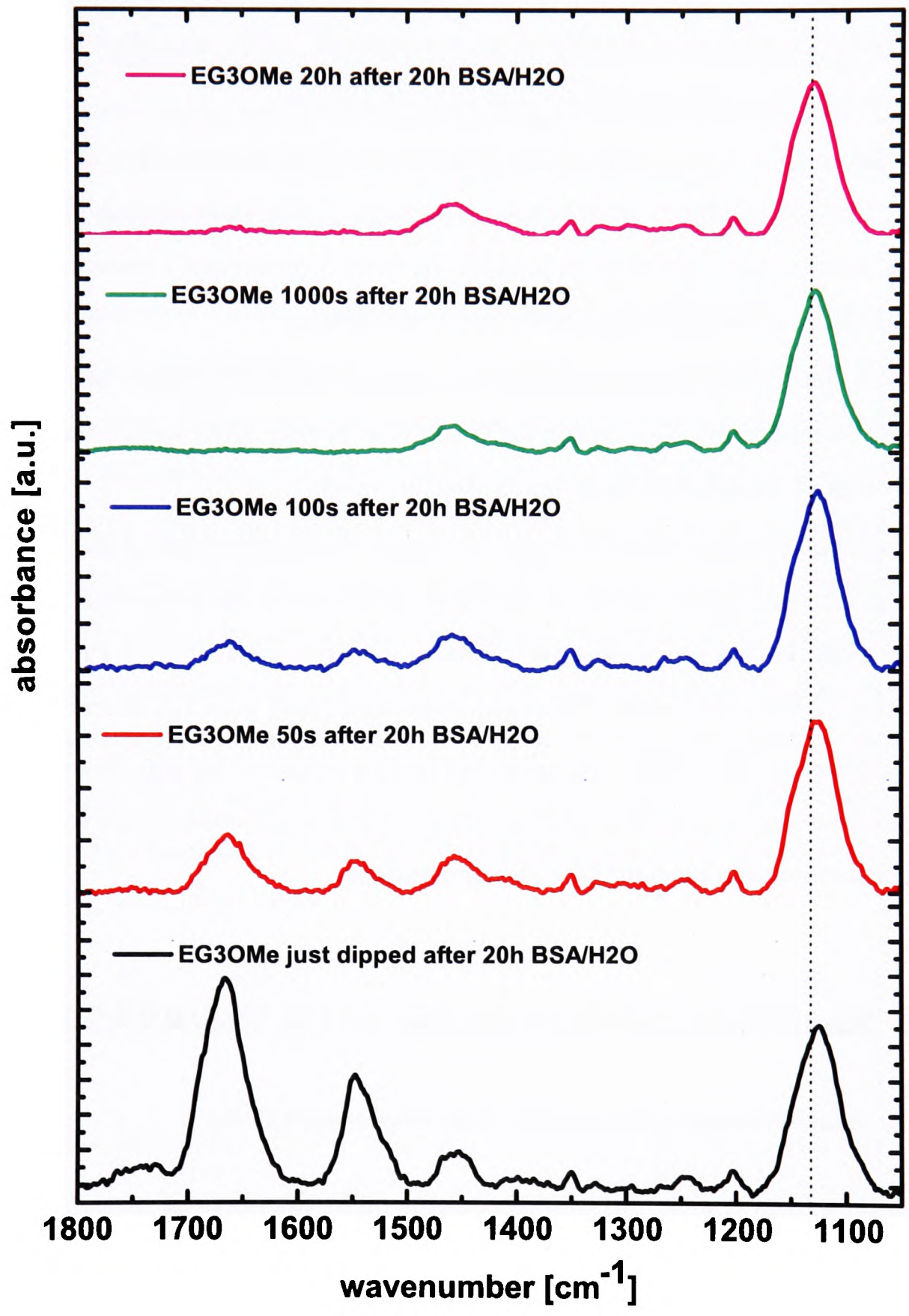


Figure 5.14.: Amide band and C-O-C peaks (resolution 4 cm^{-1}) for different surface coverages (immersion times) in air after 20 h exposure to a 15 wt % BSA/H_2O solution. SAM formation was interrupted after 1, 50, 100, and 1000 s and 20 h (from bottom to top, respectively). The spectra have been normalised to the same C-O-C peak height. For short immersion times (i.e., low surface coverage), the adsorbed amount of BSA is higher (see text).

5.4.6. Conclusions

By means of (polarisation-modulated) infrared reflection adsorption spectroscopy, the peak positions of the ether vibrational mode in methoxy-tri(ethoxy) undecanethiol self-assembled monolayers were measured before and after immersion in water as well as in situ, under a water layer of 1-3 μm.

A shift of this peak to lower wavenumbers is observed after 18 h of exposure to water. The peak shifts on average are about 5 cm^{-1}, but those of individual samples varied. In situ measurements on samples in direct contact with water show a peak shift of about 17 cm^{-1}, along with a peak broadening.

In situ data taken for samples with increasing surface coverage (achieved by an increase in immersion time in the OEG solution during SAM formation) indicate a decrease in the peak shift upon immersion in water.

As an explanation of these findings, we suggest the penetration of water molecules into the ethylene glycol region of the SAM, resulting in the formation of hydrogen bonds with the oxygen atoms and thereby causing a lowering of the vibrational frequency of the ether band. This is in good agreement with the literature [16, 17].

In conclusion, this study has provided in situ evidence for significant hydration effects of triethylene glycol-terminated thiol SAMs, which are thought to be relevant to interactions with proteins in aqueous solutions.

5.5. Simulation and optimisation of the PMIRRAS signal

5.5.1. Mathematical framework and implementation

The results from in situ measurements obtained in the previous section require the precise control of experimental parameters, such as the thickness of the water layer between sample and BaF_2 prism, and the angle of incidence of the infrared light. The signal-to-noise ratio was lower compared to air measurements, owing to additional refractions and reflections at the prism-water and water-SAM interfaces, and also owing to absorption of the water layer itself. It was found that the signal-to-noise ratio in the wavelength region of the relevant peak varied strongly depending on the incident angle of the light and the liquid used (H_2O or D_2O).

As the refractive indices of the materials involved in the optical setup vary with wavelength, and the FRESNEL coefficients for a stack of optical layers vary with angle in a non-trivial way, it is not possible to predict the ideal conditions for the best signal-to-noise ratio for a given setup just by simple considerations. Therefore the FRESNEL equations were implemented into the IgorPro [41] software for the purpose of determining the optimum experimental conditions. The formalism for the calculation of the reflectivity of the sample and the experimental validation of the code will be discussed in this section.

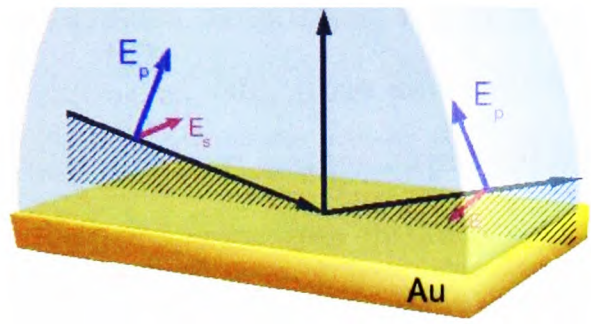
The propagation of electromagnetic waves through stratified media has been discussed in detail in the literature [42–44]. The present calculation uses the formalism and notation used by Hansen [45]. The basic implementation was obtained from Corn's group [46] and was extended to describe a four layer system including s- and p-polarised light. From the resulting reflectivity for the whole stack, the PMIRRAS difference signal was computed (**Equation 3.25**) in order to compare these calculations with actual experimental data. The BESSEL function was not included, since the experimental spectra were corrected and the implicit BESSEL function removed. The four layer stack is sketched in **Figure 5.15** and the formalism by Hansen is briefly described in the following section. The Fresnel equations (**Equations 3.13-3.15**) derived in **Section 3.1.3.3** can be re-written for the interface between two layers j and $j+1$ in the stack:

$$r_p^j = \frac{\hat{n}_{j+1}^2 \xi_j - \hat{n}_j^2 \xi_{j+1}}{\hat{n}_{j+1}^2 \xi_j + \hat{n}_j^2 \xi_{j+1}} \qquad t_p^j = \frac{2\hat{n}_{j+1}^2 \xi_j}{\hat{n}_{j+1}^2 \xi_j + \hat{n}_j^2 \xi_{j+1}} \tag{5.7}$$

$$r_s^j = \frac{\xi_j - \xi_{j+1}}{\xi_j + \xi_{j+1}} \qquad t_s^j = \frac{2\xi_j}{\xi_j + \xi_{j+1}} \tag{5.8}$$

where $\xi_j = \hat{n}_j \cos\theta_j = \sqrt{\epsilon_j^2 - \epsilon_1^2 \sin^2(\theta_1)}$ and $\epsilon_j = \hat{n}^2$. Care has to be taken when calculating the square root of the complex expression for ξ, since the resulting hyperbolic functions are periodic and only the positive values of the real and imaginary parts must be used for the calculation. If the thickness of layer j is denoted by d_j and the complex variables

$$q_j = \frac{\xi_j}{\hat{n}^2} \quad \text{and} \quad \beta_j = \frac{2\pi d_j}{\lambda} \xi_j \tag{5.9}$$



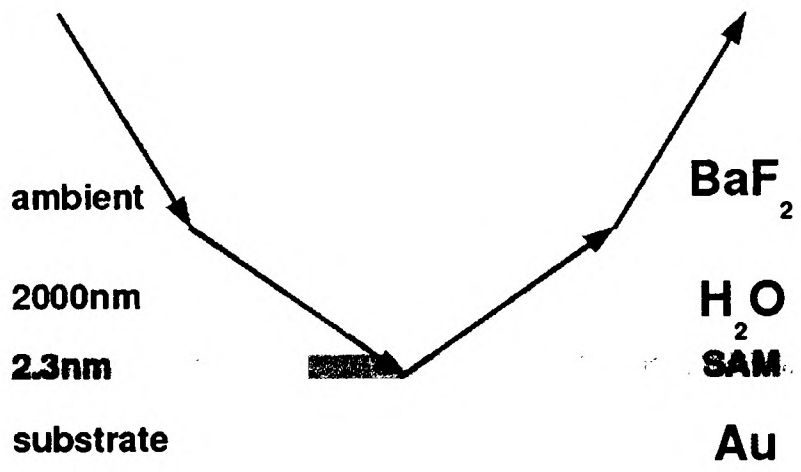


Figure 5.15.: Generic arrangement of layers used in the PMIRRAS calculation and experiments.

are defined for convenience, then the optical matrices for layer j take the form

PARALLEL (P) POLARISATION

$$M_j^p = \begin{pmatrix} \cos\beta_j & -\frac{i}{q_j}\sin\beta_j \\ -iq_j\sin\beta_j & \cos\beta_j \end{pmatrix} \tag{5.10}$$

PERPENDICULAR (S) POLARISATION

$$M_j^p = \begin{pmatrix} \cos\beta_j & -\frac{i}{\xi_j}\sin\beta_j \\ -i\xi_j\sin\beta_j & \cos\beta_j \end{pmatrix} \tag{5.11}$$

In general for an N-layer system, $N-1$ matrices can be defined, since the ambient medium is semi-infinite. For the above-mentioned four layer system, three matrices

are needed. In order to calculate the reflectivity of the whole stack, the characteristic matrix

$$M^{s,p} = \prod_{j=1}^{N-1} M_j^{s,p} = \begin{pmatrix} m_{11}^{s,p} & m_{12}^{s,p} \\ m_{21}^{s,p} & m_{22}^{s,p} \end{pmatrix} \tag{5.12}$$

has to be computed. Then the reflection coefficients for the whole stratified medium can be expressed using the following relations:

$$r_p = \frac{(m_{11}^p + m_{12}^p q_N)q_0 - (m_{21}^p + m_{22}^p q_N)}{(m_{11}^p + m_{12}^p q_N)q_0 + (m_{21}^p + m_{22}^p q_N)} \tag{5.13}$$

$$r_s = \frac{(m_{11}^s + m_{12}^s \xi_N)\xi_0 - (m_{21}^s + m_{22}^s \xi_N)}{(m_{11}^s + m_{12}^s \xi_N)\xi_0 + (m_{21}^s + m_{22}^s \xi_N)} \tag{5.14}$$

The reflection coefficients r_s and r_p for the entire stack are then used to compute the PMIRRAS signal r_{calc} (see also **Equation 3.25**)

$$r_{calc}(\theta) = \frac{I_p - I_s}{I_p + I_s} \sim \left(\frac{\Delta R}{R}\right)_{exp} \tag{5.15}$$

The final signal is obtained by calculating the relative reflectance of the sample. This is given by the difference between the reflectance of the stack with SAM and that without it:

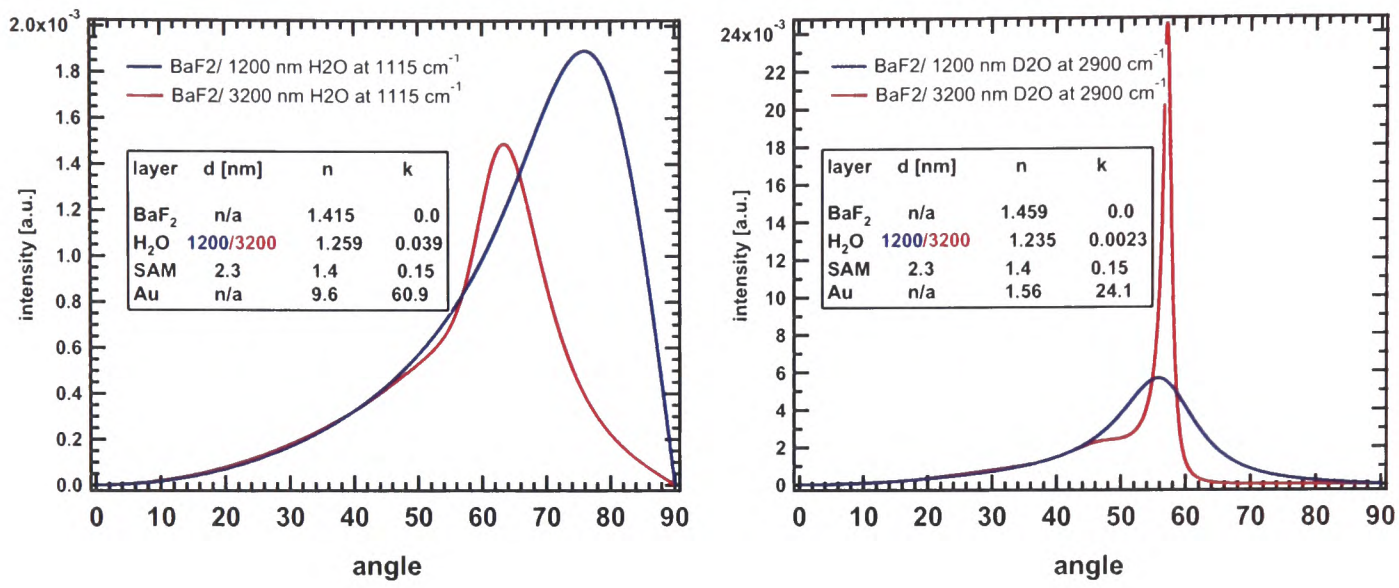
$$I_{calc}(\theta) = r_{calc}^{SAM} - r_{calc}^{noSAM} \tag{5.16}$$

The IgorPro code plots r_s and r_p for the entire stack and the total PMIRRAS signal I_{calc}. The software can calculate these quantities as a function of angle for fixed thicknesses of SAM and water layer, or the signal can be evaluated at a given angle as a function of the thickness of either SAM or water layer. The resulting functions are very helpful for the determination of the ideal experimental conditions regarding optimum angle of incidence and the impact of the thickness of the water layer. In addition, the optical constants for H_2O and D_2O, which vary considerably in the mid-infrared region, can be automatically loaded from the tabulated values of Bertie et al. [47]. The refractive index of the BaF_2 half cylinder is calculated using following SELLMEIER approximation [48]:

$$n_{BaF_2}^2 = 1 + \frac{0.643356\lambda^2}{\lambda^2 - 0.057789^2} + \frac{0.506762\lambda^2}{\lambda^2 - 0.10968^2} + \frac{3.8261\lambda^2}{\lambda^2 - 46.3864^2} \tag{5.17}$$

This approximation is valid at 25° C in the wavelength range of λ = 37707.4 to 966.5 cm^{-1}. The optical constants of gold were taken from [49].

Some examples are shown to illustrate the importance of the choice of incident angle and thickness of the water layer for the system which was investigated in this thesis by using PMIRRAS. The typical shape of reflectivity curves for the present

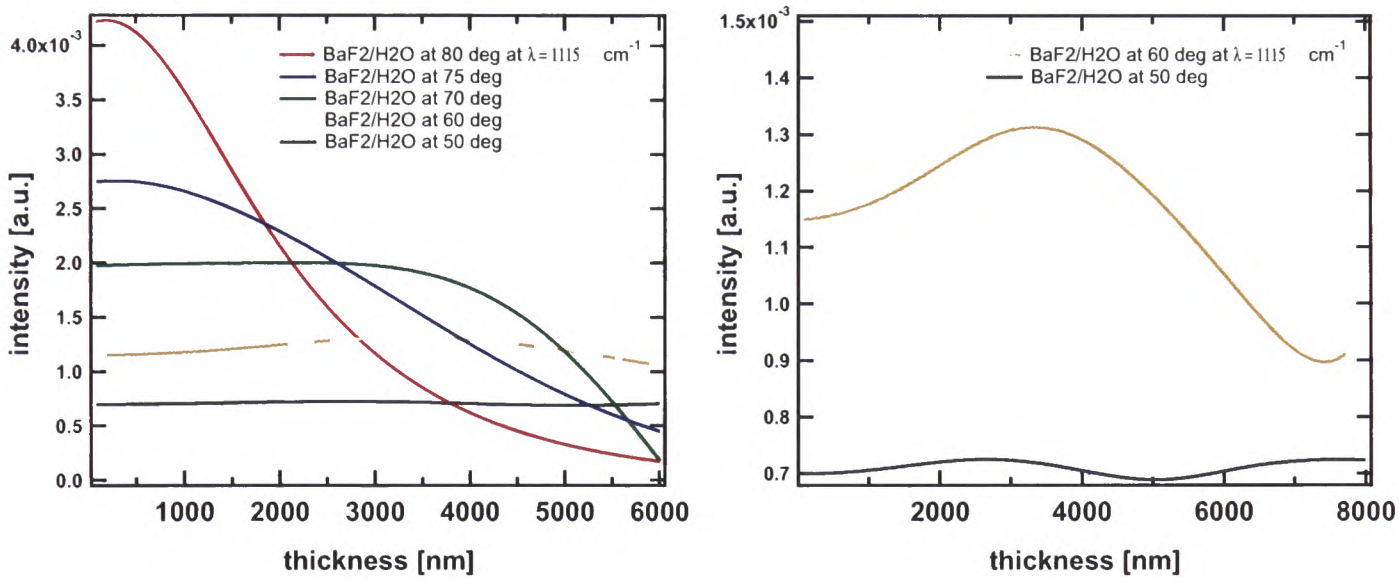


(a) (b)

Figure 5.16.: (a) Simulation of the C-O-C peak intensity at 1115 cm^{-1} for a four layer system consisting of barium fluoride, H_2O, monolayer and gold substrate (optical constants are shown in the inset). (b) Simulation of the C-H peak intensity at 2900 cm^{-1} for a four layer system consisting of barium fluoride, D_2O, monolayer and gold substrate (optical constants are shown in the inset).The blue lines denote a water thickness of 1200 nm, while the red line represents 3200 nm of water.

four layer system is a smoothly rising curve with a broad peak at angles higher than 50°, which falls rather abruptly to zero at 90°. However, the position and width of the peak strongly depends on the thickness of the water layer sandwiched between barium fluoride half cylinder and the sample. Whereas for relatively thin layers of H_2O, i.e. around 1000 nm, the peak is rather broad, centred at around 75°, the situation changes if the water layer becomes thicker (~3000 nm). Then the peak becomes much sharper and shifts towards lower angles. This means that the observed intensity of the IR absorption band (e.g. that of the C-O-C stretching vibration) can vary by a factor of up to seven between an angle of incidence of 80° compared to the optimum angle at 63° (**Figure 5.16a**). A more dramatic effect can be observed for D_2O due to its difference in refractive index compared to the barium fluoride in the CH stretching region. If absorption peaks in the CH region (around 2900 cm^{-1}) are measured, then a variation of the thickness from 1200 to 3200 nm can lead to a complete loss of signal at angles away from the optimum angle at

around 58°, as shown in **Figure 5.16b**. This behaviour is caused by the difference in refractive index, which leads to total reflection between the BaF_2 half cylinder and the water layer (the exact critical angle varies with wavelength). However, due to the relatively high imaginary part of the refractive index (equivalent to the absorption coefficient) for H_2O at 1115 cm^{-1}, the electromagnetic wave can still propagate into the water beyond the critical angle. In contrast, the absorption coefficient for D_2O at 2900 cm^{-1} is very small, and there is only the evanescent wave present at angles higher than the critical angle. However, even in this case the intensity does not vanish immediately, since the evanescent field penetrates to depths of the order of the wavelength (i.e. a few micrometres) into the water.



(a) (b)

Figure 5.17.: (a) Simulation of the C-O-C peak intensity at 1115 cm^{-1} for a four layer system consisting of barium fluoride, H_2O, monolayer and gold substrate for different, but fixed incident angles as a function of thickness of the water layer. (b) Detailed view of the plots for 50 and 60°.

Finally, the peak intensity can be plotted for a fixed angle as a function of the thickness of the water layer. An overview of the results are shown in **Figure 5.17**. The absorption peak intensity drops exponentially with the thickness of the water layer at angles much larger than the critical angle. The intensities are almost constant for angles smaller than the critical one, and show an oscillatory behaviour in the simulations. This is due to interference effects, when the thickness is of the order of the wavelength of the light. This effect is small even in the calculations, and it is not expected to be present in actual experiments due to roughness of half cylinder and sample, and also due to potential misalignment (i.e. the water layer is not a

slab of constant thickness, but has rather a wedged shape as a consequence of the mechanical assembly).

5.5.2. Comparison of calculations and experiments

In order to validate the software and compare it with experimental data, a systematic study of the angular dependence of the PMIRRAS was performed on the Bio-Rad FTS-6000 system (see **Section 4.6**). With this setup it was possible to access angles between 40 and 90° using the liquid cell (see **Section 4.7**). As a generic sample, a gold wafer coated with an EG6OMe terminated alkanethiol was employed. The study focused on the angle dependent intensity of the very strong C-O-C absorption band at about 1117 cm^{-1}. First, the sample was measured at incident angles ranging from

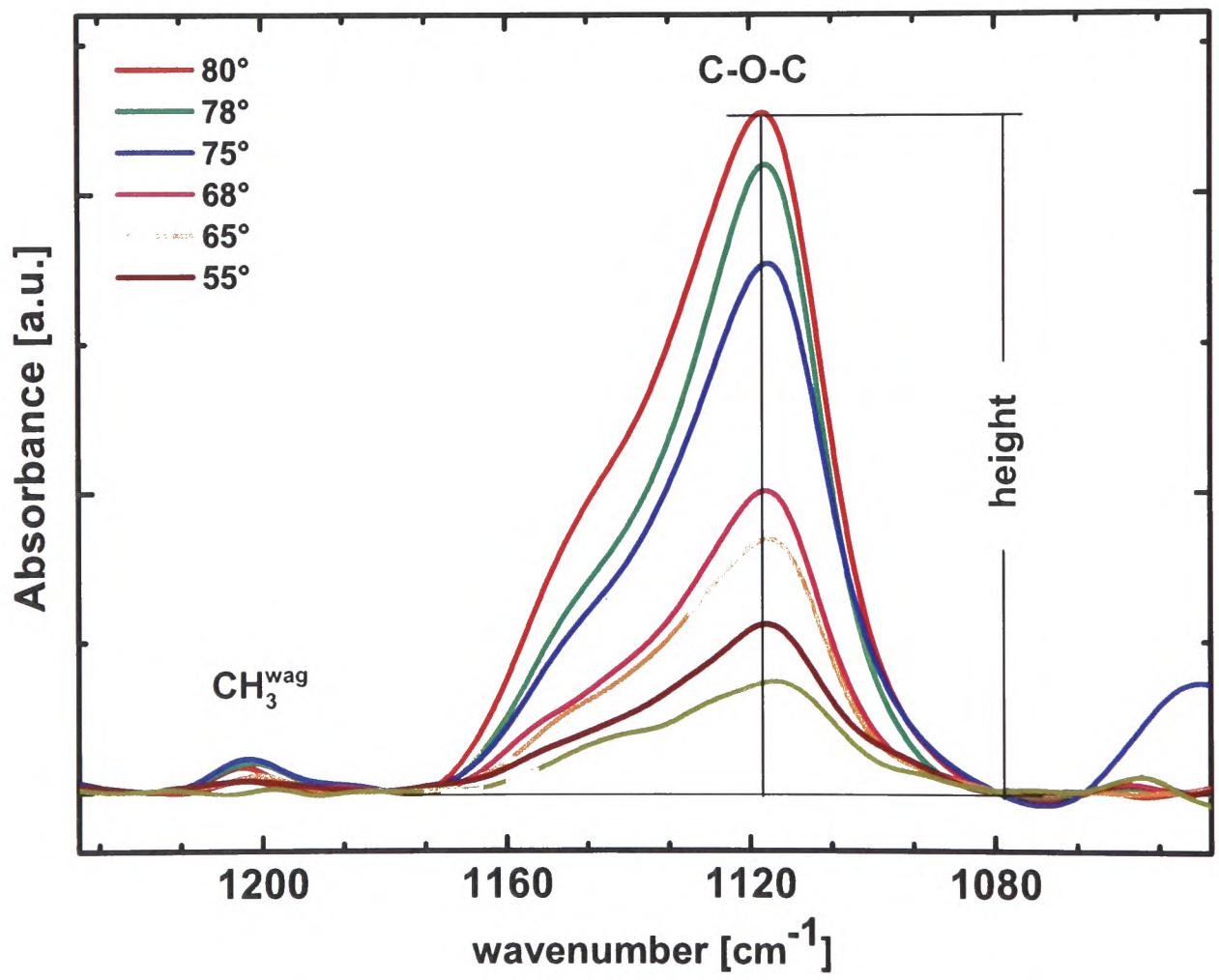


Figure 5.18.: Measured C-O-C peak heights for various angles on an EG6OMe coated SAM in air.

45 to 85° with respect to the surface normal of the sample. Because the measured PMIRRAS spectra still contained a second order BESSEL function, they had to be baseline-corrected in order to obtain the true spectrum (the same correction

procedure was employed for all samples). A set of seven points at positions 1260, 1220, 1180, 1080, 1065,1050 and 1030 cm^{-1} was used for all samples to interpolate the shape of the baseline. The interpolation point were chosen to lie well away from the peak of interest in the spectrum. This standard correction procedure was necessary for the determination of the peak intensity for different samples, especially for the in situ measurements, where the whole angle series could not be measured without refilling the liquid cell.

The EG6OMe sample was measured in air (**Figure 5.18**). The peak heights were determined and compared to the calculated values. The measured values were only multiplied by a constant factor to account for the efficiency of the optics in the experimental setup. As can be seen from **Figure 5.19**, the measured values are in excellent agreement with the calculated curve. The data points at angles higher than about 80° are slightly lower than the calculated curve. This can be explained by the large size of the footprint of the beam compared to the sample at grazing angles, as was verified in measurements with different sized samples. If the sample is sufficiently long in the direction of the beam, then the overspill can be minimised or even eliminated and the data points are commensurate with the calculated values. The peak heights were taken to be the vertical distance between the abscissa of the corrected spectra and the highest point of the C-O-C peak at about 1118 cm^{-1} (**Figure 5.18**). An error was estimated by repeated measurements of one sample at one given angle at different times and calculating the standard deviation of the measured values.

A second series of measurements was performed in situ, using the liquid cell described in **Section 4.7**, where the EG6OMe SAM was in contact with a thin layer of water[4] The duration of one in situ measurement at a resolution 8 cm^{-1} was about 20 minutes including the time required for the calibration of the instrument after the angle was changed. In addition, the thickness of the water layer was determined by an ellipsometry measurement of about 15 min duration before and after the PMIRRAS measurement.

[4]The solubility of BaF_2 is about 1.8 g/kg in water at room temperature [50]. In order to avoid damage to the BaF_2 half cylinder as a consequence of prolonged exposure to water a 0.1M NaF/water solution was used instead.

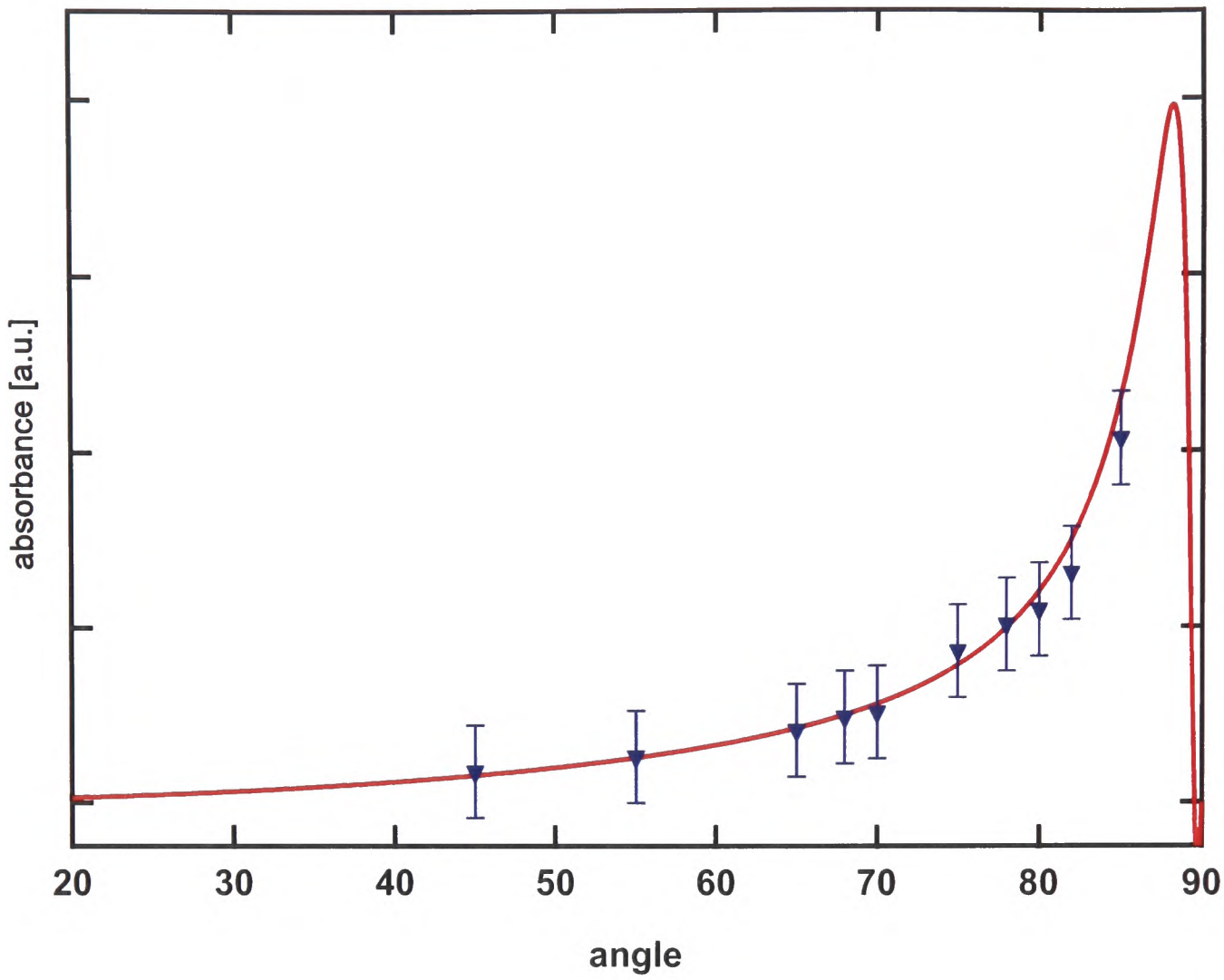


Figure 5.19.: Comparison of calculated and measured reflectivities for various angles on an EG6OMe coated SAM in air.

layer	d [nm]	n	k
BaF_2	n/a	1.4148	0.0
H_2O	1800	1.2588	0.03922
SAM	2.8	1.4	0.14
Au	n/a	9.38	60.08

Table 5.8.: Optical constants for the PMIRRAS calculation in Figure 5.20.

The results of the angle dependent measurements and the calculation are compared in **Figure 5.20**. The optical constants used for the four layer model are listed in **Table 5.8**. Establishing the systematical error for the in situ measurements was more difficult than for the data taken in air. All measurements were repeated for the same angle at least three times, the peak height was averaged and the standard deviation taken as the error. The data point at 80° was taken nine times under similar conditions and the standard deviation of these measurements was taken as error estimate for the data points at 45, 55, 67.5 and 82.5 degrees, which were mea-

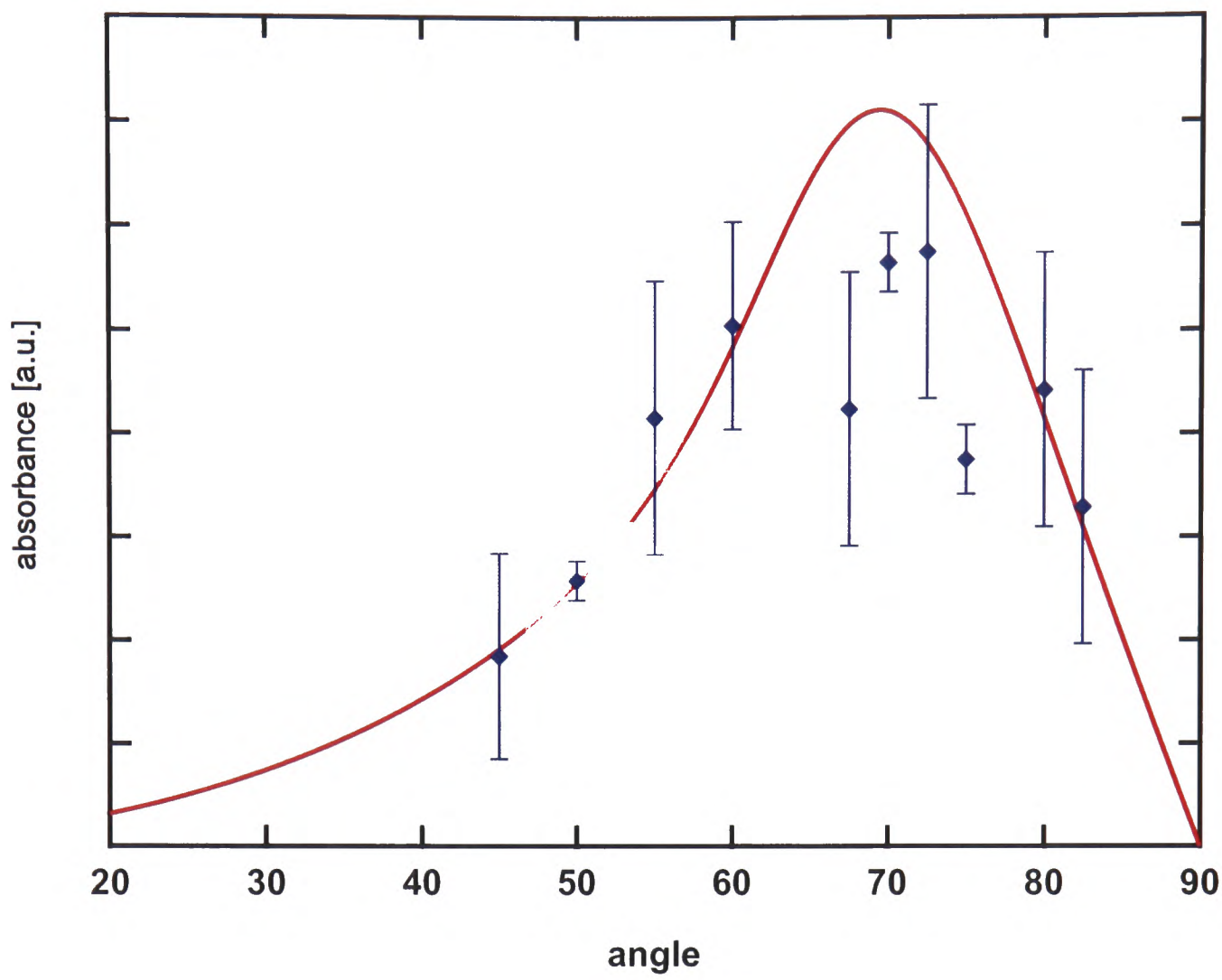


Figure 5.20.: Comparison of calculated and measured reflectivities (average of two or three measurements) for various angles on an EG6OMe coated SAM in a 0.1M H_2O/NaF solution. The red line is the PMIRRAS calculation for a four layer stack with optical constants listed in **Table 5.8**.

sured only once. Despite the large error bars, the experimental data reproduce well the trend of the calculation. One reason for potential deviations was the variation in the thickness of the water layer, since the same fixed thickness was used for the calculation of all angles. To avoid the impact of this variation, theoretical peak heights were computed for each measured angle, considering the exact measured thickness for that particular measurement. These values are plotted together with the corresponding experimental data in **Figure 5.21**.

Note that the data points in **Figure 5.21** do not have error bars associated with them, since the values originate from only one measurement. It is obvious that the correction for the actual thickness of the water layer leads to a very good agreement of experimental and calculated data. The deviations that still remain can be attributed to the fact that the thickness measurements possess a systematic error themselves. During the experiments it was noticed that, under certain conditions, for instance when the sample is not entirely parallel to the barium fluoride prism,

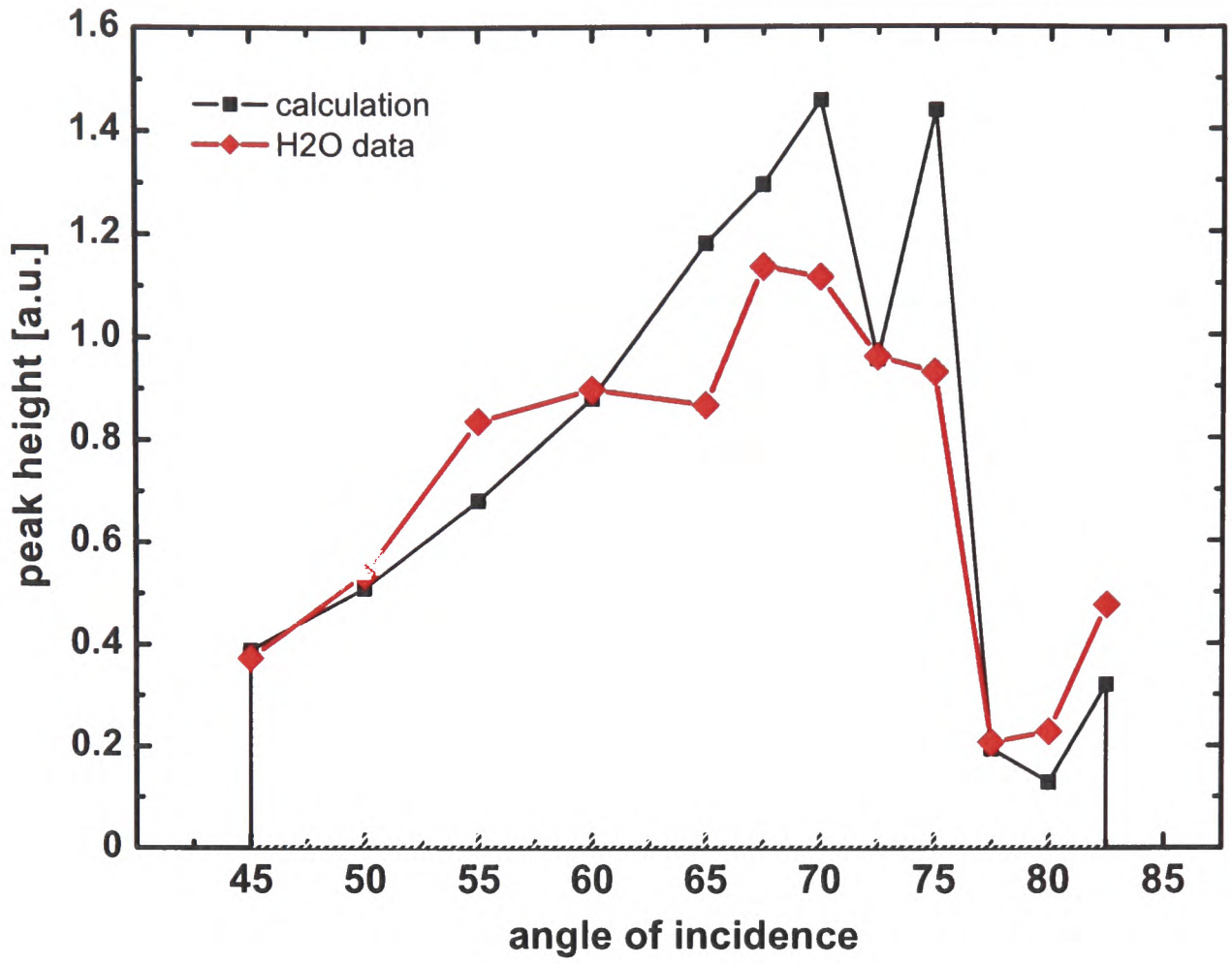


Figure 5.21.: Comparison of calculated and measured reflectivities for various angles on an EG6OMe coated SAM in a 0.1M H_2O/NaF solution. The red data points are the measured data and the black squares are the PMIRRAS calculation for a four layer stack with optical constants listed in **Table 5.8** considering the exact measured water layer thickness. Connecting lines and the hatched area have been drawn as a guide for the eye.

thickness measured by the relatively small laser spot (ca. 1×2 mm^2, may vary from the actual range of thicknesses over which the much larger beam of infrared light is averaging (ca. 0.5×3 cm^2).

To conclude, this study demonstrates the importance of choosing and controlling the experimental parameters (incident angle, thickness of the water layer, sample size etc.), in particular for in situ PMIRRAS experiments. The presented software can serve as an aid for the selection of the optimum settings regarding angle of incidence and thickness of the liquid layer when a complex multilayer system is studied, especially if the optical constants of the employed materials strongly depend on wavelength. The accuracy of the calculated data was examined by a systematic experimental study and was found to be in excellent agreement with the experimental values.

5.6. OEG SAMs in contact with non-polar solvents

The exploration of water penetration into the OEG SAM raises the question whether the observed effect is connected to the polar nature of the SAM or due to defects and loose ordering. Therefore in situ experiments with non-polar solvents ($CHCl_3$, CCl_4) have been performed to clarify this question. Solvent penetration has been described in calculations [17], where the assumption is that a non-polar solvent should penetrate even further into the SAM, solvating also the lower alkyl section and greatly disturbing the film structure. In contrast to other in situ techniques, such as SFG

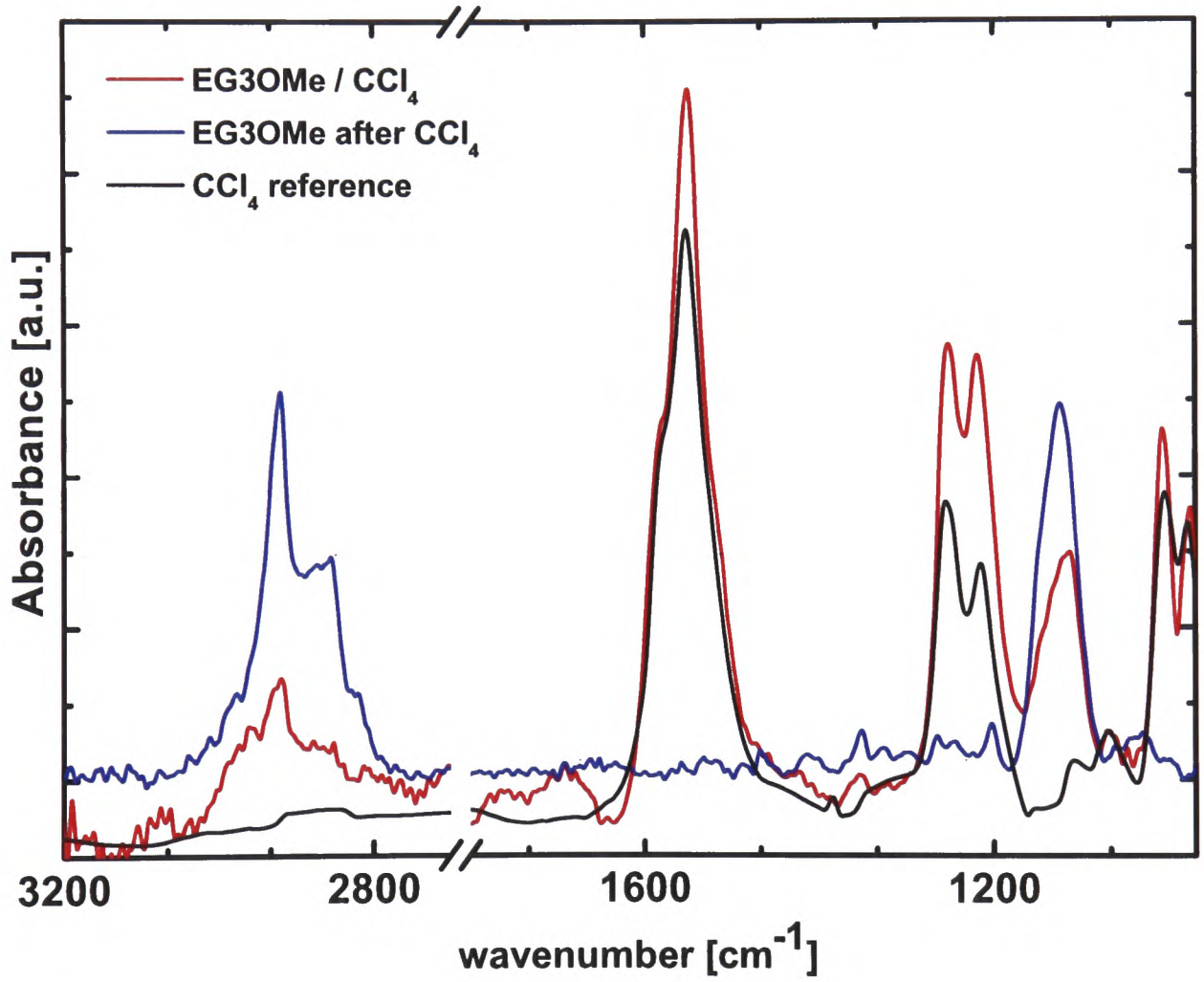


Figure 5.22.: Comparison of in and ex situ measurements of an EG3OMe terminated SAM in contact with CCl_4 (red line) and persistent red-shift of the C-O-C peak of the dry SAM after exposure to CCl_4 (blue line). A blank gold sample measured with the solvent CCl_4 (black line) is shown for comparison.

which is limited to a small wavelength range around the laser wavelength, PMIRRAS offers the possibility of observing characteristic modes of a self-assembled monolayer through a thin liquid layer over the whole mid-infrared region. However, the difficulty of PMIRRAS lies in the fact that, although it is a surface sensitive technique,

some contributions from the bulk liquid may remain in the final spectrum. For the experiments presented here, a non-polar solvent had to be chosen, which did not have bands overlapping with the characteristic C-O-C vibration of the OEG SAM. The two non-polar solvents tetrachloro methane (CCl_4) and chloroform ($CHCl_3$) were used, in order to compare the results with the calculations of Zolk et al. [17], and because their absorption bands are reasonably different from the C-O-C band.

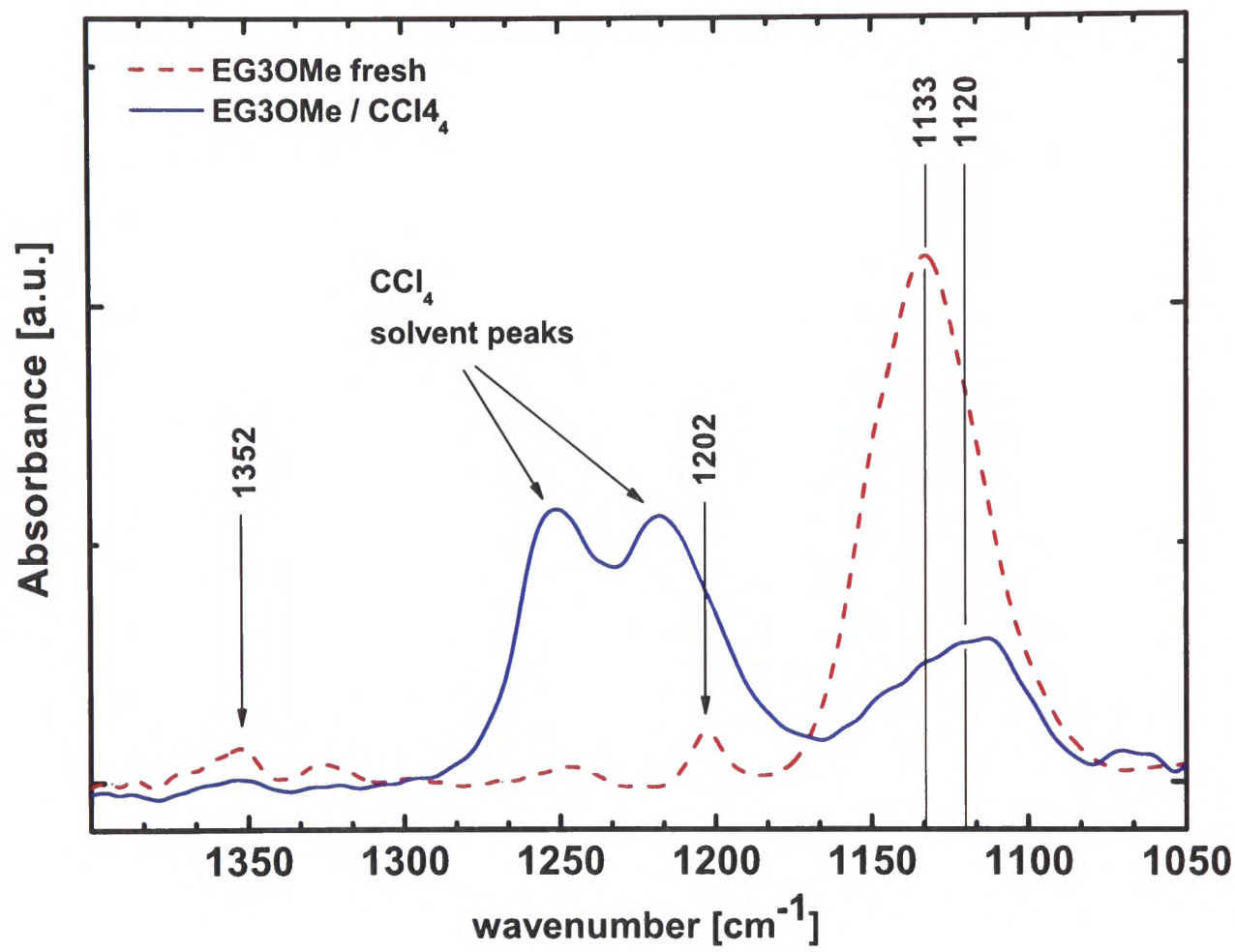


Figure 5.23.: Comparison of in and ex situ measurements of an EG3OMe terminated SAM in contact with CCl_4 (blue solid line) and the initial C-O-C peak position of the dry SAM before exposure to CCl_4 (red dashed line).

The in situ spectra with CCl_4 show a clear, strong red-shift of the C-O-C frequency by more than 10 cm^{-1}. A red-shift of about 6-7 cm^{-1} remains when the solvent is removed and the sample is measured in a dry state (**Figures 5.22** and **5.23**).

To elucidate the question about the penetration depth of a non-polar solvent into an OEG SAM, samples with different surface coverage have been studied. The focus here was on shifts of the characteristic modes of the alkyl backbone of the SAM. The samples were exposed to chloroform ($CHCl_3$) for 1 hour and the peak positions in the CH stretching region were compared before and after the exposure. A considerable blue-shift of the mode at ~2919 cm^{-1} was found along with the

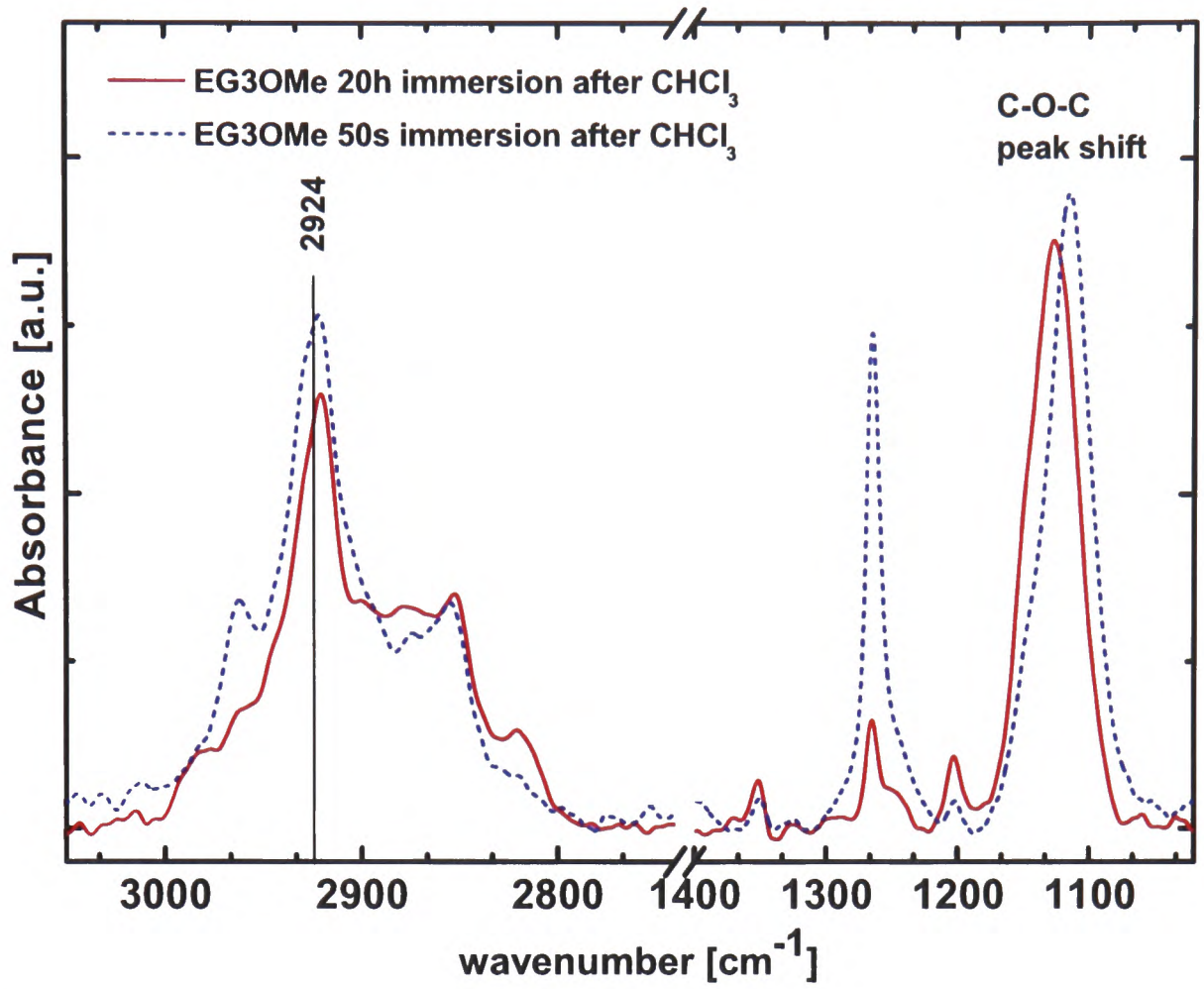


Figure 5.24.: Comparative measurements of an EG3OMe terminated SAM after exposure with $CHCl_3$ for different surface coverages: 20 h (red solid line) and 50 s SAM formation time (blue dashed line). The red-shift of the C-O-C peak is more pronounced for the lower coverage SAM and is accompanied by a blue-shift of the alkyl CH_2 asymmetric stretching vibration at $\sim$2919 cm^{-1}.

red-shift of the C-O-C frequency, as described earlier (**Figure 5.24**). As before, the sample with lower SAM coverage shows a larger red-shift of the C-O-C mode (the OEG section of the SAM). This shift, however, is accompanied by a blue-shift of about 2-3 wavenumbers in the CH stretching region. The blue-shift of the alkyl CH_2 asymmetric stretching vibration from $\sim$2919 cm^{-1} in a fresh SAM to about 2924 cm^{-1} after exposure to chloroform suggests the penetration of the solvent down into the alkyl backbone section of the SAM.

These findings represent the first in situ experimental evidence for the penetration of a non-polar solvent into an OEG terminated SAM. The red-shift of the antisymmetric C-O-C mode accompanied by a complementary blue-shift of the alkyl CH_2 stretching modes indicates that the non-polar solvent not only penetrates into the OEG part of the SAM, but also reaches to the alkane backbone, thereby inducing a higher level of disorder. These findings fully confirm the prediction by Zolk et al. [17].

6. Protein-protein interactions in solution[1]

In this chapter the effect of ionic strength on the protein-protein interaction was systematically studied using small-angle x-ray scattering on BSA as a model system, using a large range of salt and protein concentrations. BSA is a globular protein, which is readily soluble in water and stable over a wide range of salt and protein concentrations. For BSA, no liquid-liquid phase separation behaviour was reported, and under low ionic strength, the protein interaction is dominated by electrostatic repulsion. An attractive interaction was observed only at high ionic strength, $I > 1.0$ M. Therefore, we can distinguish this attractive potential induced by high salt concentration from other sources, such as van-der-Waals interactions.

6.1. Introduction

A series of samples of Bovine Serum Albumin (BSA) solutions has been studied, with protein concentration c, ranging from 2 to 500 mg/mL and ionic strength, I, from 0 to 2 M by small-angle X-ray scattering. The scattering intensity distributions were compared to simulations using an oblate ellipsoid form factor with radius of 16×42×42 Å, combined with screened Coulomb repulsive structure factor $S_{SC}(q)$ or an attractive square-well structure factor $S_{SW}(q)$. At pH=7, the BSA is negatively charged.

At low ionic strength, I <0.3 M, the total interaction exhibits a decrease of the repulsive interaction when compared to the salt free solution as the net surface charge is screened and the data can be simulated by assuming an ellipsoid form factor and screened Coulomb interaction. The structure factor proposed by Hayter and Penfold [51, 52] is sufficient to describe the repulsion dominated interaction

[1] This chapter is based on Zhang, F.; Skoda M. W. A. et al., *J. Phys. Chem. B*, 111 , **2007**, 251.

potential. At moderate ionic strength (0.3-0.5 M) the interaction is rather weak and a hard-sphere structure factor has been used to simulate the data with a higher volume fraction. Upon further increase of the ionic strength (I≥1.0 M), the overall interaction potential was dominated by an additional attractive potential, and the data could be successfully simulated by an ellipsoid form factor and a square well potential model. The fit parameters, well-depth and well-width indicate that the attractive potential caused by the high salt concentration is weak and long-ranged. Although the long-range attractive potential dominated the protein interaction, no gelation or precipitation was observed in any of the samples. In contrast to the theoretical prediction that the depletion force induced by a high salt concentration is a strong short-range attractive potential, it appears to be a rather weak long-range potential. The stability of the concentrated protein solutions under high salt concentration is explained by the hydration effect, which results in a short-range repulsive force.

Repulsive interaction screened Coulomb structure factors $S_{SC}(q)$ calculated from the fitting parameters show a strong dependence on both protein concentration and ionic strength. The repulsive force increases with protein concentration and decreases with ionic strength. The evolution of square-well structure factors $S_{SW}(q)$ indicates that the attractive force decreases with protein concentration, and only slightly increases with ionic strength for I>1.0 M. Further, it can be seen that with increasing ionic strength the protein interaction potential changes smoothly from a repulsive to an attractive potential.

6.2. Experimental details

Materials Bovine serum albumin (BSA) (product no A7638) was purchased from Sigma-Aldrich. It is a lyophilized powder with a molar molecular weight of ~66 kDa and was used as received. A batch of solutions with 12 protein concentrations ranging from 2 to 500 mg/mL and 8 salt concentrations ranging from 0 to 2.0 M were prepared. Solutions with protein concentrations less than 100 mg/ml were prepared by diluting a stock solution, while the high protein concentration solutions >100 mg/mL were prepared by directly dissolving the corresponding amount of protein powder in the solvent. Protein concentrations were determined by UV ab-

sorption based on absorption at wavelengths 410 nm and 280 nm. The extinction coefficient of BSA at 280 nm is 39020/M/cm, or 0.5912/(mg/mL)/cm, calculated from the amino acid sequence [53]. In order to avoid the affect of other ions, no buffer was used and hence the pH of all the solutions was ~7.0.

Method Small-angle X-ray scattering measurements were carried out on beam line 6.2 of the Synchrotron Radiation Source (SRS) at Daresbury Laboratory, Warrington UK [7]. The beam energy was 15.0 keV corresponding to a wavelength of 0.827 Å. The scattered intensity was registered with a 200 mm-radius quadrant detector located 3.3 m from the sample. The accessible q-range was thus from 0.013 $Å^{-1}$ to 0.45 $Å^{-1}$. The detector response was calibrated using the scattering from water. The angular scale was calibrated using the scattering peaks of Silver Behenate. Protein solutions were filled into a sample cell with two mica windows (25 μm thick) separated by a 1.0 mm PTFE spacer. In order to calculate the absolute intensity, the empty cell and salt solutions were also measured. All measurements were carried out at room temperature. The resulting data were (electronically) converted to a 1D profile by integrating around an arc. The raw data were corrected for transmission, fluctuation of primary beam intensity, exposure time, and the geometry of the detector. The absolute intensity was calibrated by the cross-section of water by **Equation 6.1**. The final corrected data used for model fitting were:

$$I(q) = \frac{d\Sigma(q)}{d\Omega}_{sample} = \frac{I(q)_{sample}}{I(0)_{water}} \times \frac{d\Sigma}{d\Omega}_{water}, \tag{6.1}$$

where $I(q)_{sample}$ is the scattering intensity of sample solution after correction, and $I(0)_{water}$ is the scattering intensity of water extrapolated to origin. $\frac{d\Sigma}{d\Omega}_{water}$ = 0.01632 cm^{-1} is the constant scattering intensity of water at 293 K [54].

6.3. Low Ionic Strength, I<0.3 M, Data Fit by the E+SC Model

In a dilute protein solution, with added salt to screen the electrostatic interaction, the total scattering intensity is the sum of the scattering of individual molecules. The data for 10 mg/mL BSA with 0.3 M NaCl have been fitted using different form factors, such as a sphere, a prolate ellipsoid, and an oblate ellipsoid, as shown in

Figure 6.1. The front view of the space filling model of a serum albumin molecule is shown as an inset to **Figure 6.1**. The yellow, red, and blue parts represent the neutral, acidic, and basic residues, respectively [55]. It is clear that, although the fitted data using all three of the form factors fit the experimental scattered intensity well for q < 0.1 Å^{-1}, the oblate ellipsoid form factor with $a = 17$ Å and $b = 42$ Å fits the data best up to 0.25 Å^{-1}. On the basis of many data sets from dilute solutions, we found that an oblate ellipsoid form factor with $a = 17 \pm 1$ Å and $b = 42 \pm 1$ Å is the best description for the shape of BSA molecules in solution and gives a radius of gyration of 27.6 Å. These values were fixed in the following data-fitting procedure. As pointed out by Hayter and Penfold [51, 52], at low ionic strength,

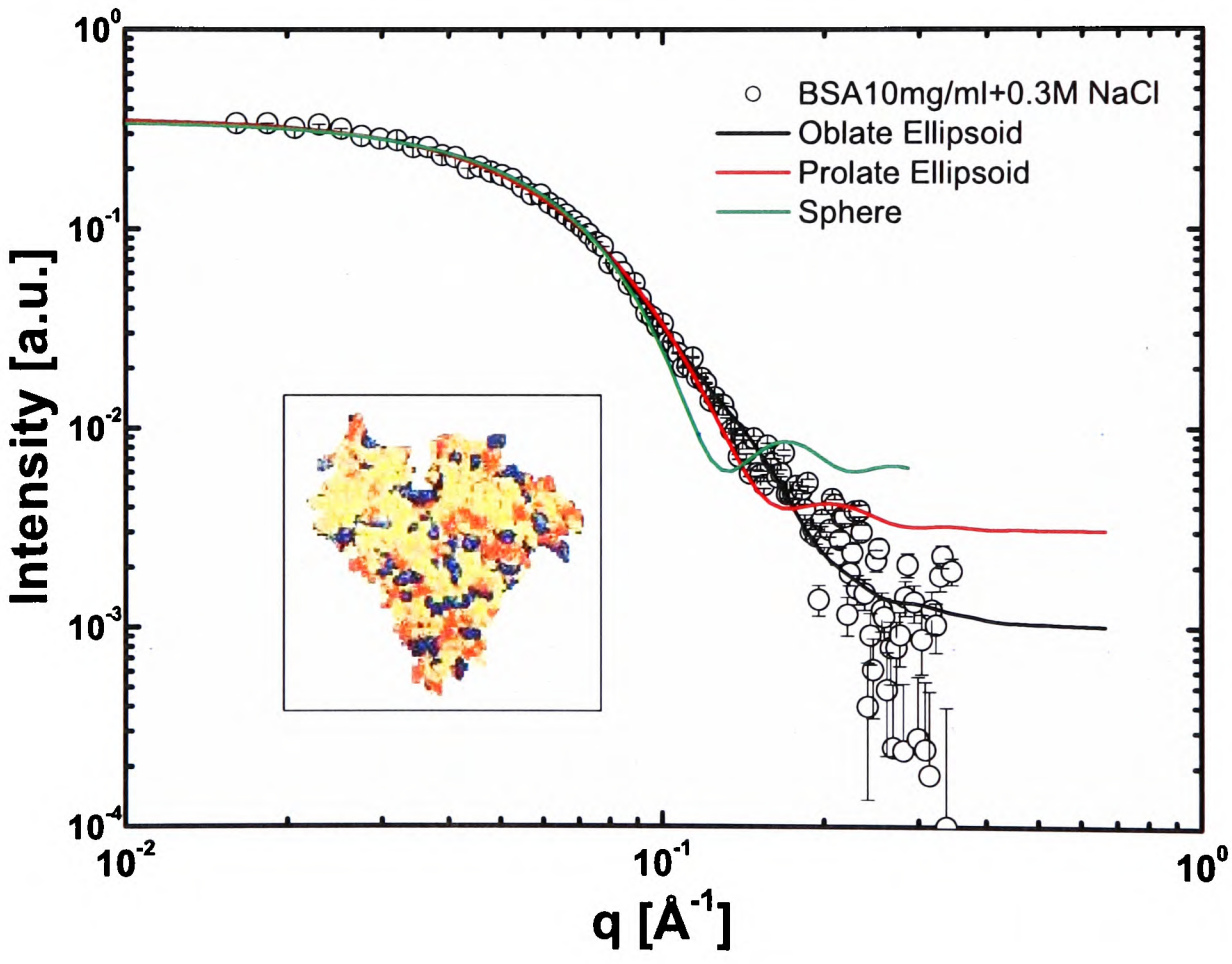


Figure 6.1.: Scattered intensity and simulation by three form factors for a protein solution of 10 mg/mL with 0.3 M NaCl. It was shown that an oblate ellipsoid shape with a = 17 Å and b = 42 Å provided the best fit. Note that the calculated curves become constant for high q values since our model calculation includes a constant experimental background. The inset is the front view of the space-filling model of serum albumin with basic residues coloured in blue, acidic residues in red, and neutral ones in yellow.

the weakly attractive van der Waals part of the colloid (DLVO) potential will have little effect on the time-averaged structure because the repulsive, screened Coulomb

potential is much larger than thermal energies at small interparticle separations. The structure factor proposed by these authors has been successfully used to predict the pronounced interaction peaks in small-angle neutron scattering (SANS) experiments for micellar solutions and protein solutions [56–58]. The scattering intensity was fitted using an ellipsoid form factor combined with the screened Coulomb structure factor (E+SC).

Figure 6.2 shows the experimental scattering intensity distribution and simulations for protein solutions with no added salt. When the protein concentration is less than 10 mg/mL, the solution is dilute, protein molecules are well-separated, and no interactions between them are observed ($\bar{S}_h(q) = 1$); the total scattering intensity is the sum of the scattering of the individual molecules. The experimental intensity profiles can be fitted by an oblate ellipsoid form factor.

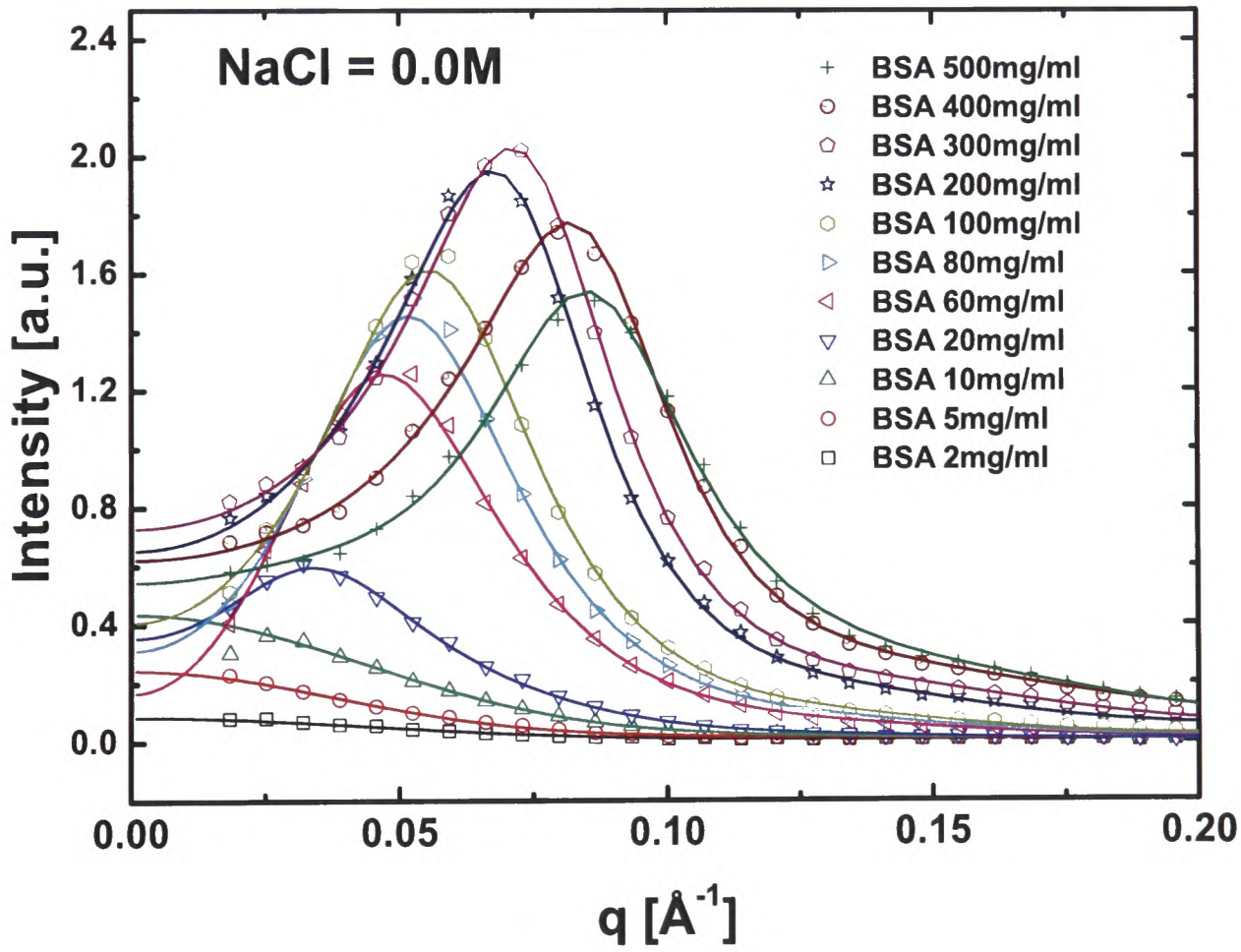


Figure 6.2.: Scattered intensity and theoretical fit by an ellipsoidal form factor and screened Coulomb potential model (E+SC) for a wide range of protein concentrations at zero ionic strength. The data of very low protein concentrations (2, 5, and 10 mg/mL) were fitted using an ellipsoidal form factor only. Only every 10th data point is shown for clarity. The error bar is estimated to be smaller than the size of the marker.

With increasing protein concentration, a pronounced correlation peak at finite q was observed, and the peak position changed with the protein concentration; the peak shifted to higher q values, and its intensity initially increased and reached a maximum at 300 mg/mL before decreasing. **Figure 6.3** shows the data at low ionic strength, I = 0.05 M. The data can be fitted by including a form factor only, up to 20 mg/mL. The correlation peaks for higher protein concentrations (c≥40 mg/ mL) are broadened and have a higher scattering intensity at a low q range compared with those for the data with no added salt (**Figure 6.2**). However, at such a low ionic strength, the interaction can still be described by a screened Coulombic potential. Similar results were obtained for the data fitting at I = 0.1 M (**Figure 6.4**); the repulsive interaction is further reduced as expected.

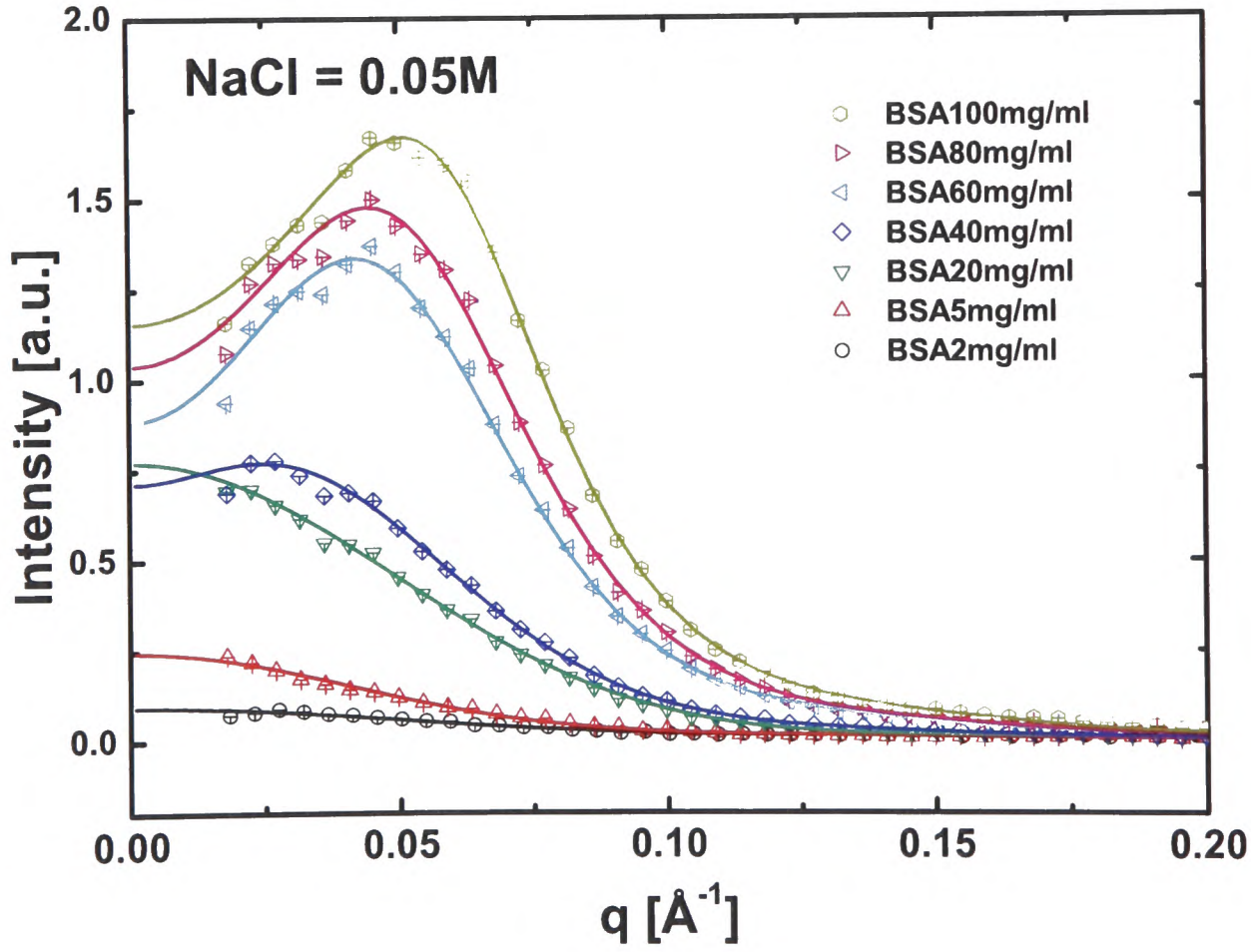


Figure 6.3.: Scattered intensity and theoretical fit by an ellipsoidal form factor and screened Coulomb potential model (E+SC) for a wide range of protein concentrations at a lower ionic strength. For I = 0.05 M, the data of 2, 5, and 20 mg/mL were fitted using an ellipsoidal form factor only. Only every 10th data point is shown for clarity. The error bar is estimated to be smaller than the size of the marker.

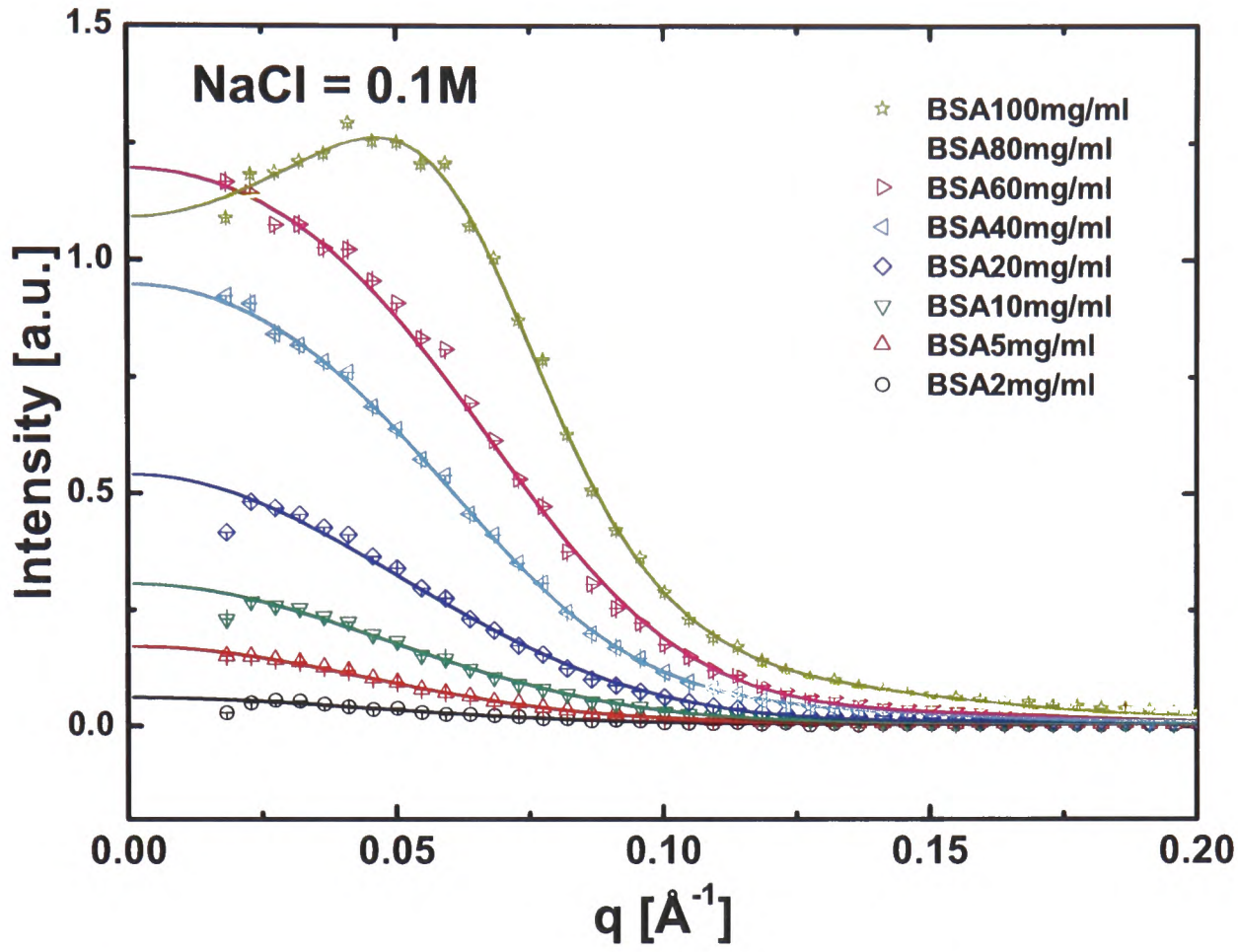
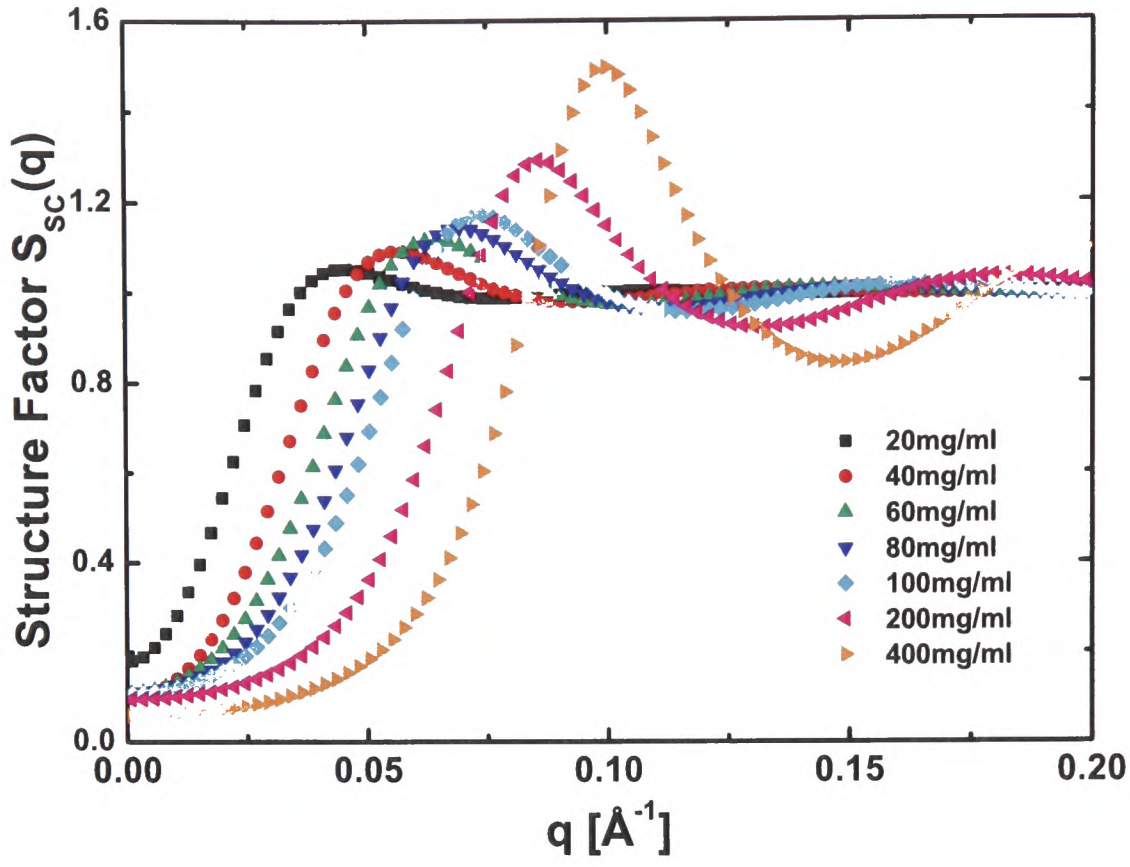
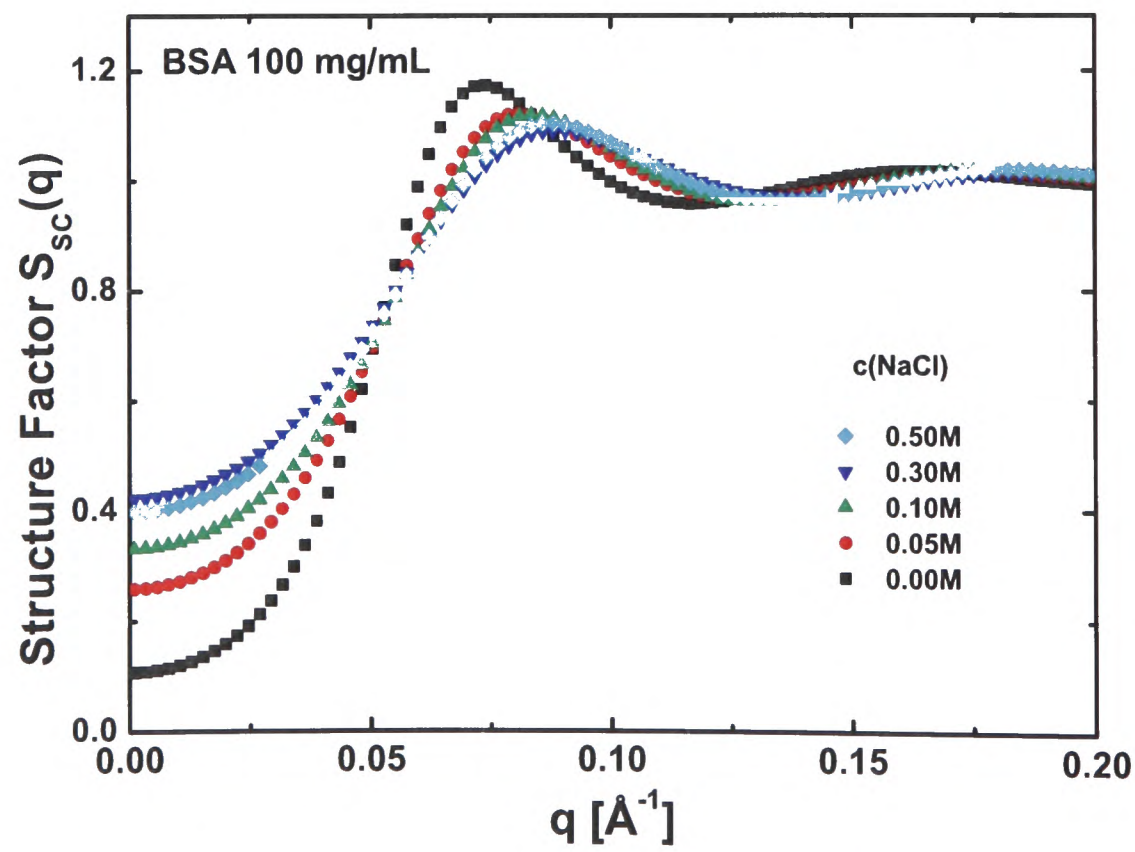


Figure 6.4.: Scattered intensity and theoretical fit by an ellipsoidal form factor and screened Coulomb potential model (E+SC) for a wide range of protein concentrations at a lower ionic strength. For I = 0.1 M, the data of BSA (2-20 mg/mL) were fitted using an ellipsoidal form factor only. Only every 10th data point is shown for clarity. The error bar is estimated to be smaller than the size of the marker.

The effective structure factors, $S_{SC}(q)$, calculated from the fitting parameters are plotted in **Figure 6.5**. **Figure 6.5a** presents the evolution of $S_{SC}(q)$ with protein concentration with no added salt. The structure factor at q = 0 is equal to the normalised osmotic compressibility. A screened Coulombic structure factor of $S_{SC}(0) < 1$ indicates the dominance of the repulsive interaction, while the decrease of $S_{SC}(0)$ with protein concentration suggests the increase of a repulsive force. The first peak of $S_{SC}(q)$ represents the correlation between a pair of protein molecules in the solution. The peak position shifts to higher q values, suggesting a decrease in the correlation distance with increasing protein concentration. **Figure 6.5b** presents the evolution of $S_{SC}(q)$ for BSA (100 mg/mL) with ionic strength. $S_{SC}(0)$ increases with increasing ionic strength, and the first peak becomes broad and shifts



(a)



(b)

Figure 6.5.: Structure factor, $S_{SC}(q)$ (screened Coulomb potential), calculated from **Figures 6.2-6.4** as a function of protein concentration (a) and ionic strength (b).

its position to a higher q value. Therefore, an increase in ionic strength decreases the repulsive force and weakens the correlation between protein molecules in solution.

Table 6.1.: Fitting parameters for an ellipsoidal form factor and a screened Coulomb potential model (E+SC) for a BSA solution with low ionic strength. (The errors of the fitting parameters pertaining to the fitting procedure are better than 1%, but the systematical errors, including sample preparation, raw data correction, and calibration, are estimated to <10%. The same condition applies to **Tables 6.2** and **6.3**)

c(BSA)	c(NaCl)	ϕ [%]	ϕ [%]		ionic strength	
$[mg/mL]$	$[M]$	(UV-vis)	(fitted)	charge	$[mM]$	κ_D^{-1} $[nm]$
20	0	1.38	1.45	10	0.91	0.96
40	0	2.97	3.76	10	1.4	0.77
60	0	4.65	5.93	11	1.5	0.75
80	0	6.13	7.98	12	3.0	0.53
100	0	7.55	10.0	13	5.8	0.37
	0.05		9.81	14	44.6	0.14
	0.1		9.42	23	161	0.072
	0.3		8.87	21	285	0.054
	0.5		9.00	36	506	0.041
200	0	14.5	16.9	18	32	0.16
300	0	19.2	20.2	17	38	0.15
400	0	23.2	29.4	9	9.8	0.29
500	0	27.4	32.8	7	3.5	0.49

The temperature, T (293 K), the dielectric constant of water ($\epsilon = 80.1$), and the form factor dimensions were fixed during the fitting procedure, and the variables, ionic strength (I), surface charge (z), and volume fraction (ϕ), were used as fitting parameters. The fit parameters are summarised in **Table 6.1**. It was found found that the volume fraction is systematically higher than the calculated value. Chen and co-workers studied BSA solutions by small-angle neutron scattering (SANS) [56,57], and they fitted their data by assuming a prolate ellipsoid with a/b = 3.5, combined with the structure factor proposed by Hayter and Penfold [51,52]. Although the fits were satisfactory, they found that the measured volume fraction is always smaller than the true values. It is interesting to note that, when the prolate ellipsoid form factor is used to fit the data, in this work, the fitted volume fractions are smaller than the calculated value. Therefore, it is believed that this discrepancy is due to the fact that neither the prolate nor the oblate ellipsoid can perfectly describe the shape of BSA in solution.

For the solutions with no added salt and c $\leq$ 100 mg/mL, the fitted ionic strength is less than 0.005 M, as expected. The surface charge ranges from 10 to 13. According to the proton titration result [59] and chloride anion binding data of Scatchard et al. [60], the BSA molecule in a pH = 7.0 solution, and without added salt, has a negative charge value of around 10; when 0.3 M LiCl is added, the charge increases to 20. The results of the fit to the present data for c = 100 mg/mL with increasing ionic strength are also presented in **Table 6.1**. The surface charge increased with ionic strength, as is expected due to the binding of chloride anions [60].

6.4. Moderate Ionic Strength, I = 0.3 and 0.5 M

With increasing ionic strength, due to screening, both the range and the strength of the interaction are decreased. At I = 0.3 or 0.5 M, the ionic strength is so high that almost all electrostatic interactions are screened. Although the experimental scattering intensity at protein concentrations of less than 40 mg/mL can still be satisfactorily fitted by the form factor only, it fails to fit the data with higher protein concentrations. When using a hard sphere structure factor, the fit is reasonably good, as shown in **Figure 6.6**, and the fitted volume fraction is also higher, as summarised in **Table 6.2**. The interaction potential seems to depend strongly on the protein concentration. For example, at c = 100 mg/mL and I = 0.3 and 0.5 M, the data can also be fitted by E+SC, as shown in **Table 6.1**. The repulsive potential at a high protein concentration may be due to the binding of anions. Nossal et al. [57] studied the BSA in an unbuffered solution with 0.2 M NaCl, and they found that a Yukawa form of the potential could be used to fit the experimental data. However, the obtained surface charge was unrealistically high (up to 100).

Table 6.2.: Fitting parameters from an ellipsoidal form factor and hard-sphere model (E+HS) for protein solutions with moderate ionic strength.

c(BSA) [mg/ml]	c(NaCl) [M]	ϕ [%] (UV-vis)	ϕ [%] fitted ϕ [%]
40	0.3	2.97	2.94
60	0.3	4.65	5.70
80	0.5	6.13	8.37
100	0.5	7.55	10.1

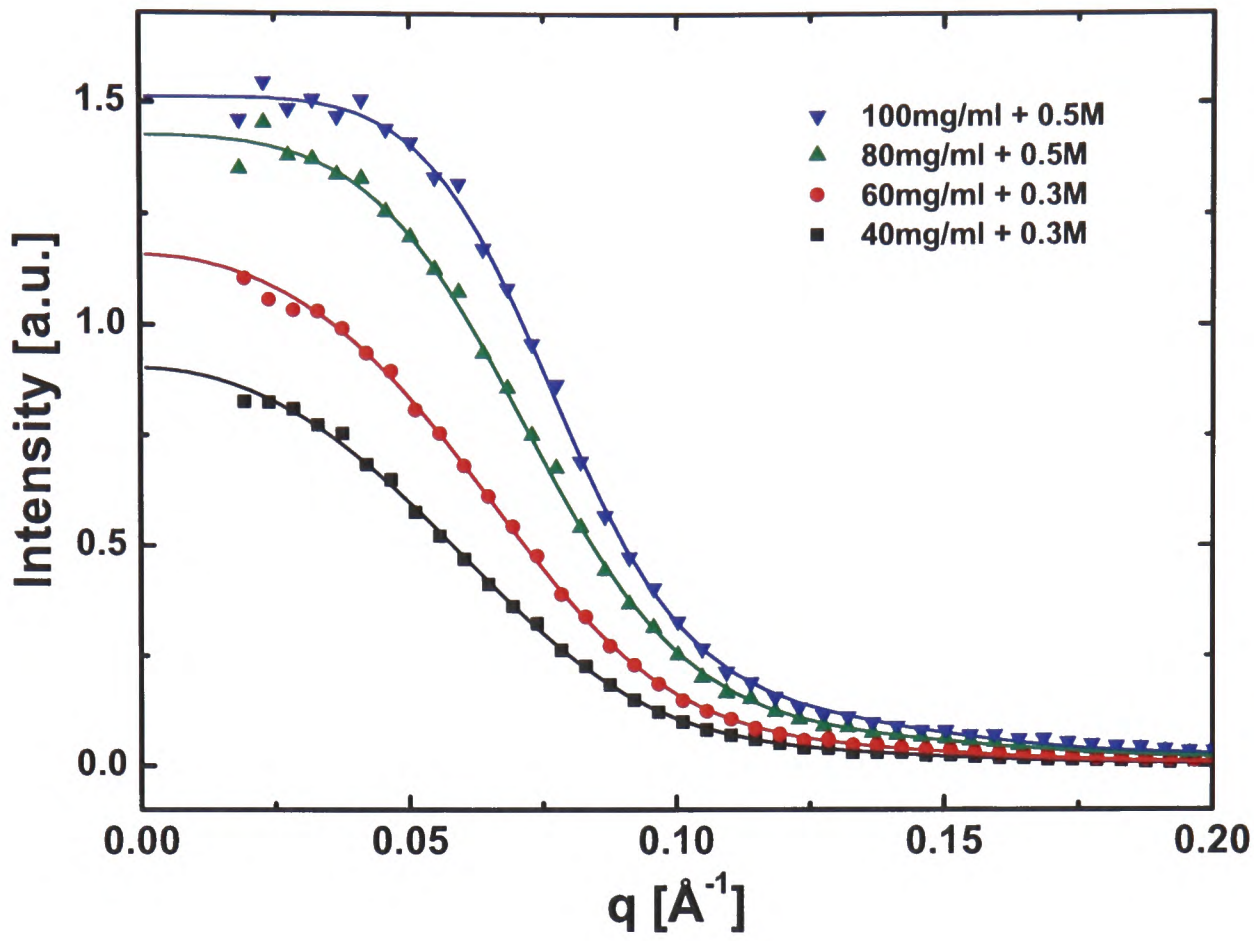


Figure 6.6.: Scattered intensity and model fit from an ellipsoidal form factor and hard-sphere model (E+HS) at medium ionic strengths, 0.3 and 0.5 M. Only every 10th data point is shown for clarity.

6.5. High Ionic Strength, I > 0.5 M, Data Fit by the E+SW Model

Graphs (a) and (b) of **Figure 6.7** show the data at a very high ionic strength, I = 1.0 and 2.0 M, respectively. Similar results were observed for I = 1.5 M (data not shown). The increase of the low q-range scattering intensity indicates the presence of an attractive potential. **Figure 6.7c** indicates that the forward intensity, I(0), decreases with ionic strength. The data for low protein concentration (c < 10 mg/mL) were fitted by the form factor only. The attractive interaction dominated in other samples and the data can be fitted well by combining the form factor with a square-well structure factor. The fit parameters are given in **Table 6.3**. In all of the fits, positive well depth values were obtained, which indicated the presence of an attractive interaction. The strength of the attraction decreased with increasing protein concentration, from 1.5 to 0.04 k_BT. At the same time, the well width

increased with protein concentration from 1.6 to 2.5, implying that this is a medium to long-range interaction.

Table 6.3.: Fitting parameters from an ellipsoidal form factor and square-well potential model (E+SW) for protein solutions with a high ionic strength, I $\geq$ 1.0 M.

c(BSA) [mg/mL]	c(NaCl) [M]	ϕ [%]	well depth [k_BT]	well width δ
10	1.0	0.708	1.240	1.83
	1.5		1.500	1.65
	2.0		1.500	1.66
20	1.0	1.51	0.462	1.85
	1.5		0.691	1.57
	2.0		0.996	1.59
40	1.0	2.97	0.199	1.94
	1.5		0.259	1.80
	2.0		0.305	1.82
60	1.0	4.65	0.079	2.20
	1.5		0.135	2.06
	2.0		0.105	2.05
80	1.0	6.13	0.047	2.45
	1.5		0.052	2.34
	2.0		0.065	2.21
100	1.0	7.55	0.041	2.43
	1.5		0.050	2.34
	2.0		0.070	2.22

Figure 6.8 shows the effective structure factor, $S_{SW}(q)$, calculated from the fitting parameters. The evolution of $S_{SW}(q)$ as a function of protein concentration (**Figure 6.8a**) and ionic strength (**Figure 6.8b**) is quite different than that of $S_{SC}(q)$ (**Figure 6.5**). With increasing protein concentration, $S_{SW}(0)$ decreases. Once the attractive potential dominates, an increase in the ionic strength only slightly affects $S_{SW}(q)$ (i.e., $S_{SW}(0)$ increases only slowly with I). It is worth noting that the square-well model contains both a repulsive (hard-sphere potential) and an attractive part in the potential (**Equation 3.60**). The contribution to the total structure factor from the hard-sphere potential is presented in **Figure 6.8c**, which shows a strong volume dependence in the low q range. Therefore, the decrease of $S_{SW}(0)$ with increasing protein concentration is mainly due to the excluded-volume effect. Other potential models, such as a sticky hard-sphere model with the Percus-Yevick (PY) closure, have also been tested (data not shown). The sticky hard-sphere

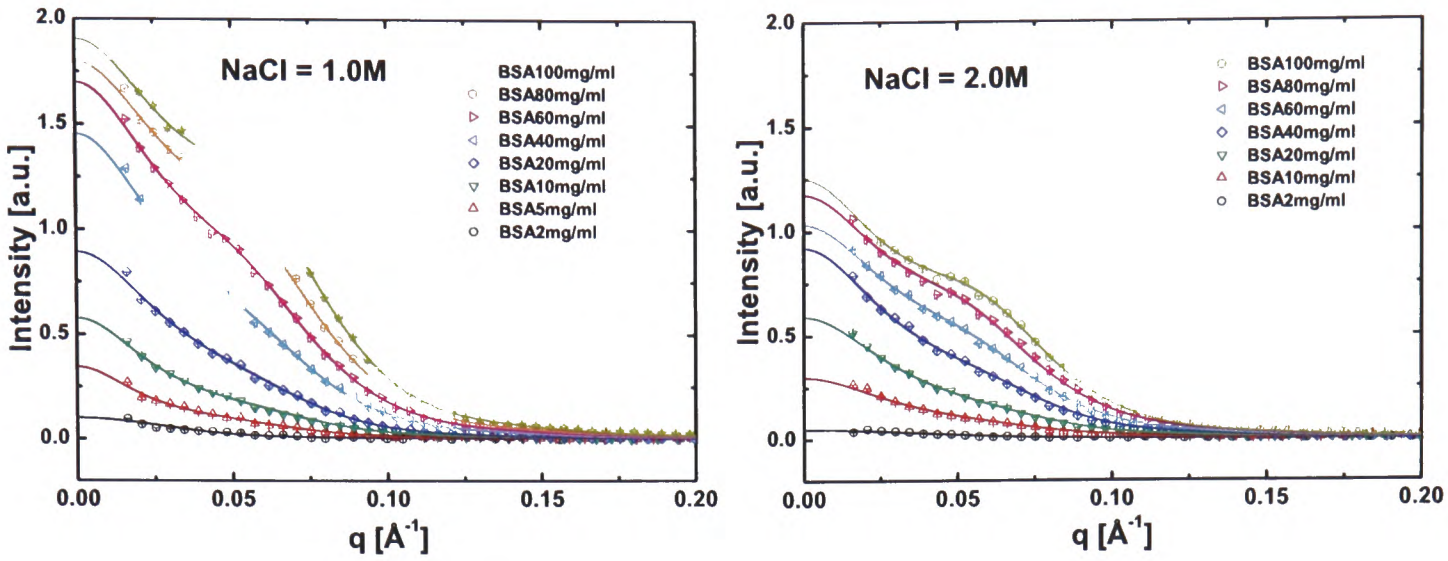
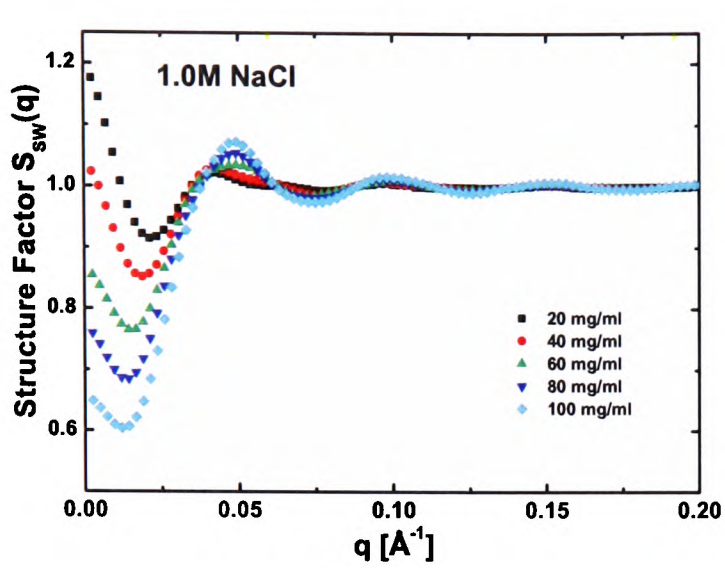
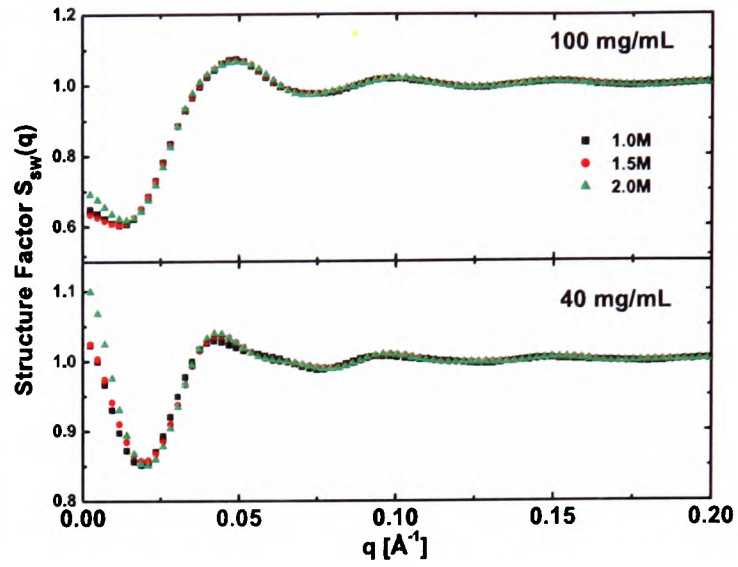


Figure 6.7.: Scattered intensity and theoretical fit from an ellipsoidal form factor and square-well model (E+SW) for protein solutions at high ionic strength. (a) I = 1.0 M, the data of very low protein concentrations (2 and 5 mg/mL) were fitted using an ellipsoidal form factor only; (b) I = 2.0 M, the data of 2 mg/mL were fitted using an ellipsoidal form factor only; and (c) c = 100 mg/mL with different ionic strengths. Only every 10th data point is shown for clarity.

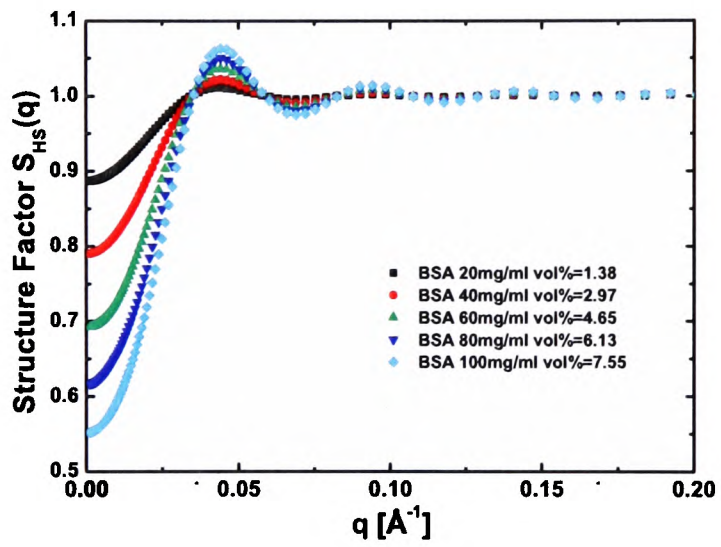
(SHS) structure describes a narrow, attractive square-well potential [61, 62]. The mathematics behind the SHS structure factor (the PY closure) is much more appropriate for an attractive potential. However, the fitting parameters were unrealistic. Therefore, there may be additional effects such as the formation of a small amount of aggregation or clustering or other interactions involved, as discussed below. In this case, a more complex potential may be needed, such as the two- Yukawa potential model used by Liu et al., in order to simulate a mixed potential [63]. However,



(a)



(b)



(c)

Figure 6.8.: Calculated structure factor, $S_{SW}(q)$, as a function of protein concentration (a) and ionic strength (b). Graph (c) presents the contribution of the hard-sphere effect to the overall structure factor, $S_{SW}(q)$, as a function of protein concentration.

these refinements are beyond the scope of these experiments, the goal of which was to obtain an interaction phase diagram, such as **Figure 6.9**.

According to Kuehner et al. [64], the attractive interaction at a high salt concentration, caused by the excluded-volume effect of ions, gives rise to a strong (several k_BT), short-range (a few Å) attractive potential. However, in the present results, although the attractive interaction dominates the overall interaction potential between proteins, we find that this potential is a rather weak ($<1k_BT$), long-range potential, extending up to several tens of Å, that can be satisfactorily described by a square-well structure factor (**Table 6.3**). On the other hand, an overall attractive

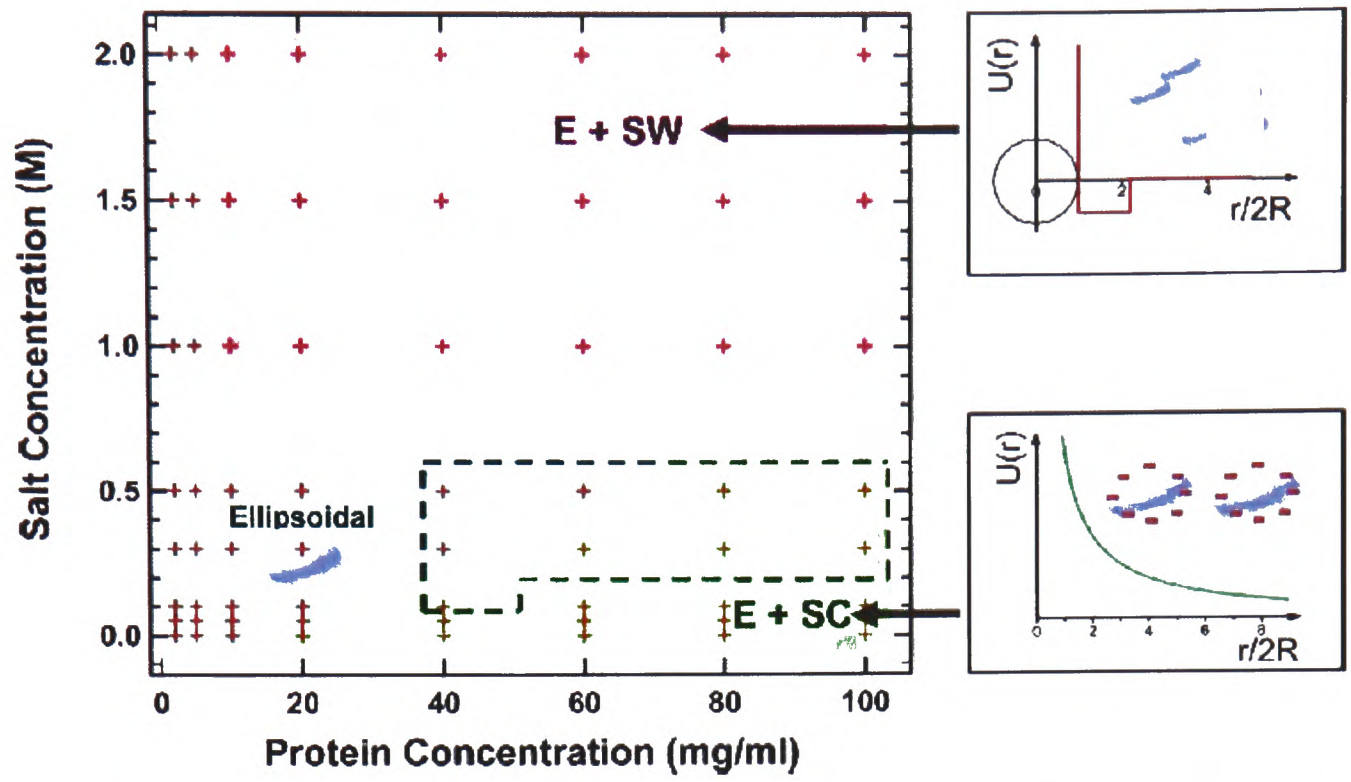


Figure 6.9.: Approximate phase diagram of the interaction as a function of protein concentration and ionic strength, based on the model described in **Section 3.3**. Note that the boundaries are, of course, not thought to be sharp. In the map, "Ellipsoidal" means the data were fitted by a form factor only. E+SC: data fitting by an ellipsoidal form factor combined with a screened Coulombic structure factor. E+SW: ellipsoidal form factor combined with square-well structure factor.

interaction potential will lead to aggregation or gelation. Yet, for all of the solutions investigated in this work, no matter how high the ionic strength, no aggregation or gelation was observed visually. Thus, it is believed that there must be a short-range, repulsive potential dominating when proteins are very close to each other. The hydration force may be the most likely source of a short-range, repulsive potential [65]. Arakawa and Timasheff [66] studied the preferential interactions of BSA in a concentrated salt solution, and they found that proteins are preferentially hydrated at a high concentration of NaCl.

The results presented above indicate that, in order to fully understand the protein-protein interaction in solution, the interaction between a protein and salt has to be taken into account. It has been shown that up to a moderate salt concentration ($I \sim 0.1$-0.3 M), the neutralisation of charges on the protein is dominant, which leads to a "salting in" effect. This is in good agreement with the observation that chloride anions prefer to bind on the surface of a protein and increase the surface charges, as shown in **Table 6.1**. At a high salt concentration, the protein-salt interaction is dominated by the unfavourable interaction between the salt ions and the hydrophobic residues of the protein, producing a "salting out" effect. Depend-

ing on the hydration property of the ions, a kosmotrope (strongly hydrated ion) can stabilise proteins at a high concentration, but chaotropes (weakly hydrated ion) at high concentrations destabilise proteins due to the direct interactions with the protein [67, 68]. Sodium chloride is a kosmotrope [68], which tends to stabilise the protein at a high salt concentration. Combined with the hydration effect, which results in a short-range, repulsive interaction between a pair of proteins, it is reasonable that the overall weak and long-ranged attraction does not lead to the aggregation of proteins.

6.6. Interaction Phase Diagram

An interaction phase diagram showing the complete set of data over a wide range of protein concentrations and ionic strengths is given in **Figure 6.9**. From our fitting results, the solution phase behaviour can be divided into three regions based on the protein-protein interaction. At low protein concentrations, combined with the screening effect of adding salt, the solutions are approaching ideal behaviour, that is, there are no correlations between protein molecules. The scattering intensity can be successfully fitted using an oblate ellipsoid form factor. With increasing protein concentration, while keeping the ionic strength low, the screened Coulomb repulsive interaction dominates the overall interaction between protein molecules. The intensity spectra can be fitted satisfactorily by taking into account both the form factor and an interference structure factor, $\bar{S}(q)$. The calculation of $\bar{S}(q)$ is based on the interaction potential between charged colloidal particles consisting of a hard sphere plus a screened Coulomb potential. At very high salt concentrations, $I \geq 1.0$ M, the interaction potential between protein molecules is dominated by an attractive potential. The data can be fitted using a form factor plus a square-well structure factor. However, in contrast to the strong, short-range potential predicted from the depletion effect under a high salt concentration, our results show a weak and long-range, attractive potential, which strongly depends on the protein concentration.

It should be noted that the boundaries between the three regions are, of course, not sharp and that the data are not directly inverted, but rather they are fitted using model potentials. While this procedure gives reasonably realistic results, it

certainly also has its limit. For example, in the area enclosed by the dashed polygon (**Figure 6.9**), the overall interaction is rather weak. In this region, none of the mentioned form and structure factors lead to satisfactory fits. It is likely that a more sophisticated structure factor is necessary to describe the interaction behaviour in this salt and protein concentration range by considering the detailed anion binding, hydration, etc.

6.7. Conclusions

From the results obtained by fitting the data and analysis of the calculated, effective structure factor, it can be seen that, with the addition of salt (increasing the ionic strength), the protein interaction potential changes smoothly from a repulsive to an attractive potential. Without salt addition or at a low ionic strength ($I < 0.3$ M), the screened Coulomb structure factor is sufficient to describe the repulsion-dominated interaction potential. At a moderate ionic strength ($I \sim 0.3$-0.5 M), the surface charges are completely screened, and the interaction can be described by a hard-sphere potential with a high volume fraction. At a high ionic strength, $I > 1.0$ M, the overall protein-protein interaction is dominated by an attractive potential. Whereas theory predicts that the depletion force induced by a high salt concentration is a strong, short-range attractive potential, it appears that it can also be a rather weak, long range, attractive potential. The stability of a concentrated protein solution under high salt concentration is explained by the hydration effect, which results in a short-range, repulsive force. Repulsive interaction, screened Coulomb structure factors, $S_{SC}(q)$, calculated from the fitting parameters, show a strong dependence on both protein concentration and ionic strength. The repulsion force increases with protein concentration and decreases with ionic strength. The evolution of square-well structure factors, $S_{SW}(q)$, indicates that the attractive force decreases with protein concentration, and it only slightly increases with ionic strength for $I > 1.0$ M.

7. Proteins at the SAM/water interface

Information about the nature of the interactions between oligo (ethylene glycol) (OEG) terminated SAMs and proteins can be derived by the analysis of the structure of the solid-liquid interface. Therefore, the protein density profile at the SAM/protein solution interface is mapped using neutron reflectivity. The fitting results reveal an oscillating behaviour of the protein density around the bulk value with decaying amplitude on a length scale of 4-5 nm (decay length). Amplitude, period and decay length are found to vary only slightly, of the order of a few percent, with temperature and ionic strength of the protein solution. The latter observation contradicts the assumption of mainly electrostatic contributions to the repulsive potential of the protein resistant monolayers. This result is in agreement with small-angle scattering experiments on a similar system of OEG monolayer protected gold nanoparticles and proteins.

7.1. SAMs on flat interfaces

7.1.1. Introduction

This section elaborates on the surface-protein interactions that may be present between OEG SAMs and proteins in solution.

When proteins in solution are facing a flat surface there are three possible scenarios of their interaction with that surface:

(i) proteins adsorb irreversibly onto the surface (they may or may not denature upon adsorption),

(ii) proteins adsorb temporarily on the surface, but can be removed, for instance by applying a shear force parallel to the surface (the energy necessary to remove an adsorbed protein is of the order of k_BT and hence an equilibrium state will be established between adsorption and desorption),

(iii) there is no adsorption at all and the proteins remain in solution.

The mechanisms leading to adsorption (i) have been discussed in **Section 2.3.2**. The second case of reversible adsorption is very difficult to quantify and to distinguish from case (iii). For the case where no adsorption occurs, some repulsive interaction has to be assumed, since it is competing against the omnipresent attractive (van der Waals and hydrophobic) interactions between protein and substrate. This repulsive interaction can be of electrostatic, entropic or energetic nature, or a mixture of these. Electrostatic and entropic interactions are fundamentally different, the former being of long range, while the latter is roughly of the order of the diameters of the objects involved. Energetic contributions could arise from the change in free energy due to the dislocation of tightly bound water molecules during the adsorption process. Furthermore, the effective range of the electrostatic interaction depends on the charges present, which have a screening effect. Thus, the strongest interaction is expected when there are no charges in the solution. Entropic forces are more complex and depend strongly on the specific details of the system, such as geometry and chemical potentials, and it is difficult to formulate a generic description. The protein resistance of poly(ethylene glycol) protected surfaces is thought to be purely entropic/enthalpic in origin [69,70] and for OEG coated surfaces the presence of electrostatic forces has been suggested based on AFM experiments [71, 72]. The assumption of electrostatic repulsive forces between proteins and OEG terminated surfaces has two major consequences: the electrostatic potential will establish a characteristic density distribution function of the proteins in solution, and this function will strongly depend on the ionic strength of the solution. The density function and its range have been calculated by D. Schwendel [73] and will be described briefly in the following paragraph. Based on the measurements of Feldman et al. [71] the repulsive force can be described as an exponential function

$$F(z) = A \exp(-z/z_0), \tag{7.1}$$

where $A = 0.8\ nN$ is the maximum force at the surface and $z_0 = 18.67\ nm$ is its decay constant, as determined experimentally by Feldman et al. [71]. The repulsive force creates a protein flow away from the surface, which is balanced by diffusion towards the surface, along the concentration gradient. After consideration of viscos-

ity, particle density and diffusion coefficient, the following differential equation has to be solved for the equilibrium case:

$$\frac{dn(z)}{dz} = \frac{A}{6\pi\eta r D} \cdot n(z) \cdot \exp(-z/z_0) \tag{7.2}$$

Here, $n(z)$ denotes the protein number density at distance z from the surface, r is the protein radius, D the diffusion coefficient and η is STOKES' friction coefficient. This yields

$$n(z) = n_\infty \exp(-Bz_0 \exp(-z/z_0)) \tag{7.3}$$

for the protein concentration as a function of distance from the interface. n_∞ is the bulk concentration in the solution and $B = \frac{A}{6\pi\eta r D}$. The calculated value for B for a

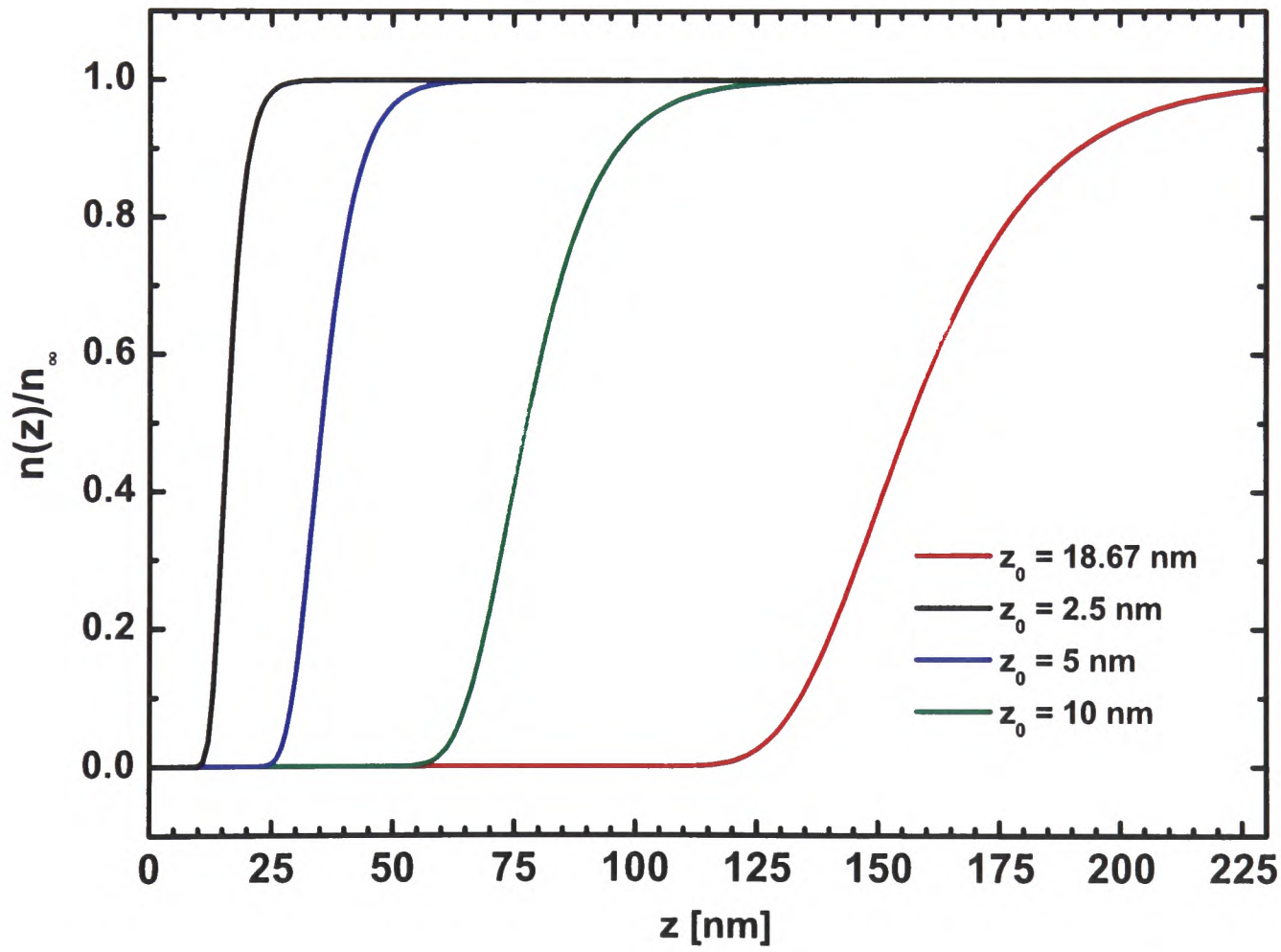


Figure 7.1.: Calculated protein density profiles (normalised to bulk density) for an EG3OMe terminated surface in contact with a 15 wt % BSA solution based on the force-distance measurements of Feldman et al. [71]. The value of z_0=18.67 nm is directly extracted from the AFM measurements. Three other decay constants are shown for comparison.

15 wt % concentrated BSA solution, as used in the present reflectivity experiments, is $B = 16.17$ Å^{-1}. The concentration profile of the protein solution can now easily be

calculated (**Figure 7.1**). The calculated profiles show that, depending on the decay constant that is assumed, there is a region of approximately 10-100 nm with almost vanishing protein concentration, followed by a steep rise to the bulk value of the concentration. The repulsive force and therefore the decay constant will be reduced if there are charges present in the solution, and the extent of the protein depleted region should vary as a function of the ionic strength. The neutron reflectivity experiments presented in this section aim to measure the density profile close to the interface of protein solutions in contact with protein resistant OEG terminated monolayers.

7.1.2. Results from neutron reflectivity: calibration of sensitivity

The system presented in **Section 5.2** comprised of the quartz substrate, Cr and Au layers, the SAM and the liquid phase, is already intricate, and its complexity is further increased when studied in contact with proteins in solution. The behaviour of the free proteins in solution as a function of protein and salt concentration is known from the studies described in **Section 6**, and the behaviour of water at an OEG terminated surface was discussed in **Section 5.2**. The experimental sensitivity was increased by contrast matching of SAM and solutions, and complementary adsorption studies served to calibrate the achievable resolution for the studied system (see paragraph below). With these prerequisites it is possible to study the structure of the solid-liquid interface between OEG SAMs and protein solutions with high accuracy.

Proteins such as BSA or lysozyme will adsorb on non-inert surfaces as discussed in **Section 5.2.3**. In order to calibrate the sensitivity limits of the system, an identical system was used, where only the protein resistant, OEG terminated SAM was replaced by a non-resistant, alkanethiol (HS-$(CD_2)_{17}$-CD_3) SAM of similar thickness. The amount of adsorbed protein is known from other studies, such as Silin et al. [26], where the volume fraction of adsorbed BSA on a CH_3 terminated alkanethiol SAM is about 0.23 of a monolayer (~80 ng/cm^2) and for lysozyme approximately 0.26 of a monolayer (~100 ng/cm^2) [74], depending on pH (see also **Section 5.2.3**). Therefore measurements on this known system are used to determine to what extent an additional layer affects the reflectivity profile and how sensitive the subsequent fitting routines are to these subtle changes. Prior to the adsorption experiment

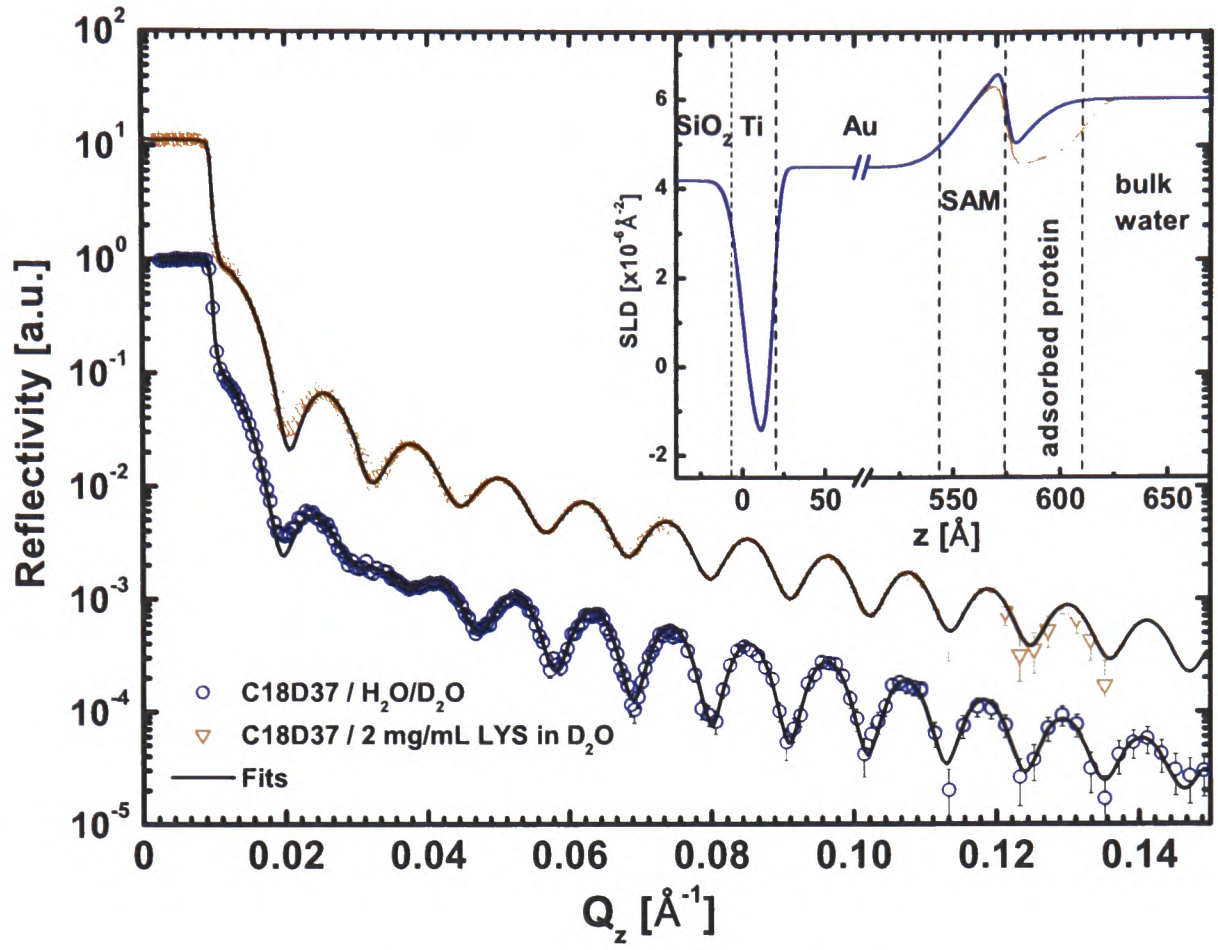


Figure 7.2.: Measured reflectivity curves and fitted real space profiles (inset) for a deuterated octadecyl mercaptan SAM in contact with an H_2O/D_2O mixture (blue circles) and in contact with a 2 mg/mL lysozyme solution with identical scattering length density (orange triangles). The fit for the lysozyme measurement shows an adsorbed layer of about 2.6 nm thickness and a volume fraction of about $\phi = 0.3$. The curves are offset vertically by a factor of 10.

with a 2 mg/mL lysozyme solution in D_2O, reflectivity data of the same sample was taken in contact with an H_2O/D_2O mixture, adjusted to match the scattering length density of the protein solution. Thereby, the two data sets can be compared immediately: in the case of no changes at the solid-liquid interface, the H_2O/D_2O and the protein data set should be identical. On the other hand, any changes in the density profile at the interface should cause changes in the measured profile. An example of such a measurement is shown in **Figure 7.2**. The fit for the measurement with the lysozyme solution reveals an adsorption layer of about 2.7 nm thickness and a scattering length density of $5.0{\times}10^{-6}$ Å^{-2}, corresponding to a volume fraction of approximately $\phi = 0.3$. The integrated area of this layer is $A = 25 \times 10^{-6}$ Å^{-1}. These values serve as a benchmark for the sensitivity of the measurement: a change of this magnitude in the density profile produces very easily discernible changes in

the reflectivity curve (at low q) and it can be extrapolated that even smaller effects, of the order of $A = 10 \times 10^{-6}$ Å^{-1} integrated area, are easily detectable.

7.1.3. Results from neutron reflectivity: density profiles and discussion

In order to avoid ambiguity for the fitted neutron reflectivity profiles, prior to each measurement with protein solutions, a measurement of the same system was performed with pure D_2O. This reference profile was fitted and subsequent data were fitted using the parameters obtained from the reference measurement for the chromium and gold layers. When the fit converged, the parameters for the metal layers were also included in the fit. The new fitted values for Cr and Au did not differ by more than ±2 Å. In **Figure 7.3** the reference measurement against pure D_2O is shown.

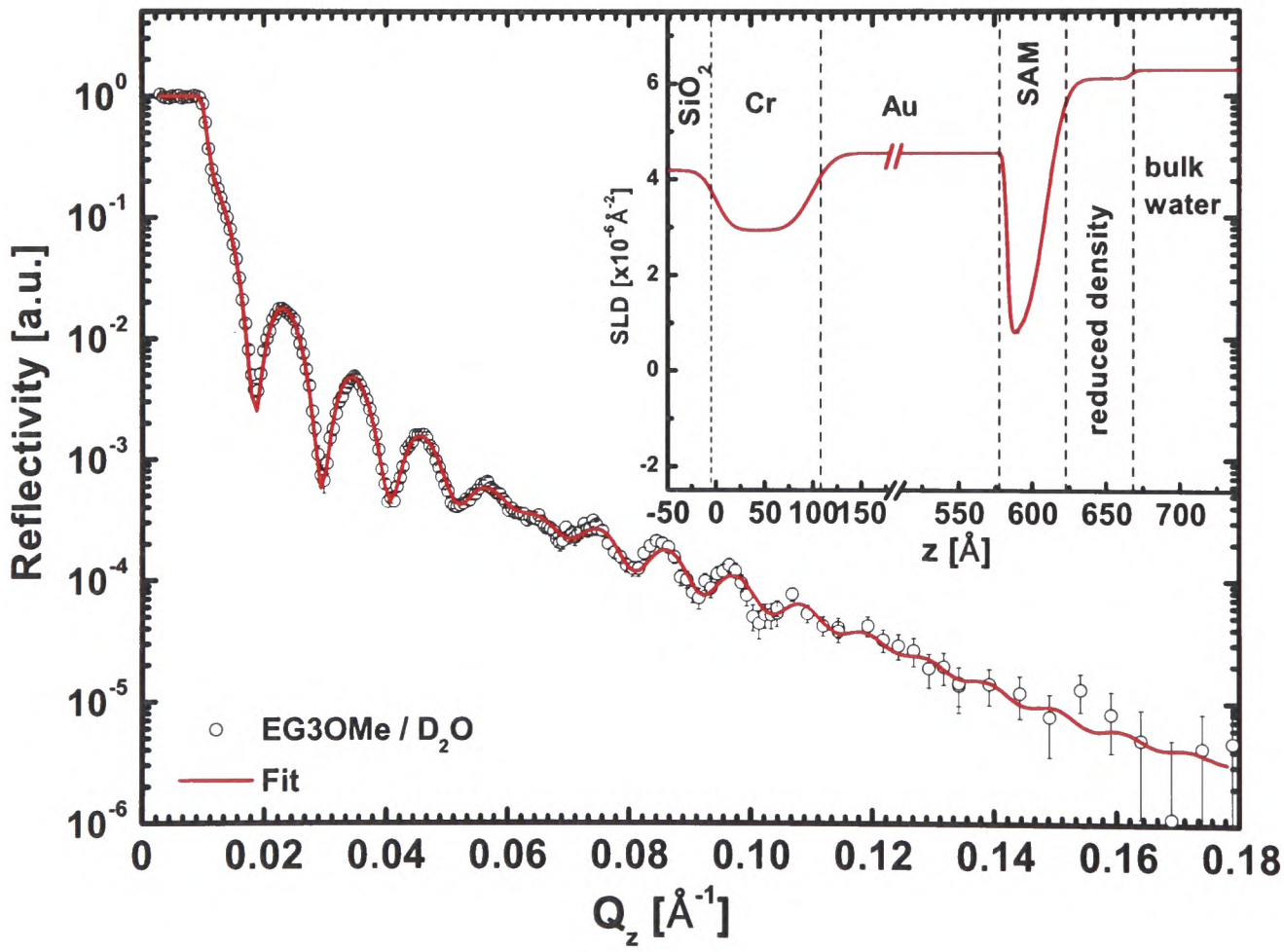


Figure 7.3.: Reflectivity data with best fit and corresponding scattering length density profile of an EG3OMe SAM in contact with pure D_2O. The real space profile shows a region of reduced water density close to the SAM.

Again, as discussed in **Section 5.2**, a region of about 5 nm with reduced water density is clearly visible. The fitted values are listed in **Table 7.1**. The subsequent

layer	d [Å]	SLD [$\times 10^{-6}$Å^{-2}]	σ [Å]
quartz	n/a	4.18	n/a
Cr	99.0	2.93	14.7
Au	482.6	4.41	18.6
SAM	29.2	1.1	10.0
reduced density layer	55.5	6.03	2.3
bulk	n/a	6.24	3.2
Hamilton: $b = 3$, $\nu = 201$; $\mathcal{R}_{3,201,0.005} = 1.035$, $\mathcal{R} = \sqrt{\chi_0^2/\chi_1^2} = 1.125$			
N$_\sigma$ test: N$_\sigma^1$=1.46, N$_\sigma^0$=4.20			

Table 7.1.: Fit parameters for the fit in **Figure 7.3** with 201 data points, including a reduced density water layer. Confidence tests favour the model with an additional layer.

measurement was preformed using a 15 wt % concentrated BSA/D_2O solution. The relatively high protein concentration was necessary for achieving a suffiently high contrast in the case of a protein depleted layer. The data were fitted using the values obtained from the pure D_2O measurement as starting parameters. Then, one and two additional layers were introduced to account for changes at the solid liquid interface. The goodness-of-fit and likelihood of the one, two and three box models were compared using HAMILTON and N$_\sigma$ tests. All datasets could be fitted most satisfactorily by using a three layer model with an oscillatory structure: adjacent to the SAM a layer with increased scattering length density is observed, followed by a region where the scattering length density is lower than that of the bulk phase. Then a layer with a more or less pronounced reduction protein density follows (with an increased scattering length density compared to the bulk value), which extends up to about 4-6 nm into the bulk solution. This characteristic behaviour is illustrated in **Figure 7.4**.

Oscillating decay model. Here, it is important to note that for a concentrated (15 wt %) aqueous protein solution, a reduced scattering length density compared to the bulk value represents a locally higher protein concentration, while a value above the bulk scattering length density is equivalent with a lower protein density. Since the obtained real space profiles suggest an oscillating behaviour of the protein density at the SAM/solution interface, a model with an analytical profile function

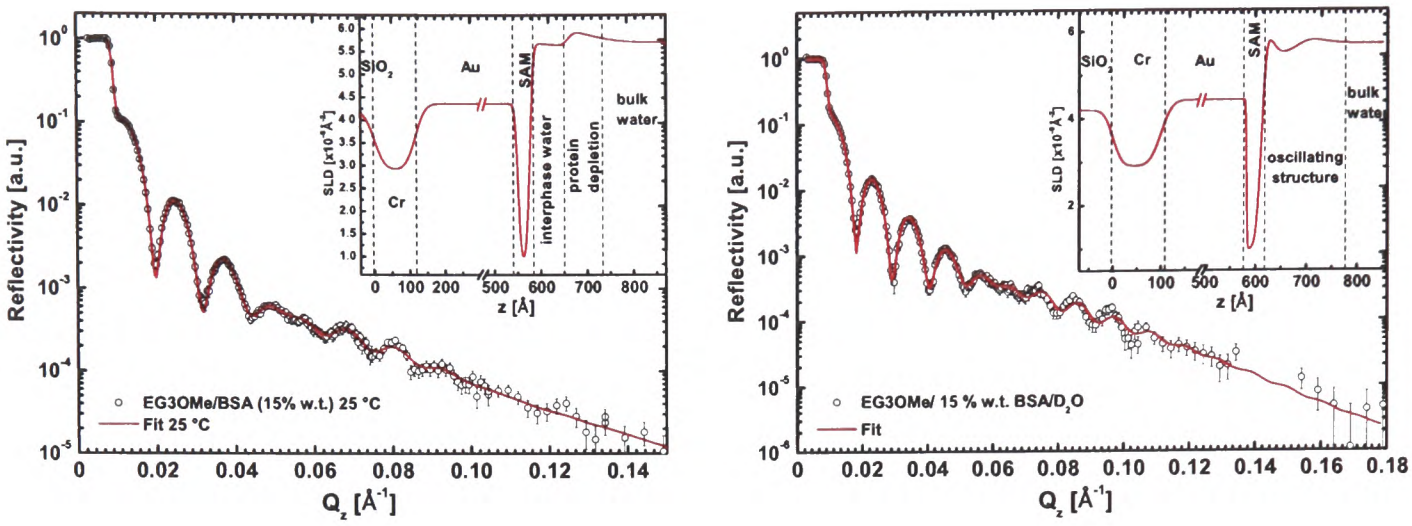


Figure 7.4.: Reflectivity data with best fit and corresponding scattering length density profiles for two different samples of an EG3OMe SAM in contact with a 15 wt % BSA/D_2O solution. The real space profile shows an oscillatory structure of the protein density profile adjacent to the SAM. For exact fitting results, see **Table 7.2**.

layer	**d [Å]**		**SLD** $[\times 10^{-6}\text{Å}^{-2}]$		σ **[Å]**	
	(a)	(b)	(a)	(b)	(a)	(b)
quartz	n/a	n/a	4.18	4.18	n/a	n/a
Cr	115.6	99.0	3.04	2.93	20.2	14.7
Au	433.9	482.6	4.47	4.41	21.2	18.6
SAM	26.0	29.0	0.85	0.96	6.7	1.3
layer 0	n/a	18.7	n/a	6.18	n/a	8.3
layer 1	80.0	53.6	5.61	5.47	5.8	12.0
depletion layer	37.7	33.1	6.10	5.90	14.7	19.8
bulk	n/a	n/a	5.69	5.71	81.0	32.9

Hamilton (a): $b = 3$, $\nu = 199$; $\mathcal{R}_{3,199,0.005} = 1.036$, $\mathcal{R} = \sqrt{\chi_1^2/\chi_2^2} = 1.189$

Hamilton (b): $b = 3$, $\nu = 197$; $\mathcal{R}_{3,197,0.005} = 1.036$, $\mathcal{R} = \sqrt{\chi_2^2/\chi_3^2} = 1.037$

N_σ test (a): N_σ^2=12.60, N_σ^1=12.66

N_σ test (b): N_σ^3=1.60, N_σ^2=2.25, N_σ^1=5.91

Table 7.2.: Fit parameters for the fits in **Figure 7.4a,b**, including an oscillating protein density away from the surface. Confidence tests strongly reject models with no or only one additional layer with a probability of 99.5%.

was employed. An oscillating sinusoidal function with damped amplitude was used to describe the scattering length density profile of the solution close to the SAM[1]:

$$SLD(z) = A \sin\left(\frac{2\pi}{\lambda} z + \phi\right) e^{-z/\xi}, \tag{7.4}$$

where A is the amplitude of the oscillation in units 10^{-6} Å^{-2}, λ its wavelength, ϕ the phase and ξ the decay constant for the damping. The roughness of the bulk layer was kept at zero, such that the resulting model has 18 parameters, which is the same number of parameters as for a two layer model. The new model with the analytical function was found to converge more reliably and the parameters (A, λ, ϕ and ξ) are better suited for the comparison of fits from different data sets. A comparison of the

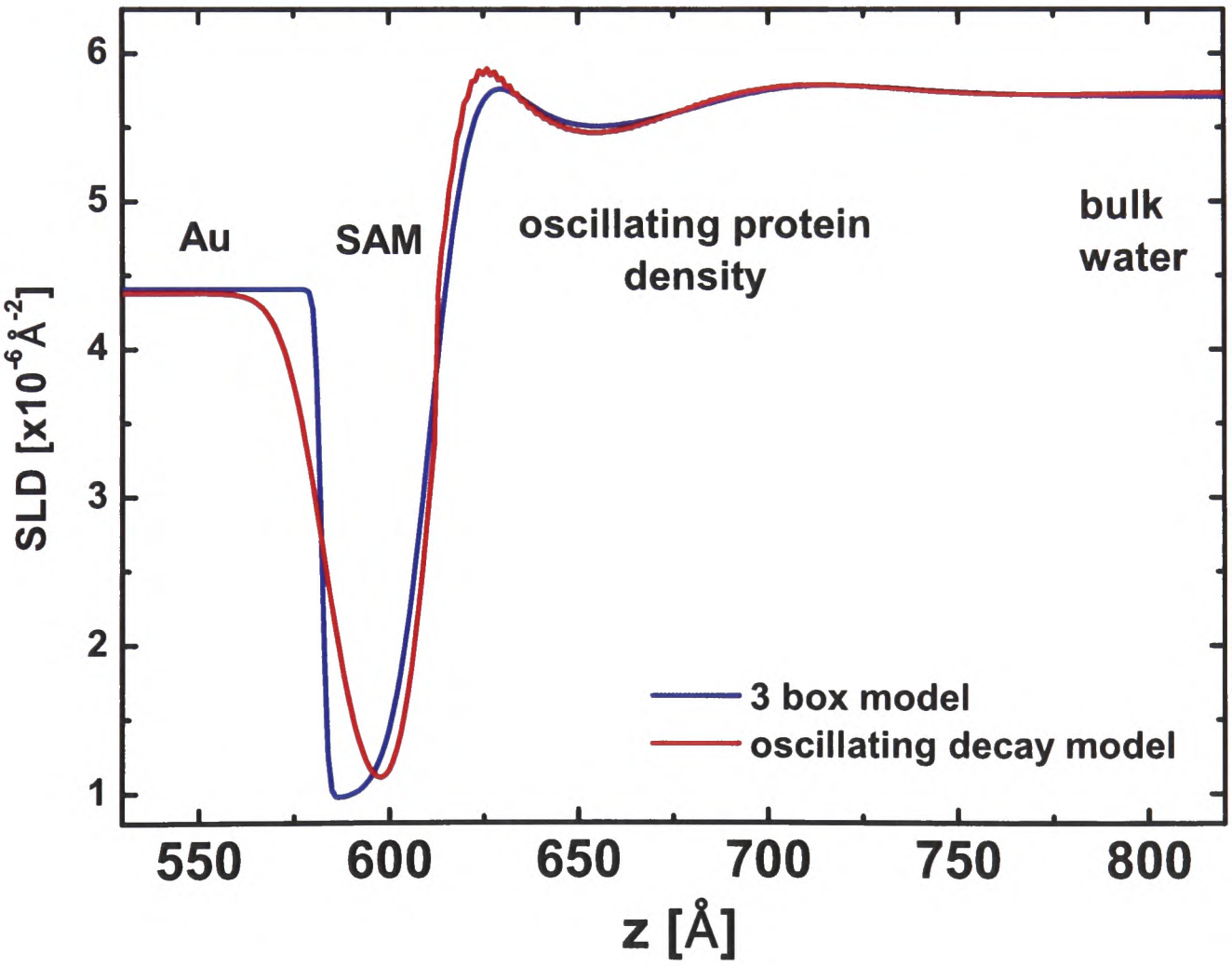


Figure 7.5.: Comparison of a 3 box fitting model with an oscillating decay model ($SLD(z) = A \sin\left(\frac{2\pi}{\lambda} z + \phi\right) e^{-\frac{z}{\xi}}$) for the data set shown in **Figure 7.4b**. In the fitting process the SAM parameters were also allowed to vary. Both models are very similar and show the oscillating structure of the protein density close to the SAM. The parameters of the analytical function are: $A = 0.92 \cdot 10^{-6}$ Å^{-2}, $\lambda = 116.8$, $\phi = 1.95$ and $\xi = 37.8$.

[1]The analytical function was split into 2 Å wide boxes with zero roughness within the Parratt32 fitting software.

oscillating decay model with a box model is presented in **Figure 7.5**. The shapes of the fitted real space profiles differ only little between the three layer model and the model with the analytical oscillating function. Furthermore, the parameters of the SAM, in particular the roughness, which were also allowed to vary during the fitting process, are more realistic than in the three layer model fit.

The fit parameters of the analytical function were determined as $A = 0.92 \cdot 10^{-6}$ Å^{-2}, $\lambda = 116.8$, $\phi = 1.95$ and $\xi = 37.8$. The oscillating protein density distribution function at the SAM/solution interface is characteristic for the behaviour of a charged hard sphere mixture at a hard wall. The region closest to the SAM has a scattering length density of around $6 \cdot 10^{-6}$ Å^{-2} and width of approximately 3 nm, which is consistent with a protein depleted region with reduced density water as discussed in **Section 5.2**. The following dip in the density profile down to $\sim 5.5 \cdot 10^{-6}$ Å^{-2} with an extent of about 30-40 Å indicates a slightly higher protein concentration compared to the bulk: a volume fraction of ~0.2 can be calculated from the scattering length densities of BSA and D_2O, whereas the bulk volume fraction is about 0.13. The next protein depletion region is less pronounced than the first one and the oscillations are damped out quickly after approximately 150-180 Å.

Concentration dependence. The oscillating nature of the protein density profile at the SAM-solution interface suggests a layering of the protein molecules induced by the presence of the hard boundary (substrate). This is characteristic for hard sphere layering near a hard wall [75, 76]. It is reasonable to assume that the oscillation period is related to the packing density of the proteins (or hard spheres). In order to confirm this assumption, further measurements with higher protein concentrations were performed. Lower concentrations than 15 wt % turned out to be problematic due to insufficient contrast. **Figure 7.6** shows a measurement of a partially deuterated EG3OMe SAM in contact with a 27 wt % BSA/D_2O/H_2O solution, that was index matched to gold. As before, the reflectivity profile can be fitted with an oscillating decay function at the SAM-solution interface. It is important to note that the period of the oscillation is reduced as a consequence of the higher protein density in solution: the average inter-particle spacing is reduced. The decay length is increased at the same time.

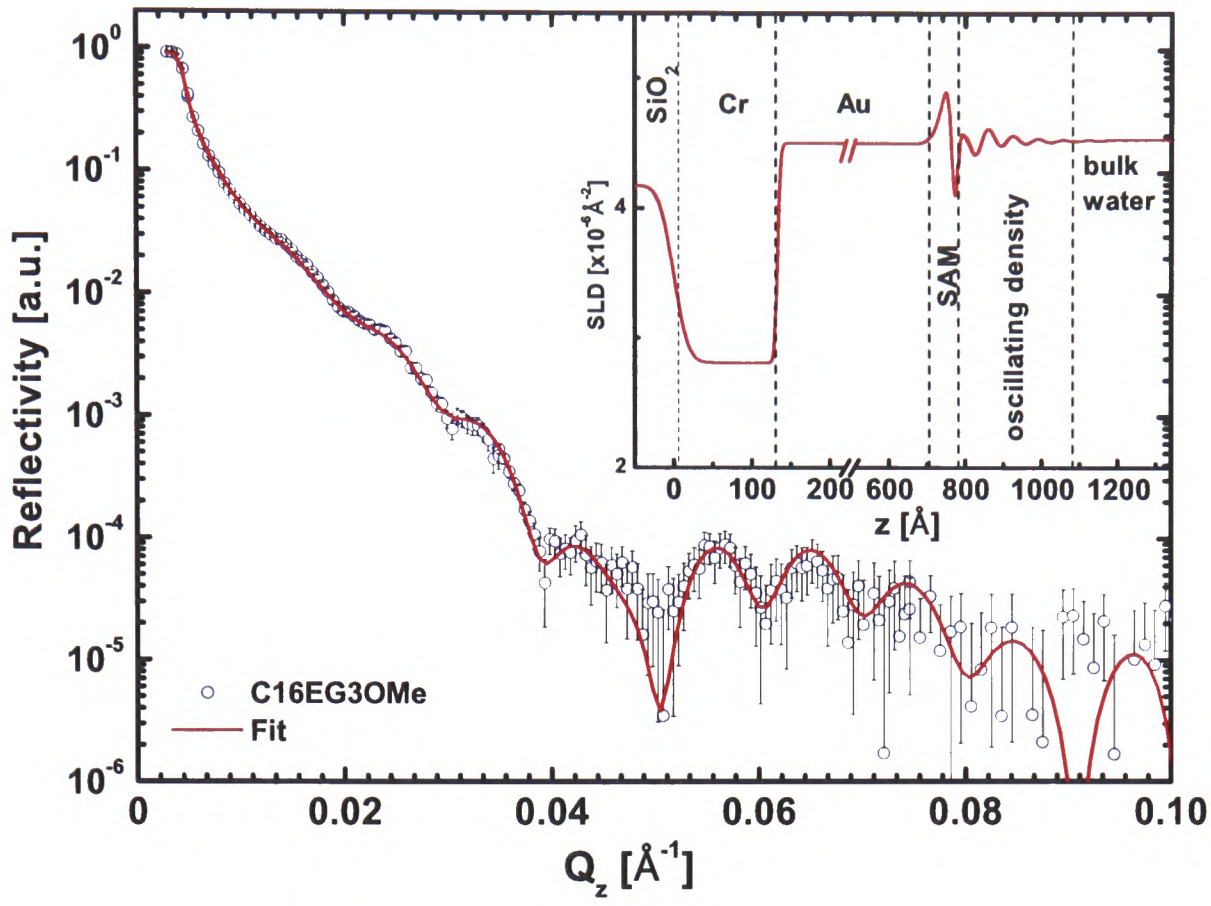


Figure 7.6.: Reflectivity curve and real space profile of a partially deuterated EG3OMe SAM in contact with a 27 wt % BSA/D_2O/H_2O solution, that was index matched to gold.

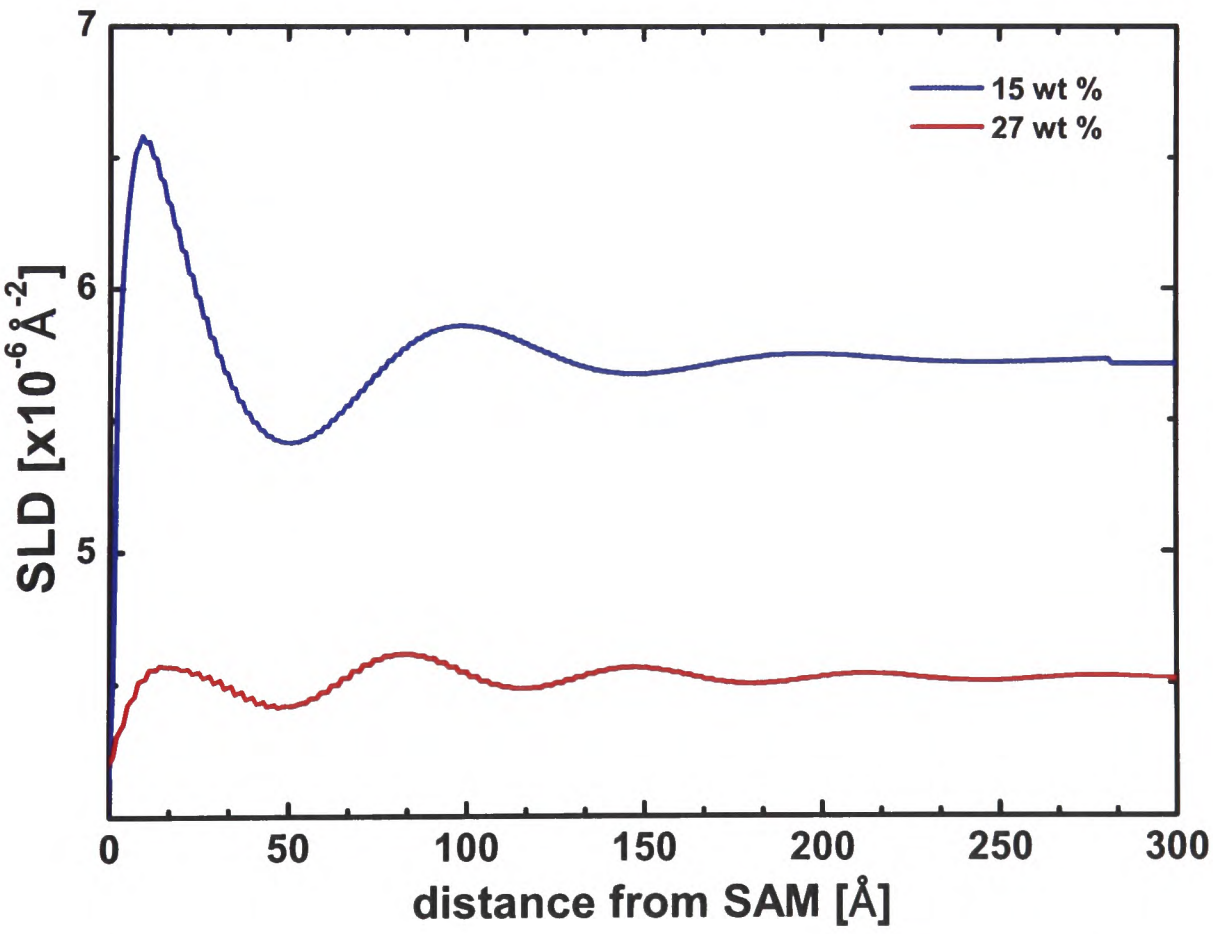


Figure 7.7.: Comparison of the oscillating protein density close to an EG3OMe SAM for a 15 (blue line) and a 27 wt % (red line) protein solution. The oscillation period is reduced at higher protein concentration.

H_2O was added to the solution for the 27 wt % sample, such that it was index matched to the scattering length density of gold. Therefore, the scattering length density difference between the protein-depleted solvent (H_2O/D_2O mixture) and the bulk solution was decreased in this case. This results in a considerably smaller amplitude compared to the 15 wt % sample, which was not index matched. A comparison of the profiles at 15 and 27 wt % is shown in **Figure 7.7**.

BSA concentration	15 wt %	27 wt %
amplitude A [$\times 10^{-6}$]	0.62	0.02
period λ [Å]	108.8	64.8
phase ϕ	2.3	2.2
decay length ξ [Å]	57.1	86.1

Table 7.3.: Parameters of the fitted oscillating decays shown in **Figure 7.7** for an EG3OMe SAM in contact with protein solutions of varying concentration.

7.1.4. Sensitivity of models

The model used to describe the protein density at the solid-liquid interface is a damped oscillating function with the following four parameters: amplitude A, period and phase of the oscillation λ and ϕ respectively, and the decay length ξ. This model was chosen because it described the profile with less parameters and yielded the best goodness-of-fit compared to box-models. However, it is a rather complex model and therefore a brief discussion of the sensitivity of the parameters is given in this section. For this purpose, by taking a typical measurement (form **Figure 7.9**), each parameter is varied stepwise, while keeping all other parameters fixed, and the resulting χ^2 values are plotted against the parameter value (**Figure 7.8**). From the plots it can be deduced that period and phase are found in a well defined minimum, whereas the amplitude and the decay length of the density oscillation have somewhat broader minima. Following these considerations the maximum uncertainty can be estimated, and it can be said that the fitted values of period λ are accurate to about ± 10 Å, the decay length to about ± 15 Å, and the amplitude to approximately $\pm 2 \times 10^{-7}$ Å^{-2}. The phase is the most accurately defined parameter due the nature

of the system: the region with lowest protein density is found at the solid interface, and that is where the oscillation begins.

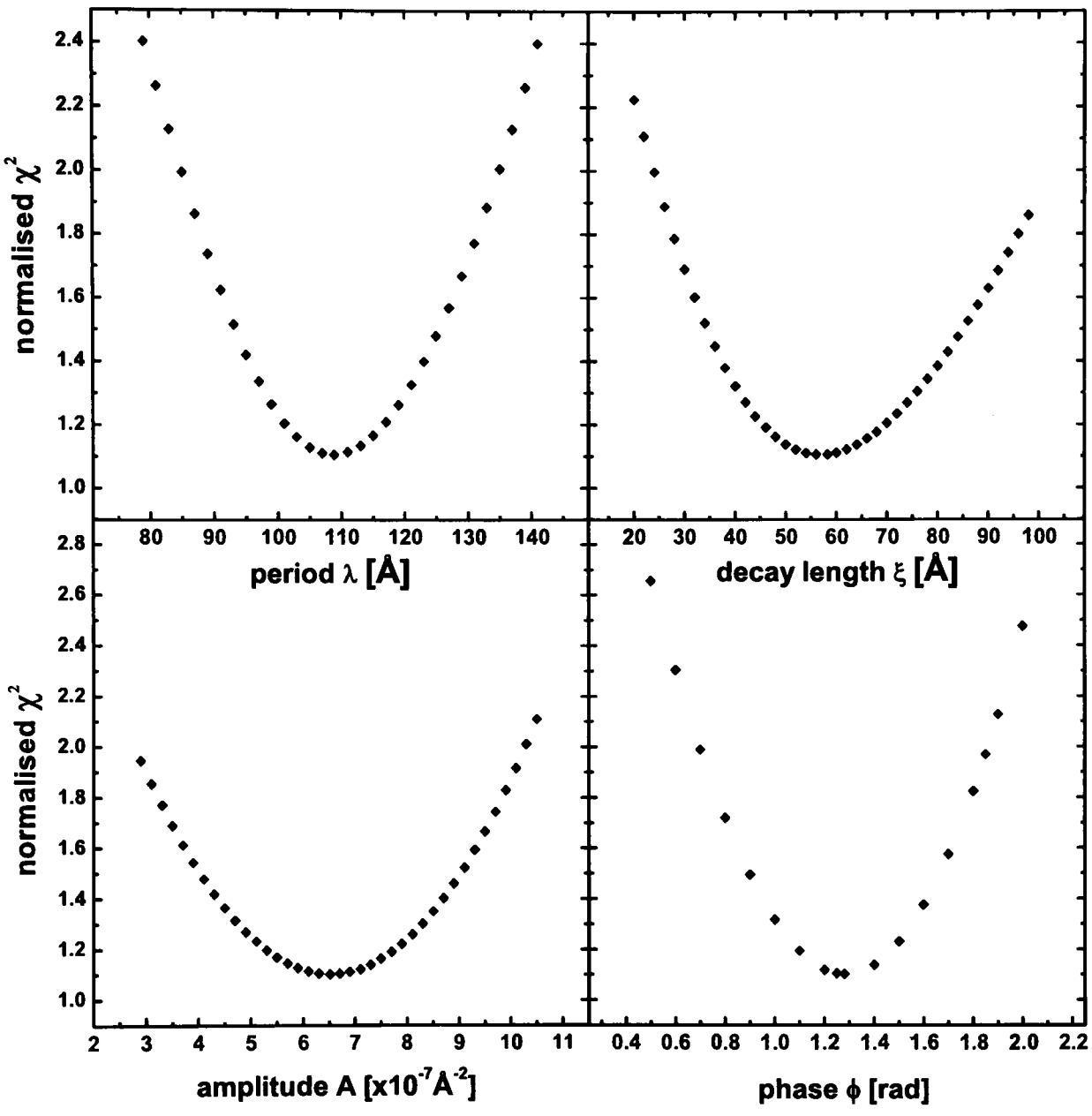


Figure 7.8.: χ^2 distribution as a function of the four parameters amplitude A, period and phase of the oscillation λ and ϕ respectively.

The errors on the fitted values can be calculated from the plots in **Figure 7.8** based on the parameter value obtained when the χ^2 increased by 10%. The fitted values for the oscillating decay parameters have then the following errors: period $\lambda = (108.8 \pm 8.0)$ Å, decay length $\xi = (58.25 \pm 13.0)$ Å, amplitude $a = (6.519 \pm 1.250) \times 10^{-7}$ Å^{-2} and the phase $\phi = (1.281 \pm 0.175)$. These values are representative for all presented measurements.

7.1.5. Salt effects

In **Section 7.1.2** it was outlined that data from AFM experiments [71] suggest that the repulsive force exerted by the OEG SAM on the dissolved proteins has electrostatic contributions. This can be concluded from the fact the measured forces scaled with the ionic strength of the solution according to DLVO[2] theory.

The results presented in this section address the issue of electrostatic forces in the OEG SAM and protein system by means of neutron reflectivity. The NaCl concentration of a 15 wt % BSA/D_2O solution was varied from 0 to 1.0 M and the corresponding reflectivity profiles were recorded. It was found that the real space protein concentration profile showed an oscillatory behaviour (as discussed in **Section 7.1.2**). The amplitude and period of the oscillations changed slightly between the two extreme concentrations (0 and 1.0 M), but a clear oscillatory behaviour still persisted at a salt concentration of 1.0 M, where the electrostatic repulsion is completely screened (see **Section 6**) and the overall protein-protein interaction is dominated by an attractive potential. Thus, these findings indicate a rather small contribution of electrostatic interactions for the studied system.

The ionic strength dependence was measured in a series of experiments using the same protein solution (15 wt % BSA in D_2O). The following concentration steps were measured: 0^3, 0.05, 0.2 and 1.0 M. For each step, the protein solution was extracted from the sample cell, the volume measured and the appropriate amount of NaCl was added. Then, after the salt had dissolved, the solution was slowly re-injected into the sample cell. The sample was re-mounted and re-aligned and the new measurement started. As before, fitting of the reflectivity data revealed the typical oscillating protein density close to the SAM. Data, fit and corresponding real space profile for the first measurement of the salt series are shown in **Figure 7.9**.

The fitting parameters for a model with a sinusoidal decay are listed in **Table 7.4**. Amplitude, period and decay constant are consistent with the previously described measurements with BSA solutions.

---

[2]The DLVO theory is named after Derjaguin, Landau, Verwey and Overbeek who developed it in the 1940s. The theory describes the force between charged surfaces interacting through a liquid medium. It combines the effects of the van der Waals attraction and the electrostatic repulsion due to the so called double-layer of counterions. The electrostatic part of the DLVO interaction is computed in the mean field approximation.

[3]The (intrinsic) ionic strength of a pure BSA solution was measured with a conductometer and corresponds to a 0.01 M NaCl solution as a consequence of dissolved amino acid residues.

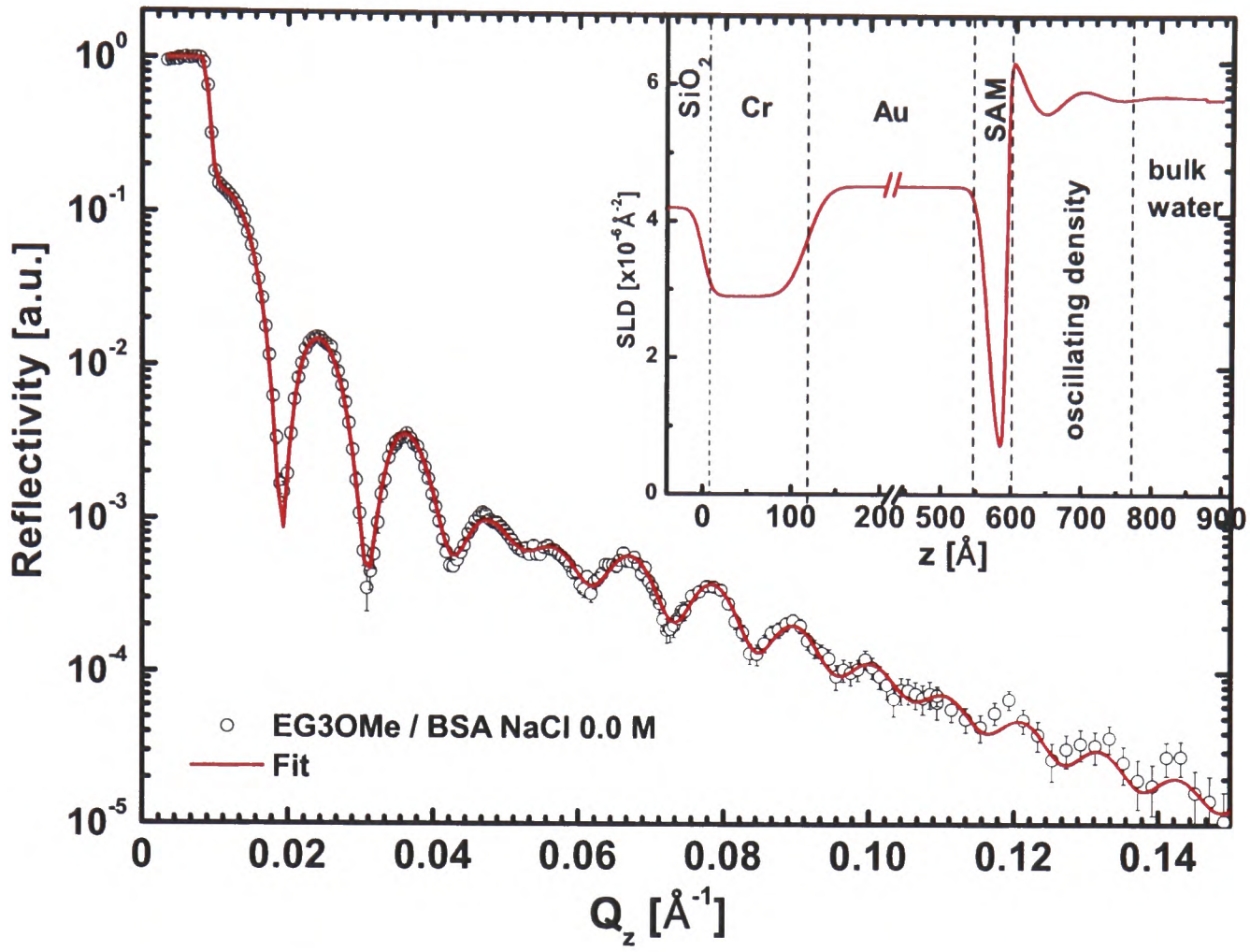


Figure 7.9.: EG3OMe SAM in contact with a 15 wt % BSA solution at room temperature with no added salt.

layer	**d [Å]**	**SLD** [$\times 10^{-6}$Å^{-2}]	σ [Å]
quartz	n/a	4.18	n/a
Cr	117.1	2.89	8.6
Au	450.0	4.5	17.6
SAM	27.1	0.4	12.1
layer 0	2.0	5.82	4.0
oscillating decay: $A = 0.62$, $\lambda = 108.8$, $\phi = 2.3$, $\xi = 57.1$			
bulk	n/a	5.77	0
Hamilton: $b = 3$, $\nu = 216$; $\mathcal{R}_{3,216,0.005} = 1.033$, $\mathcal{R} = \sqrt{\chi_1^2/\chi_{oscill}^2} = 1.345$			
N$_\sigma$ test: N$_\sigma^{oscill}$=2.04, N$_\sigma^1$=11.52			

Table 7.4.: Fit parameters for the fit in **Figure 7.9** with 216 data points: EG3OMe SAM in contact with a 15 wt % BSA solution at room temperature with no added salt.

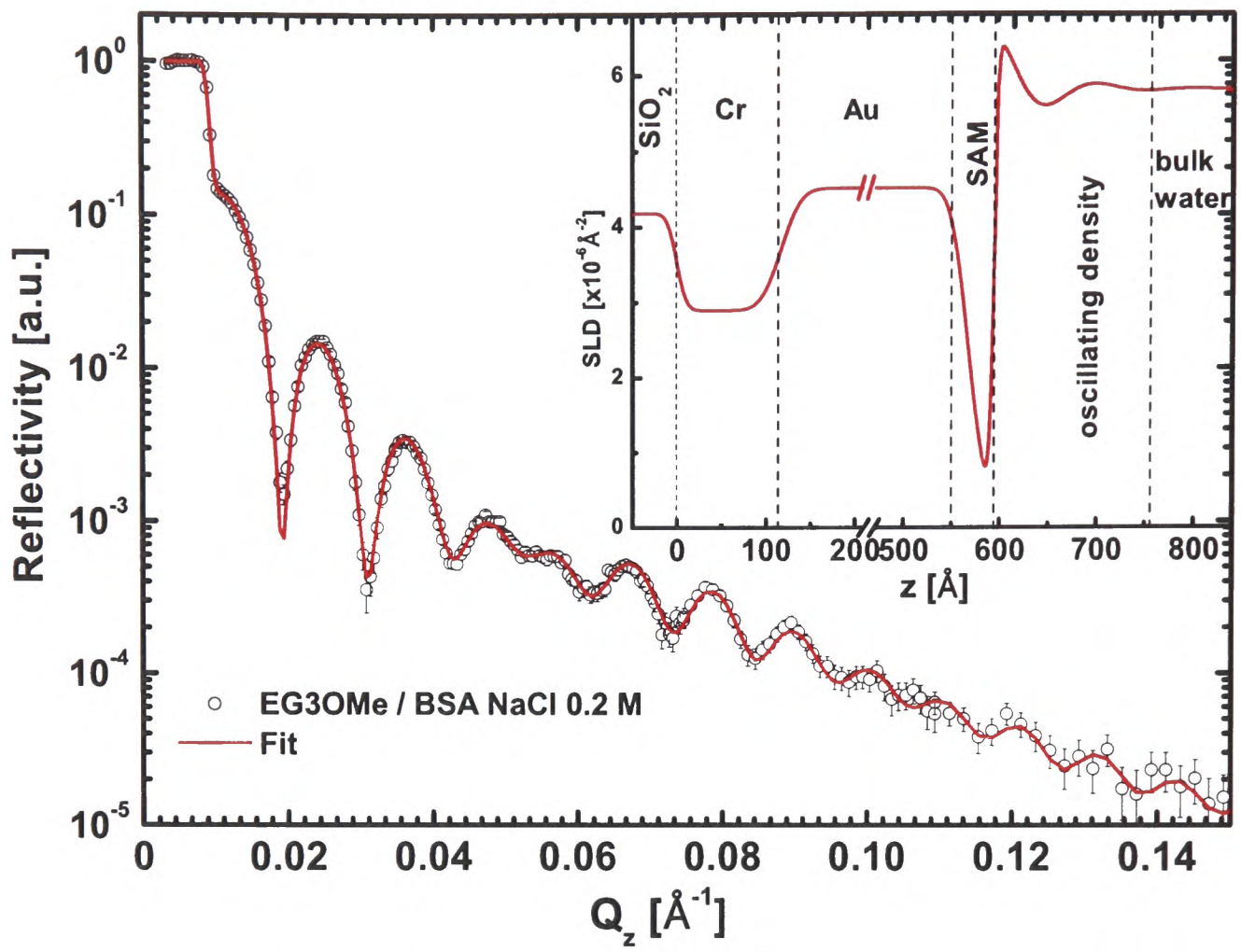


Figure 7.10.: EG3OMe SAM in contact with a 15 wt % BSA solution at room temperature in a 0.2 M NaCl solution.

layer	**d [Å]**	**SLD** [$\times 10^{-6}$Å^{-2}]	σ [Å]
quartz	n/a	4.18	n/a
Cr	117.1	2.89	8.6
Au	450.0	4.5	17.6
SAM	27.1	0.4	12.1
layer 0	3.0	5.79	3.7
oscillating decay: $A = 0.68$, $\lambda = 103.4$, $\phi = 1.28$, $\xi = 45.7$			
bulk	n/a	5.77	0
Hamilton: $b = 3$, $\nu = 224$; $\mathcal{R}_{3,224,0.005} = 1.032$, $\mathcal{R} = \sqrt{\chi_1^2/\chi_{oscill}^2} = 1.220$			
N$_\sigma$ test: N$_\sigma^{oscill}$=8.81, N$_\sigma^1$=17.5			

Table 7.5.: Fit parameters for the fit in **Figure 7.10** with 224 data points: EG3OMe SAM in contact with a 15 wt % BSA solution at room temperature in a 0.2 M NaCl solution.

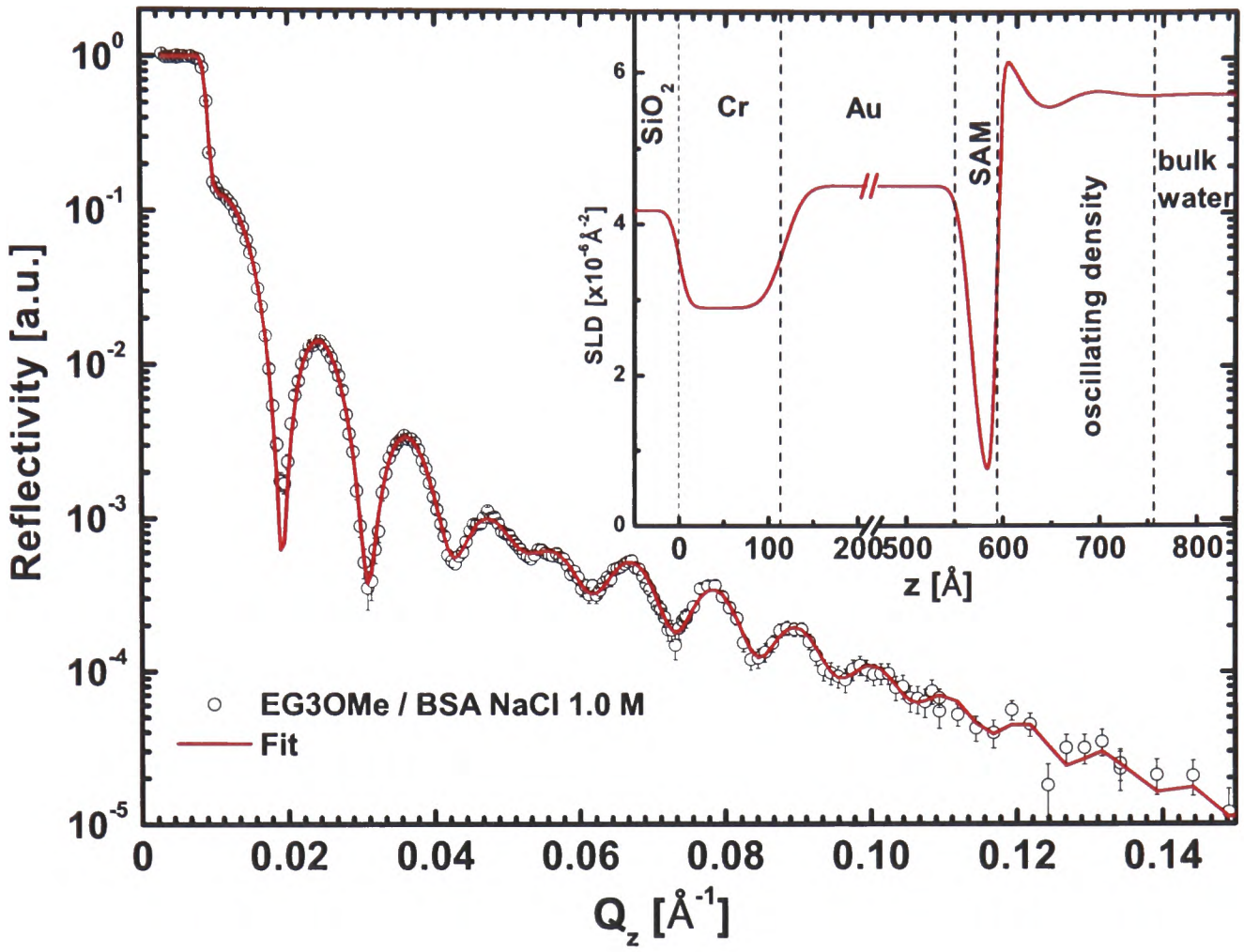


Figure 7.11.: EG3OMe SAM in contact with a 15 wt % BSA solution at room temperature in a 1.0 M NaCl solution.

layer	**d [Å]**	**SLD** [$\times 10^{-6}$Å^{-2}]	σ [Å]
quartz	n/a	4.18	n/a
Cr	117.1	2.89	8.6
Au	450.0	4.5	17.6
SAM	26.5	0.4	10.8
layer 0	5.1	5.71	4.5
oscillating decay: $A = 0.56$, $\lambda = 102.9$, $\phi = 1.32$, $\xi = 40.9$			
bulk	n/a	5.71	0
Hamilton: $b = 3$, $\nu = 216$; $\mathcal{R}_{3,216,0.005} = 1.032$, $\mathcal{R} = \sqrt{\chi_1^2/\chi_{oscill}^2} = 1.220$			
N$_\sigma$ test: N_σ^{oscill}=8.81, N_σ^1=17.5			

Table 7.6.: Fit parameters for the fit in **Figure 7.11** with 216 data points: EG3OMe SAM in contact with a 15 wt % BSA solution at room temperature in a 1.0 M NaCl solution.

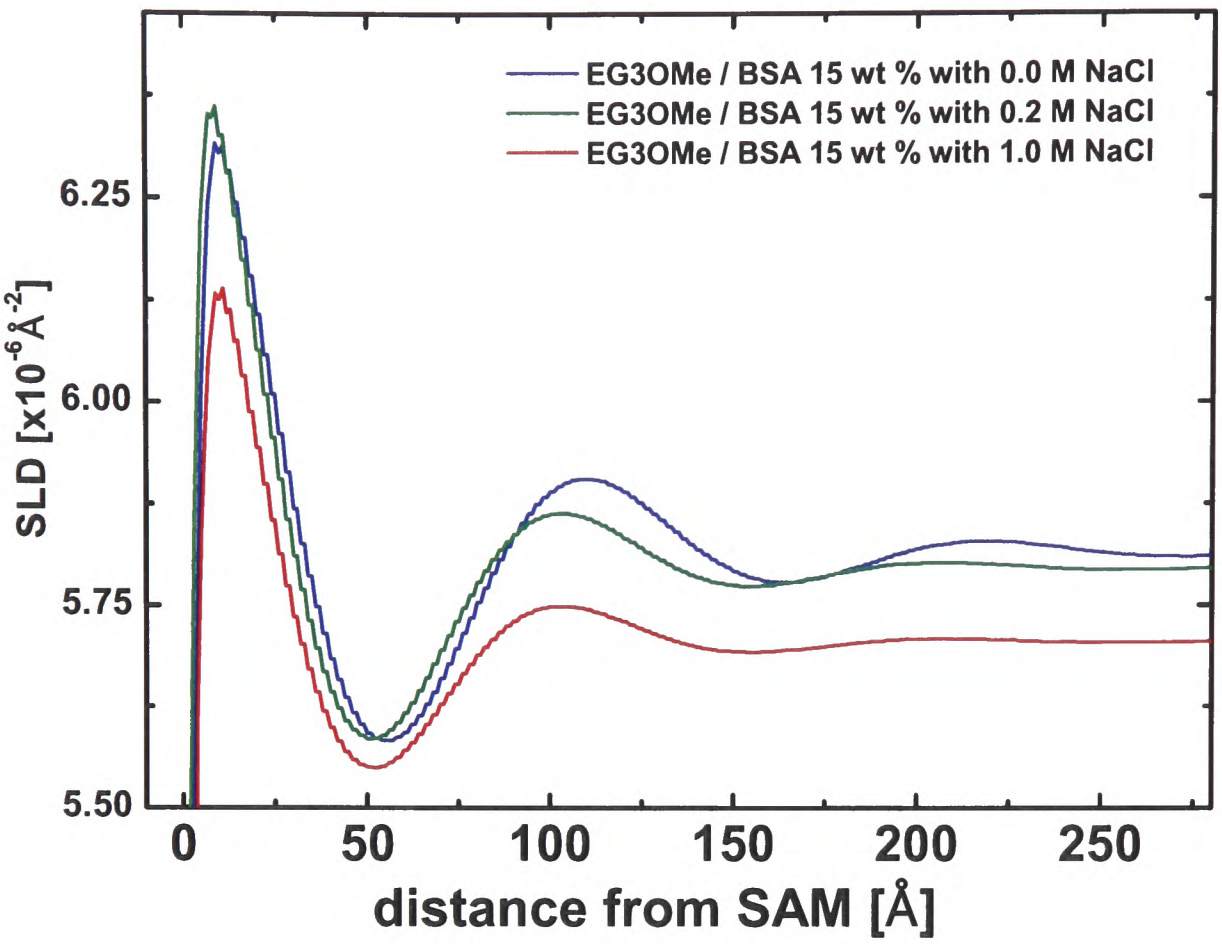


Figure 7.12.: Oscillating protein density in the vicinity of an EG3OMe terminated SAM for different NaCl concentrations in a 15 wt % BSA/D_2O solution. The lower bulk value for the 1.0 M solution is due to a slightly higher BSA concentration.

When the NaCl concentration is increased to 0.2 M, only small changes are visible in the reflectivity data. Accordingly, the subsequent fitting yields parameters very similar to those for the pure BSA solution. However, a slight trend towards smaller periods and stronger damping can be observed: the amplitude remains almost constant (0.62 to 0.68), the period of the oscillation is slightly decreased from 108 to 103 Å and the decay constant of the damping decreases to 46 Å from previously 57 Å. Upon increasing the NaCl concentration to 1.0 M, where the electrostatic interactions between the proteins (and between the proteins and the surface) are fully screened, the fitting values follow the same trend: the oscillation amplitude is now slightly lower at 0.56×10^{-6}Å^{-2}, the period is almost as for the 0.2 M solution and the oscillation is more strongly damped, with $\xi \approx 41$ Å (**Figure 7.11**).

An overview over the protein density distribution in the vicinity of an EG3OMe terminated self-assembled monolayer is presented in **Figure 7.12**. A clear trend

towards less pronounced oscillations at higher salt concentrations is visible. However, the overall changes are small, with the largest deviations being at distances larger than 80 Å from the SAM, indicating that the observed effects are mostly due to screening effects in the bulk (see **Section 6**). The additional fact that the protein depleted region adjacent to the SAM, comprised of reduced density water, does not change significantly upon increasing the NaCl concentration, suggests that the electrostatic contribution to the protein repelling forces of the SAM is rather limited. These findings are in agreement with the small-angle scattering experiments on mixtures of OEG SAM protected gold colloids and proteins described in **Section 7.2**. It may be speculated that one major contribution to the non-fouling properties of OEG SAMs is the formation of a tightly bound hydration layer, that is promoted by the structure and internal hydrophilicity of the SAM. The properties of this hydration layer have been studied for the present thesis and are discussed in detail in **Section 5**.

7.1.6. Effect of Temperature

The systems and phenomena discussed in this thesis are not only of interest on a fundamental level, but also related to biophysical and biomedical applications, such as protein resistant coatings for implants or stents. In this context, the understanding of the behaviour of the protein resistant SAM and its ability to withstand the non-specific adsorption of proteins as a function of temperature is of great importance. Furthermore, the results of Schwendel et al. [24] demonstrated, that monolayers with slightly different chain length, in this case EG3OMe and EG6OMe terminated ones, can show very different behaviour when temperature is changed. It was found, that the protein resistance of EG3OMe monolayers is affected by a temperature lower than 11 °C and small amounts of adsorbed protein could be observed, while the EG6OMe SAM remained resistant even at the lower temperature. The results of Schwendel et al. [24] showed adsorption of the protein fibrinogen at low temperatures. In contrast, the neutron reflectivity measurements presented here required the use of the water soluble protein BSA. Therefore, the experiments of Schwendel et al. have been repeated using the protein BSA, which was used for the in situ neutron reflectivity studies. **Figure 7.13** shows a comparison of EG3OMe SAMs exposed to a 15 wt % BSA/H_2O solution for 20 hours at room temperature, and at

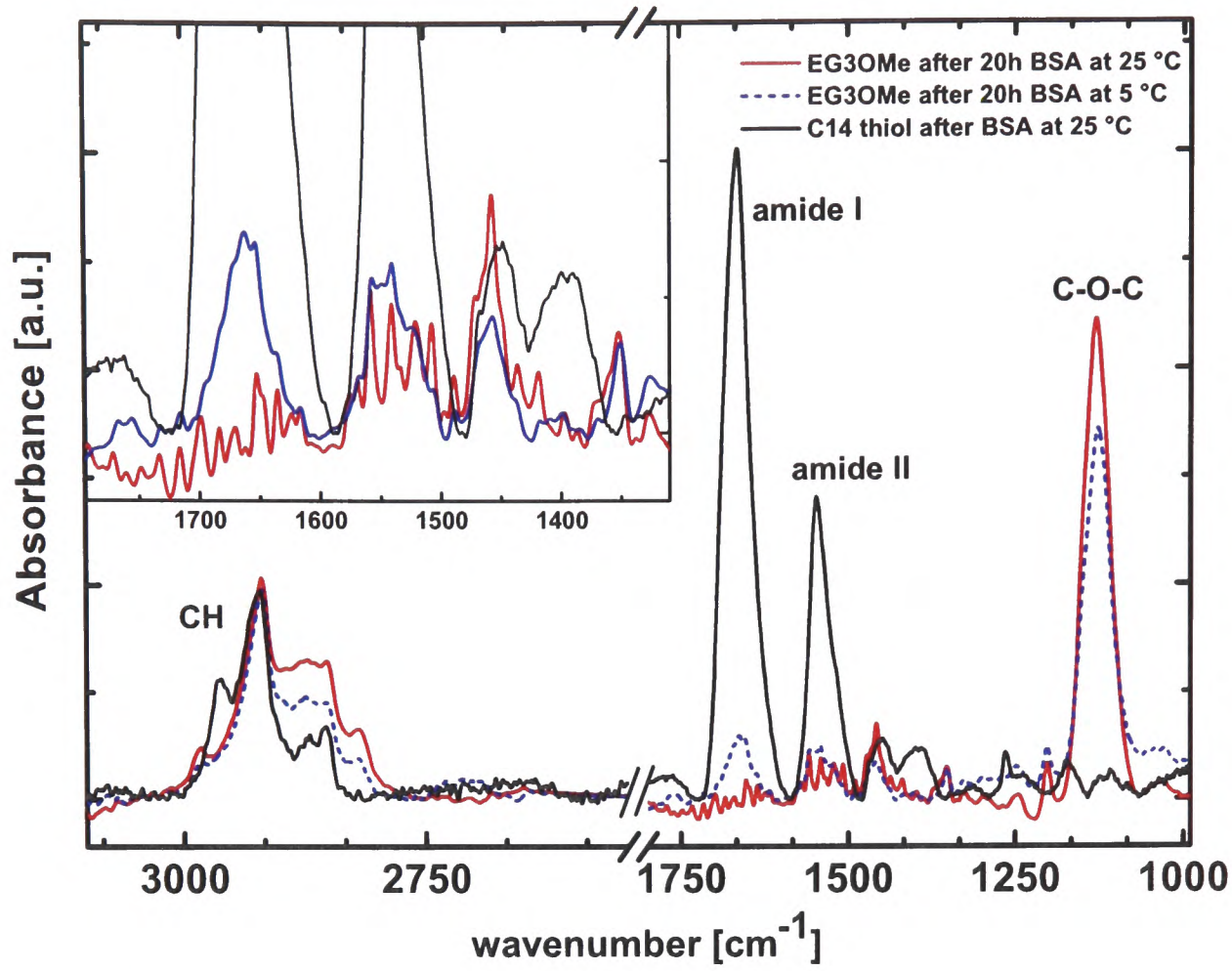


Figure 7.13.: PMIRRAS data in air of two identical EG3OMe samples taken after 20h exposure to a 15 wt % BSA solution at room temperature (red solid line) and at 5 °C (blue dotted line). As a comparison, data is shown for a non-resistant C14 alkanethiol SAM after exposure to a BSA solution (black line). The spectrum was normalised to the strongest CH stretching band. The adsorbed amount of BSA on the C14 alkanethiol SAM is much larger than on the low temperature EG3OMe SAM.

5 °C. After the incubation time, the two identical samples were removed from their BSA solutions by slowly diluting the solution using copious amounts of ultrapure water of the same temperature. Finally, the samples were rinsed and blow dried in a soft argon stream. This procedure was necessary in order to prevent the accidental adsorption of BSA by Langmuir-Blodgett like transfer when the samples were removed from the highly concentrated solutions. On the other hand, it was also ensured that any remaining traces of BSA were irreversibly bound and could not be removed by rinsing. The dried samples were immediately measured using PMIRRAS.

BSA adsorption, characterised by the amide bands at 1550 and 1660 cm^{-1}, is clearly visible on the sample that was incubated at low temperature. The room temperature sample shows only residual water vapour vibrations in the amide region. However, a comparison with a non protein resistant C14 alkanethiol sample, that

was exposed to the same BSA solution at room temperature, demonstrates that the adsorbed amount of BSA on the low temperature EG3OMe sample is very small[4].

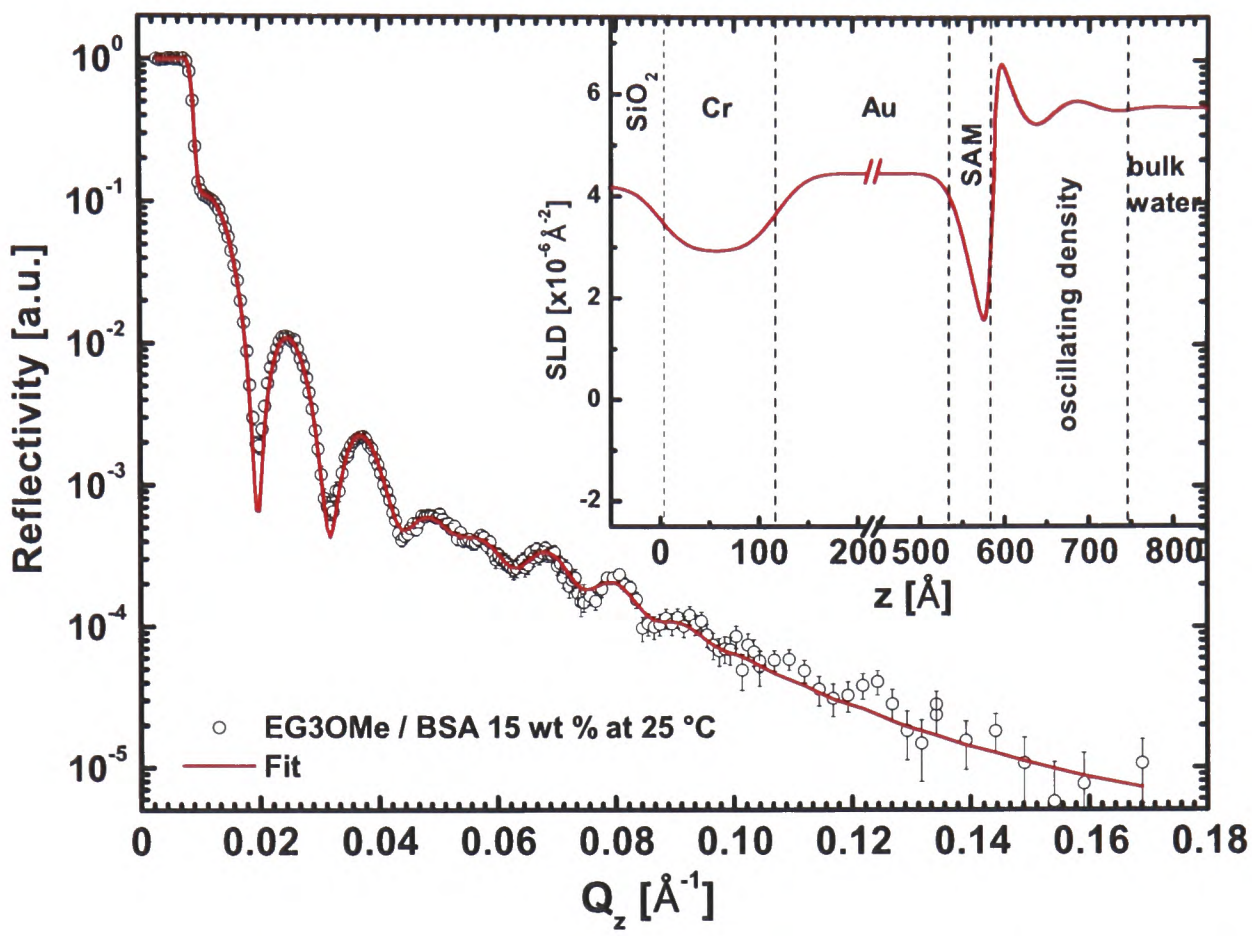


Figure 7.14.: EG3OMe SAM in contact with a 15 wt % BSA solution at 25 °C.

The neutron reflectivity study presented in this section is concerned with the detailed analysis of the structure at the solid-liquid interface between OEG terminated SAMs and protein solutions as a function of temperature. The same approach for the systematic analysis of the protein density profile is used as in the previous section. The reflectivity data are fitted using a box model with an additional sinusoidal decaying function describing the protein density in the solution close to the monolayer.

The experiments were performed in the temperature adjustable cell described in **Section 4.3**. The sample cell was mounted and the temperature set to 25 °C. After the system had equilibrated, the sample was aligned to the neutron beam and the reflectivity was recorded (**Figure 7.14**). For the subsequent measurement at 5 °C, the temperature was gradually lowered and the sample was left to equilibrate for one hour. The sample was then re-aligned to correct for potential thermal contraction

[4]To allow for a comparison of the adsorbed amounts on the low temperature EG3OMe sample and on the reference alkanethiol sample, the spectra were normalised to the strongest CH stretching peak.

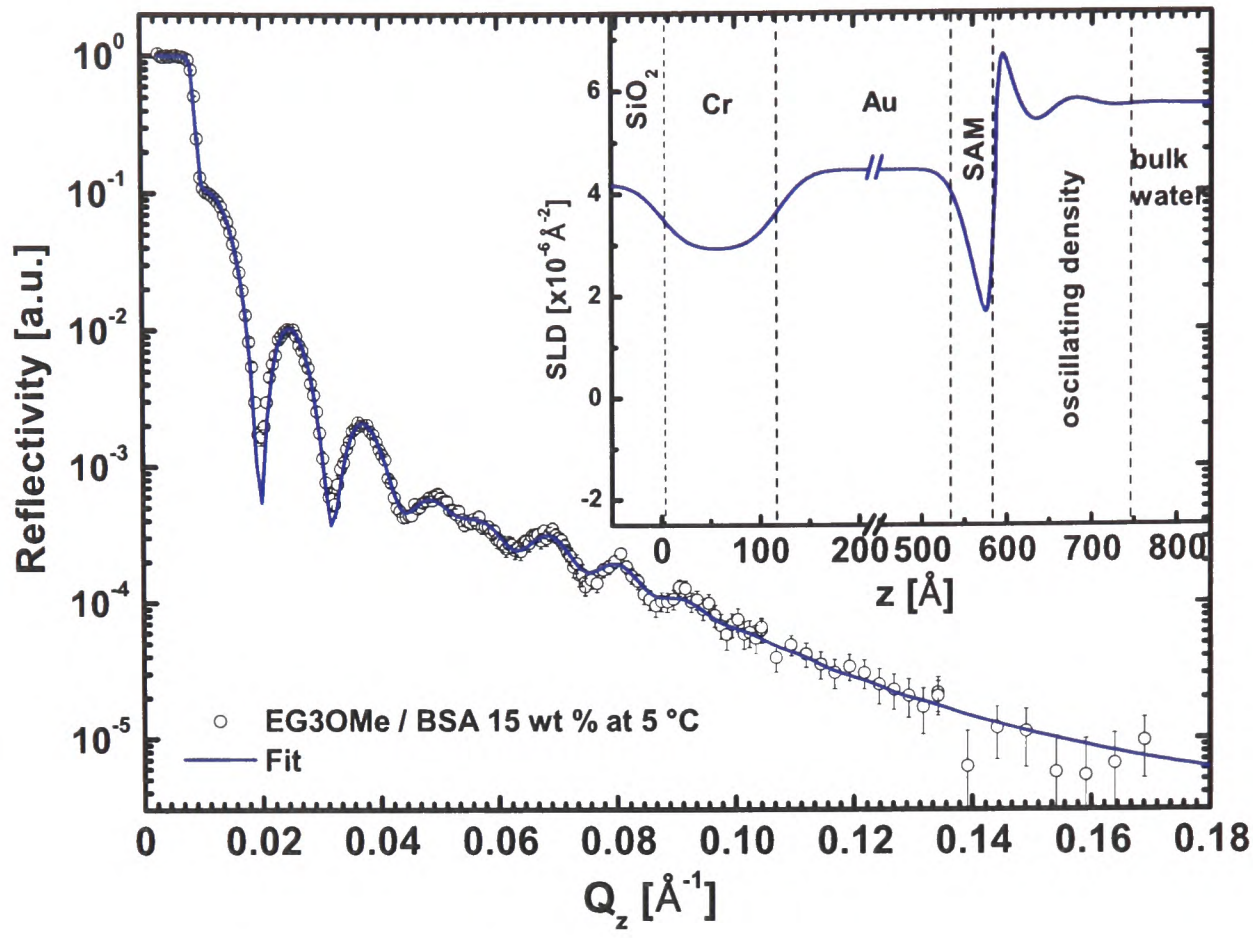


Figure 7.15.: EG3OMe SAM in contact with a 15 wt % BSA solution at 5 °C.

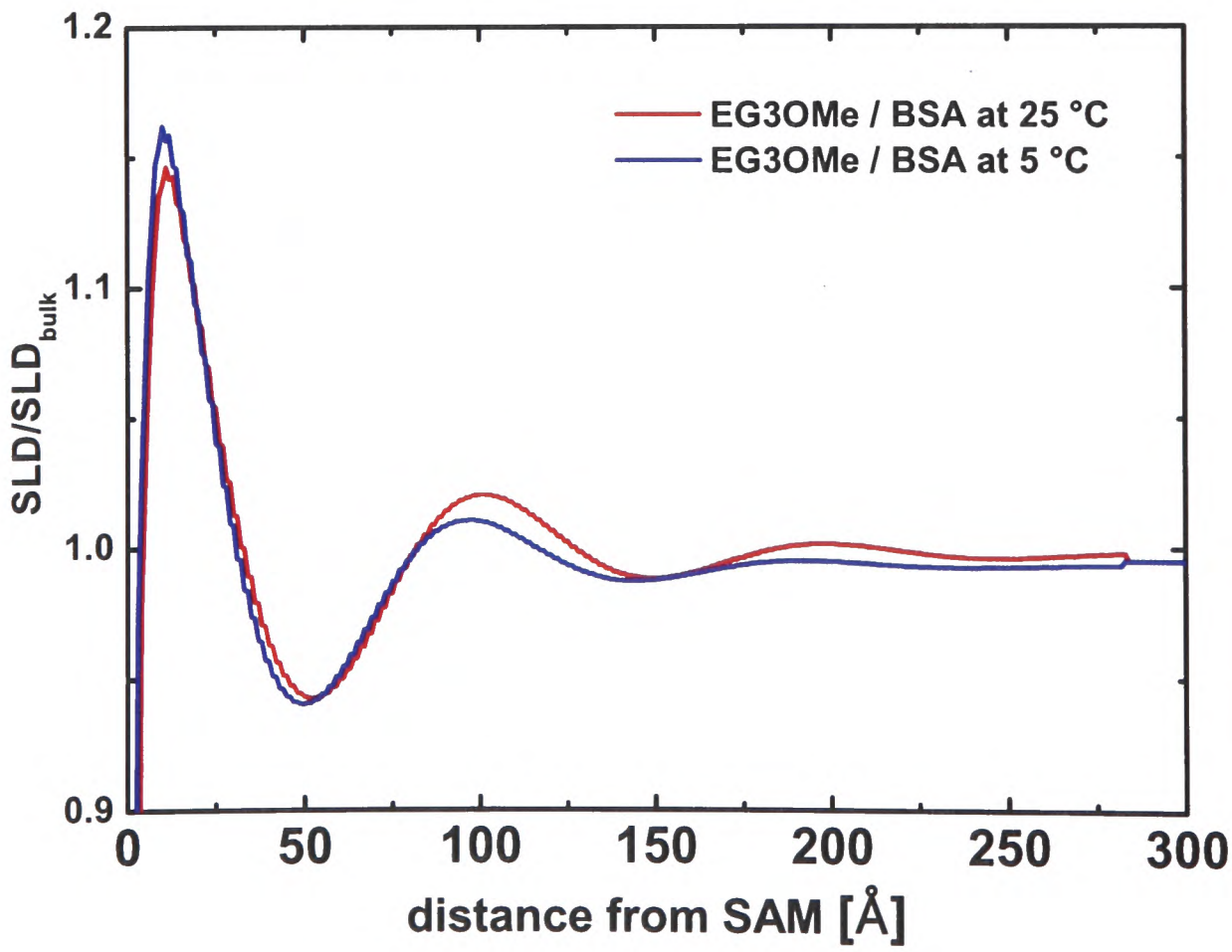


Figure 7.16.: Comparison of the fitted protein density profiles at 25 (red line) and 5 °C (blue line) of an EG3OMe monolayer in contact with a 15 wt % BSA/D_2O solution.

of the cell. The temperature was monitored at regular intervals during the measurement and was kept constant with a maximum deviation of ±0.5 °C. **Figure 7.15** shows the data, fit and real space profile for the EG3OMe sample in contact with a 15 wt % BSA/D_2O solution at 5 °C.

It was found that the oscillating structure of the protein density in the vicinity of the SAM persists down to a temperature of 5 °C, even though the amplitude and period of the oscillation are slightly decreased. The first minimum in the scattering length density is somewhat lower at 5 °C, indicating a higher volume fraction of proteins close to the SAM.

The juxtaposition of the reflectivity data at 25 and 5 °C (**Figure 7.16**) reveals a slight decrease in the amplitude, period and decay length of the density oscillations, but the changes are rather small.

7.1.7. Conclusions

The density profile of a protein solution near an OEG SAM protected gold surface has been studied in detail using neutron reflectivity. It was found that the protein density oscillates around the bulk value by about ±15% of this value with a period of ~10 nm, and that the oscillations are damped out quickly over a length of about 20 to 30 nm, with a decay constant of approximately 5 nm. The lowest density is found very close to the SAM, where, in a region of 3-4 nm, the scattering length density of the solution reaches a value of 90 to 98% that of pure water. Whether this value is due to a small volume fraction of protein that is not excluded from that region, or due to a reduced density water layer as found in the measurements without proteins, cannot be determined by this method. However, this region is strongly depleted of proteins. Further away from the SAM, this is followed by a region of about 4-5 nm, where the protein density is 5-8% higher than the bulk value. After that the density oscillations are rapidly damped out until the density reaches its bulk value. The oscillating behaviour of the protein density in the vicinity of the wall is characteristic for hard sphere layering near a hard wall [75,76]. The fact that the proteins are charged, only impacts on the effective hard sphere radius [77]. While the oscillation period in hard sphere liquids with high packing fractions is of the order of the hard sphere diameter, it is to be expected that, for a more dilute solution, the period will tend towards a value similar to the inter-particle spacing.

The period observed in the neutron reflectivity measurements lies in the range of 103 to 108 Å for a 15 wt % BSA solution. This value is in excellent agreement with the average inter-particle spacing obtained from the SAXS measurements of BSA in solution (cf. **Chapter 6**): the maximum of the scattered intensity in **Figure 6.2** at 200 mg/mL (which corresponds to the concentration of 15 wt %) is at approximately $q = 0.06$ Å^{-1}, which corresponds to an average inter-particle distance of $2\pi/q \approx$ 105 Å.

The impacts of temperature and ionic strength of the solution were also studied for this system. An increase of the NaCl concentration to 0.2 M leads to a slight decrease in amplitude and period of the protein density oscillation. At a concentration of 1.0 M NaCl the oscillation is almost completely damped out after 15 nm. However, the amplitude and width of the protein depleted layer adjacent to the SAM and the neighbouring region with increased protein density hardly change even at a 1.0 M NaCl concentration. This indicates that the interaction of proteins with the SAM is almost unaffected by the salt, while the structure further away, in the bulk, is disturbed due to the screening effect of the salt on the protein charge. Thus it can be concluded that electrostatic interactions play only a minor role in the phenomenon of protein resistance of OEG terminated SAMs.

The variation of temperature of the protein solution from room temperature to 5 °C caused little change in the measured density profile. A small reduction of amplitude and period of the oscillation could be observed. No indication of protein adsorption could be found in situ. Thus, the breakdown of the protein resistance of EG3OMe terminated SAMs at low temperature observed ex situ with FTIR could not be confirmed by these in situ measurements. However, since the amount of adsorbed BSA found in the the ex situ FTIR experiments was very small, it is conceivable that it was well below the sensitivity of the neutron reflectivity measurements. Alternatively, it may be speculated that the adsorption found ex situ is due to Langmuir-Blodgett like transfer during the rinsing and drying procedure or that adsorption of protein to areas containing defects in the SAM is promoted by the low temperature environment.

7.2. SAMs on curved interfaces[5]

The following sections are organised as follows: first the characterisation of OEG decorated gold colloids is presented. Second, the influence of ionic strength on the stability of OEG decorated gold colloids and the protein-protein interactions in solution are investigated. The last part explores the phase behaviour of the binary mixtures as a function of protein concentration and ionic strength.

7.2.1. Characterisation of OEG decorated gold colloids

The citrate-stabilised gold colloids with a diameter of 5 nm show a characteristic absorption peak at wave length of about 520 nm in the UV-vis spectra. Upon decoration with EG6OMe, the reaction is characterised by a clear peak shift to a higher wavelength (524 nm). **Figure 7.17** presents typical UV-vis spectra of a gold colloid solution (2R = 22 nm) before and after OEG decoration. As a comparison,

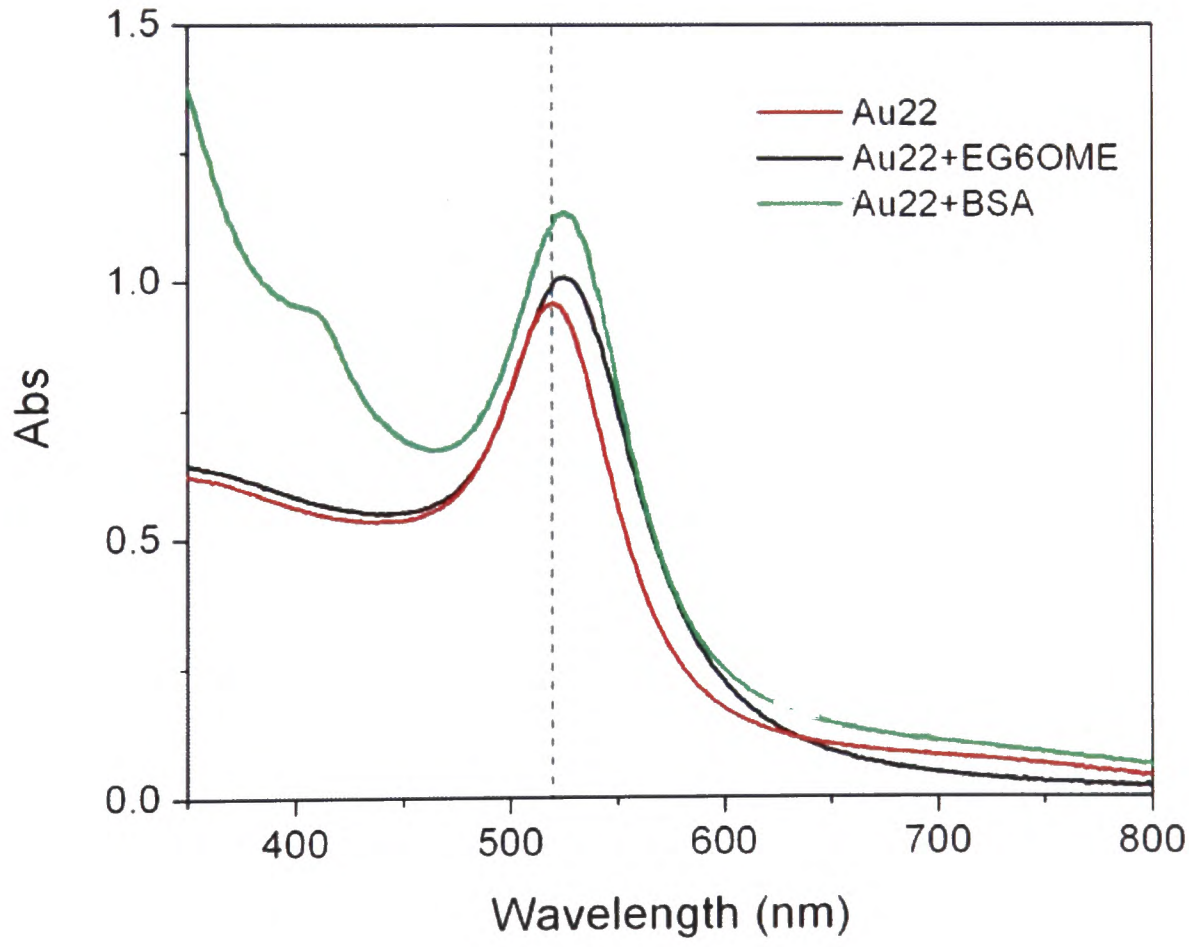


Figure 7.17.: UV-vis spectra of gold colloid solution with 2R = 218 Å before and after decoration by EG6OMe, as comparison, a spectra of colloid solution with BSA is also shown.

[5]This section is based on F. Zhang, M. W. A. Skoda et al.,"Gold Nanoparticles Decorated with Oligo(ethylene glycol) Thiols: Protein Resistance and Colloidal Stability", *J. Phys. Chem. A* **2007**.

a spectrum of the citrate stabilised colloid solution mixed with 200 mg/ml BSA is also shown in **Figure 7.17**. A clear shift of about 4 nm indicates the absorption of BSA molecules at the negatively charged colloid surface [78]. Both OEG SAM and absorbed BSA layer stabilise the colloidal gold solutions.

The number density of colloidal solution is about 10^{12} particles per millilitre, which corresponds to a volume fraction of less than 0.003 vol %. The colloid with OEG SAM might be described best by a core-shell form factor. However, due to the very large contrast, i.e. difference in electron density between gold ($\rho = 130.5 \times 10^{10}$ cm^{-2}) and OEG SAM ($\rho = 7.293 \times 10^{10}$ cm^{-2}), the contribution of SAM to the total scattering intensity is very small. Therefore, the data analysis was carried out by using a standard model with least square fitting. Recalling **Equations 3.63** and **3.64**, the total scattering intensity in a polydispersed and dilute colloidal solution with homogeneous electron density can be written:

$$I(Q) = N_0 \Delta\rho \int_0^\infty f(r) r^6 P^2(Qr)\, dr,$$

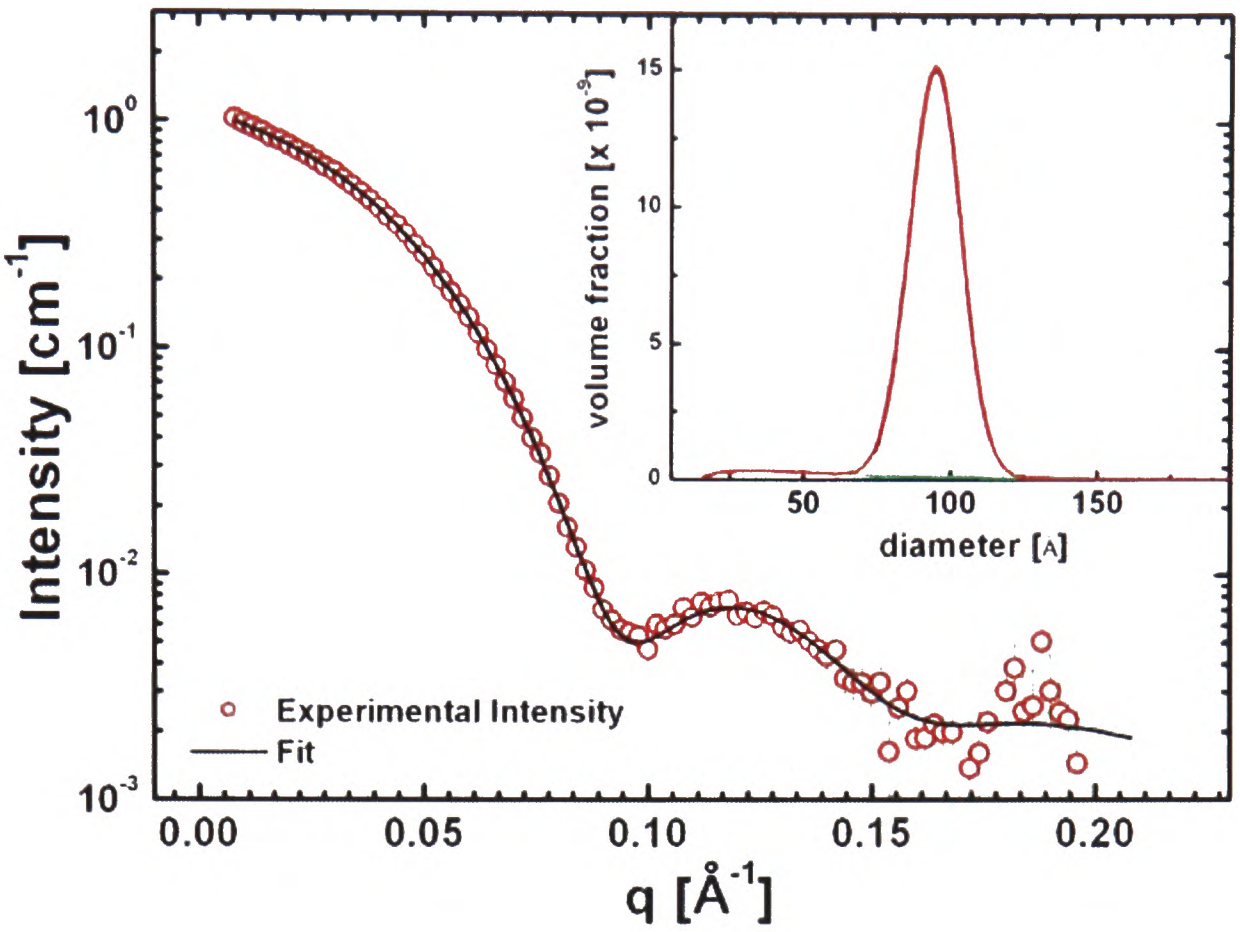
where N_0 is the number of the colloidal particles per unit volume and $\Delta\rho$ is the difference in scattering length densities between colloid and solvent (water), and $P(Qr)$ is the form factor of a spherical colloid:

$$P(Qr) = \frac{3\left(\sin(Qr) - Qr\cos(Qr)\right)}{(Qr)^3}.$$

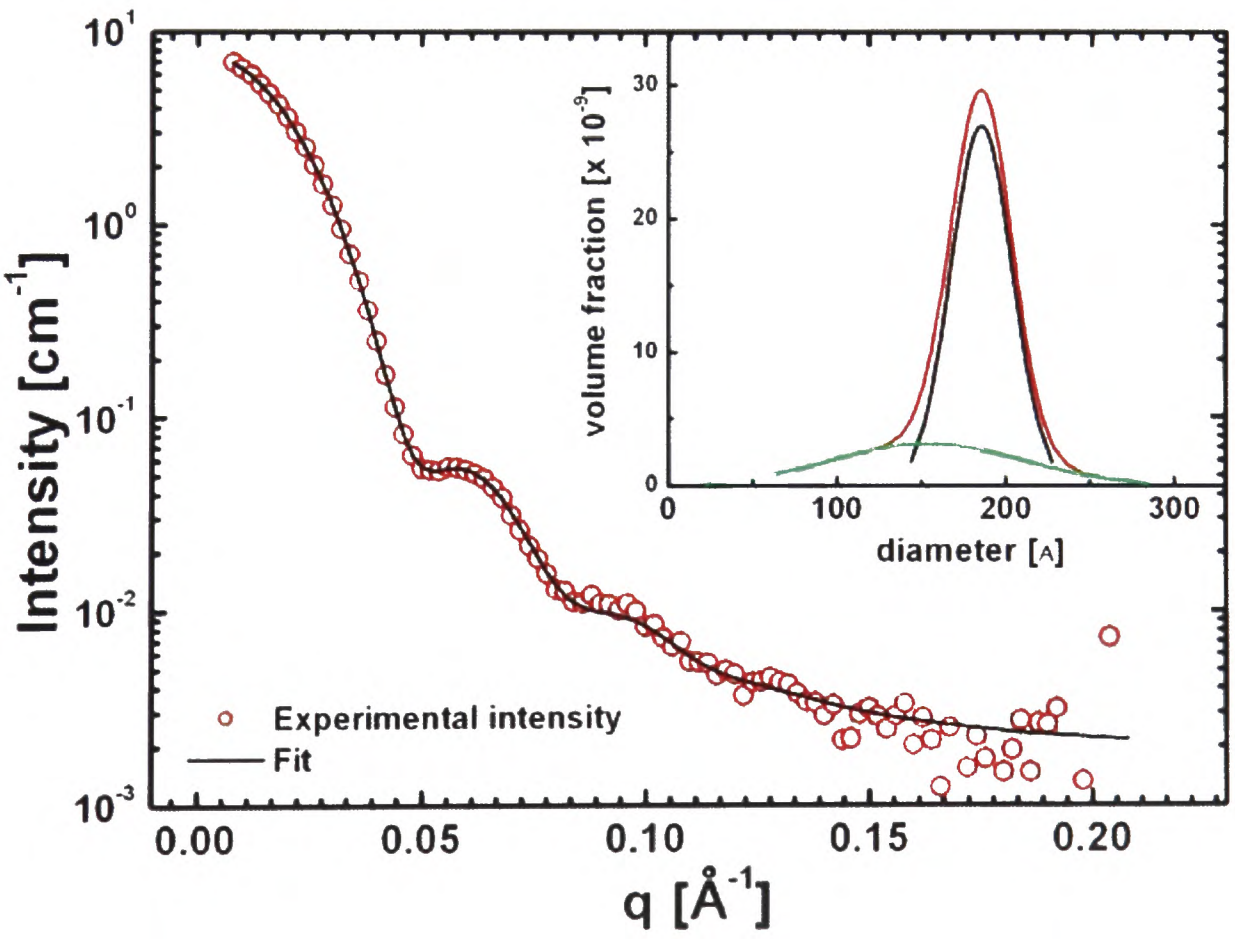
$f(r)$ is the normalised Gaussian distribution function reflecting the size distribution of the nanoparticles:

$$f(r) = \frac{1}{\sigma\sqrt{2\pi}} \exp\left[-\frac{1}{2\sigma^2}(r - \bar{r})^2\right], \tag{7.5}$$

where $\bar{r}$ is the average radius as determined in the data fitting procedure and σ is the standard deviation that corresponds to the width of size distribution. Since the colloidal particles can be regarded as non-interacting, the structure factor can be taken to be unity. Data fitting was performed on Irena SAS modelling macros for Igor Pro developed by J. Ilavsky [79]. **Figure 7.18** displays the SAXS experimental data with model fitting for two sizes of gold colloids. The mean sizes of gold colloids after



(a)



(b)

Figure 7.18.: Experimental scattering intensity with model fitting of EG6OMe decorated gold colloids studied by SAXS, (a) Au9EG and (b) Au19EG.

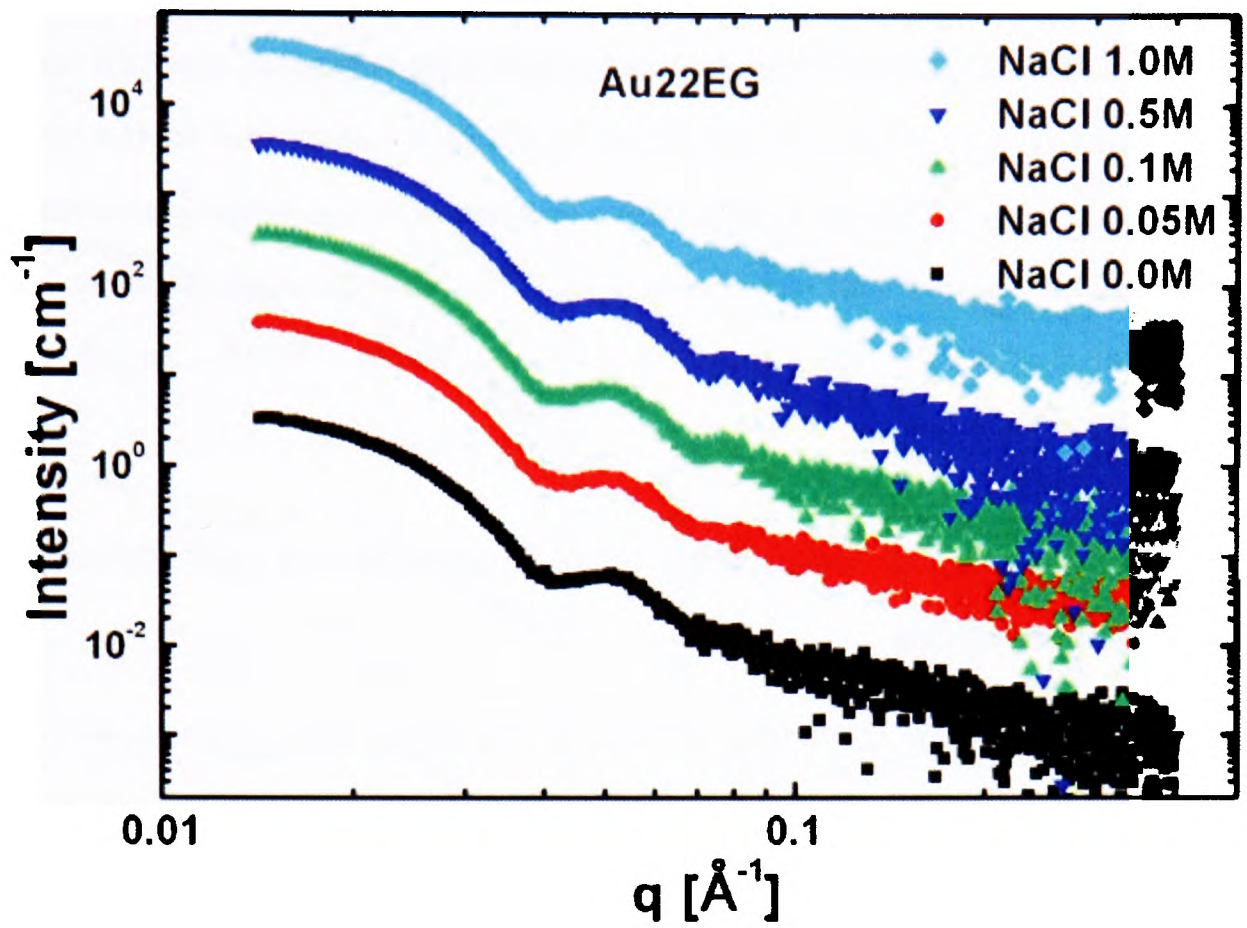
decoration were characterised by small-angle x-ray scattering as listed in **Table 7.7**. The experimental data can be very well fitted by the theoretical model. The size distribution gives a major component close to the size as specified in the product catalogue. It is interesting to see that the gold colloids labelled as 20 nm purchased from British Biocell International show a mean size of 18.9 nm, while colloids from Sigma-Aldrich give a mean size of 21.8 nm. This difference will be important for the following results.

Size/ abbrev.	Source	Particles per mL*	Mean size $2R \pm \sigma$ [nm]	Volume fraction(s) [$\times 10^{-9}$]	Crit. BSA conc. [mg/mL]
Au9EG	BBI	5.7×10^{12}	9.5±0.87	1.34	> 500
Au19EG	BBI	7×10^{11}	18.8±1.6/10.8±9.7	1.22/0.32	380-400[a] 320-450[b] 280-310[c] 280-310[d]
Au22EG	Sigma	n/a	21.9±1.2	0.5	180-200
Au37EG	BBI	9×10^{11}	36.9±2.2/28.7±5.8	0.54/0.94	60-80

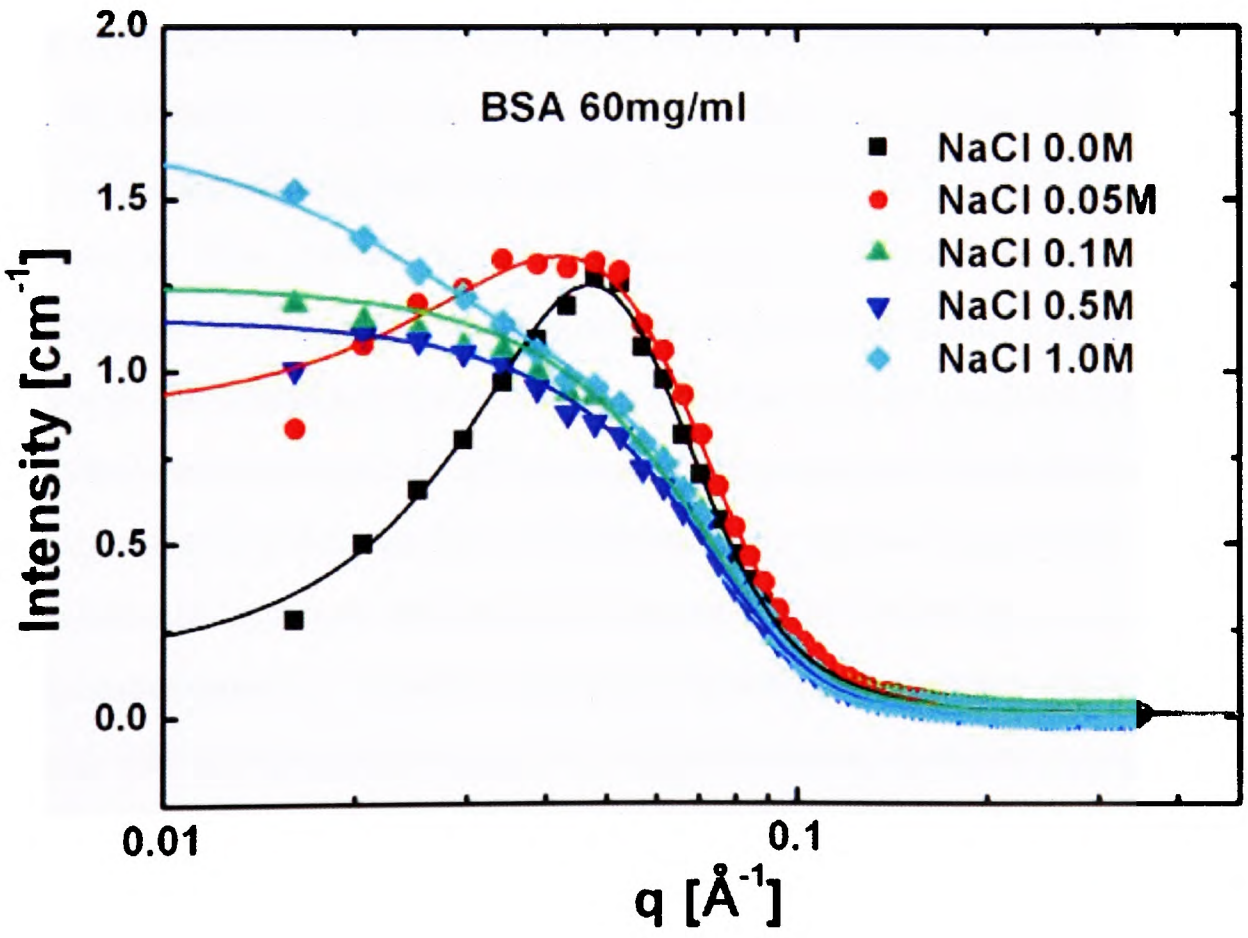
Table 7.7.: Gold colloids used in this thesis and related parameters determined by SAXS. *Numbers obtained from on-line product catalogue http://www.bb-international.com/research.htm [a,b,c,d] The values of a-d correspond to NaCl concentration of 0.0, 0.1, 0.3 and 0.5 M.

7.2.2. Effect of ionic strength (NaCl) on functionalised gold colloidal and protein solutions

OEG decorated gold colloidal solutions are very stable against variations of the ionic strength. **Figure 7.19a** shows a set of SAXS data for Au22EG with various salt concentrations (offset for clarity). The scattering profiles are identical, indicating that salt does not affect the stability of gold colloids in this regime. This observation indicates that the stabilisation of gold colloid by OEG SAM is mainly due to the entropic effect, rather than to the absorbed surface charge. This observation is in good agreement with the results reported by Weisbecker et al. [1] who found that OEG decorated gold colloids are stable in a wide range of ionic strength and pH. In contrast to OEG decorated gold colloidal solutions which show a good stability to salt, protein interactions strongly depend on the ionic strength.



(a)



(b)

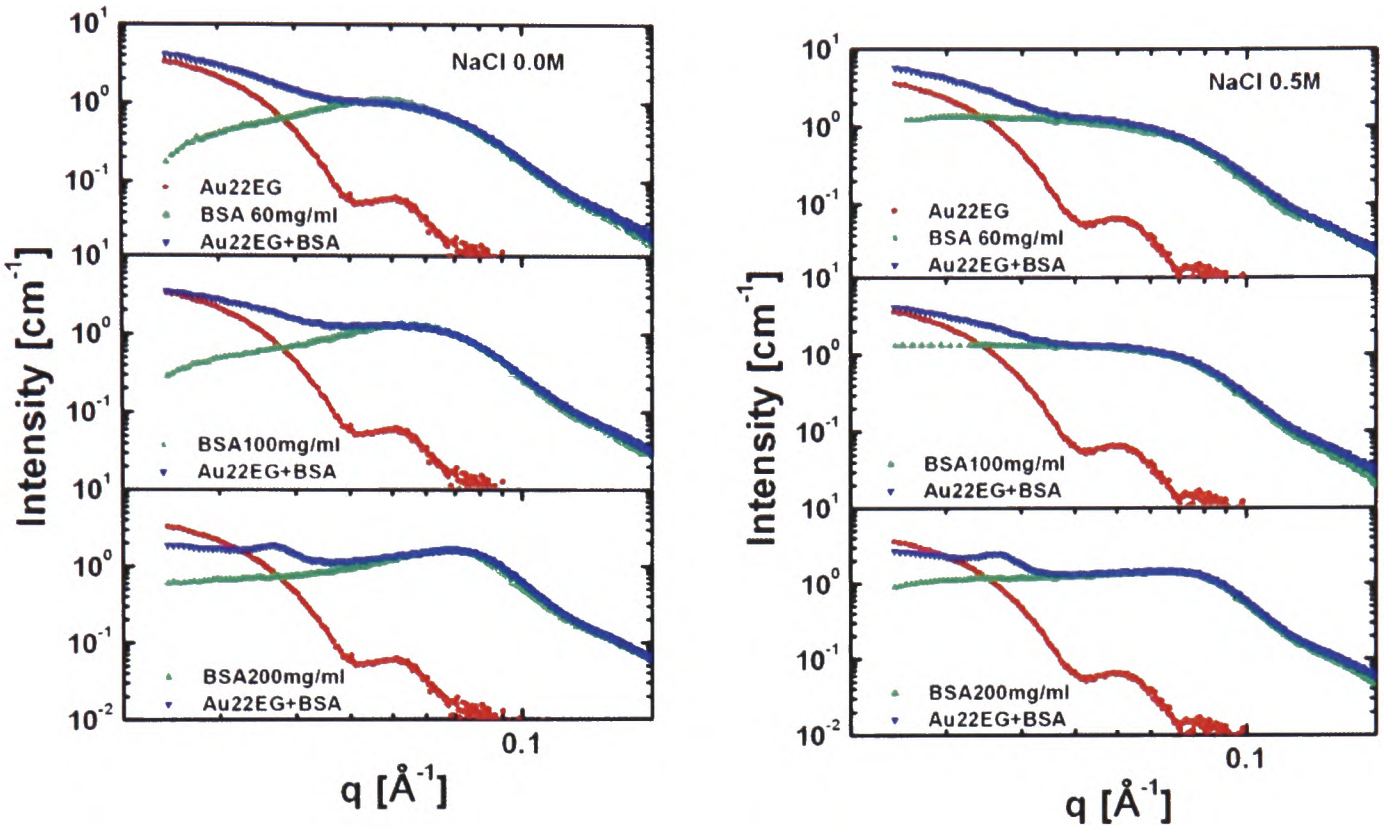
Figure 7.19.: Effect of salt concentration on (a) Au22EG solution and (b) BSA solution of 60 mg/mL characterised by SAXS.

In **Chapter 6** it was shown that the electrostatic interaction dominates the repulsive interaction between negatively charged BSA molecules in aqueous solution. On adding salt, the surface charges are increasingly screened, and at very high salt concentration (>1.0 M), an attractive interaction arises due to the excluded-volume effect of ions. **Figure 7.19b** shows one example for protein concentrations of 60 mg/mL at various salt concentrations. The overall interaction at low salt concentration is repulsive and turns into a weak attractive interaction at high salt concentration.

7.2.3. Interaction of proteins with OEG functionalised gold colloids in mixed solutions

Figure 7.20 shows the scattering profiles of Au22EG with different amounts of protein. For comparison, the SAXS profiles from pure colloidal and pure protein solutions are also presented. The scattering from the pure colloidal solution has been described in **Figure 7.18**. The data can be fitted by a sphere form factor with a Gaussian distribution. The scattered intensity increases significantly towards the origin. The scattering profiles from pure protein solution show a maximum intensity at finite q values, i.e. q_{max} = 0.048, 0.055, and 0.066 $Å^{-1}$ for protein solutions of 60, 100 10 and 200 mg/mL, respectively. The scattering profiles from the mixtures show the combined features: a significant increase of intensity with decreasing q in the low q range (<0.03 $Å^{-1}$), which is the typical feature of scattering from the pure colloidal solution, and a scattering maximum which almost overlaps with the scattering profile from the pure protein solution in the high q range (>0.03 $Å^{-1}$). While the scattering intensity distribution from the mixtures in the high q range (protein regime >0.03 $Å^{-1}$) almost completely follows the scattering intensity of the pure protein solution, the overall scattering intensity at low q range decreases with increasing protein concentration; this is only partially due to the decrease of scattering intensity of proteins. When the protein concentration is above a critical protein concentration, i.e. 200 mg/mL, a new sharp scattering maximum appears at q = 0.0267 $Å^{-1}$. **Figure 7.20b** shows the SAXS results of protein-colloidal mixture with 0.5 M NaCl. Similar results were obtained for salt concentrations from 0.05 to 1.0 M (data not shown). As shown in **Figure 7.19**, adding salt does not affect the scattering intensity distribution of pure colloidal solution, while for protein

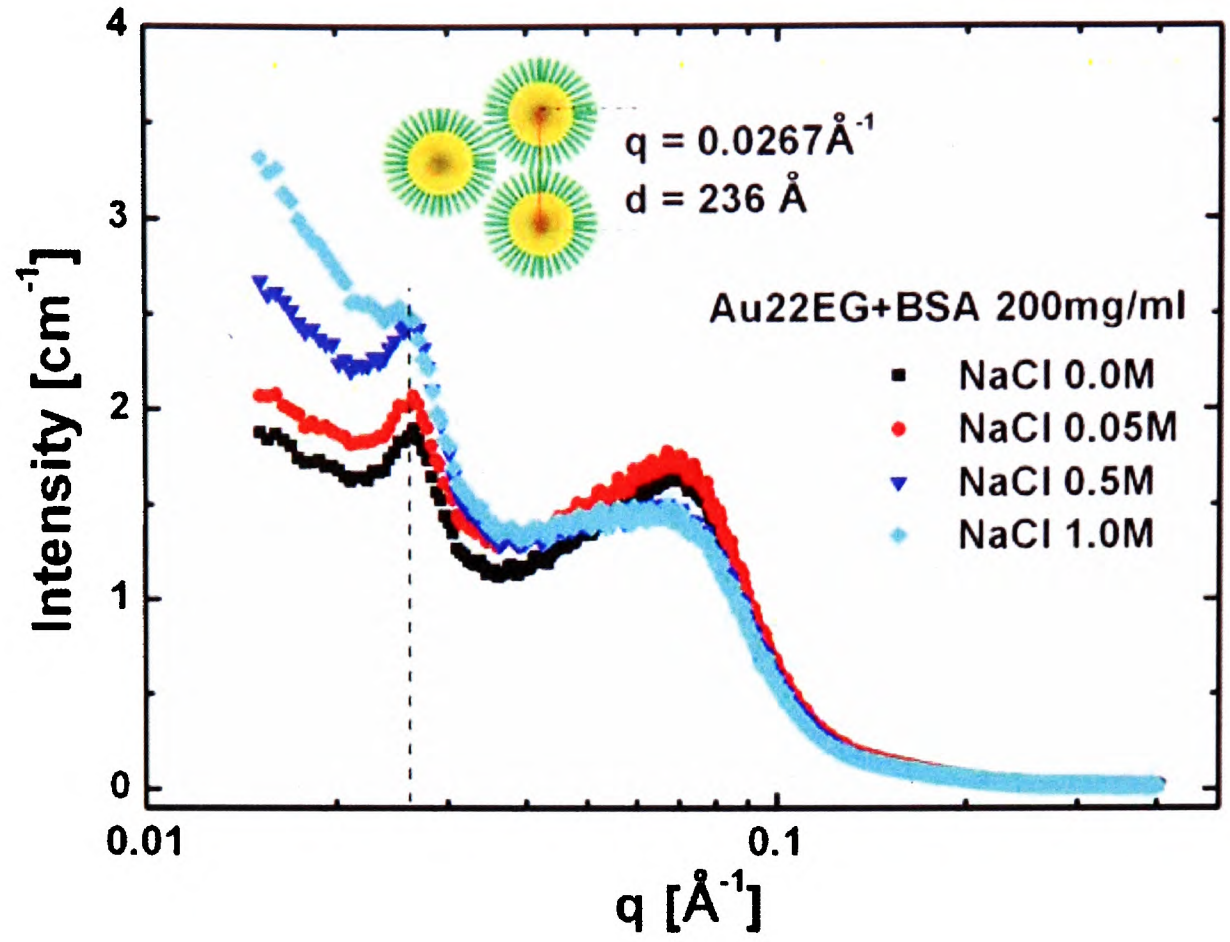
solutions it does. Nevertheless, at large q the total scattering profiles of the mixtures still qualitatively follow the features of the scattering profile of the pure protein solution. **Figure 7.21** shows the aggregation of Au22EG and Au19EG, respectively,



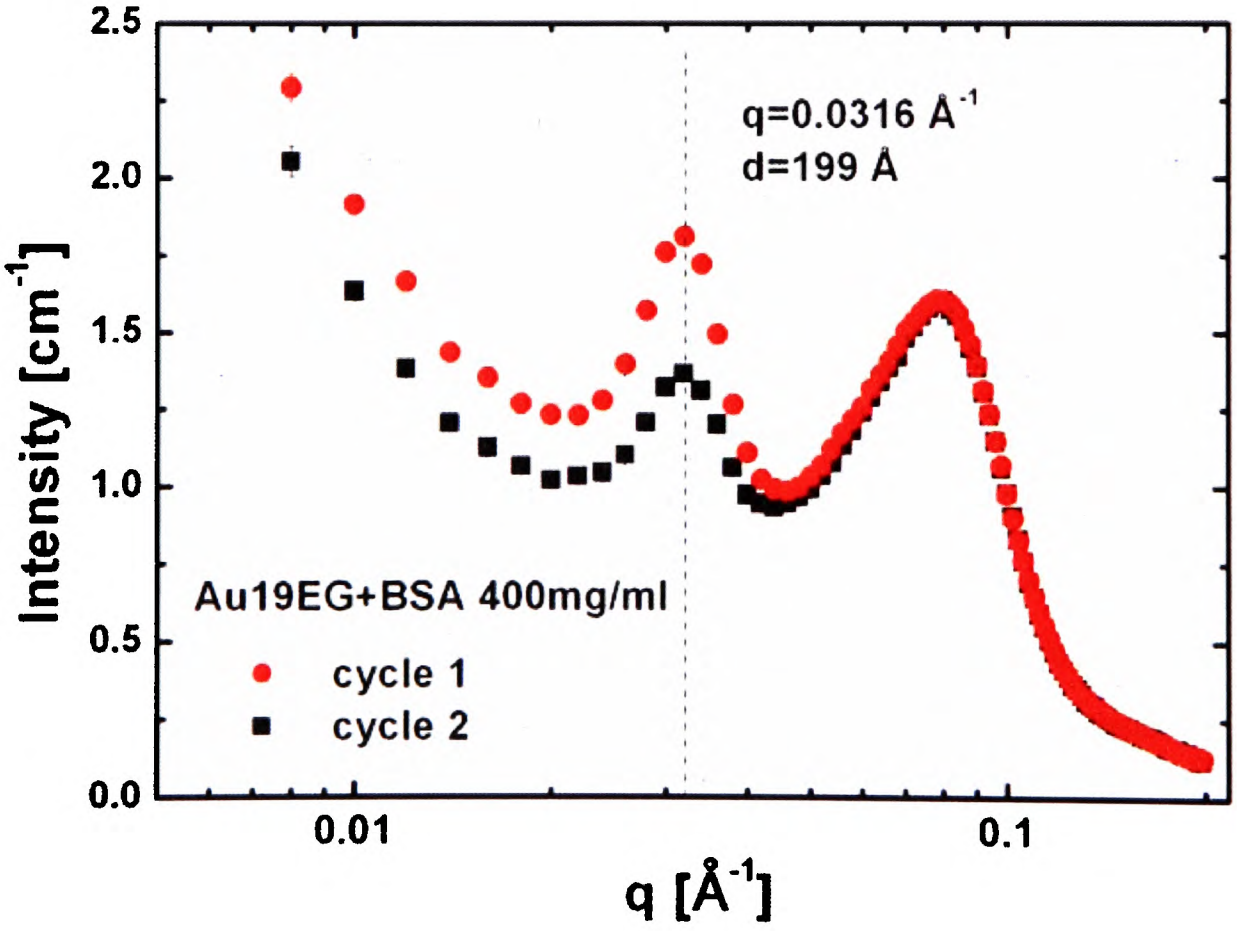
(a) (b)

Figure 7.20.: Mixture of OEG-coated gold colloids and protein solutions studied by SAXS (a) SAXS profiles of Au22EG solutions with different BSA concentrations without adding salt. (b) SAXS profiles of Au22EG plus BSA with 0.5 M NaCl.

upon adding protein above the critical protein concentration. For Au22EG with 200 mg/mL BSA, the new peak at a low $q = 0.0267$ Å^{-1}, which corresponds to a centre-to-centre distance of 236 Å, and the peak position does not change with adding salt (**Figure 7.21a**). For Au19EG, no aggregation occurs when the protein concentration is less than 300 mg/mL. **Figure 7.21b** shows that at 400 mg/mL, a sharp peak appears at $q = 0.0316$ Å^{-1}, corresponding to a centre-to-centre distance of 199 Å. The difference between the centre-to-centre distance and the averaged mean size of gold colloids is mostly due to the finite thickness of the OEG SAM; however, the spread of the experimental values, renders it difficult to determine the thickness of the SAM precisely. Moreover, it can be expected that the SAM exhibits some conformational distortions and also not necessarily full coverage. Its effective thickness will thus be below the theoretical maximum value of 28 Å (the length of the solvated EG6Me molecules in a closely packed SAM without tilting) [14].



(a)



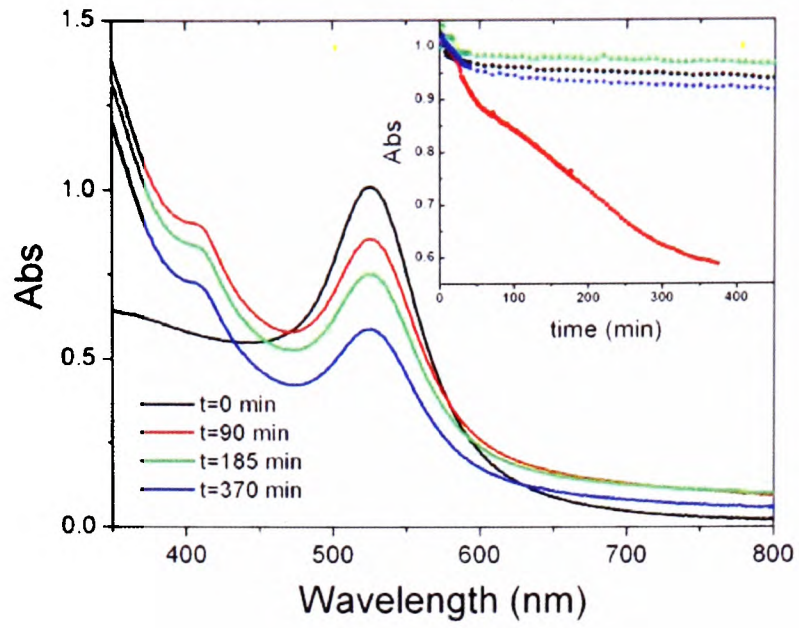
(b)

Figure 7.21.: (a) SAXS results of Au22EG and BSA 200 mg/mL with various salt concentration. When the BSA concentration was 200 mg/mL, the colloids in the Au22EG solution form aggregates and a sharp peak at q = 0.0267 $Å^{-1}$ is observed in the SAXS profile, corresponding to an inter-particle distance of 236 Å. (b) SAXS result of Au19EG with 400 mg/mL BSA; aggregation was observed for protein concentrations 350 mg/mL. The peak position $q = 0.0316$ $Å^{-1}$ corresponds to an inter-particle distance of 199 Å.

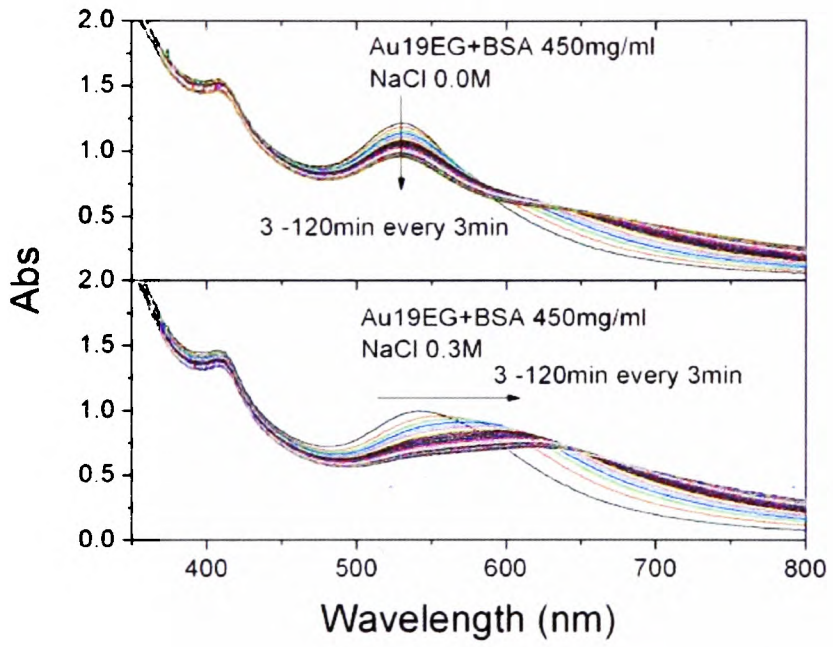
Hence, even allowing for significant experimental error, it is likely that the conformation of OEG molecules at a curved interface is greatly disturbed by the curvature. It is expected that the smaller the size of colloid, and hence the larger the curvature of interface, the greater the disorder of the OEG SAM.

It has to be noted that the SAXS measurements for protein-colloid mixtures usually commenced about 1 or 2 hours after the sample was prepared. From UV-vis measurements (see below), it is clear that for Au22EG with 200 mg/mL BSA, the flocculation process takes several hours until the colloids precipitate out. The time window of the SAXS measurements is thus in the intermediate stage of the aggregate formation in solution. Two consecutive cycles measured on a time scale of 30 min for Au19EG with 400 mg/mL BSA in **Figure 7.21b** show a decrease of the Bragg peak indicating the precipitation of colloidal clusters; it is important to note that the peak position remained constant. However, the kinetics strongly depends on the size of colloids and protein concentration. In another case, i.e. Au37EG with 100 mg/mL BSA, most of the colloids had precipitated when the measurements started, and only the scattering intensity from proteins was observed. More detailed studies of the kinetics of the aggregation are beyond the scope of this work and will be discussed elsewhere [80].

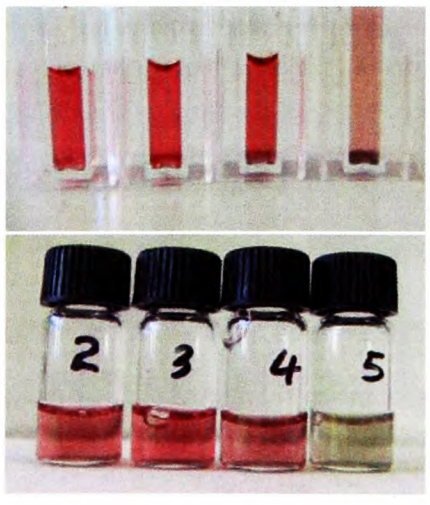
UV-vis spectroscopy has been used to determine the critical protein concentration in various colloidal solutions. **Figure 7.22a** presents selected in situ UV-vis spectra of Au22EG solutions with a BSA concentration of 200 mg/mL. While the peak intensity decreases with time, its position stays constant. When adding proteins with a concentration of less than 200 mg/mL, the peak position still remains constant but the peak intensity at wavelength of 525 nm decreases slightly. The peak intensity as a function of time has been plotted in the inset of **Figure 7.22a** with various BSA concentrations. The peak intensities decrease in arbitrary units from 1.01 to 0.96, 0.93, and 0.90 for protein concentrations of 0, 40, 80, and 160 mg/mL, respectively. The slight decrease of absorbance is due to the diluting effect of adding protein powder to the solutions. Once the protein concentration is equal or higher than 200 mg/mL, the peak intensity decreases continuously from 1.01 to less than 0.6 within 400 min; the peak position does not change in this time period. This continuous decrease cannot be explained by the diluting effect; rather, it is due to the aggregation and flocculation of EG6 decorated gold colloids.



(a)



(b)



(c)

Figure 7.22.: Real-time UV-vis spectra for (a) Au22EG with various BSA concentrations; (b) Au19EG with BSA at ionic strength of 0.0 and 0.3 M; and (c) Colorimetric results of Au22EG (top), conditions are same as (a) and Au19EG solution (bottom) at ionic strength of 0.3 M with BSA concentrations of 180, 220, 270, and 310 mg/mL, a critical concentration in the range of 270-310 mg/mL was determined.

The UV-vis spectra in **Figure 7.22a** show that the peak intensity decreases dramatically, at the same time, the spectra in the wavelength range of 600 to 800 nm increase with time. This is characteristic of aggregate formation in such a system [1,81]. A colour change from pink to yellow corresponding to the UV-vis spectra has been shown in **Figure 7.22c** (top) when the BSA concentration increased from 40 to 200 mg/mL. In addition, after several hours, some black precipitates could be observed at the bottom of the cuvette. These precipitates are large aggregates of colloids. In contrast to the irreversible aggregation upon chemisorption of alkanethiols [1,82], it is interesting to see that the aggregates can be re-dispersed by diluting the solution with water, and the colour changes back to pink again.

The critical protein concentration, c*, for various colloidal solutions has also been determined. For a given colloidal number density (**Table 7.7**), it is found that the critical protein concentration is very sensitive to the size of colloids. For example, c* for Au22EG is around 200 mg/mL, while for Au37EG, this value is only 50~70 mg/mL. For a slightly smaller colloid, Au19EG, c* increases to ~350 mg/mL. For Au9.3EG, no obvious colour or UV-vis spectra change could be observed up to 500 mg/mL of BSA.

We have also studied the effects of salt on colloid aggregation. Generally, adding salt (which reduces the Debye length) to the mixtures increases the aggregation speed of colloids and decreases the critical protein concentration. **Figure 7.22b** shows typical UV-vis spectra for Au19EG with 450 mg/mL BSA with and without added salt. Without salt, the peak position remains constant and the intensity decreases continuously as seen in **Figure 7.22a**. When salt is added (0.3M NaCl), the peak not only decreases in intensity, but also shows a strong red shift. The colour of the solution changes from pink to dark blue within 10 min, indicating the formation of large colloidal clusters (**Figure 7.22c** bottom). After more than 4 hours, the aggregates precipitate out and the solution becomes yellow, the colour of the BSA solution. Note that in both cases, the aggregation process is reversible, i.e. diluting the solution by adding water leads to dissolution of the aggregates and the solution becomes pink again. A detailed analysis of the change in kinetics upon adding salt in the mixtures is beyond the scope of this work and will be addressed in detail elsewhere [80]. Here, we only note the decrease of critical protein concentration upon adding salt. For example, the same Au19EG colloidal solution, without adding salt,

c* is 380~400 mg/mL, and with 0.1 and 0.3 M NaCl, the c* is reduced to 320~350, 280~310 mg/mL respectively (see **Table 7.7** and **Figure 7.22c** lower part), c* does not change significantly upon further increasing salt concentration to 0.5 M.

7.2.4. Discussion of the interactions in mixed solutions

Generally, interactions are translated into correlations between particles, which then enter the structure factor measured in small angle scattering. Interactions in *mixed* dispersions are related to the *partial* structure factors. In binary mixtures, i.e. protein and functionalised gold colloidal solution, the partial structure factors are protein-protein interaction $S_{pp}(q)$, colloid-colloid interaction $S_{cc}(q)$ and protein-colloid interaction $S_{pc}(q)$. Partial structure factors are usually determined by small angle neutron scattering with a contrast matching technique [83–88]. For the theoretical calculation of partial structure factors the detailed interactions of all components need to be known. In our case, the structure factor of colloid-colloid interactions in the pure colloidal solution is equal to unity due to the very low volume fraction. The protein-protein interactions in pure protein solutions have been reported in **Chapter 6** and can be described by a screened Coulomb structure factor at low salt concentration and a square-well structure factor with attractive potential at very high salt concentration due to the excluded-volume effect of the ions. The protein-colloid interaction is not known, but it is perhaps reasonable to expect a short-ranged repulsive potential (see below discussion on ionic strength effect).

In mixtures, the interactions may change. While the protein-protein interactions in the mixtures do not change very much as shown from SAXS measurements (**Figure 7.20a** and **b**), the colloid-colloid interactions change with increasing protein concentration. The formation of colloidal aggregates above a critical protein concentration indicates that the addition of proteins results in an effective attraction between colloids. The attractive interaction between gold particles can be understood by the depletion effect [83–85], [89–91]. The depletion interaction under various conditions is presented schematically in **Figure 7.23**. In a mixture of hard spheres with two different sizes (**Figure 7.23a**), small particles are expelled from the "forbidden region" between two large particles. This depletion effect leads to an unbalanced osmotic pressure pushing the large particles together, which results in an effective attraction between the two large particles. This attraction potential

depends on the size ratio between small and large particles and their volume fraction. In our experiments, we observed an enhancement of the depletion effect, i.e. the decrease of critical protein concentration, with increasing colloid size. However, the depletion effect in our system is more complicated than for a mixture of hard spheres because of the electrostatic repulsive interaction between proteins, which results in a strong ionic strength dependence of the colloidal stability.

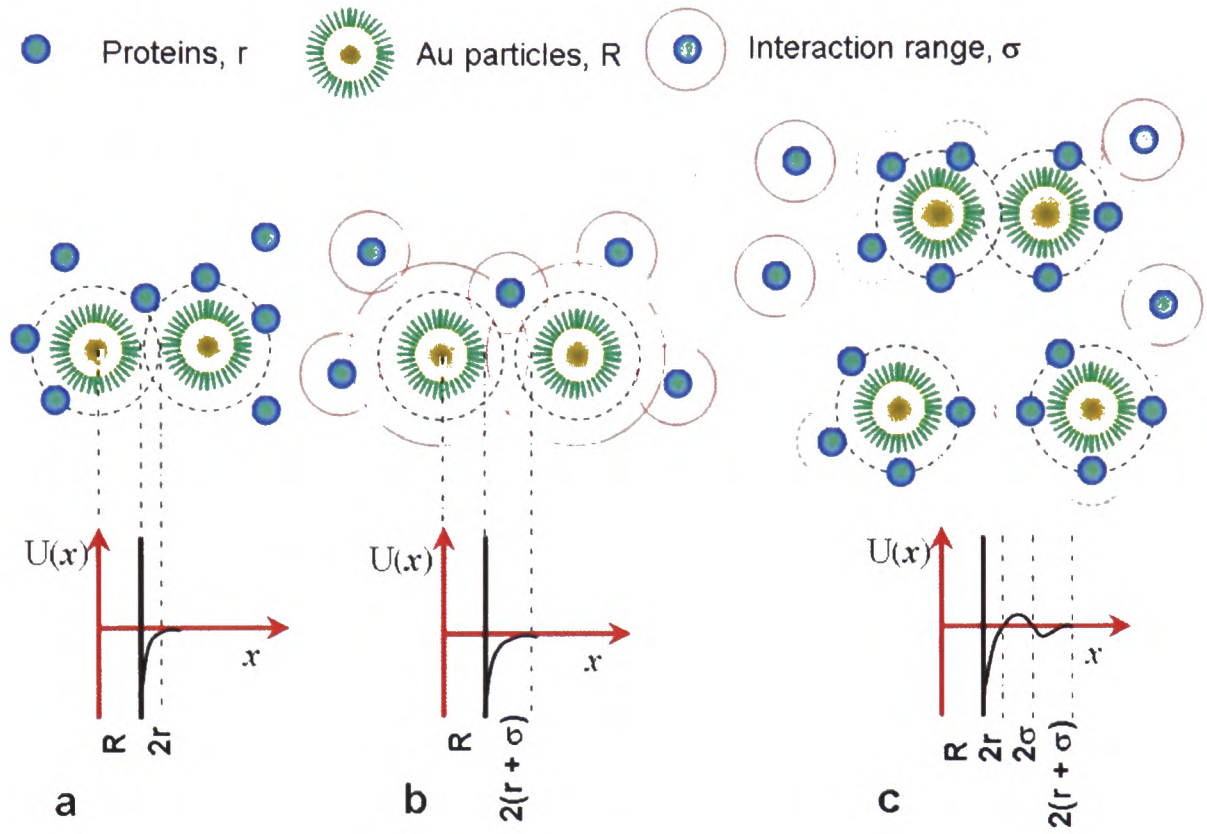


Figure 7.23.: Schematic drawing of depletion interaction under various conditions, (a) both particles are hard spheres, the depletion interaction has a range of 2r; (b) both particles have an external repulsive potential with interaction range σ. The effective interaction between big particles is an enhanced depletion interaction with a range of $2(r + \sigma)$; (c) Small particles have an external repulsive potential of σ, while big particles are hard spheres. The effective interaction between a pair of big particles shows an "oscillation" potential. When adding salt to this solution, the external Coulombic repulsion is screened, the whole system is back to the condition of (a). For detailed description, see text. (Figure courtesy of F. Zhang)

When both particles have an external repulsive potential with interaction range σ (**Figure 7.23b**), the effective interaction between large particles is an enhanced depletion interaction with a range of $2(r + \sigma)$. If the small particles have an external repulsive potential of σ, while the big particles are hard spheres (**Figure 7.23c**), then the interaction between small and big particles is still a hard sphere interaction. The repulsion between small particles leads to a layer of accumulated particles around the large particles. The dashed half-circle around them indicates the repulsive interaction to other small particles. When the inter-particle distance, D, of a pair

of big particles is such that 2R<D<2R+2r, a similar depletion interaction as **Figure 7.23a** occurs. If the inter-particle distance is increased, 2R+2r<D<2R+2r+2σ, the repulsion between the "absorbed" layer creates a repulsive zone with a range of 2σ; further increase of the distance, 2R+2r+2σ < D < 2R+2r+2σ+2(r+σ), leads to a depletion interaction similar to **Figure 7.23b**. Therefore, the effective interaction between a pair of big particles shows an "oscillation" potential, that is damped out very fast [84]. When adding salt to this solution, the external Coulombic repulsion is screened, and the whole system is back to the condition of **Figure 7.23a**.

UV-vis spectra indicate that adding salt decreases the critical protein concentration (see **Table 7.7**) and also speeds up the aggregation (**Figure 7.22b**). Upon adding salt directly into the colloidal solution, the spectra do not change at all (data not shown). Interactions between the OEG decorated gold colloids include attractive van der Waals forces, which is the major reason for the flocculation of colloidal solutions. If there are no repulsive interactions to balance the van der Waals forces, the gold colloids will aggregate [1]. In the case of OEG decorated gold colloids in solution, the repulsive interactions may arise from surface charge, i.e. negative charge due to the tightly bound layer of hydroxide ions [17, 71, 92], or the steric or entropic effect of the OEG SAM layers. Our experimental results indicate that the resulting colloidal solutions are stable at ionic strengths up to 1.0 M. In this case the surface charge is completely screened. In contrast, native, citrate stabilised colloidal gold is very sensitive to ionic strength and aggregates quickly upon addition of salt. Therefore, it can be concluded that the repulsive interaction due to surface charge is rather limited for OEG protected gold colloids.

In the mixture of colloid and protein, the protein molecules are negatively charged; if the colloidal surface is also negatively charged, then the electrostatic repulsive interaction will enhance the depletion effect in solution (see **Figure 7.23b**) [83]. Upon adding salt, the surface charges are screened, and the depletion effect will be relatively reduced. This is in contradiction to our experimental observation; when adding salt we observed an enhanced depletion effect: a faster aggregation of colloid, or lower critical protein concentration. This observation also contradicts the idea of the existence of a significant surface charge on the colloidal surface.

Hence, the repulsive interaction in a colloidal solution is more likely to originate principally from the entropic effects of the OEG SAM layer, which is a rather short

ranged interaction of the order of the thickness of the hydration layer. The interaction between colloid and protein is also related to this short ranged repulsive interaction. Compared to the long-ranged repulsive interaction between protein molecules, the colloid is rather "neutral" to the protein molecules. In this case, an oscillatory structure force arises, which reduces the depletion effect (**Figure 7.23c**) [83, 89]. Due to the fact that protein molecules repel each other through a long-range repulsion of a range $s \gg 2r$, they tend to accumulate near inert colloidal surfaces; a repulsion at contact followed by oscillations will then appear at high protein density in the colloid-colloid effective potential [83]. When adding salt with concentrations of less than 0.3 M, the surface charges of proteins are progressively screened, the oscillation effect is reduced, and c* decreases. For salt concentrations larger than 0.3 M, the surface charge is severely screened and adding more salt does not change the effective interaction significantly, as shown in **Table 7.7**.

7.2.5. Conclusions

Based on our results and discussions presented above, we reach the following conclusions. Firstly, OEG SAMs stabilise colloidal gold in solution in a wide range of temperature, ionic strength and pH. In addition, such OEG protected gold colloids do not bind to protein indicating the protein resistance of the OEG SAM. Secondly, the interactions between protected colloid and protein in mixtures, which determine the mechanism of protein resistance of the OEG SAM, show a rather short-ranged, mainly entropic repulsive contribution. Thirdly, the decorated colloids can form aggregates upon adding protein above a critical concentration, c*. The aggregates can be re-dissolved by diluting the solution. Our results demonstrate that adding proteins to such a colloidal solution creates an attractive depletion interaction between colloids. This depletion effect is enhanced with increasing the size of colloids due to the enhanced imbalance of osmotic pressure. A decrease of c* was observed by using a larger size of colloid. The effective interaction between colloids also depends on the ionic strength of the solution as observed as the decrease of c* upon increasing the ionic strength. This effect of ionic strength can be explained by screening of the surface charge of proteins, which changes the interaction potential between colloids from an oscillatory potential to a pure depletion attractive potential as schematically presented in **Figure 7.23**.

Bibliography

[1] C.S. Weisbecker, M.V. Merritt, and G.M. Whitesides. Molecular self-assembly of aliphatic thiols on gold colloids. *Langmuir*, 12(16):3763–3772, 1996.

[2] K. Aslan and V.H. Perez-Luna. Surface modification of colloidal gold by chemisorption of alkanethiols in the presence of a nonionic surfactant. *Langmuir*, 18(16):6059–6065, 2002.

[3] A. Schreyer, R. Siebrecht, U. Englisch, U. Pietsch, and Zabel H. Adam, the new reflectometer at the ill. *Physica B*, 248:349–354, 1998.

[4] D. G. Bucknall, J. Penfold, J. R. P. Webster, A. Zarbakhsh, R. M. Richardson, A. Rennie, J. S. Higgins, R. A. L. Jones, P. Fletcher, R.K. Thomas, S. Roser, and E. Dickinson. Surf - a second generation neutron reflectometer. *ICANS-XIII*, pages 123–129, 1995.

[5] *http://www.isis.rl.ac.uk/OpenGENIE/.*

[6] V. Zamlynny. *Electrochemical and Spectroscopic Studies of Pyridine Surfactants at the Gold-Electrolyte Interface.* PhD thesis, University of Guelph, Canada, 2002.

[7] R. J. Cernik, P. Barnes, G. Bushnell-Wye, A. J. Dent, G. P. Diakun, J. V. Flaherty, G. N. Greaves, E. L. Heeley, W. Helsby, S. D. M. Jacques, J. Kay, T. Rayment, A. Ryan, C. C. Tang, and N. J. Terrill. The new materials processing beamline at the SRS Daresbury, MPW6.2. *Journal of Synchrotron Radiation*, 11(2):163–170, Mar 2004.

[8] H.-G. Haubold, K. Gruenhagen, M. Wagener, H. Jungbluth, H. Heer, A. Pfeil, H. Rongen, G. Brandenburg, R. Moeller, J. Matzerarth, P. Hiller, and H. Halling. *Rev. Sci. Instrum.*, 60:1943–1946, 1989.

[9] R. M. J. Jacobs. Bruker d8 advance technical specification. *http://saf.chem.ox.ac.uk/*, 2006.

[10] E. A. Vogler. Water and the acute biological response to surfaces. *J. Biomater. Sci. Polym. Ed.*, 10:1015–1045, 1999.

[11] J. Israelachvili and H. Wennerstrom. Role of hydration and water structure in biological and colloidal interactions. *Nature*, 379:219–225, 1996.

[12] R. Steitz, T. Gutberlet, T. Hauss, B. Klosgen, R. Krastev, S. Schemmel, A. C. Simonsen, and G. H. Findenegg. Nanobubbles and their precursor layer at the interface of water against a hydrophobic substrate. *Langmuir*, 19:2409–2418, 2003.

[13] M. W. A. Skoda, F. Schreiber, R. Dahint, and M. et al. Grunze. *To be submitted for publication*, 2007.

[14] D. Schwendel, T. Hayashi, R. Dahint, A. Pertsin, M. Grunze, R. Steitz, and F. Schreiber. Interaction of water with self-assembled monolayers: Neutron reflectivity measurements of the water density in the interface region. *Langmuir*, 19:2284–2293, 2003.

[15] H.I. Kim, J.G. Kushmerick, J.E. Houston, and B.C. Bunker. Viscous "interphase" water adjacent to oligo(ethylene glycol)-terminated monolayers. *Langmuir*, 19(22):9271–9275, 2003.

[16] R. L. C. Wang, H. Kreuzer, and M. Grunze. The interaction of oligo(ethylene oxide) with water : a quantum mechanical study. *J. Phys. Chem. Chem. Phys*, 2:3613–3622, 2000.

[17] M. Zolk, F. Eisert, J. Pipper, S. Herrwerth, W. Eck, M. Buck, and M. Grunze. Solvation of oligo(ethylene glycol)-terminated self-assembled monolayers studied by vibrational sum frequency spectroscopy. *Langmuir*, 16:5849–5852, 2000.

[18] J. Zheng, L. Li, S. Chen, and S. Jiang. Molecular simulation study of water interactions with oligo (ethylene glycol)-terminated alkanethiol self-assembled monolayers. *Langmuir*, 20:8931–8938, 2004.

[19] C. Braun. Parratt32 version 1.6, www.hmi.de/grossgeraete/bensc.

[20] J. Ihringer. A quantitative measure for the goodness of fit in profile refinements with more than 20 degrees of freedom. *J. Appl. Crystallogr.*, 28(5):618–619, Oct 1995.

[21] W. C. Hamilton. Sginificance tests on the crystallographic r factor. *Acta Cryst.*, 18:502–510, 1965.

[22] F. Schreiber. Structure and growth of self-assembling monolayers. *Prog. Surf. Sci.*, 65:151–257, 2000.

[23] P. Harder, M. Grunze, and R. Dahint. Molecular conformation in oligo(ethylene glycol)-terminated self-assembled monolayers on gold and silver surfaces determines their ability to resist protein adsorption. *J. Phys. Chem. B*, 102:426–436, August 1998.

[24] D. Schwendel, R. Dahint, S. Herrwerth, M. Schloerholz, W. Eck, and M. Grunze. Temperature dependence of the protein resistance of poly- and oligo(ethylene glycol)-terminated alkanethiolate monolayers. *Langmuir*, 17(19):5717–5720, 2001.

[25] Y. M. Efimova. *Proteins at surfaces.* PhD thesis, Technische Universiteit Delft, 2006.

[26] V. Silin, H. Weetall, and D.J. Vanderah. Spr studies of the nonspecific adsorption kinetics of human igg and bsa on gold surfaces modified by self-assembled monolayers (sams). *J. Colloid Interface Sci.*, 185:94–103(10), January 1997.

[27] M. L. Ferrer, R. Duchowicz, B. Carrasco, J. G. de la Torre, and A. U. Acuna. The Conformation of Serum Albumin in Solution: A Combined Phosphorescence Depolarization-Hydrodynamic Modeling Study. *Biophys. J.*, 80(5):2422–2430, 2001.

[28] P. Ball. How to keep dry in water. *Nature*, 423:25–26, 2003.

[29] D. A. Doshi, E. B. Watkins, J. N. Israelachvili, and J. Majewski. Reduced water density at hydrophobic surfaces: Effect of dissolved gases. *PNAS*, 102(27):9458–9462, 2005.

[30] J. Fick. *Charakterisierung von biokompatiblen Oberflächen mittels Vibrations-Summenfrequenzspektroskopie und Neutronenreflektometrie.* PhD thesis, Universität Heidelberg, 2005.

[31] R. Valiokas, S. Svedhem, S.C.T. Svensson, and B. Liedberg. Self-assembled monolayers of oligo(ethylene glycol)-terminated and amide group containing alkanethiolates on gold. *Langmuir*, 15(10):3390–3394, 1999.

[32] S.Herrwerth, W. Eck, S. Reinhardt, and M. Grunze. Factors that determine the protein resistance of oligoether self-assembled monolayers - internal hydrophilicity, terminal hydrophilicity, and lateral packing density. *J. Am. Chem. Soc.*, (125):9359–9366, July 2003.

[33] L. Malysheva, A. Onipko, R. Valiokas, and B. Liedberg. First-principle dft and mp2 modeling of infrared reflection-absorption spectra of oriented helical ethylene glycol oligomers. *J. Phys. Chem. B*, 109(27):13221–13227, April 2005.

[34] M. Ostblom, R. Valiokas, P. Konradsson, S.C.T. Svensson, B. Liedberg, M. Garrett, and D.L. Allara. Ice nucleation and phase behavior on oligo(ethylene glycol) and hydroxyl self-assembled monolayers: Simulations and experiments. *J. Phys. Chem. B*, 110(4):1830–1836, 2006.

[35] A.M. Bittner, M. Epple, K. Kuhnke, R. Houriet, A. Heusler, H. Vogel, A.P. Seitsonen, and K. Kern. Conformations of an amino-amido-thiolate self-assembled layer on gold in air and in electrolytes. *J. Electroanal. Chem.*, 550-551:113–124, 2003.

[36] I. Engquist, M. Lestelius, and B. Liedberg. Hydrogen bond interaction between self-assembled monolayers and adsorbed water molecules and its implications for cluster formation. *J. Phys. Chem.*, 99:14198–14200, 1995.

[37] T. H. Ong, P. B. Davies, and C. D. Bain. Sum-frequency spectroscopy of monolayers of alkoxy-terminated alkanethiols in contact with liquids. *Langmuir*, 9:1836–1845, 1993.

[38] D. J. Vanderah, H. La, J. Naff, V. Silin, and K. A. Rubinson. Control of protein adsorption: Molecular level structural and spatial variables. *J. Am. Chem. Soc.*, 126(42):13639 –13641, October 2004.

[39] D. K. Schwartz. Mechanisms and kinetics of self-assembled monolayer formation. *Annu. Rev. Phys. Chem.*, 52:107–137, 2001.

[40] F. Schreiber, A. Eberhardt, T. Y. B. Leung, P. Schwartz, S. M. Wetterer, D. J. Lavrich, L. Berman, P. Fenter, P. Eisenberger, and G. Scoles. Adsorption mechanisms, structures, and growth regimes of archetypal self-assembling system: decanethiol on au(111). *Phys. Rev. B*, 57:12476, 1998.

[41] WaveMetrics Inc. Igor pro 5. *http://www.wavemetrics.com/*, 2005.

[42] Max Born and Emil Wolf. *Principles of Optics: Electromagnetic Theory of Propagation, Interference and Diffraction of Light.* Cambridge University Press; 6th Edition, 1997.

[43] F. Abelés. *Ann. Phys.*, 5:596, 1950.

[44] F. Abelés. *Advanced Optical Techniques.* John Willey&Sons, New York, 1967.

[45] W. Hansen. Electric fields produced by the propagation of plane coherent electromagnetic radiation in a stratified medium. *J. Opt. Soc. Am*, 58:380–390, 1968.

[46] R. M. Corn. *http://corninfo.ps.uci.edu/writings/Ref4txt.html.*

[47] J. E. Bertie, M. K. Ahmed, and H. H. Eysel. Infrared intensities of liquids. 5. optical and dielectric constants, integrated intensities, and dipole moment derivatives of h20 and d20 at 22° c. *J. Phys. Chem.*, 93:2210–2218, 1989.

[48] I. H. Malitson. Refractive properties of barium fluoride. *J. Opt. Soc. Am.*, 54:628, 1964.

[49] Luxpop Inc. *www.luxpop.com.*

[50] Wikipedia. en.wikipedia.org/wiki/barium-fluoride.

[51] J. B. Hayter and J. Penfold. An analytic structure factor for macroion solutions. *Mol. Phys.*, 42:109–118, 1981.

[52] J. P. Hansen and J. B. Hayter. Interaction of proteins in solution from small-angle scattering: A perturbative approach. *Mol. Phys.*, 46:651–656, 1982.

[53] M. Kozak. Glucose isomerase from *streptomyces rubiginosus* - potential molecular weight standard for small-angle x-ray scattering. *J. Appl. Crystallogr.*, 38(3):555–558, Jun 2005.

[54] Doris Orthaber, Alexander Bergmann, and Otto Glatter. SAXS experiments on absolute scale with Kratky systems using water as a secondary standard. *Journal of Applied Crystallography*, 33(2):218–225, Apr 2000.

[55] D. C. Carter and J. X. Ho. Structure of serum albumin. *Adv. Protein Chem.*, 45:153–203, 1994.

[56] D. Bendedouch and S.-H. Chen. Structure and interparticle interactions of bovine serum albumin in solution studied by small-angle neutron scattering. *J. Phys. Chem.*, 87:1473–1477, 1983.

[57] R. Nossal, C. J. Glinka, and S. H. Chen. Small angle neutron scattering studies of concentrated protein solutions: I. bovine serum albumin. *Biopolymers*, 25:1157, 1986.

[58] D. Bendedouch and S.-H. Chen. Effect of an attractlve potential on the interparticle structure of ionic micelles at high salt concentration. *J. Phys. Chem.*, 88:648–652, 1984.

[59] C. Tanford, S. A. Swanson, and W. S. Shore. Hydrogen ion equilibria of bovine serum albumin. *J. Am. Chem. Soc.*, 77:6414–6421, 1955.

[60] G. Scatchard, I. H. Scheinberg, and S. H. Jr. Armstrong. Physical chemistry of protein solutions. iv. the combination of human serum albumin with chloride ion. *J. Am. Chem. Soc.*, 72:535, 1950.

[61] R. J. Baxter. Percus-yevick equation for hard spheres with surface adhesion. *J. Chem. Phys.*, 49(6):2770–2774, 1968.

[62] S. V . G. Menon, C.Manohar, and K.Srinivasa Rao. A new interpretation of the sticky hard sphere model. *J. Chem. Phys.*, 95:9186, 1991.

[63] Y. Liu, W.-R. Chen, and S.-H. Chen. Cluster formation in two-yukawa fluids. *J. Chem. Phys.*, 122:044507, 2005.

[64] D. E. Kuehner, H. W. Blanch, and J. M. Prausnitz. Salt-induced protein precipitation: Phase equilibria from an equation of state. *Fluid Phase Equilib.*, 116:140–147, 1996.

[65] D. N. Petsev and P. G. Vekilov. Evidence for non-dlvo hydration interactions in solutions of the protein apoferritin. *Phys. Rev. Lett.*, 84:1339–1342, 2000.

[66] T. Arakawa and S.N. Timasheff. Preferential interactions of proteins with salts in concentrated solutions. *Biochemistry*, 21:6545–6552, 1982.

[67] R. A. Curtis, J. M. Prausnitz, and H. W. Blanch. Protein-protein and protein-salt interactions in aqueous protein solutions containing concentrated electrolytes. *Biotechnol. Bioeng*, 57:11–21, 1998.

[68] K. D. Collins. Charge density-dependent strength of hydration and biological structure. *Biophys. J.l*, 72:65–76, 1997.

[69] S. I. Jeon, J. H. Lee, J. D. Andrade, and P. G. de Gennes. Protei-surface interactions in the presence of polyethylene oxide. *J. Coll. Int. Sci.*, 142(1):149–157, August 1990.

[70] I. Szleifer. Protein adsorption on surfaces with grafted polymers: A theoretical approach. *Biophys J.*, 72:595–612, 1997.

[71] K. Feldman, G. Hähner, N. D. Spencer, P. Harder, and M. Grunze. Probing resistance to protein adsorption of oligo(ethylene glycol)-terminated self-assembled monolayers by scanning force microscopy. *J. Am. Chem. Soc.*, 121(43):10134 –10141, October 1999.

[72] M. A. Rixman, D. Dean, C. E. Macias, and C. Ortiz. Nanoscale intermolecular interactions between human serum albumin and alkanethiol self-assembled monolayers. *Langmuir*, 19:6202–6218, January 2003.

[73] D. Schwendel. *Untersuchung der Grenzphasenbildung von Oligo(ethylenglykol)-terminierten Alkanthiolatmonolagen auf Gold in Kontakt mit Wasser und wäßriger Proteinlösung.* PhD thesis, Universität Heidelberg, 2003.

[74] Y.-Y. Luk, M. Kato, and M. Mrksich. Self-assembled monolayers of alkanethiolates presenting mannitol groups are inert to protein adsorption and cell attachment. *Langmuir*, 16:9604–9608, June 2000.

[75] R. Roth and S. Dietrich. Binary hard-sphere fluids near a hard wall. *Phys. Rev. E*, 62(5):6926–6936, Nov 2000.

[76] C. N. Patra. Structure of binary hard-sphere mixtures near a hard wall: A simple weighted-density-functional approach. *The Journal of Chemical Physics*, 111(14):6573–6578, 1999.

[77] C. Bechinger and R. Dahint. Private communication. 2007.

[78] S.H. Brewer, W.R. Glomm, M.C. Johnson, M.K. Knag, and S. Franzen. Probing bsa binding to citrate-coated gold nanoparticles and surfaces. *Langmuir*, 21(20):9303–9307, 2005.

[79] Jan Ilavsky. Irena 2 package of sas data evaluation and modeling macros for igor pro. *http://www.uni.aps.anl.gov/ ilavsky/irena.html*, 2006.

[80] M. W. A. Skoda, F. Zhang, and et al. *To be submitted for publication*, 2007.

[81] A.A. Lazarides and G.C. Schatz. Dna-linked metal nanosphere materials: Structural basis for the optical properties. *J. Phys. Chem. B*, 104(3):460–467, 2000.

[82] K.S. Mayya, V. Patil, and M. Sastry. On the stability of carboxylic acid derivatized gold colloidal particles: The role of colloidal solution ph studied by optical absorption spectroscopy. *Langmuir*, 13(15):3944–3947, 1997.

[83] L. J. Belloni. Colloidal interactions. *Phys. Condens. Matter*, 12:R549–R587, 2000.

[84] X. Ye, T. Narayanan, P. Tong, and J. S. Huang. Neutron scattering study of depletion interactions in a colloid-polymer mixture. *Phys. Rev. Lett.*, 76(24):4640–4643, Jun 1996.

[85] X. Ye, T. Narayanan, P. Tong, J. S. Huang, M. Y. Lin, B. L. Carvalho, and L. J. Fetters. Depletion interactions in colloid-polymer mixtures. *Phys. Rev. E*, 54(6):6500–6510, Dec 1996.

[86] H. J. M. Hanley, G. C. Straty, and P. Lindner. Partial scattered intensities from a binary suspension of polystyrene and silica. *Langmuir*, 10:72–79, 1994.

[87] R. H. Ottewill, H. J. Hanley, A. R. Rennie, and G. C. Straty. Small-angle neutron-scattering studies on binary-mixtures of charged-particles. *Langmuir*, 10:3757–3765, 1995.

[88] N. Lutterbach, H. Versmold, V. Reus, L. Belloni, Th. Zemb, and P. Lindner. Charge-stabilized liquidlike ordered binary colloidal suspensions. 2. partial structure factors determined by small-angle neutron scattering. *Langmuir*, 15(2):345–352, 1999.

[89] C. N. Likos. Effective interactions in soft condensed matter physics. *Phys. Rep.*, 348:267–439, 2001.

[90] W. C. K. Poon. The physics of a model colloid-polymer mixture. *J. Phys.: Condens. Matter*, 14(33):R859–R880, 2002.

[91] M. Dijkstra, R. van Roij, and R. Evans. Phase diagram of highly asymmetric binary hard-sphere mixtures. *Phys. Rev. E*, 59(5):5744–5771, May 1999.

[92] C. Dicke and G. Hähner. Interaction between a hydrophobic probe and tri(ethylene glycol)-containing self-assembled monolayers on gold studied with force spectroscopy in aqueous electrolyte solution. *J. Phys. Chem. B*, 106(17):4450–4456, January 2002.

8. Summary and conclusion

8.1. Summary and perspectives

The main achievement of this project is the successful application of *in situ* methods, such as neutron reflectivity and polarisation modulation infrared spectroscopy (PMIRRAS), for the detailed study of interfacial phenomena between OEG functionalised gold surfaces and protein solutions. The interactions of non-fouling OEG monolayer protected surfaces with proteins have been investigated in order to elucidate the mechanisms that lead to the repulsion of proteins. The interaction of water with the monolayers, which plays a crucial role for the non-fouling properties, but is also of general interest for biological and biotechnological systems, has been studied in great detail.

A strong interaction of OEG SAMs with water has been identified by two complementary methods: PMIRRAS studies have shown that a significant amount of water molecules penetrate into the OEG terminated monolayer, causing conformational changes of the OEG moieties. The amount of water and the subsequent changes were more pronounced when the surface coverage was smaller, most probably owing to an increased number of defects within the monolayer. Measurements of the protein adsorption showed more pronounced adsorption on the low coverage samples. In addition, neutron reflectivity measurements have revealed a rather extended region of a low density water phase adjacent to the monolayer. This region contains water with a density of about 90-95% that of bulk water and extends up to 5-7 nm into the bulk. These findings indicate that the OEG monolayer induces significant ordering of the water molecules at the interface, a phenomenon which plays a major role for the inertness of these surfaces. The extent and density of this "interphase" water did not change significantly at temperatures lower than room temperature, where a partial breakdown of the protein resistance was observed. This implies that

the onset of protein adsorption on protein resistant monolayers at low temperature is not or not only due to changes in the "interphase" water.

The interaction of proteins with OEG SAMs (and with each other) has been studied in detail by neutron reflectivity and small-angle x-ray scattering. The profile of the protein concentration in the vicinity of the SAM has been mapped, and the potential between OEG coated gold nanoparticles and proteins has been studied. It is found that the protein density close to a surface coated with an OEG monolayer oscillates around the bulk value with a period of about 100 Å, and that the oscillations are damped out with a decay length of 50-60 Å. This behaviour is characteristic of hard sphere ordering in the vicinity of a wall, as described by Roth and Dietrich [75], which in turn implies the absence of long range interactions. This observation was confirmed by measurements at varying ionic strength of the protein solution, where only small changes in the period and decay length of the oscillation are observed. This suggests that charges play only a minor role for the protein repulsive properties of OEG SAMs. Further support for this finding is given by small-angle scattering and UV-visible data on OEG protected gold colloids, clearly showing no ionic strength dependence of the colloid-protein interaction.

The ordering and layering of hard spheres close to a wall usually manifests itself in an oscillating decay of the sphere density with a period related to the hard sphere diameter[1] [76]. In our experiments, the period of the density oscillation was around 10 nm, which is close to the dimension of the BSA molecules. However, the non-spherical shape of the BSA and the influence of the charge have an unknown impact on the layering at the SAM-solution interface. The investigation of these questions is beyond the scope of this thesis, and further studies are necessary to illuminate these aspects of the SAM-protein interaction.

The successful application of PMIRRAS for the in situ study of monolayers on gold in contact with liquids has been demonstrated in this work; an implementation of the mathematical framework for the simulation of the signal obtained for such systems has been presented. These tools can also be applied to other systems, such as monolayers on silicon or sapphire. Although beyond the scope of this thesis, the in situ observation of structural changes in proteins upon adsorption is also possible.

[1] The behaviour of charged hard spheres is similar to that of neutral ones, with the only difference that the 'hard sphere' diameter is extended due to the electrostatic interaction.

In the same context, the in situ liquid cell can be adapted for temperature dependent measurements, opening up a variety of possible in situ studies of monolayers and proteins.

Neutron reflectivity studies have revealed the water and protein density profile at the solid-liquid interface of OEG terminated SAMs, partly by using contrast matching techniques, including the targeted deuteration of the monolayer. The experiments presented in this thesis have been performed exclusively on monolayers self-assembled on gold. Despite the complexity of the resulting system comprised of substrate, multiple metal layers, SAM and liquid phase, very good results were obtained. The same methods can be applied to systems of monolayers directly assembled on silicon of silicon oxide. This is a simplified system compared to the gold based one, which has advantages from the scattering point of view. However, monolayers on silicon are more difficult to produce than via the 'thiol-on-gold route'. Owing to this, such systems have not been studied as extensively yet and represent an interesting field of research, not least for their potential for a variety of applications in nano and biotechnology.

In a similar fashion, the small-angle scattering experiments on monolayer protected gold colloids can be easily transferred to silver colloids. On flat surfaces, OEG SAMs on silver are known to lose their non-fouling properties because of their higher packing density. The variation of the colloid diameter offers the possibility of inducing a variable degree of disorder and packing density, and the importance of chain mobility can be studied easily.

8.2. Methodical achievements

The work presented in this thesis was concerned with the investigation of oligo (ethylene glycol) (OEG) self-assembled monolayers (SAMs) and their interactions with water and aqueous protein solutions *in situ* and under physiological conditions. For this purpose three major techniques have been employed: neutron reflectivity, polarisation modulation infrared spectroscopy (PMIRRAS) and small-angle x-ray scattering. While neutron reflectivity and small-angle scattering are well known and widely used methods, PMIRRAS is less common and has recently become more popular for measurements in electrochemistry due to the use of gold electrodes.

Development of in situ PMIRRAS In the present work PMIRRAS has been applied to the in situ study of OEG SAMs in contact with water and protein solutions. For this purpose a spectroscopic cell assembly has been developed, to facilitate the observation of these systems through a thin layer of liquid. With this setup, the thickness of the liquid layer could be adjusted reproducibly to 1-4 μm, which was sufficient to achieve a good signal-to-noise ratio. The exact thickness of the liquid layer could be measured precisely for each sample using single wavelength ellipsometry.

Contrast enhanced neutron reflectivity The neutron reflectivity measurements at room temperature were performed using a MACOR built liquid cell in order to minimise incoherent background scattering from the solution (MACOR contains boron, which has a high absorption cross section for thermal neutrons). In order to achieve the best contrast at the solid-liquid interface, custom made, partly deuterated OEG SAMs were used. Contrast matching of SAM and solution to the gold scattering length density not only increased the sensitivity of the system; by using the same contrast for water (H_2O/D_2O mixture) and the protein solution, it was also possible to compare the reflectivity curves of the reference and the protein measurement immediately for the same sample.

A. Implementation of Abeles' matrix formalism

A.1. Hansen's notation implemented in IgorPro

```
function PMIRRAS3(sam)
Variable sam

Variable lm,n0,lambda
NVAR wavenumber = root:packages:bi_layers:wavenumber
NVAR startangle = root:packages:bi_layers:varyStartAngle
NVAR endangle = root:packages:bi_layers:varyEndAngle
NVAR startthickness = root:packages:bi_layers:varyStartThickness
NVAR endthickness = root:packages:bi_layers:varyEndThickness
NVAR evalpoints = root:packages:bi_layers:evalPoints
NVAR n1re = root:packages:bi_layers:paramRe_1
NVAR n2re = root:packages:bi_layers:paramRe_4
NVAR n3re = root:packages:bi_layers:paramRe_3
NVAR n4re = root:packages:bi_layers:paramRe_2
NVAR n1im = root:packages:bi_layers:paramIm_1
NVAR n2im = root:packages:bi_layers:paramIm_4
NVAR n3im = root:packages:bi_layers:paramIm_3
NVAR n4im = root:packages:bi_layers:paramIm_2
NVAR d2 = root:packages:bi_layers:paramD_4
NVAR d3 = root:packages:bi_layers:paramD_3

lambda = 1/wavenumber*1E7 //wavelength in nm
lm = lambda/1E3 //wavelength in um
print lm



Print n0

if(sam==1)
dowindow /k PMIRRAS_signal
endif

//killwaves PM, pRp, prs, angle, reflp,refls

// and remove n and k box


If (sam==1)
Make/O/N=(evalpoints+1) withsam
endif
If (sam==0)
Make/O/N=(evalpoints+1) nosam
endif

Make/O/N=(evalpoints+1) angle,thickness,rad,pRp, pRs, z1,z2, PM
Make/O/N=(evalpoints+1)/C reflp, refls,xi1,xi2,xi3,xi4,q1,q2,q3,q4,
b2,b3,ct,ct2,cts,ct2s
```

```
Make/O/N=(evalpoints+1)/C m2n11, m2n12,m2n21,m2n22,m3n11,
m3n12,m3n21,m3n22
Make/O/N=(evalpoints+1)/C m11,m12,m21,m22
Make/O/N=(evalpoints+1)/C m2n11s, m2n12s,m2n21s,m2n22s,
m3n11s,m3n12s,m3n21s,m3n22s
Make/O/N=(evalpoints+1)/C m11s,m12s,m21s,m22s
Variable /C n1,n2,n3,n4,e1,e2,e3,e4
DefaultFont/U "Helvetica"

NVAR varypar = root:Packages:bi_layers:varyParameter
NVAR fixedangle = root:Packages:bi_layers:angle

if  (varypar== 2)
thickness = (endthickness-startthickness)*x/evalpoints
thickness = thickness + startthickness
endif

// evalpoints gives range of angles; 2000 is number of points:

angle = (endangle-startangle)*x/evalpoints
angle = angle + startangle //  0 is the start of the range of angles
rad = angle*pi/180 //  Converts angle in degrees to radians

if (varypar == 2)
rad = fixedangle*pi/180
endif

//  Assign complex indices of refraction, n; calculate


n1 = cmplx(n1re,n1im) //  the dielectric constants, e
e1 = n1*n1
n2 = cmplx(n2re,n2im)
e2 = n2*n2
n3 = cmplx(n3re,n3im)
if(sam==0)
   n3=n2 //switch off SAM
endif
e3 = n3*n3
n4 = cmplx(n4re,n4im)
e4 = n4*n4


//  Use e to calculate values of xi
xi1 = n1*cmplx(cos(rad),0)

xi2 = e2 - e1*cmplx((sin(rad))^2,0)
ct = r2polar(xi2) // 3 lines to get square root of the
ct2 = cmplx(sqrt(real(ct)), abs(imag(ct)/2)) // complex wave by going to
xi2= p2rect(ct2) // polar coordinates

xi3 = e3 - e1*cmplx((sin(rad))^2,0)
ct = r2polar(xi3) // ct and ct2 just temporary waves
ct2 = cmplx(sqrt(real(ct)),abs(imag(ct)/2)) // in the square root calc
xi3 = p2rect(ct2)

xi4 = e4 - e1*cmplx((sin(rad))^2,0)
ct = r2polar(xi4)
ct2 = cmplx(sqrt(real(ct)),abs(imag(ct)/2))
xi4 = p2rect(ct2)

if  (varypar== 2)
b2 = cmplx(2*pi*thickness/lambda,0)
endif
if  (varypar== 1)
b2 = cmplx(2*pi*d2/lambda,0)
endif
//b2 = cmplx(2*pi*d2/lambda,0)
b2 = b2*xi2 // calc of the beta values (called b here)
b3 = cmplx(2*pi*d3/lambda,0)
```

```
b3 = b3*xi3
q1 = xi1/e1 // calc of q values
q2 = xi2/e2
q3 = xi3/e3
q4 = xi4/e4

// reflectivity calc of p-polarized light

z1 = cos(real(b2))*cosh(imag(b2)) // calc real part of the cosine of b2
z2 = -sin(real(b2))*sinh(imag(b2)) // calc imag part of the cosine of b2
m2n11 = cmplx(z1,z2) // the 1,1 element of matrix M2
m2n22 = m2n11 // the 2,2 element is the same
z1 = sin(real(b2))*cosh(imag(b2)) // calc real part of the sine of b2
z2 = cos(real(b2))*sinh(imag(b2)) // calc imag part of the sine of b2
m2n12 = cmplx(0,-1)*cmplx(z1,z2)/q2 // calc 1,2 element of matrix M2
m2n21 = cmplx(0,-1)*cmplx(z1,z2)*q2 // calc 2,1 element of matrix M2
z1 = cos(real(b3))*cosh(imag(b3)) //
z2 = -sin(real(b3))*sinh(imag(b3)) //
m3n11 = cmplx(z1,z2) //
m3n22 = m3n11 // same as above
z1 = sin(real(b3))*cosh(imag(b3)) // but now for matrix M3
z2 = cos(real(b3))*sinh(imag(b3)) //
m3n12 = cmplx(0,-1)*cmplx(z1,z2)/q3 //
m3n21 = cmplx(0,-1)*cmplx(z1,z2)*q3 //

m11 = m2n11*m3n11 + m2n12*m3n21 //
m12 = m2n11*m3n12 + m2n12*m3n22 // M2 * M3 = M
m21 = m2n21*m3n11 + m2n22*m3n21 //
m22 = m2n21*m3n12 + m2n22*m3n22 //

ct = (m11 + m12*q4)*q1 // ct and ct2 are temporary waves
ct2 = m21 + m22*q4 // used to calc reflectance, r

reflp = (ct - ct2)/(ct + ct2) //
prp = magsqr(reflp) * 100 // calc % reflectivity of p-polarized light

    // reflectance calculation of s-polarised light

z1 = cos(real(b2))*cosh(imag(b2)) // calc real part of the cosine of b2
z2 = -sin(real(b2))*sinh(imag(b2)) // calc imag part of the cosine of b2

m2n11s = cmplx(z1,z2) // the 1,1 element of matrix M2
m2n22s = m2n11s // the 2,2 element is the same

z1 = sin(real(b2))*cosh(imag(b2)) // calc real part of the sine of b2
z2 = cos(real(b2))*sinh(imag(b2)) // calc imag part of the sine of b2

m2n12s = cmplx(0,-1)*cmplx(z1,z2)/xi2 // calc 1,2 element of matrix M2
m2n21s = cmplx(0,-1)*cmplx(z1,z2)*xi2 // calc 2,1 element of matrix M2

z1 = cos(real(b3))*cosh(imag(b3)) //
z2 = -sin(real(b3))*sinh(imag(b3)) //

m3n11s = cmplx(z1,z2) //
m3n22s = m3n11s // same as above

z1 = sin(real(b3))*cosh(imag(b3)) // but now for matrix M3
z2 = cos(real(b3))*sinh(imag(b3)) //

m3n12s = cmplx(0,-1)*cmplx(z1,z2)/xi3 //
m3n21s = cmplx(0,-1)*cmplx(z1,z2)*xi3 //

m11s = m2n11s*m3n11s + m2n12s*m3n21s //
m12s = m2n11s*m3n12s + m2n12s*m3n22s // M2 * M3 = M
m21s = m2n21s*m3n11s + m2n22s*m3n21s //
m22s = m2n21s*m3n12s + m2n22s*m3n22s //

ct = (m11s + m12s*xi4)*xi1 // ct and ct2 are temporary waves
ct2 = m21s + m22s*xi4 // used to calc reflectance, r

refls = (ct - ct2)/(ct + ct2) //
```

```
prs = magsqr(refls) * 100 // calc % reflectivity of s-polarized light

if(sam==0)
dowindow /k reflectivity_nosam
if  (varypar == 1)
   Display/K=1 /N=reflectivity_nosam /W=(400,0,800,210) pRp vs angle
   AppendToGraph /C=(0,0,65535)  pRs vs angle
   Label bottom "angle"
endif
if  (varypar == 2)
   Display /K=1/N=reflectivity_nosam /W=(400,0,800,210) pRp vs thickness
   AppendToGraph /C=(0,0,65535)  pRs vs thickness
   Label bottom "thickness [nm]"
endif


Legend
ShowInfo
endif
if(sam==1)
dowindow /k reflectivity_sam
if  (varypar == 1)
   Display /K=1/N=reflectivity_sam pRp vs angle
AppendToGraph /C=(0,0,65535)  pRs vs angle
Label bottom "angle"
endif
if  (varypar == 2)
Display /K=1/N=reflectivity_sam pRp vs thickness
AppendToGraph /C=(0,0,65535)  pRs vs thickness
Label bottom "thickness [nm]"
endif
Legend
ShowInfo
endif

killwaves rad, z1,z2, xi1,xi2,xi3,xi4,q1,q2,q3,q4,b2,b3,ct,ct2, cts,ct2s,m2n11, m2n12
killwaves m2n21,m2n22,m3n11,m3n12,m3n21,m3n22, m11,m12,m21,m22
killwaves m2n21s,m2n22s,m3n11s,m3n12s,m3n21s,m3n22s, m11s,m12s,m21s,m22s,m2n11s,m2n12s


PM=(prp-prs)/(prp+prs)
if(sam==1)
withsam=PM
endif
if(sam==0)
nosam=PM
endif
//Display /N=PMIRRAS_signal /W=(0,280,400,500) PM vs angle
end
```

A.2. Calculation of the mean square electric field at the metal surface

```
//-------------------------------------------------------------
Double_t abeles(TComplex n0, TComplex n1, TComplex k1,
TComplex theta0, Double_t wavenr, Double_t d1)
//-------------------------------------------------------------
{
    Int_t j;
    TComplex I(0,1);
    TComplex n[4];
    TComplex rp[4], tp[4];
    TComplex theta[4];
    TComplex delta[4];
    TComplex K[3];
    Double_t h[3];
    Double_t LambdaSqr;
```

```
    Double_t F;

// Au : n(2900) = 1.56     k(2900) = 24.09
// Au : n(1130) = 9.38     k(1130) = 60.08
// Au : n(2100) = 2.98     k(2100) = 33.46

    n[1] = n1 + k1*I;
    n[2] = 2.98 + 33.46*I;

    LambdaSqr = TMath::Power(1/wavenr,2);

// refractive index of BaF2 after Sellmeier

    n[0] = n0;

    h[1] = d1; // water thickness in um

    delta[0] = 0;
    theta[0] = theta0 * TMath::Pi()/180;

    for(Int_t j=1; j<3; j++){
      theta[j] = TComplex::ASin(n[j-1]/n[j] * TComplex::Sin(theta[j-1]));

      delta[j] = 2*TMath::Pi()*wavenr*n[j]*TComplex::Cos(theta[j])*h[j];

      rp[j] = (n[j-1]*TComplex::Cos(theta[j]) - n[j]*TComplex::Cos(theta[j-1]))
            / (n[j-1]*TComplex::Cos(theta[j]) + n[j]*TComplex::Cos(theta[j-1]));

      tp[j] = (2*n[j-1]*TComplex::Cos(theta[j-1]))
            / (n[j-1]*TComplex::Cos(theta[j]) + n[j]*TComplex::Cos(theta[j-1]));
    }

    K[2] = 2*TMath::Pi()*wavenr*n[2]*TComplex::Cos(theta[2]);

    F = TComplex::Power(TComplex::Abs((tp[1]*tp[2] * TComplex::Exp(I*K[2]*(h[1]-h[1]))
      * TComplex::Sin(theta[2])) / (TComplex::Exp(-I*delta[1])
      + rp[1]*rp[2]*TComplex::Exp(I*delta[1]))),2);

    return F*1e6;
}
```

B. Measured water layer thicknesses for in situ PMIRRAS

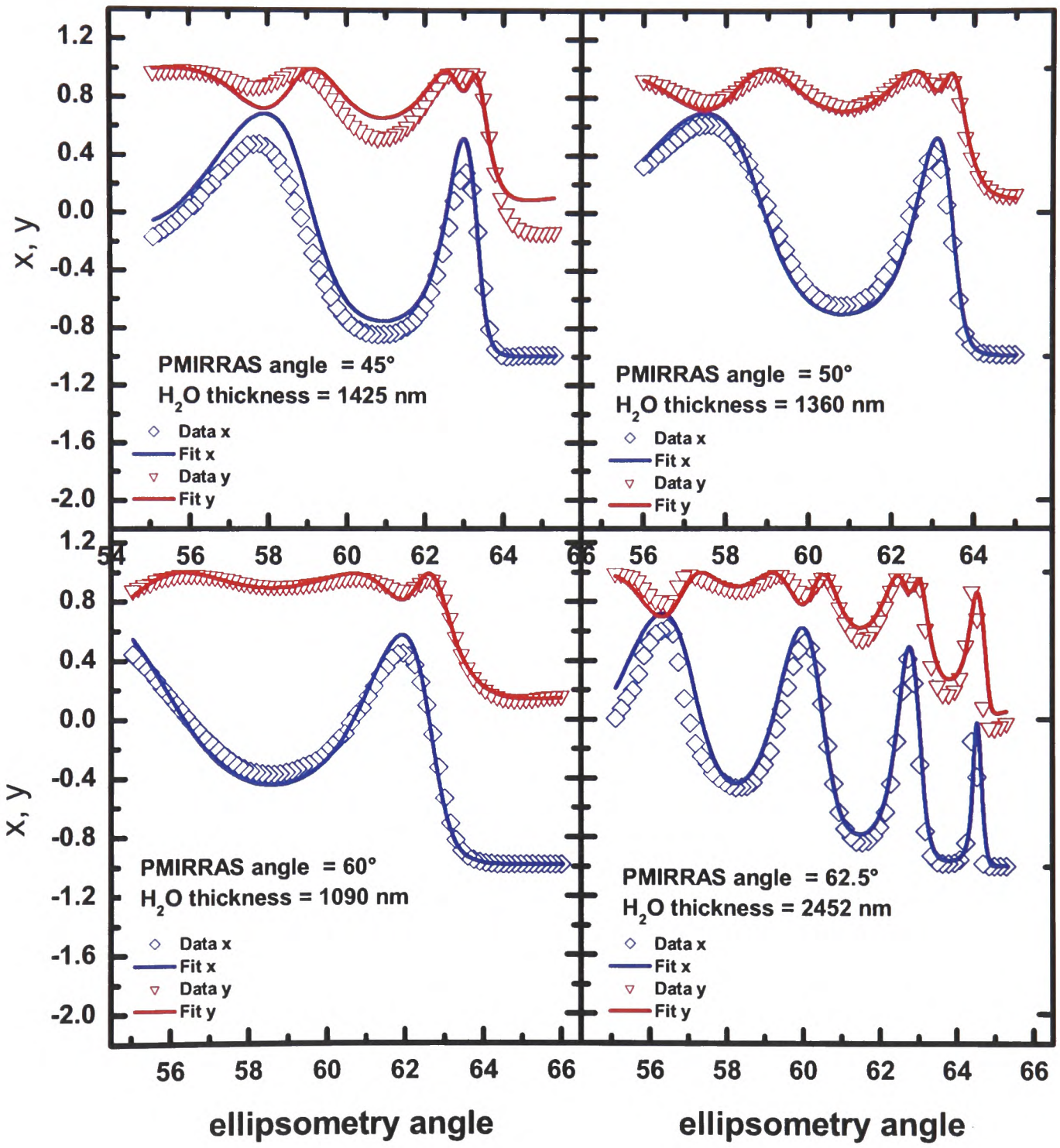


Figure B.1.: Ellipsometric measurements of the thickness of the water layer between barium fluoride half cylinder and sample. Each listed thickness corresponds to the PMIRRAS measurement at the given angle (45, 50, 60 and 62.5°).

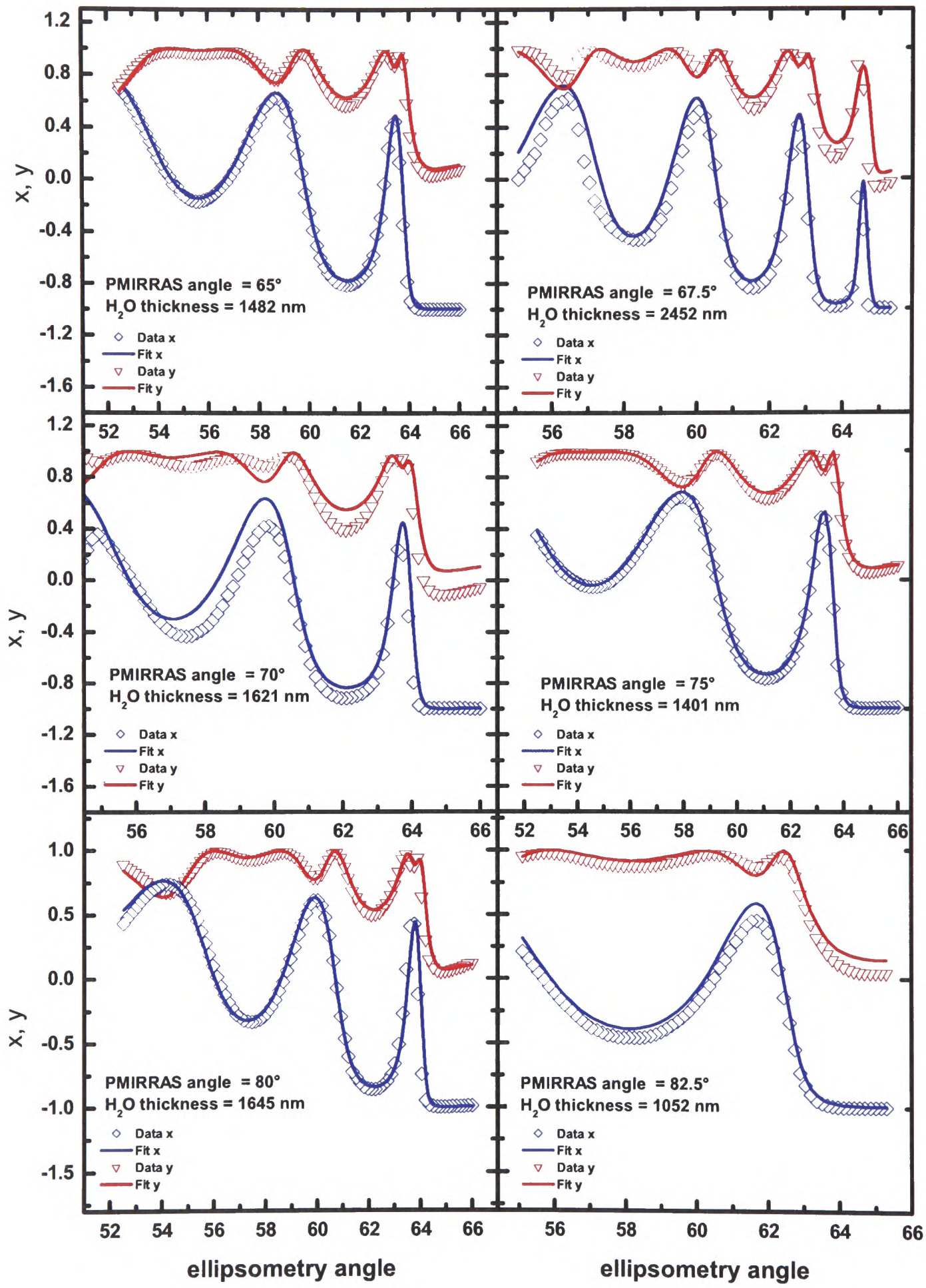


Figure B.2.: Ellipsometric measurements of the thickness of the water layer between barium fluoride half cylinder and sample. Each listed thickness corresponds to the PMIRRAS measurement at the given angle (65, 67.5, 70, 75, 80 and 82.5°).

C. Fitting software

Parratt32 This software obtained from the Hahn-Meitner Institut in Berlin uses a box model and calculates the reflectivity for a multilayer system based on PARRATT's recursive algorithm including roughness in the NEVOT-CROCE approximation. The fitting is based on the NEWTON minimisation algorithm for the least-squares sum. The least-suqres sum allows given error, 1/y and logarithmic weighting. The software also allows the use of built-in and user defined analytic functions, but the convergence speed of the fit is relatively low.

YAPP Yet Another Parratt Program is a proprietary software developed by the author in collaboration with A. Gerlach and is tailored for the use with analytical profile functions. The scattering length density profile or a part of it can be defined as an analytic function, which is then split into small boxes (of appropriate width) with zero roughness. The reflectivity calculation is performed using PARRATT's recursive algorithm including roughness in the NEVOT-CROCE approximation. The code is implemented in FORTRAN and the graphical user interface uses the XForms package (C++). The fitting routine employs the MINUIT package from CERN's cernlib libraries. This algorithm converges very fast and reliably. This software was partly used for the fitting of the oscillating damped functions of the protein solution datasets.

SURFace Developed by J. Webster and S. Langridge at ISIS, UK [1], this software was used for the determination of the appropriate starting parameters for particular datasets because of its user-friendly slider applets. SURFace also employs the fully dynamic Parratt formalism.

[1] http://www.isis.rl.ac.uk/LargeScale/SURF/technical/surface.htm

D. List of acronyms and symbols

AFM	Atomic Force Microscopy
AuXEG	EG6OMe protected gold colloid of diameter X
BaF_2	Barium Fluoride
BSA	Bovine Serum Albumin
CaF_2	Calcium Fluoride
DLVO	The DLVO theory is named after Derjaguin, Landau, Verwey and Overbeek
EG3OMe	$HS\text{-}(CH_2)_{11}\text{-}(O\text{-}CH_2\text{-}CH_2)_3\text{-}OCH_3$
EG6OMe	$HS\text{-}(CH_2)_{11}\text{-}(O\text{-}CH_2\text{-}CH_2)_6\text{-}OCH_3$
FIR	Far Infrared
FTIR	Fourier Transform Infrared (Spectroscopy)
IR	infrared
MIR	Mid Infrared
NIR	Near Infrared
OEG	Oligo(ethylene glycol)
PEG	Poly(ethylene glycol)
PMIRRAS	Polarisation Modulation Infrared Reflection Absorption Spectroscopy
PY	Percus-Yevick
RAIRS	Reflection Absorption InfraRed Spectroscopy
ρ	value of the scattering length density (neutrons)
SAM	self-assembled monolayer
SAXS	Small-angle X-ray Scattering
SFG	Sum-frequency generation
σ	surface roughness
SLD	scattering length density
χ^2	(normalised) least-square sum (chi-square)

207

E. Photographs of experimental setup

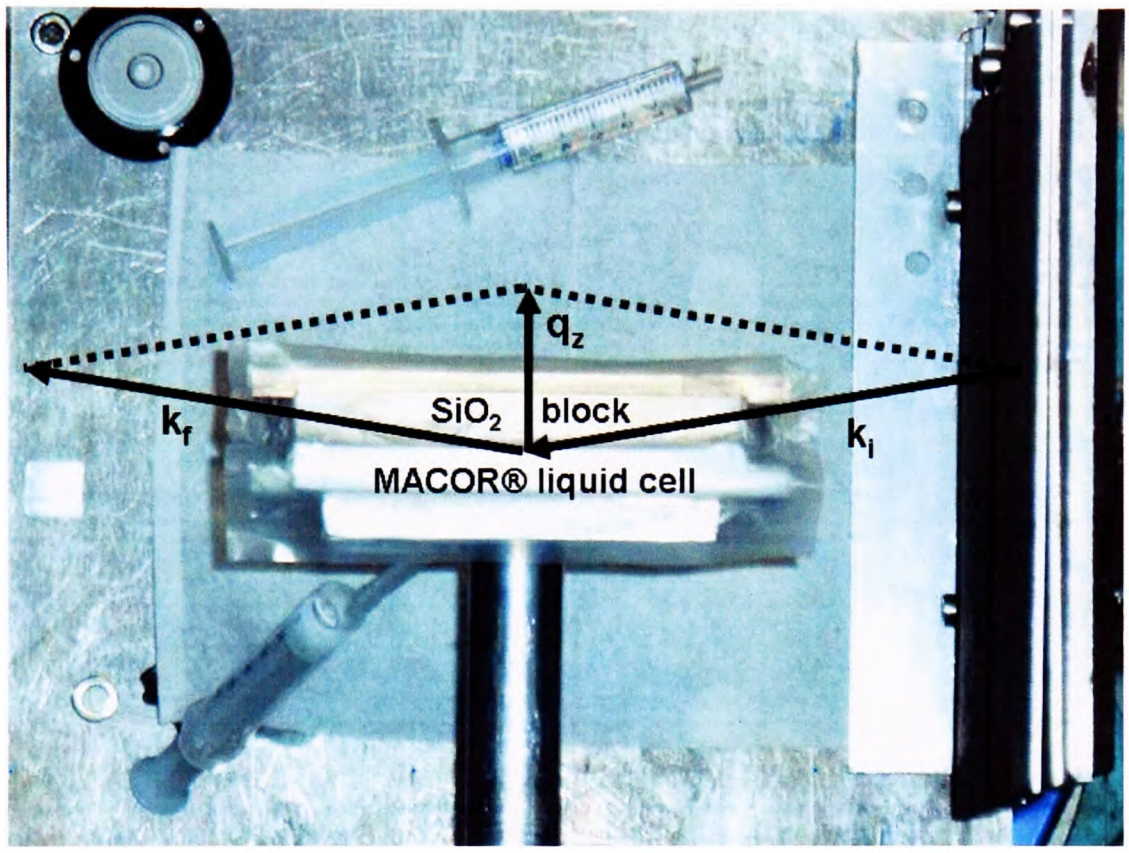


Figure E.1.: Photograph of the liquid cell for neutron reflectivity. Assembly of quartz block on the MACOR liquid cell.

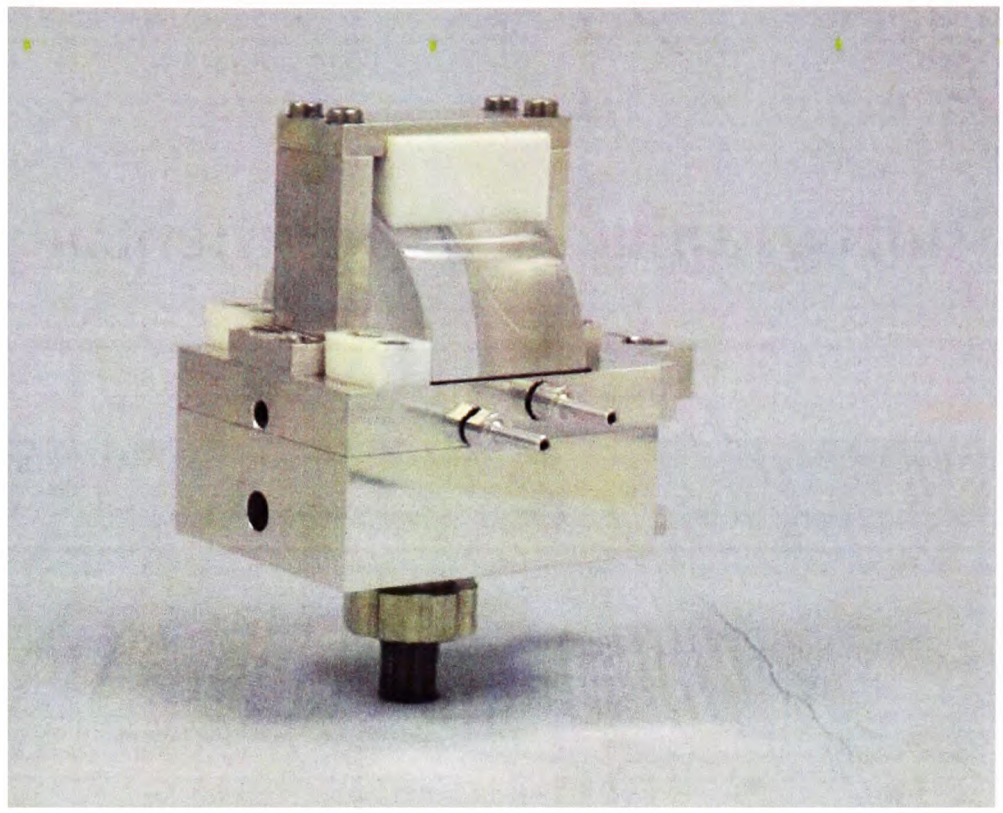


Figure E.2.: Photograph of the liquid cell for PMIRRAS shown assembled with the barium fluoride half cylinder.

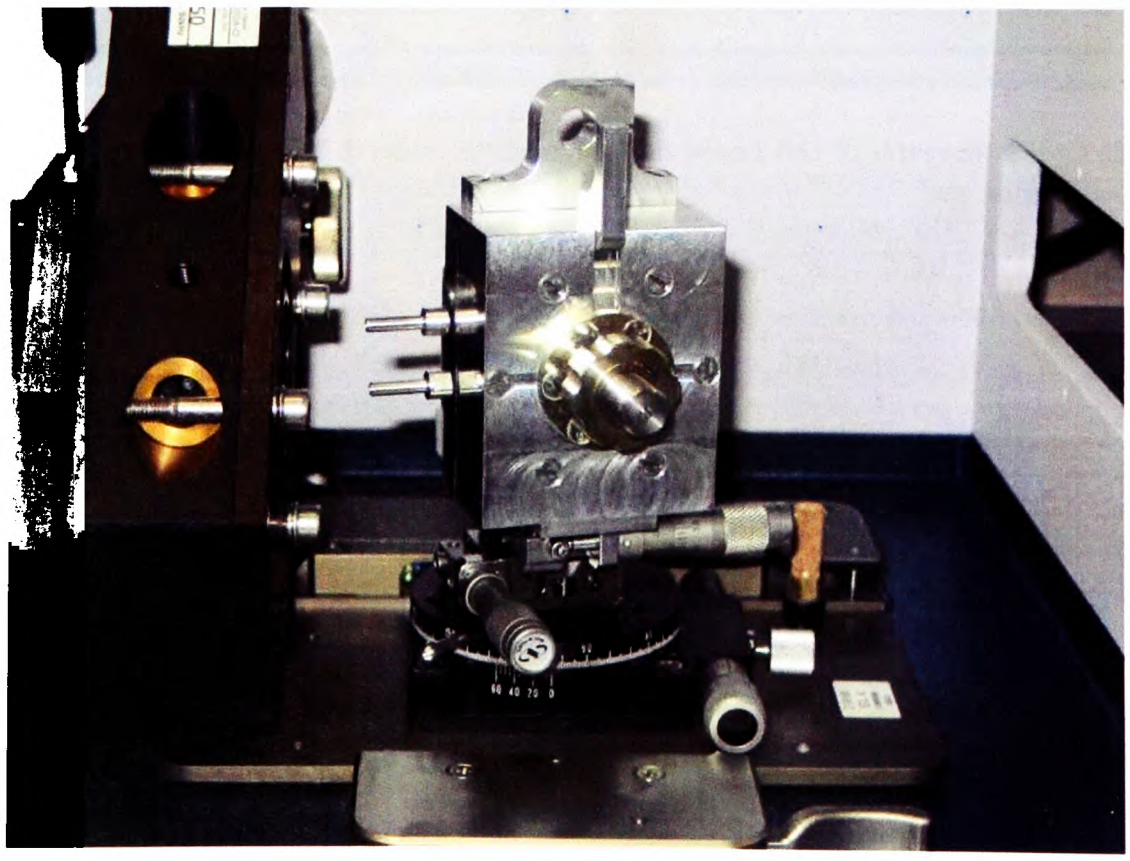


Figure E.3.: Photograph of the liquid cell for PMIRRAS mounted on the translation-rotation stage (side view).

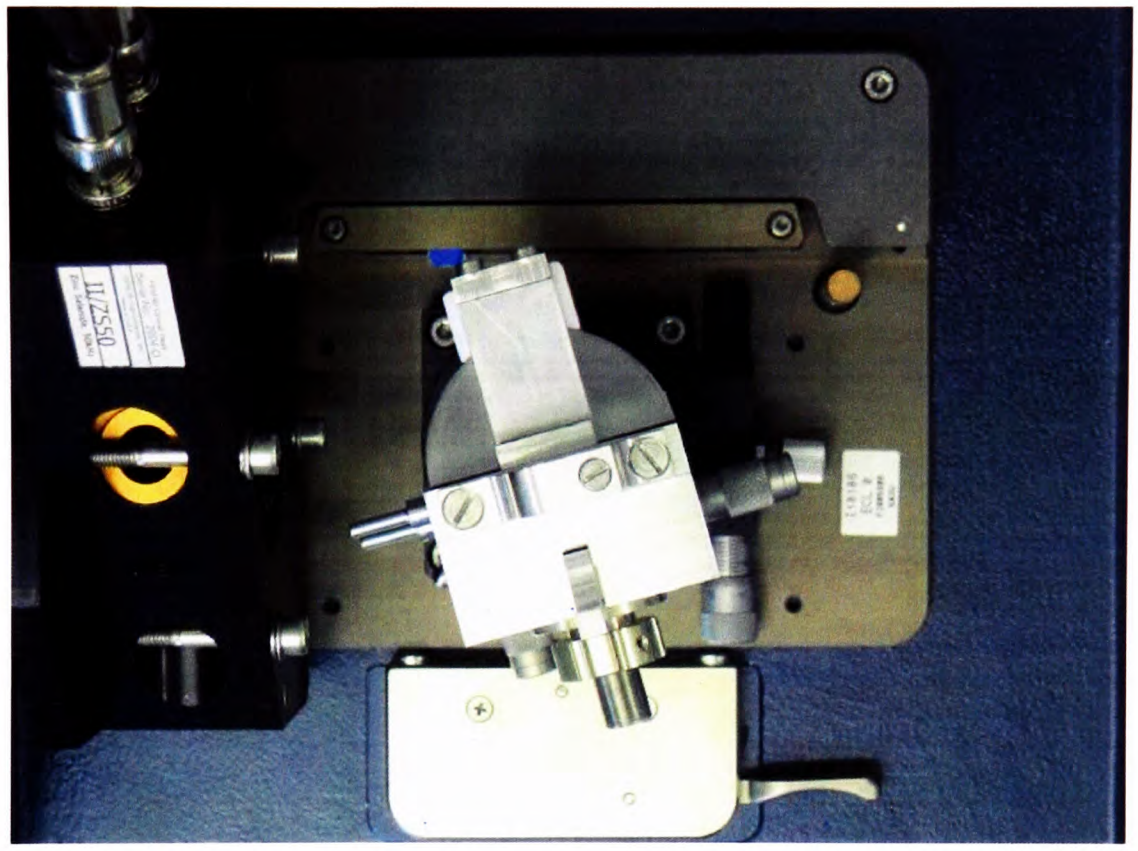


Figure E.4.: Photograph of the liquid cell for PMIRRAS mounted on the translation-rotation stage (top view).